HYBRID NANOCOMPOSITES FOR PHOTOCATALYTIC APPLICATIONS

Ph. D Thesis

Bhabhina N M

HYBRID NANOCOMPOSITES FOR PHOTOCATALYTIC APPLICATIONS

Thesis

Submitted to the Faculty of Science

University of Calicut in Partial Fulfilment of the

Requirements for the Degree of

DOCTOR OF PHILOSOPHY

By

BHABHINA. N. M

Under the Guidance of

Dr. SINDHU. S

Department of Nanoscience and Technology

University of Calicut

Kerala-673635

June – 2018

UNIVERSITY OF CALICUT
Department of Nanoscience & Technology

Calicut University P.O.,
Kerala, 673635, INDIA
✆ 0494 2407373, 2407374
Email:nanohod@uoc.ac.in
www.universityofcalicut.info

CERTIFICATE

This is to certify that the thesis entitled "**Hybrid Nanocomposites for Photocatalytic Applications**" is a bona-fide record of research work carried out by Smt. Bhabhina N M, under my supervision in partial fulfilment of the requirements for the award of the degree of Doctor of Philosophy in Nanoscience and Technology of the University of Calicut. The plagiarism check is carried out and this work or part thereof has not been presented before for the award of any other degree. Also certify that she has incorporated the suggestions and corrections pointed out by the examiners in the revised thesis.

Dr. Sindhu. S

(Supervising Guide)

Assistant Professor

Department of Nanoscience and Technology

University of Calicut

DECLARATION

Certified that the thesis bound herewith is an authentic record of the work on "**Hybrid Nanocomposites for Photocatalytic Applications**" carried out by me under the supervision of Dr. Sindhu S, Assistant Professor, Department of Nanoscience and Technology, University of Calicut in partial fulfilment of the requirements for the award of the degree of the Doctor of Philosophy of the University of Calicut, and further that no part thereof has been presented before for any other degree.

University of Calicut

29/ 06/ 2018 **BHABHINA N M**

This thesis is dedicated to my parents and in-laws

For giving me strength and firm support to chase my dream

ACKNOWLEDGEMENT

This thesis is the culmination of my journey of Ph.D and when looking back with a sense of fulfilment, I humbly realize that a great many people including my family members, friends, lab-mates, well-wishers and various institutions have significantly contributed to accomplish this huge task. It's my fortune to gratefully acknowledge their generous co-operation and splendid support throughout the research tenure.

Foremost, I wish to express my deepest gratitude to ***Dr. Sindhu S,*** *Assistant professor, Department of Nanoscience and Technology, University of Calicut for giving me a chance for doing the work under her supervision. I sincerely thank her from the bottom of my heart for her unwavering support, motivation, encouragement and patience from the start of the project till date. Her own zeal for perfection, passion, scientific ideas, and unflinching courage has always inspired me to do more. I will remain grateful and truly indebted to her throughout my life time.*

No research is possible without requisite facilities and infrastructure. Special acknowledgement requires for my institute, ***University of Calicut*** *and my department,* ***Nanoscience and Technology*** *for providing me excellent facilities, materials and resources for my research. Also I feel very grateful to Council for Scientific and Industrial Research (****CSIR****) for funding my research.*

I would like to thank ***Dr. Mohammed Shahin Thayyil****, former co-ordinator, Department of Nanoscience and Technology, for all the help rendered during the course. My heartfelt thanks are due to Smt.* ***Dhanya K*** *and Smt.* ***Thasneema K K,*** *non-teaching staffs of our department and* ***Sangeetha T G****, Librarian of our department. Special thanks to* ***Mr. Krishnakumar K*** *and* ***Mr. Mani****, former assistants of Nanoscience and Technology for their help from the earlier stages of the project.*

I will remain ever grateful and indebted to ***Abdul faizal****,* ***Maya Ravunni*** *(Research scholars, Dept. of Botany),* ***Dr. Sujith A*** *(Asst. professor, NITC) and* ***Suja P Sundaran*** *(Research scholar, NITC) for their valuable assistance during the application study of my samples. Also with my heart and soul I thank* ***Dr. Soney Vargheese*** *(Assistant professor, NITC, Calicut),* ***Nishaina Sahadev*** *and* ***Rose Mary*** *(Research scholars, NITC, Calicut) for their help in sample analysis.*

I take this opportunity to express my sincere gratitude to my teachers ***Dr. Devadasan K K*** *(Rtd. Professor, Department of Chemistry, MCC, Calicut) and* ***Dr. Sheeba P S*** *(Associate professor, Department of chemistry, MCC, Calicut), who introduced me to my supervisor. Besides, I take this opportunity to remember with gratitude the teachers of my alma mater, Malabar Christian College:* ***Dr. Marykutty, Dr.Susanna Seth, Dr. Sudhakaran K, Dr. Rema V T, Dr. Haris C, Dr. Sreejith M Nair, Lt. Elsy Shereena, Dr. Prajila*** *and* ***Ms. Jeeja Rani****. Also, The teachers of Providence Women's College,* ***Smt. Meenakshi, Smt. Lakshmi Devi, Dr. Gigy Abraham, Sr. Neetha*** *and* ***Sr. Asha,*** *who mentored me during the under graduate years, are fondly remembered.*

To my labmates, ***Dr. Jabeen Fatima M J, Dr. Niveditha C V, Nijisha P, Dharsana M V, Rajitha R, Jyothilakshmi V P,*** *thank you for extending helping hands in many critical moments. Special thanks to* ***Sreed Sharma, Ajisha P C, Saneesh P, Jithin*** *and other M.Tech students of Nanoscience and Technology. Also I convey my sincere thanks to* ***Dr. Krishna priya*** *and* ***Sreelakshmi****. The friendship with all of you will remain a sweet experience to be cherished forever. Special thanks to* ***Mrs. Seena*** *for designing the cover page of my thesis.*

I respectfully acknowledge my uncles, ***Sri. Jayaprakash*** *and* ***Sri. Aneesh babu,*** *who inspired and motivated me in early stages of my life with their knowledge and values. Had they not given me their thoughts of wisdom and inspiration, I wouldn't have relentlessly pursued this enlightening journey.*

My heartfelt regards goes to my parents, ***Smt. Prabhavathi*** *and* ***Sri. Bhaskaran*** *for the care, pain and sacrifices they have made to shape my life and giving me liberty to choose what I desired. Salute to my lovely brother,* ***Bhabhith*** *and sister in law,* ***Deepthi*** *for their enduring love and support. Words would never say how grateful I am to my father in law,* ***Sri.Viswanathan*** *and mother in law,* ***Smt. Saraswathi****, for their encouragement. I greatly value their evergreen love and deeply appreciate their unconditional support. Big thanks to my brother in law,* ***Visal*** *and sister in law,* ***Shima*** *for their help and co-operation. I owe thanks to my better-half,* ***Vikas*** *for helping me to keep things in perspective. His continued and unfailing love, understanding and support always keep my spirits up. I appreciate my little angel,* ***Dyuthi*** *for the patience she showed during my hectic schedule as a researcher.*

'Finally, humble thanks to Almighty for everything He has given me'

BHABHINA N M

CONTENTS

LIST OF FIGURES & TABLES

LIST OF PUBLICATIONS

1. **Bhabhina N M,** P A Faisal, Jabeen F M J, Dharsana M V, Sindhu S, Shining black nanoscopic ternary zincospiroffite: A panchromatic light harvester for depollution, *Mater. Des.*, **2019**, 165, 107600.
2. **Bhabhina N M,** Sindhu S, Bromine-Induced Defects in Anion-Deficient Zinc Oxide as Stable Photocatalysis Promoters, *Chemistry Select*, **2018**, 3, 13345-13354.
3. **Bhabhina N M,** Rajita R, Sindhu S, Surface modification of oxygen-deficient ZnO nanotubes by interstitially incorporated carbon: a superior photocatalytic platform for sustainable water and surface treatments, *Appl. Nanosci.,* **2018**, 8 (6), 1545-1555.
4. **Bhabhina N M**, Nijisha. P, Sindhu S, Anchoring of polymeric precursor on oxygen deficient ZnO nanotubes: A chelation assisted combined nucleation-growth-dissolution synthesis strategy, *Mater. Des.*, **2017**, 130, 426-432.
5. **Bhabhina N M**, Nijisha P, Niveditha C V, Rajita R, Sindhu S, Inorganic–organic semiconductor hybrid nanocomposite for anti-corrosion applications, *Mater. Today Proceedings,* **2018**, 5 (8), 16380-16387
6. Nijisha P, **Bhabhina N M,** Sindhu S, Application of gel electrolyte in dye sensitized solar cells, *Nanosystems: Physics, Chemistry, Mathematics,* **2016**, 7 (4), 752–754.
7. Rajita R, **Bhabhina N M,** Dharsana M V, Sindhu S, Green synthesis of zinc oxide nanoparticles using extract of averrhoa bilimbi and their photoelectrode applications, *Mater. Today Proceedings,* **2018**, 5 (8), 16472-16477.
8. Niveditha C V, Jabeen Fatima M J, Rajita R, **Bhabhina N M,** Sindhu. S, Effect of number of cycles in potentiodynamic deposition of p-type copper oxide and its supercapacitor applications, *Mater. Today Proceedings,* **2018**, 5 (8), 16419-16458.

9. Nijisha P, **Bhabhina N M**, Sindhu S, Comparative monitoring of organic and organometallic dye performances on quasi solid state dye sensitized solar cell, *J. Nanoparticle Res*, **2019**, Under Review.
10. Rajita R, **Bhabhina N M**, Nijisha P, Niveditha C V, Sindhu S, Metal photocatalysis by red and black nano-gold colloids: A rational design through green pathway, *Mater. Res. Express*, **2019**, Under Review.
11. Dharsana M V, Nijisha P, **Bhabhina N M**, Sindhu S, Highly stable ethylene glycol capped blue emitting antimony selenide quantum dots via hydrothermal approach, *Appl. Nanosci*, **2019**, Under Review.
12. Rajita R, Niveditha C V, Nijisha P, **Bhabhina N M**, Sindhu S, The deterministic role of resonance energy transfer in the performance of bio-inspired colloidal silver nanoparticles incorporated dye sensitized solar cells, *Mater. Res. Bull*., **2019**, Under Review.

BOOK CHAPTERS

1) **Bhabhina N M**, Sindhu S, Bio-epistem: An anthology of research papers in science, Edited by P K Babu, MES publishers (2018) **ISBN: 978-93-5321-814-0**
2) **Bhabhina N M**, Ajisha P C, Dharsana M V, Jyothilakshmi V P, Sindhu S, Advanced polymeric systems: Applications in nanostructured materials, composites and biomedical fields, Edited by Satheesh Babu, River publishers, 2018, Accepted
3) Nijisha P, **Bhabhina N M**, sindhu S, Application of nanostructured materials for energy and environmental technology, Chapter 36, Pages 145-148, Edited by Rajendran V, Manivasakan P, Geckeler K E, Bloomsberry publishing India Pvt. Ltd. (2015) **ISBN : 978-93-85436-91-8**

ACHIEVEMENT

- **ACS Best Poster Award - International Conference on Chemistry and Physics of materials (ICCPM-2018), Thrissur, 19-21 December 2018.**

CONFERENCE PRESENTATIONS

1. **Bhabhina N M** and Sindhu S, Hybrid Semiconductor Nanocomposites as Photocatalyst; The Current Scenario, *National Seminar on Materials Chemistry (MCS-2014), Providence Women's College, Calicut,* October 30-31, **2014**
2. **Bhabhina N M,** Jabeen Fatima M. J and Sindhu S, Surface Morphology Enhances Photocatalysis ; An Observation on Dye Degradation, *National Seminar on Materials Chemistry (MCS-2014), Providence Women's College, Calicut,* October 30-31, **2014**
3. **Bhabhina N M,** Nijisha. P, Niveditha C. V, Rajita Ramanarayanan, and Sindhu S, Inorganic – organic semiconductor hybrid nanocomposite for Anti-corrosion applications, *International Conference on Material Sciences (SCICON-16), Amrita Viswavidya Peetham, Etimadai,* December 19-21, **2016**, **ISBN 978-93-86176-47-9**
4. **Bhabhina N M,** Jyothilakshmi V P and Sindhu S, Highly Crystalline Thermally Stable Polymer Hybrid Nanocomposite for Solar Photocatalysis, *Second International Conference on Advanced Polymeric Materials (ICAPM 2017), MG University, Kottayam,* 7-9 April **2017**
5. **Bhabhina N M,** Ajisha P. C, Dharsana M. V, Jyothilakshmi V. P and Sindhu S, Synthesis and Characterisations of Polymer-Metal Oxide Hybrid Nanocomposites for Photocatalysis: A Comparative Study,*4th International conference on Nanoscience and Nanotechnology (ICONN-2017), SRM University, Chennai,* 9-11 August **2017**

6. **Bhabhina N M,** Sindhu S, Influence of non-metal dopant on the photocatalytic efficiency of ZnO nanotubes, *International conference on material science and technology (ICMST-2018), VSSC, Thiruvananthapuram,* 10-13 October **2018**

7. **Bhabhina N M** , Sindhu S, Enhanced Photocatalytic Activity by Polymer Assisted Black ZnO Nanotubes for Water and Surface Treatments, *International conference on Chemistry and Physics of materials (ICCPM-2018), St. Thomas' College, Thrissur,* 19-21 December **2018**. **ISBN 978-81-935819-1-9**

8. **Bhabhina N M,** Sindhu S, Carbon as photocatalytic promoter in zinc oxide nanotubes**,** *MESMAC international conferences 2019, D. G.M. M. E. S College, Mampad*, 15-17 January **2019**. **ISBN: 978-93-5321-814-0**

9. Nijisha P, **Bhabhina N M** and Sindhu S, Application of gel electrolyte in dye sensitized solar cells, *International Conference on Nanomaterials and Nanotechnology (Nano-15) December 07-10*, **2015**

10. Nijisha P, **Bhabhina N M** and Sindhu S, Quasi solid state electrolyte : An alternative to liquid electrolyte in DSSC, *Fourth International Conference on Frontiers in Nanoscience and Technology (Cochin Nano-2016) Februvary 20-23*, **2016**

11. Rajita R, **Bhabhina N M**, Dharsana M V and Sindhu S, Green synthesis of zinc oxide nanoparticles using extract of averrhoa bilimbi and their photoelectrode applications, *International Conference on Advanced Materials (SCICON-16) December 19-21*, **2016**, **ISBN 978-93-86176-47-9**

12. Ajisha P C, **Bhabhina N M** and Sindhu S, Synthesis of Polymer Nanocomposites for Photocatalytic Applications, *Second International Conference on Advanced Polymeric Materials (ICAPM 2017), April 7-9,* **2017**

13. Dharsana M V, **Bhabhina N M**, Jyothilakshmi V P and Sindhu S, Antimony selenide electrodeposition optimisation over TiO_2 photoanode for photovoltaic application,

International conference on Nanoscience and Nanotechnology (ICONN 2017), SRM University, August 9-11, **2017**

14. Jyothilakshmi V P, **Bhabhina N M**, Dharsana M V and Sindhu S, Low temperature wet chemical synthesis of Lead sulphide, *International conference on Nanoscience and Nanotechnology (ICONN 2017), SRM University, August 9-11,* **2017**

15. Fadeela C U, Dharsana M V, **Bhabhina N M**, and Sindhu S, *International conference on Nanoscience and Nanotechnology (ICONN 2017), SRM University, August 9-11,* **2017**

16. Niveditha C V, Jabeen Fatima M J, Rajita R, **Bhabhina N M** and Sindhu S, Effect of number of cycles in potentiodynamic deposition of p-type copper oxide and its supercapacitor applications, *International Conference on Advanced Materials (SCICON-16) December 19-21,* **2016**, **ISBN 978-93-86176-47-9**

ABBREVIATIONS

Sl No	Full Form	Abbreviations
[1]	Advanced oxidation process	AOP
[2]	Polychlorinated dibenzodioxins	PCDDs
[3]	Polychlorinateddibenzofurans	PCDFs
[4]	Ultra-Violet	UV
[5]	Band gap	Eg
[6]	National Nanotechnology Initiative	NNI
[7]	Highest Occupied Molecular Orbital	HOMO
[8]	Lowest Unoccupied Molecular Orbital	LUMO
[9]	Zinc Oxide	ZnO
[10]	Polyvinylpyrrolidone	PVP
[11]	Potassium Bromide	KBr
[12]	Tellurium powder	Te
[13]	X-ray Diffraction	XRD
[14]	Fourier Transform Infrared Spectroscopy	FTIR
[15]	Energy Dispersive Spectroscopy	EDS
[16]	X-ray Photoelectron Spectroscopy	XPS
[17]	Electronic Spectroscopy for Chemical Analysis	ESCA
[18]	Diffuse Reflectance Spectroscopy	DRS
[19]	Photoluminescence Spectroscopy	PL
[20]	Scanning Electron Microscopy	SEM
[21]	Transmission Electron Microscopy	TEM
[22]	Selected Area Electron Diffraction	SAED

[23]	Methylene Blue	MB
[24]	Oxygen Vacancy	V_0
[25]	Superoxides	O_2^-
[26]	Hydroxyl free radicals	OH^o
[27]	Volatile Organic Compounds	VOC
[28]	Terephthalic Acid	TTA
[29]	2-Hydroxy terephthalic acid	HTTA
[30]	Polyaniline	PANI
[31]	PANI/ZnO nanocomposite	PNZ
[32]	PVP/ZnO nanocomposite	PVZ
[33]	PANI/PVP/ZnO nanocomposite	PPZ
[34]	PANI/PVP blend	PP
[35]	Carbon embedded ZnO using PANI	CPNZ
[36]	Carbon embedded ZnO using PVP	CPVZ
[37]	Carbon embedded ZnO using PANI&PVP	CPPZ
[38]	Infra-red	IR
[39]	Density of States	DOS
[40]	Dimethyl sulfoxide	DMSO
[41]	Emeraldine salt of polyaniline	ES
[42]	Bromine doped ZnO	DZ
[43]	Zinc Tellurium Oxide	ZTO
[44]	*Escherichia. Coli*	*E. Coli*

Foreword…..

The last few decades have witnessed a phenomenal growth in the manifold applications of Nano materials. Besides paving way for a number of innovative industrial applications, the scientific communities across the globe recognises the role of semiconductor nanoparticles in mitigating the ill effects of large scale industrial pollution. The ability to fine tune the band gap and surface area of these semiconductor nanoparticles makes them the ideal candidates for such explorations. The hybrid materials formed through doping or embedding other organic/inorganic/polymer materials on the surfaces of these nanoparticles exhibit several powerful, unique characteristics derived from the synergy of the components. When it comes to environmental remediation, these nanosystems open up a plethora of possible applications with minute quantities and the usage of solar power.

The zinc oxide nanoparticles, with their comparatively easier synthesis, biocompatibility and superior efficacy, have a distinct advantage over others, thanks to their ability to degrade a broad range of pollutants. Among the various physical and chemical synthesis approaches sol-gel synthesis method is found to be economic, simple, repeatable and easy size tunable route for nanomaterials. When solubility of precursors comes into consideration hydrothermal method is the next easy, cost effective method for the synthesis of highly crystalline phase pure materials.

The present work is concerned with the synthesis of zinc oxide nanosystems by employing minimum precursors using sol-gel method. The effects of varying concentrations of precursors on the properties of ZnO nanosystems were studied in detail. Among the three ZnO nanotubes with varying surface properties, the one which exhibit increased

photocatalytic activity was used for further studies. Hybrid nanocomposites of ZnO were prepared with polymeric assistance. In addition to this, experimenting with various percentages of dopants were done and monitored closely the photocatalytic improvements. Moreover, novel nanoparticles of zincospiroffite were synthesized through hydrothermal approach and their photocatalytic activity was studied. Further, the generation of reactive oxygen species (OH^o) was analysed through experimental technique.

Chapter 1 puts forth a brief introduction on the significance of the photochemical advanced oxidation processes (AOP) over non photochemical AOPs for the environmental depollution processes. The advantage of using solar energy as a renewable energy source for the environmental remediations is explored in detail. Here a brief outline is given on the attempts to exploit the unique properties of nanomaterials as photocatalysts on such futuristic applications as water purification, antifogging and anti-bacterial remedies.

Chapter 2 concerned with the precursors used in synthesising various nanosystems, the relative advantages of sol-gel and hydrothermal methods used for the synthesis and the various basic characterization techniques undertaken to analyse their properties were discussed in detail. The characterisation of the synthesized powdered samples includes structural, morphological and optical analysis. Structural characterizations includes X-ray diffraction, Raman Spectroscopy, Energy dispersive spectroscopy, X-ray photoelectron spectroscopy and Fourier transform infrared spectroscopy. The morphological analysis was done by scanning electron microscopy and transmission electron microscopic techniques. The optical characterizations were analysed with spectroscopic techniques such as diffuse reflective spectroscopy and photoluminescence spectroscopy.

The experimental works are divided into four chapters in which ***Chapter 3*** deals with the synthesis of zinc oxide nanotubes and analysis of their physicochemical

characteristics. Here the precursor concentrations were optimized so as to obtain highly active photocatalyst. The antibacterial activity and the hydrophilic nature of the synthesized nanoparticles were tested.

Chapter 4 explains how hybrid nanocomposites of zinc oxide were prepared with polymer assistance. Two polymers, polyaniline and polyvinylpyrrolidone, were chosen for the study. Carbon embedded ZnO obtained from the post thermal treatment of the polymer encapsulated ZnO were analysed and their photocatalytic activity got compared. Antibacterial activity and hydrophilicity of the synthesized samples were analysed.

Chapter 5 focused on bromine doped ZnO nanocomposites. Using KBr precursor, various percentages of bromine doped ZnO systems were synthesized and compared their properties. Besides, their photocatalytic activity was tested by monitoring their efficiency in degrading a textile dye. Among the four samples, the highly active photocatalyst was further tested for its antibacterial and anti-fog activities.

Chapter 6 depicts synthesis, characterisations and dye degradation studies of a novel photocatalyst $Zn_2Te_3O_8$. The hydrophilicity of the material is monitored by measuring contact angles. The material's efficacy in inhibiting pathogenic microbes was also studied.

In ***Chapter 7***, all the results were compared and detailed interpretations were made on them. Myriads of futuristic applications that can be achieved by enhancing the properties of these materials are mentioned.

Though pure ZnO is a potential photocatalyst for curing various environmental remedies, its properties can be tuned by the addition of impurities to explore its maximum performance. Doping enhances the activity of pure ZnO by inducing defects in the ZnO

crystals. The synthesis protocol as well as selection of precursors also turns out to be crucial players for getting ideal photocatalyst.

The current work is an effort to develop various zinc based photocatalysts with enhanced photocatalytic efficiency for better water purification, antibacterial and anti-fogging activity. The development of fabrics and ceramic tiles, with antibacterial properties built into them, is a highly promising concept for tackling the challenges of pollutants. Photocatalysts incorporated fabrics and ceramic tiles are attractive propositions on grounds of hygiene also.

The prospects of achieving better photocatalytic activity by fine tuning the size and morphology of the zinc oxides through opting different reaction methods, adjusting the pH of the precursor solutions, adopting various precursors or doping with other elements are envisaged here. Moreover these synthesized nanomaterials can be successfully used for various other futuristic photovoltaic and sensor applications. Surface engineering of these materials remains to be explored comprehensively by varying reaction temperature, reaction methods and changing the alkaline precursor. Metals or rare earth nanoparticles decorated ZnO nanosystems are another avenue for advanced photocatalytic technology. Reduced graphene oxide or carbon dots can be incorporated with these doped systems for enhanced photocatalytic performances.

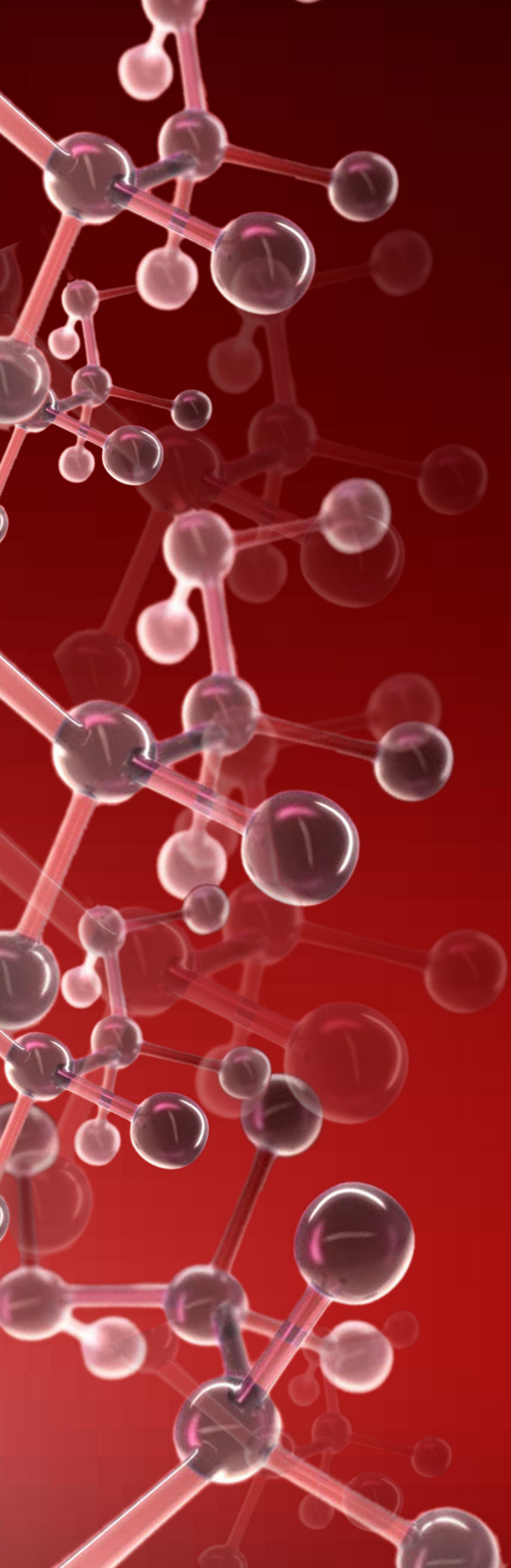

Chapter 1

Introduction

1 Introduction

1.1 Advanced Oxidation Process (AOP)

In our times, one of the foremost challenges that an environmental engineer has to tackle originates from a plethora of organic wastes[1, 2]. The hectic industrial and commercial activities have made the threat all the more grave by the last decades of the 20th century. Earlier, these hazardous organic pollutants ended up in landfills and the oceans making things rather complicated. The conventional method of incineration is widely accepted as a viable alternative. But the incineration practised as of now gives rise to serious problems in the form of toxic compounds including polychlorinated dibenzodioxins (PCDDs) and polychlorinateddibenzofurans (PCDFs)[3]. These hazardous materials released to the environment amidst the incineration process as offgas emissions and fly ash cause further ecological disasters.

Undoubtedly, rapid industrialization combined with urbanisation has taken its toll on the world's water resources. Treatment of contaminated water leaving minimal impact on the environment and that has been recognised as a formidable challenge by scientific communities across the globe. Initially, scientists focused on the removal of the pollutants by the simple coagulation and biological process[4]. But the soluble dyes cannot be degraded by these coagulation processes. Moreover, by the last decades of the 20th century these physic-chemical and biological methods of waste water treatment attained the status of mature technology necessitating to advanced methods[5]. The developing technologies have to address the ambitious limits put forward by the regulatory bodies. Moreover, the industrial waste

water treatment has become much more intricate with the micro-organisms in biological processes failing to attack the complex molecules of anthropologic pollutants. The lackluster performance of conventional treatment methods was the prime motivator for the search of novel processes and operating conditions promoting their efficiency.

Advanced oxidation processes (AOPs), earlier proposed for drinking water treatment in 1980's, have made considerable progress and further studies are being conducted on utilizing them in treating various kinds of waste water. The AOPs are a family of similar but not identical technologies that by and large centers around the production of highly reactive hydroxyl radicals[6]. AOPs takes place adopting either of the two routes explained below

A) Normal combustion, which includes the oxidation process at ambient temperature conditions (Wet Air Oxidation at 200-300^{o}C)

B) Oxidation using highly reactive intermediate species produced from high energy oxidants (OH^{o} free radicals)

Among these two processes, AOPs using OH free radicals are highly sustainable because these highly reactive oxidizing species can mineralize and degrade the organic contaminants completely. Moreover the powerful and non-selective nature of this chemical oxidant enables it to react with most of the contaminants near ambient temperature and pressure. These OH free radicals can be generated by various non-photochemical (without using light energy) and photochemical (using light energy) processes as illustrated below.

Non-photochemical processes

- Ozonation at higher pH (>8.5)
- Ozone (O_3) + hydrogen peroxide (H_2O_2)
- Ozone (O_3) + catalyst
- Fenton systems (Fe^{2+}& H_2O_2)

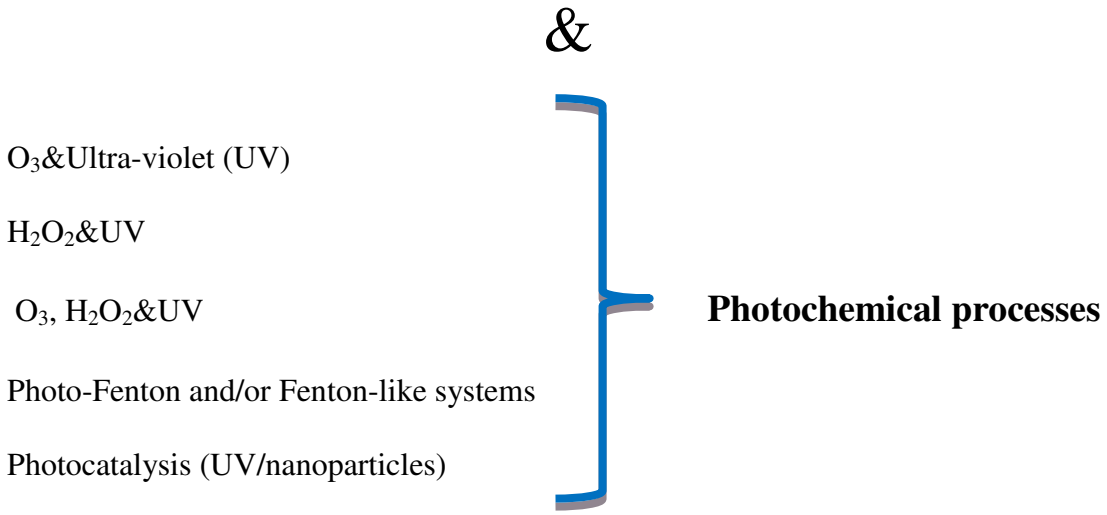

Decontamination by way of non-photochemical method fails in mineralizing or oxidizing the organic matters completely. Moreover, additional treatments are required for the completeness of the process. The incomplete oxidations might produce even more toxic by-products than the initial compound. By supplementing ozone or H_2O_2 oxidation with light radiations, complete oxidative destruction of the organic matters can be assured. This advantage has turned the photochemical methods to the most sought after decontamination technology.

1.1.1 Photochemical processes

Photochemical processes are initiated by the absorption of light energy from the UV or visible region of the spectrum consequently transient high energy excited states have been developed within the molecules. To lower the energy of these excited electrons, various photophysical and chemical reactions proceeded simultaneously through electron transfer reactions. A light source must be employed for photochemical reactions to provide required activation energy for the excitation of the molecules. The efficiency of the light absorption by the molecules is depending upon its electronic structure and wavelength of the light used for exposure. The high energy intermediates generated which can overcome large activation barriers within a short time is the main advantage of photochemical processes which cannot

be accessed by thermal reactions.

Generally the photochemical products determined by the efficiency of the light source used. Commonly used light sources are UV lamps, Flash lamps, incoherent excimer lamps, and solar light. The conventional photochemical processes for water treatments are classified as follows:

1.1.1.1 Ozone with UV radiation (O_3&UV)

Ozone releases OH free radicals by absorbing UV radiations as shown in equations below:

$$O_3 \xrightarrow{h\upsilon} O_2 + \frac{1}{2}O_2 \rightarrow (1)$$

$$\frac{1}{2}\ O_2 + H_2O\ \rightarrow H_2O_2\ \rightarrow (2)$$

$$H_2O_2\ \rightarrow 2OH^o\ \rightarrow (3)$$

But the photolysis of ozone requires high pressure mercury lamps making the method all the more expensive. To make things worse, some of the ozonation by-products are still being evaluated as carcinogenic[7].

1.1.1.2 Ozone, hydrogen peroxide with UV radiation (O_3, H_2O_2&UV)

Here hydrogen peroxide accelerates the ozonolysis in presence of UV radiations. For the pollutants which are not prone to degrade with the effect of UV radiation, the external addition of hydrogen peroxide is more beneficial. The reaction will happen as shown below:

$$O_3 + H_2O_2 \xrightarrow{h\upsilon} 2OH^0 + \frac{3}{2}O_2 \rightarrow (4)$$

1.1.1.3 Hydrogen peroxide with UV radiation (H_2O_2&UV)

Photolysis in presence of UV radiations converts hydrogen peroxide directly to OH free radicals and this process limits itself to the effective destruction of chlorinated compounds. The reactions involved in the processes are as show below:

$$2H_2O_2 \underset{\leftarrow}{\rightarrow} 2HO_2^- + 2H^+\ \rightarrow (5)$$

$$2HO_2^- \xrightarrow{hv} 2OH^0 + O_2 \rightarrow (6)$$

1.1.1.4 Photo-Fenton and/or Fenton-like system

Photo-Fenton oxidation systems involve addition of Fe^{3+} with H_2O_2/UV processes. The steps involved in the processes are given below:

$$2Fe^{3+} + 2H_2O \rightarrow 2Fe(OH)^{2+} + 2H^+ \rightarrow (7)$$

$$2Fe(OH)^{2+} \xrightarrow{hv} 2Fe^{2+} + 2OH^0 \rightarrow (8)$$

This type process predominantly depends on strength of UV irradiation as OH free radicals are generated mainly under UV irradiation. Also lower pH is mandatory (pH ~3) for the formation of $Fe(OH)^{2+}$ formation.

Photochemical water purification in the presence of H_2O_2 oxidant claims numerous advantages such as economic availability, generation of two hydroxyl radicals from the photolysis of one H_2O_2 molecule, infinite water solubility and simple procedure for the process. On the flipside, the main disadvantages include the lower absorption cross section of H_2O_2 at 254 nm. Moreover the formed OH free radicals are easily trapped by HCO_3^- and CO_3^{2-} and releases CO_3^{o-}. Further reactions are proceeded by these carbonate species and these generated carbonate radical anion oxidants have less oxidation potential than OH free radicals.

1.2 Nanomaterials for technology development

Nanotechnology is concerned with matter at dimensions of the order of one billionth of a meter (nanoscale). According to ASTM International, nanotechnology refers to materials having at least one dimension approximately between 1and 100 nm. When the material size reaches to nanoscale, their molecular organizations become different and exhibits different optical, magnetic and electrical properties[8].

M.C Roco is an eminent key architecture of the National Nanotechnology Initiative (NNI). He categorized the growth of nanotechnology into four generations. In the first

generation (2000 onwards) includes the formation of coatings or films by incorporating nanoscale elements. The second generation (2005 onwards) includes functional nanoscale elements. These nanomaterials can function in response to pH, temperature etc. The third generation (2010 onwards) is represented by multiscale architectures and three dimensional nanosystems. Contemporary research deals with fourth generation (2015 onwards) where heterogeneous systems can function at the molecular level[9, 10].

The dominance of quantum effects and increased surface area of nanomaterials contributes to high physical strength and chemical reactivity for various fascinating applications. As reactions mainly takes place at the surfaces of the particles, the decrease in particle size substantially increase the reactivity[11]. The relationship between nanocrystal sizes with the percentage of atoms that can aggregate on the surface comes obvious from the graph in Figure 1.1.

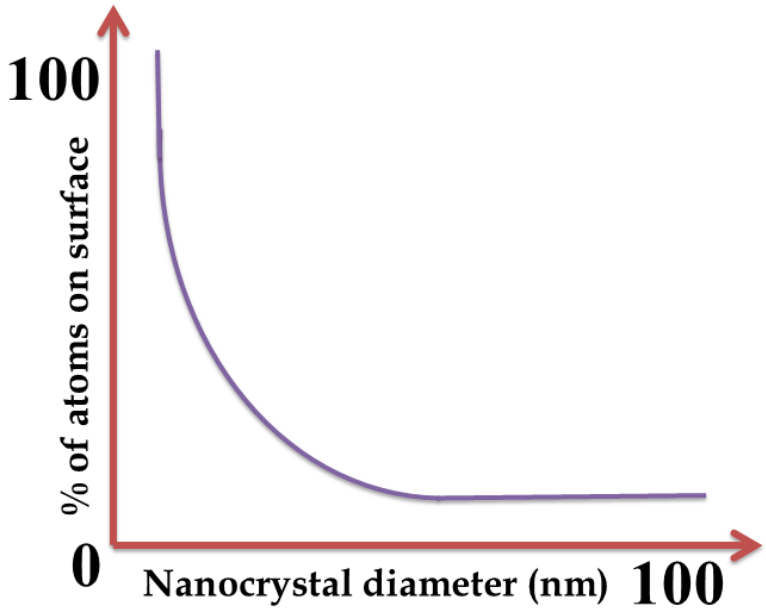

Figure 1.1 Percentage of atoms on surface with respect to size of nanomaterials

A transient polarity arises on a portion of nanoparticles because of the instantaneous shift in their electron density. The developed small charges attracted/repelled to opposite/similar charged nanoparticles lead to weak or transient intermolecular forces called

Vander Waals forces. The Brownian movements of nanoparticles are due to these transient intermolecular forces where nanoparticles are attracted to each other by Vander Waals forces via physisorption and repelled by electrostatic forces. Because of these unique properties, nanomaterials behave differently in environment and human body compared to their bulk/macro-dimension materials. The most striking feature of using nanomaterials in various futuristic applications is that only small quantity is needed for extensive applications.

1.3 Semiconductor nanomaterials

Semiconductor materials are of having conductivity either by the flow of electrons or by the positively charged holes presents in the materials and they exhibit conductivity in between conductors and insulators[12]. The electrical and optical properties of the semiconductors change drastically as a function of size as per the quantum confinement (when the size of the particle approaches Bohr's radius of an exciton). In bulk materials, the electronic motions are not restricted dimensionally, whereas size reduction restricts or confines electronic motions resulting in quantum well/quantum films, quantum wires and quantum dots[13]. The quantum confinement effect and quantization of density of states in various semiconductor nanostructures are depicted in Figure 1.2.

- ✓ Quantum well/ Nanofilm (two dimensional) – Electronic motions are confined in one dimension and free in other two dimensions
- ✓ Quantum wire/ Nanotubes (one dimensional) – Electronic motions are confined in two dimensions and free in other one dimension
- ✓ Quantum dot (Zero dimensional) – Electronic motions are confined in all three dimensions

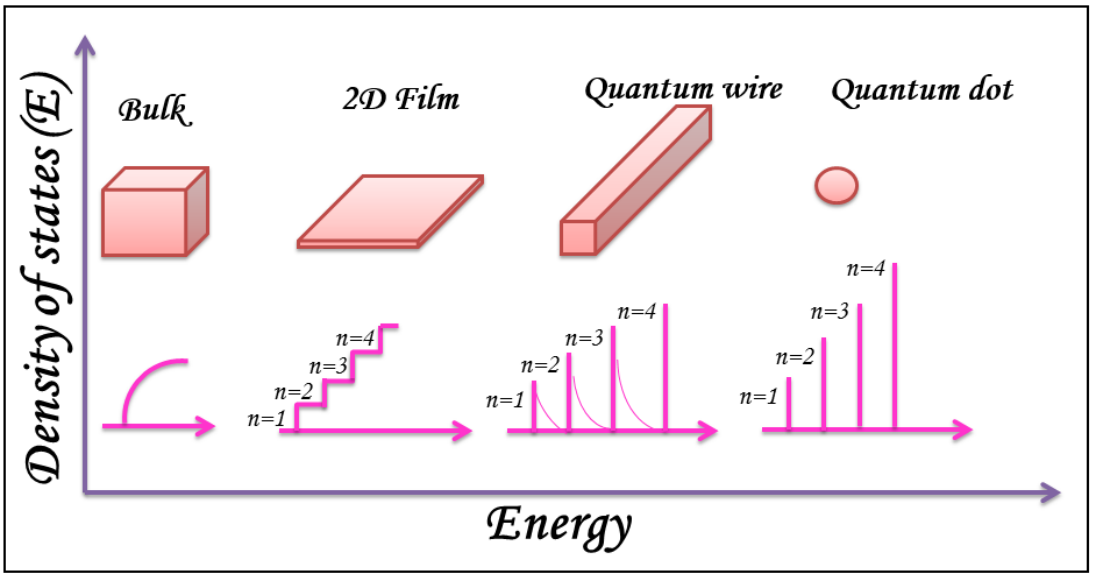

Figure 1.2 Density of states with respect to quantum confinement

The molecular energy levels combines to form energy bands in semiconductors and an electronic excitation takes place from completely filled valence bands to empty conduction bands during light exposure. The minimum energy required to excite an electron from the valence energy level to the conduction energy level equivalent to or greater than its bandgap energy (Eg). Bulk semiconducting materials have composition-dependent bandgap energy and generally the bandgap of the nanoscale materials increases compared to their bulk bandgaps[14]. When the particle absorb light photon of energy greater than or equal to Eg, excitation of electrons from the valence band to conduction band take place, leaving behind a hole. In the presence of an electric field, these negatively charged electrons and positively charged holes constitute current to an external circuit. Photo induced electrostatically bound electron-hole pair with minimum energy is called an exciton and the size of the exciton within the crystal is called Bohr exciton diameter. When the nanocrystal diamensions become smaller than this Bohr exciton diameter, the charge carriers become spatially confined with increased energy resulting in size dependant absorption and fluorescence spectra with discrete electronic transitions. The annihilation of the excitons with the emission of a photon

is called radiative recombinations. When the recombination of charge carriers happens with the release of phonon instead of photon, then it is called non-radiative recombinations[15].

In addition to inorganic semiconductors, organic semiconductors are also investigated for various applications[16]. Organic semiconductors are non-metallic in nature exhibiting semiconducting properties, in which the molecules are held together by a weak vander waal's force. Polyaniline, C_{60} etc are examples of organic semiconductors[17]. Polyaniline is widely used for the removal of contaminants through adsorption process[18]. Like inorganic semiconductors (Conduction band and valence band), organic semiconductors have discrete HOMO-LUMO energy levels.

1.4 Defects in crystals

Nanomaterials possess very small sizes compared to their bulk. Decrease of particle size accompanies with an increase of surface area thereby altering the stoichiometry of nanomaterials from its bulk, leading to different defects in the crystal. The chances of misplacing/missing (vacancies) ~~o~~f one or more atoms from its lattice sites or presence of another atom (dopant) forms defects and these types of defects arise from single atoms are called point defects (zero dimensional defects). To reduce the surface energy, point defects are normally segregated on the surface. While doping, a foreign atom is introduced in to the crystal that can bring or remove electrons to or from the solid thereby changing its electronic as well as optical properties[19]. By controlling the growth conditions and added impurities, the defects can be tuned in the nanosystems.

If the position of the entire string of the atoms is misplaced in crystal, it leads to line defects or dislocations (1D defect). Mechanical properties of metal nanocrystals can be tuned based on these dislocations as these defects are responsible for the plastic deformations. When a whole plane of atoms is missing from the crystal or misplaced, then 2D defects arises. Such type of defects are called stacking faults[20].

Defects in a crystal introduce energy levels within the bandgap, acting as trap levels, and avoid carrier recombinations[21]. Such cases the possibilities of non-radiative recombinations increase instead of radiative recombinations. Surface defects can be introduced through surface modifications which can be done either by doping or shape tuning of nanocrystals. One dimensional nanostructure such as nanorods, nanotubes or nanowires are more useful for environmental applications like photocatalysis. Nanomaterials possess significant number of surface atoms that enhances its chemical activity.

Many reports are available on the characterization of defects and their influence in adsorption and surface reactions[22]. Qualitative analyses such as photoluminescence and X-ray photoelectron spectroscopy give information on surface defects. Defects such as point defects and small dislocation loops are categorized in to defects of first kind. Defects of first kind present in the crystal redistribute the scattering intensity which leads to broaden or shift of the peaks in X-ray diffraction patterns[23]. Defects such as stacking faults, twin faults, long chains of impurities etc are included in defects of second kind. Asymmetrical peak broadening in XRD happens by the influence of defects of second kind.

Defects have significant role in the photocatalytic performance of a semiconductor metal oxide. These defects, has been highly promoted by the presence of defects in the crystal lattice. These defects can trap the photogenerated electrons and holes thereby these carriers are easily available for the generation of reactive oxygen species[24].

1.5 Zinc Oxide (ZnO)

The research on metal oxide semiconductors resulted in a paradigm shift in the effective utilization of renewable energy resources. The interest in photo induced redox reactions was spurred for the first time by Fujishima and Honda's 1972 discovery, that water could be split upon illuminating a TiO_2 single-crystal electrode[25]. Among many materials explored so far, Zinc based compounds are found to be the ideal candidate for photocatalytic

applications due to their cheap production methods, and eco-friendly nature. The compound Zinc Oxide was highly regarded by the Alchemist, who would burn zinc in air. The resulting white woolly tufts were called 'lana philosophica', ie, the philosopher's wool. Zinc oxide is one of the highly explored material due to its wide application potential such as white pigment in paints; a component in ointment for treating sun burn and sunscreen lotions; in dye sensitized solar cells, for making anti-microbial textile fabrics etc[26]. Figure 1.3 depicts ZnO powder and a typical wurtzite crystal structure of ZnO.

For the last few years nanosized ZnO gained much attention as a photocatalyst due to its distinct properties[27]. Various shapes and sizes of the nano ZnO are explored extensively due to its shape and size dependent chemical and physical properties. Though ZnO exist in various forms (rock salt, zinc blend and wurtzite), wurtzite ZnO is preferred because of its easy synthesis[28]. Synthesis of rock salt requires high pressure and zinc blend by growth on cubic substrates. Wurtzite ZnO shows high surface energy and activity compared to other two forms[29].

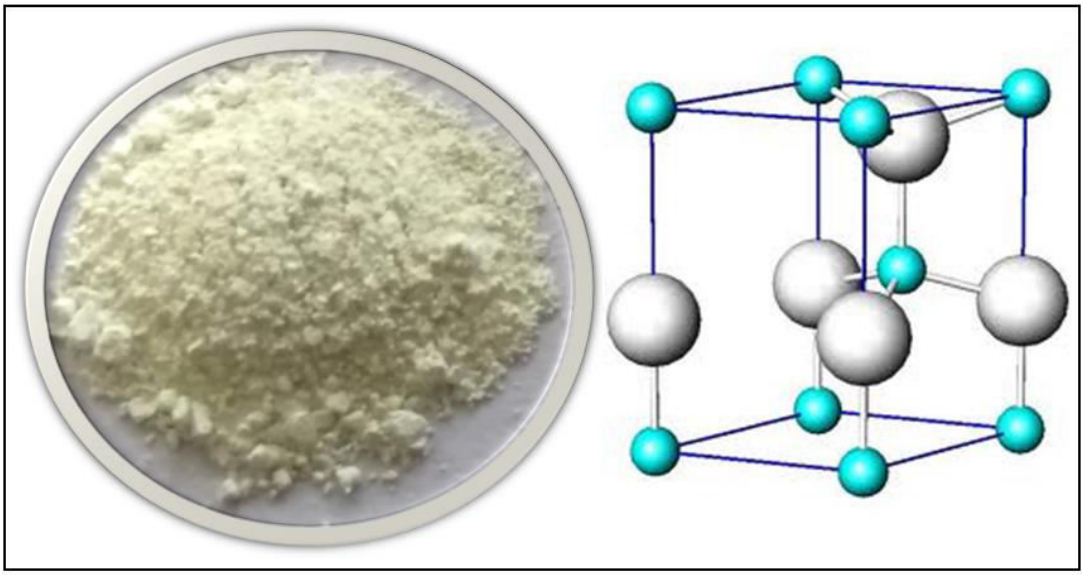

Figure 1.3 Photograph of ZnO nanopowder and crystal structure of wurtzite ZnO

1.6 Hybrid nanocomposites

Hybrid nanocomposites are multiphase materials in which one or more dimensions are in nanometer regime and exhibit either newer characteristics or a mix of the individual properties of their components. When these constituents are intimately mixed, it results in hybrid composites with high homogeneity and improved properties. Doped nanomaterials and nanocomposites come under the hybrid nanomaterials[30].

Nanocomposites usually have high interface surface area to volume ratios[31] with combinations of organic and inorganic building blocks. Nanocomposites can be prepared either by embedding inorganic particles in to organic matrix or vice versa and leads to an encapsulation or entrapments of particles in to a matrix instead of mixing[32]. Thus a nanocomposite encompasses a continuous phase (metals, polymers, ceramics etc) and dispersed phase (carbon particles, silica powders, glass fibers etc).[33] If the matrix of the nanocomposite is an organic material, it is called organic-inorganic hybrid materials; conversely they are named inorganic-organic. If inorganic or organic component do not represent matrix or filler, is referred to as nanocomposite hybrids.

Doped semiconductor nanomaterials are hybrid materials which can be prepared with ease through one-pot method. Doping process indicate the intentional addition of a foreign atom or an impurity to a host material to modify their electronic, magnetic and optical properties, functionalities and performances. These dopants can be metals, nonmetals or metalloids and can occupy at either substitutional or interstitial sites of host materials[30]. Most of the reports show that doped semiconductor nanomaterial photocatalysts perform better than undoped system[34]. Various characteristics of hybrid nanocomposites and their applications are depicted in Figure 1.4.

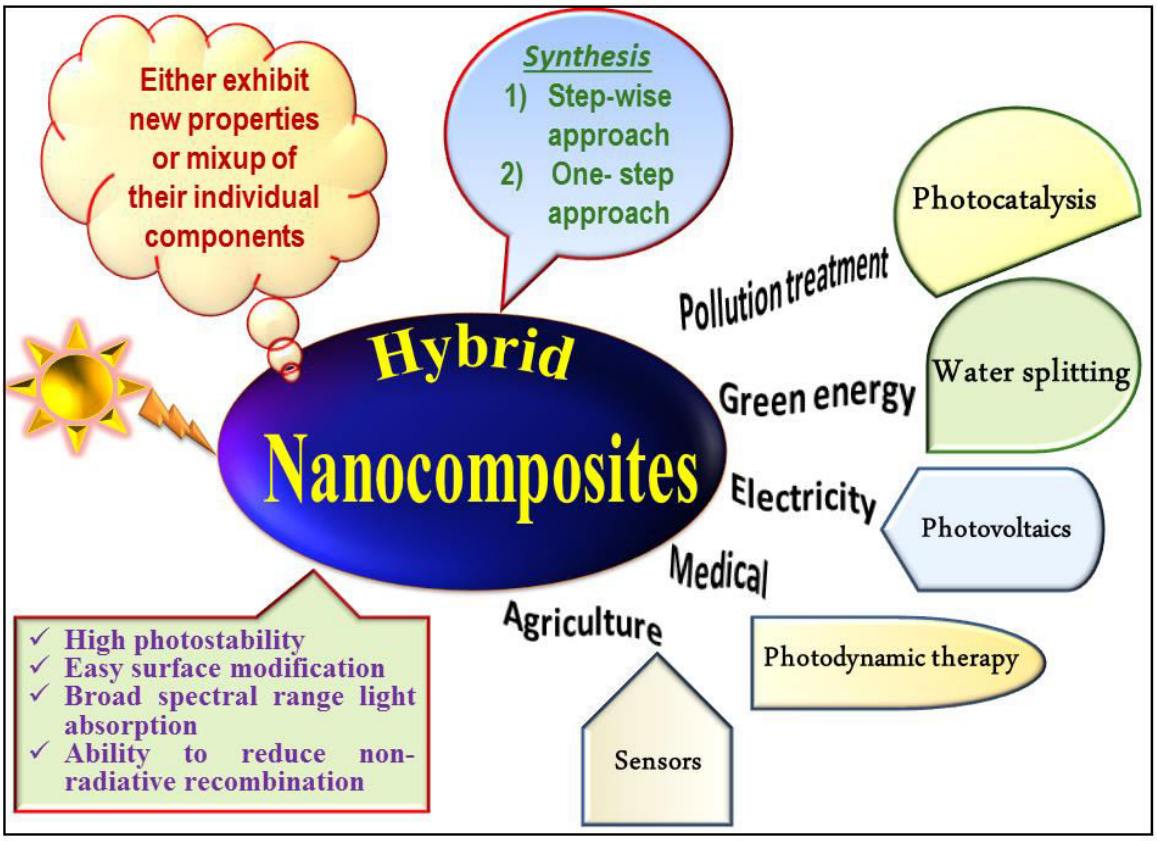

Figure 1.4 Characteristics of hybrid nanocomposites and their applications

1.7 Solar Energy – A sustainable source

Sun is one of the cooler stars (yellow in colour) in our 'milkyway galaxy'. The very presence of life on earth is indebted to the seemingly fine-tuned distance from the sun so as to ensure the perfect amount of energy for sustenance. Sun is a source of vast amount of energy and it radiates about 3.86×10^{26} joules of energy every second[35]. Relatively tiny fraction of this energy reaches on the earth's surface after a considerable loss in the atmosphere. The proper harness of this tiny part of renewable and reliable energy can create wonders in fulfilling the world's growing energy demands. So, we have to develop new materials and design suitable devices to capture solar energy efficiently and translate them into useful work, heat or other energy forms. So we have to design suitable devices and materials to capture its rays sufficiently and translate them into useful work, heat or other forms of energy. The energy emitted by the sun propagates in the form of electromagnetic radiations with a speed of 3×10^8

m/s containing ultra violet (3 – 5 %), visible (42 - 43 %) and infrared (52 - 55 %) radiations (from 0.3 – 4 µm) (Figure 1.5). An amount of 1000Wm^{-2} energy reaches earth's surface at noon time at the equator that can be utilized efficiently in accordance with the principle of energy conversion. Solar energy is a recurrent source of energy that can go a long way in meeting the ever widening energy demands of mankind.

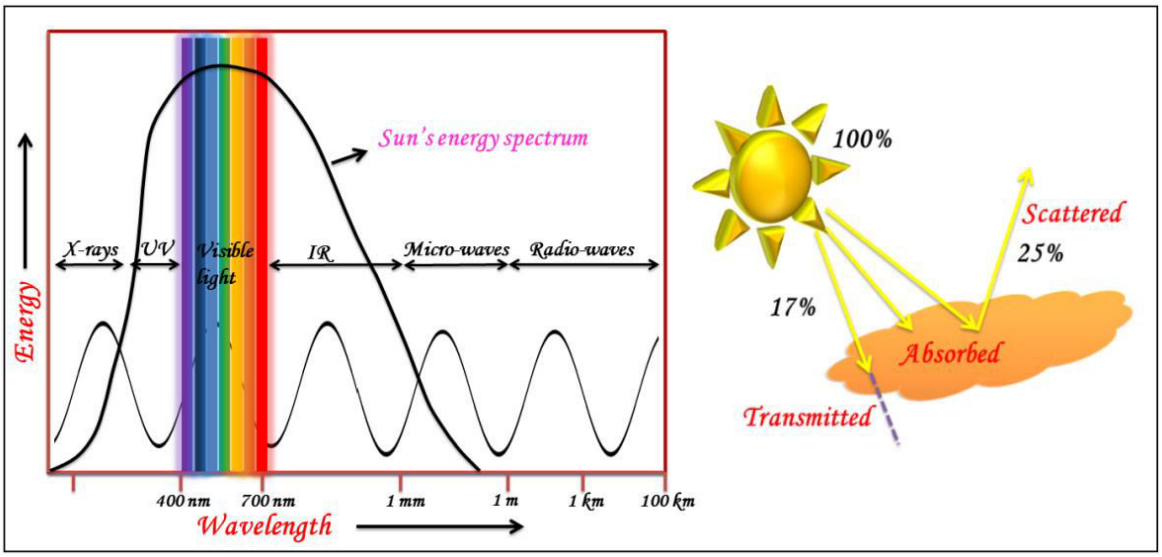

Figure 1.5 Solar energy spectrum reaching on earth's surface

Semiconductor nanomaterials have been extensively using solar energy for heterogeneous photocatalysis[36]. For the efficient utilization of solar energy, we have to develop application based materials able to absorb the entire region of solar spectrum. Moreover the material should be recyclable, cost competitive, earth abundant, easily designable, non-toxic, stable towards solar exposure, all at the same time.

1.8 Solar photocatalysis – A decisive step towards clean energy

Photocatalysis is a process in which a chemical reaction is initiated in the presence of light and gets accelerated by a catalyst. The photocatalysts speed up the photoreactions without undergoing any chemical change and without getting consumed in the reaction. Chlorophyll is the finest example for photocatalyst present in nature, which convert water and carbon dioxide into oxygen and glucose in presence of sunlight, whereas semiconductor

photocatalysts convert organic matters in to carbon dioxide and water[37]. Photocatalytic methods help addressing a bunch of environmental and energy related problems such as pollutant degradation, inhibition and disinfection of microbes and water splitting for hydrogen evolution.

Photocatalysis are of two types based on the phases involved in the chemical process: homogeneous and heterogeneous. Ozone and photo-Fenton systems are considered as homogeneous photocatalysis in which reactants and photocatalysts are in same phase. Semiconductors involved photocatalysis are heterogeneous, where the photocatalysts and reactants are in different phases.

In a heterogeneous photocatalysis, when light radiations hit on a photocatalyst it absorbs light energy having a wavelength equal to or greater than its band gap energy. This absorption of light energy triggers the ejection of electrons from the valence band of the photocatalyst. The ejected photoelectrons move to conduction band leaving holes behind in valence band. These photo generated carriers (excitons) is transported to the surface of photocatalysts to facilitate redox reactions. The photogenerated electrons help converting the surface adsorbed oxygen species to superoxide species whereas; the holes in the valence band generate hydroxyl free radicals from hydroxyl ions. These highly reactive oxygen species have the ability to degrade the adsorbed pollutant molecules on the surface of photocatalysts[38]. The pictorial representation of photocatalytic mechanism is as shown in Figure 1.6.

The highlight of using nanomaterials as photocatalyst is to enhance the performance efficiency and reusability of the photocatalyst, thereby making it as an economically viable efficient system. Photocatalysis has a distinct advantage over other physico-chemical methods as the byproducts are less harmful and easily removable. In order to explore the manifold possibilities for generating renewable energy, it is imperative to vary the parameters

and material components of the conventional photocatalysts.

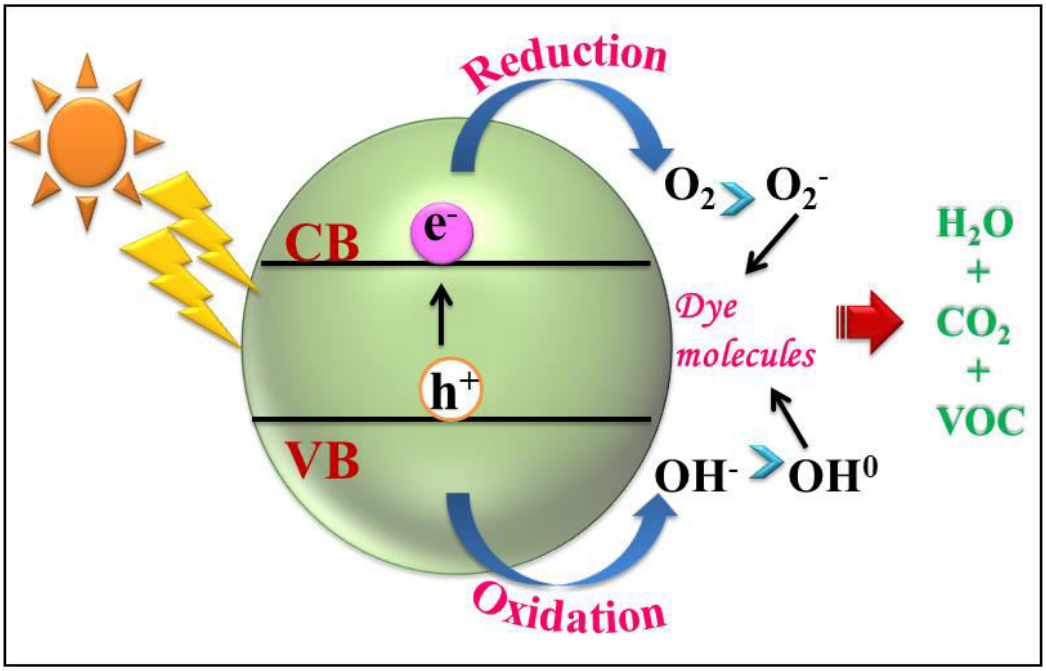

Figure 1.6 Mechanism of photocatalysis

A highly efficient photocatalyst should meet the following criteria[39]:

- ✓ Higher surface area
- ✓ Higher photon absorption coefficient
- ✓ Lower electron-hole recombinations
- ✓ High rate of photoelectrons and holes induced redox processes
- ✓ Good surface adsorption capability of photocatalyst
- ✓ Influence of bulk to surface defects
- ✓ Highly photostable, inexpensive and economical
- ✓ Chemically and biologically inert and recyclable

Photocatalytic degradation undoubtedly turns out to be an effective method to alleviate environmental hazards. Besides, the detoxification of water, photocatalytical methods can be employed in purifying air and in inactivating the pathogenic microbes. At ambient conditions, the semiconductor nanoparticles execute photocatalysis with moisture

present in the atmosphere and degrade the contaminants completely to CO_2, H_2O and other volatile compounds. Consequently photocatalysis can be applied in such diverse areas (Figutre 1.7) as water purification, Air purification, Anti fogging, Anti-bacterial and surface cleaning.

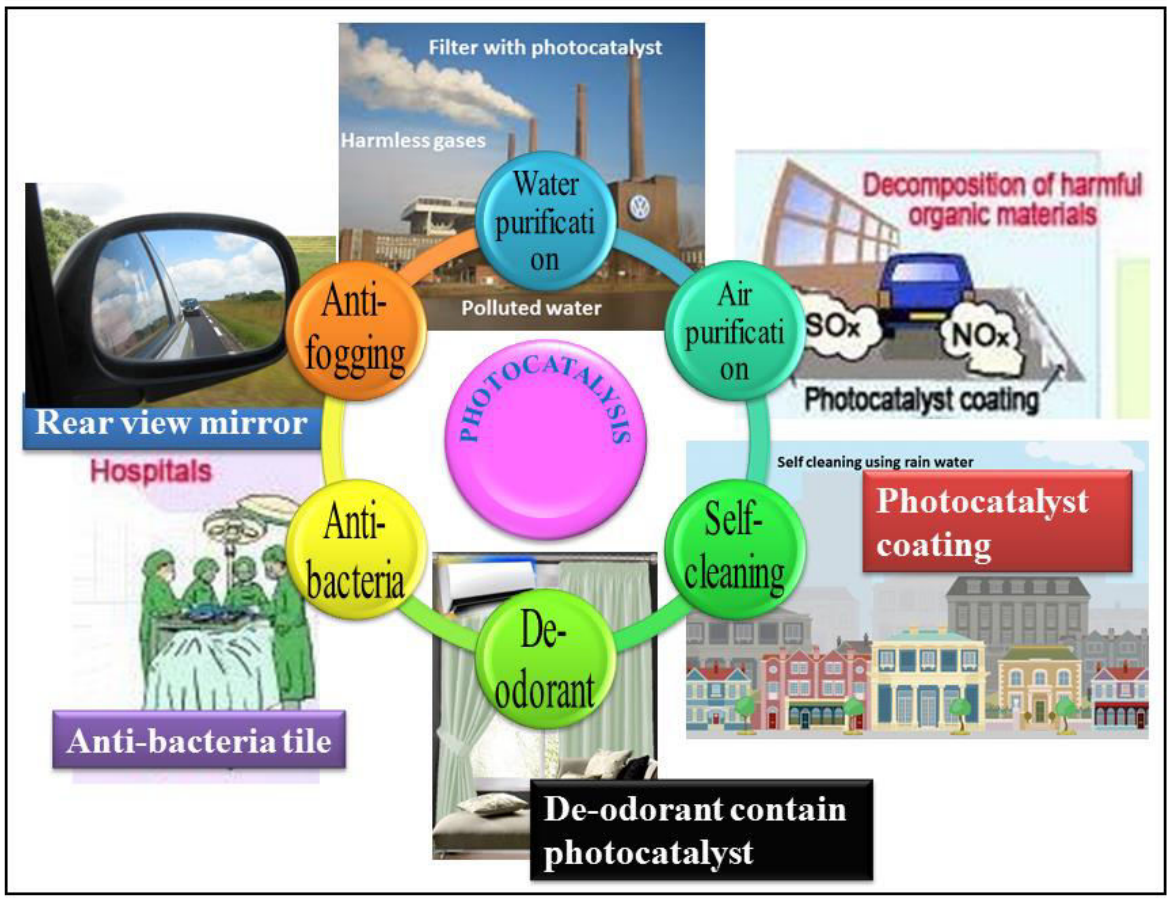

Figure 1.7 Applications of photocatalysis

1.9 Water purification

Contamination of naturally available water takes a heavy toll on our water resources creating alarmingly increasing health challenges for humans and aquatic organisms. In addressing water shortage, re-usage after purification is half the battle won. Colored synthetic dyes constitute the indispensable raw materials for several industries including textile, printing, pharmaceuticals, cosmetics, paper and color photography. Photocatalysis open up an exceptional pathway to purify the dischargeable waste water from the industries by the

potential usage of solar energy[40]. The removal of organic contaminants can be monitored in laboratory through decolouration during photocatalysis as shown in Figure 1.8.

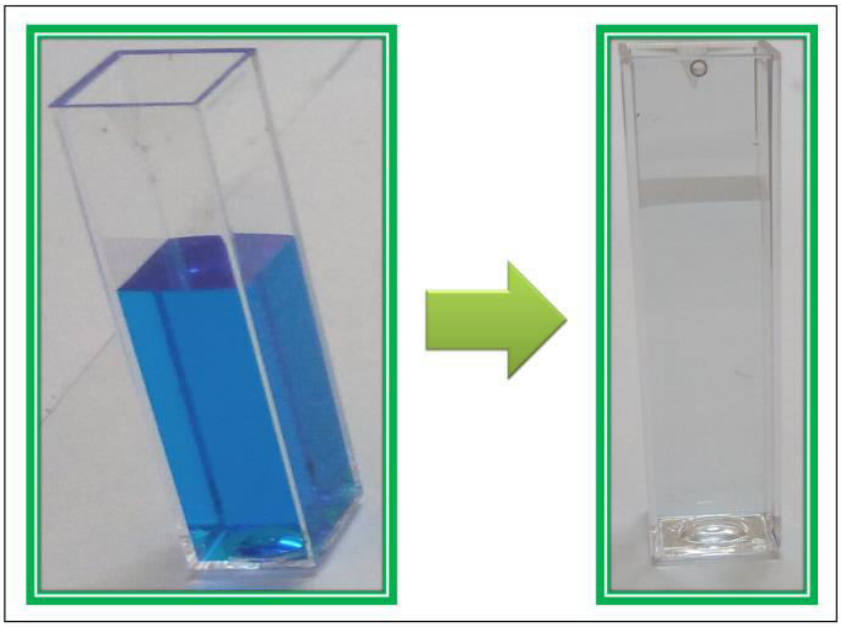

Figure 1.8 Decolorisation of dye in water by photocatalysis

1.10 Anti-fogging Activity

Water can easily spread on hydrophilic surfaces by making very small contact angles whereas super hydrophilic surfaces make a non-scattered film of water with contact angle less than 10^0 [41]. When this hydrophilicity of the materials gets coupled with gravity, the dust particles are swept away from the surfaces. Instead of forming droplets, on a super hydrophilic surface, the water form thin uniform optically clear sheet of films (Figure 1.9). Exterior walls of the building and rear view mirrors in vehicles usually get soiled from atmospheric dusts and external fumes. When the building materials or rear view glasses are coated with a nanomaterial photocatalyst, its combined action of hydrophilic, antifogging and self-cleaning ability washes away the dirt and clean the surfaces[42].

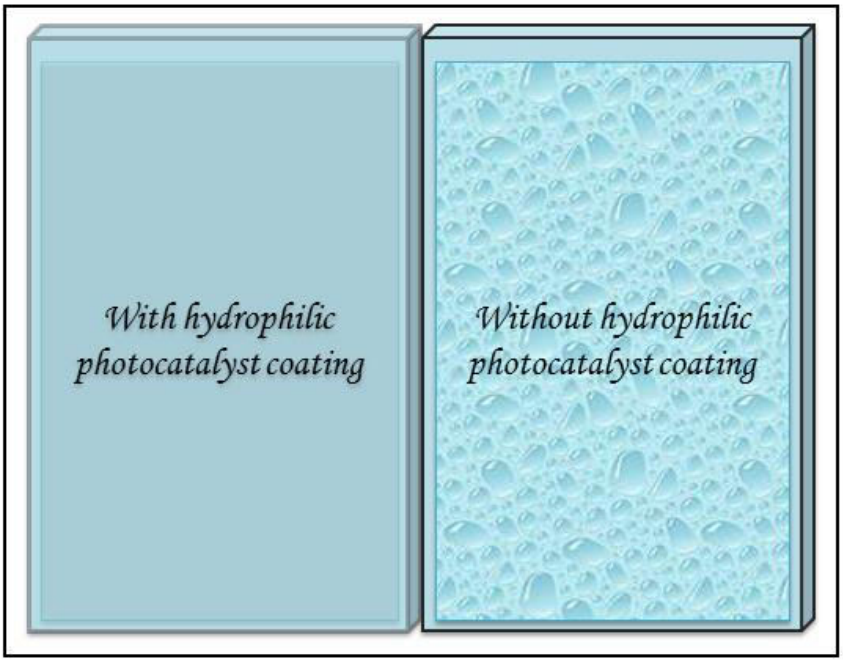

Figure 1.9 Glass surface with and without photocatalyst coating

1.10.1 Contact angle measurements

When water droplets present on a planar surface, the degree of wetting depends on the interfacial energy or surface tension between the liquid and the solid surface. The angle at which the liquid-vapor interface meets the solid surface is called contact angle. The contact angles can be either static or dynamic. If the water droplet is not moving on the horizontal planar surfaces, is called static contact angle and if the droplet is in motion on tilted surfaces, called dynamic contact angle. Dynamic contact angles are of two types, advancing or receding contact angles. The difference between the advancing and receding contact angle values is called contact angle hysteresis. Normally the advancing contact angle value is always larger than receding contact angle values. The contact angle pictures are depicted in Figure 1.10.

Young's equation describes the static contact angles in terms of interfacial surface tensions as shown in equation (9)

$$\Upsilon_{Sol-Vap} = \Upsilon_{Sol-Liq} + \Upsilon_{Liq-Vap}\, cos\theta \ldots\ldots\ldots\ldots (9)$$

Where, $\Upsilon_{Sol-Vap}$ is Solid-vapor interfacial tension

$\Upsilon_{Sol-Liq}$ is Solid-liquid interfacial tension

$\Upsilon_{Liq-Vap}$ is Liquid-vapor interfacial tension

And θ is the contact angle.

When cosθ is plotted against $\Upsilon_{Liq-Vap}$, a linear plot is obtain with negative slope. For complete wetting process, contact angle θ = 0° correspondingly the value of $\Upsilon_{Sol-Liq}$ is zero. Under these conditions surface tension is called critical surface tension Υ_{ct} and from Young's equation $\Upsilon_{ct} = \Upsilon_{Sol-Vap}$.

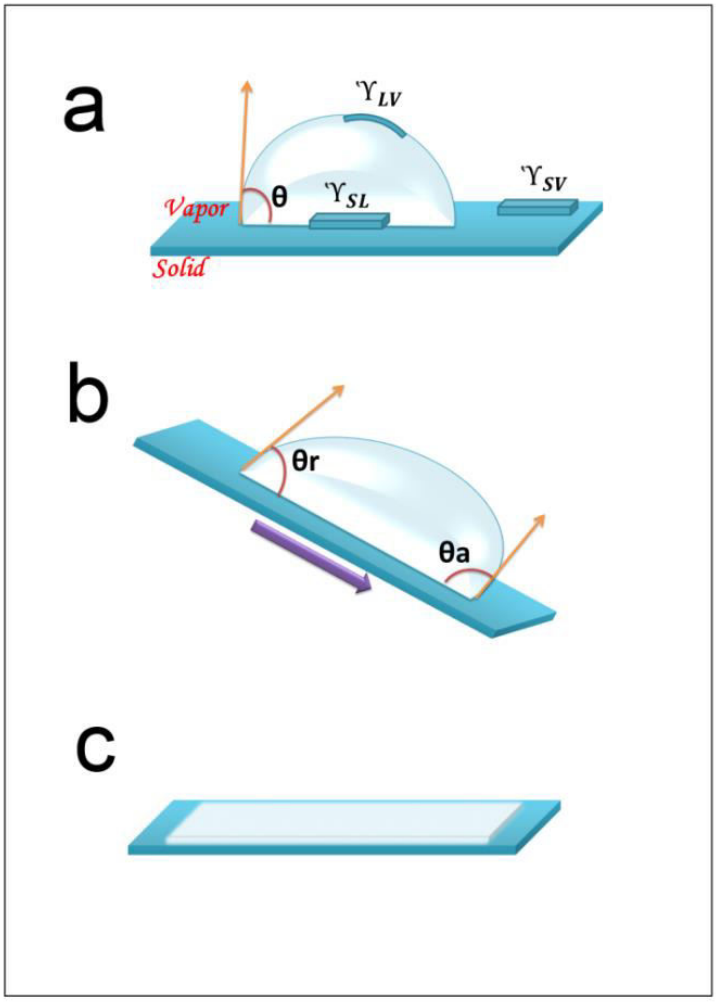

Figure 1.10 (a) A non-wetting liquid drop on a solid surface, (b) Running down the water drop with receding and advancing contact angles and (c) water spread on solid surface

1.11 Antibacterial Activity

The photocatalyst embedded ceramic wall tiles simultaneously ensures self –cleaning and bacterial inhibition properties with increased glaze[43]. Developing these types of bi-functional surfaces can go a long way in protecting the heritage monuments and in creating healthy public environments. Besides, these types of photocatalysts can be put in to use in the manufacturing textile fabrics with inherent ultraviolet protection, disinfection and self-cleaning properties[44].

Bacterial destructions by nanomaterials are takes place through four simultaneous steps.

1) Membrane dysfunctions through charge neutralizations.
2) Generation of reactive oxygen species in nanoparticles.
3) Release of respective ions from the nanocrystal lattices.
4) Internalization of nanoparticles in to the cell for complete destruction of cell[45]

Lakshmi prasanna *et al* reportes that ZnO exhibit antibacterial activity even in the absence of light or under diffused light [46]. The surface electric charges on the nanoparticles neutralize the charge on the cell wall thereby stopping the normal passage of nutrients in to the cell through cell wall. The reactive hydroxyl radicals (O_2^-, OH^o, H_2O_2) generated from nanoparticles play a critical role for the bacterial destruction, by entering into the intracellular part of the bacterial cell and damaging the DNA and chromosomes. The positive and negatively charged ions of the nanomaterilals also involved in damaging the cell as shown in Figure 1.11.

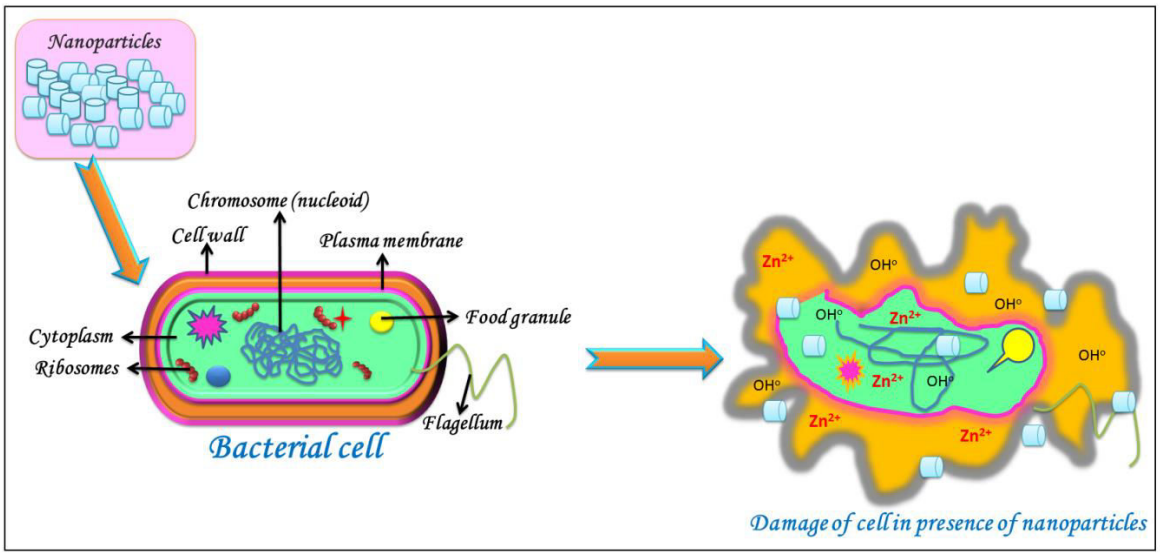

Figure 1.11 Mechanism of destruction of bacterial cell in presence of nanoparticles

1.12 Aim of the work

Semiconductor photocatalysis has been widely used for surface cleaning and water purification purposes because of its ability to degrade an extensive range of pollutants with the potential utilization of solar power. Aim of this work is to prepare pristine zinc oxide system and zinc oxide based nanocomposites with the usage of minimum precursors and a systematic study of these nanocomposites in the perspective of photocatalysis.

Zinc oxide nanotubes are decided to synthesize by varying the precursor concentrations to optimize their photocatalytic activity. Various nanocomposites are prepared by taking the most active photocatalyst among the three ZnO samples. Polymers such as polyaniline, polyvinylpyrrolidone and a polymer blend of these two polymers are used for preparation of carbon embedded ZnO nanotubes. Bromine incorporated ZnO nanotubes are also planned for synthesizing by doping of 2, 4, 6 and 8 wt% of bromine in ZnO. Additionally zinc tellurium oxide nanomaterial is also studied as a novel photocatalyst.

A detailed study on the physico-chemical properties of the prepared photocatalyst materials is planned following advanced methodologies. Structural characteristics and chemical compositions confirmation of synthesized nanomaterials are analyzed using X-ray

diffraction (XRD), Raman spectroscopy, Fourier transform infrared spectroscopy (FTIR), Energy dispersive spectroscopy (EDS) and X–ray photoelectron spectroscopy (XPS) analysis. Morphologies are obtained from scanning electron microscopy (SEM) and transmission electron microscopy (TEM) images. The absorption and emission properties are evaluated using diffuse reflectance spectroscopy (DRS) and photoluminescence (PL) measurements. Bandgaps obtained from corresponding Tauc plots drawn from absorption data.

The photocatalytic activity of the prepared photocatalysts is compared in various disciplines especially for environmental applications. In addition to this, water purification, surface hydrophilicity and bacterial inhibition studies are also planned with these synthesized photocatalysts. Water treatment process is checked by monitoring the dye degradation in presence of photocatalysts. Contact angle between the water and the photocatalyst coatings on a glass surface are measured for surface treatment and the antibacterial activity has been checked with the pathogenic microbes, *Escherichia Coli*. Additionally synthesized zinc tellurium oxide nanomaterial is studied as a novel photocatalyst and applied to all the above mentioned applications.

1.13 References

[1] X. Duan, H. Sun, S. Wang, *Acc. Chem. Res.,* **2018**, 51, 678-687.

[2] M. Sillanpaa, M. C. Ncibi, A. Matilainen, *J. Environ. Manage.* **2018**, 208, 56-76.

[3] R. Zhang, X. Wang, X. Zhang, C. Song, R. J. Letcher, C. Liu, *Environ. Sci. Technol,* **2018**, 52, 4402-4412.

[4] J. Cui, X. Wang, J. Zhang, X. Qiu, D. Wang, Y. Zhao, B. Xi, A. N. Alshawabkeh, X. Mao, *Environ. Sci. Technol.,* **2017**, 51, 8077−8084.

[5] W. Perren, A. Wojtasik, Q. Cai, *ACS Omega,* **2018**, 3, 3357−3364.

[6] V. L. Prasanna, R. Vijayaraghavan, *J. Phys. Chem. C,* **2017**, 121, 18557−18563.

[7] P. W. Seo, B. N. Bhadra, I. Ahmed, N. A. Khan, S. H. Jhung, *Sci. Rep.,* **2016**, 6:34462.

[8] K. Sellers, C. Mackay, L. L. Bergeson, S. R. Clough, M. Hoyt, J. Chen, K. Henry, J. Hamblen, *Nanotechnology and the Environment*,CRC Press Taylor and Francis group publisher, **2009**, ISBN-978-1-4200-6019-5.

[9] W. A. Goddard III, D. W. Brenner, S. E. Lyshevski, G. J.Iafrate, B. Raton, M. C. Roco, *National Nanotechnology Initiative-Past, Present and Future*, Taylor and Francis, **2007**.

[10] J. Chen, H. Doumanidis, K. Lyons, J. Murday, M. C. Roco, *National science and technology council, subcommittee on nanoscale science, engineering and technology*, National nanotechnology coordination office, **2007**.

[11] L. M. Gilbertson, E. M. Albalghiti, Z. S. Fishman, F. Perreault, C. Corredor, J. D. Posner, M. Elimelech, L. D. Pfefferle, J. B. Zimmerman, *Environ. Sci. Technol.* **2016**, 50, 3975−3984.

[12] J. Qiu, H. Hajibabaei, M. R. Nellist, F. A. L. Laskowski, S. Z. Oener, T. W. Hamann, S. W. Boettcher, *ACS Energy Lett*. **2018**, 3, 961−969.

[13] T. Pradeep, *Nano: The essentials understanding nanoscience and technology*, Tata McGraw-Hill publishers, **2007**, ISBN-13: 978-0-07-061788-9.

[14] A. M. Smith, S. Nie, *Acc Chem Res.*, **2010**, 16, 43(2), 190–200.

[15] C. Zhang, D. Guo, W. Xu, C. Hu, Y. Chen, *J. Phys. Chem. C*, **2016**, 120, 12218−12225.

[16] K. Fu, R. Wang, T. Katase, H. Ohta, N. Koch, S. Duhm, *ACS Appl. Mater. Interfaces*, **2018**, 10, 10552-10559.

[17] M. Causa, I. R. Ramirez, J. F. M. Hardigree, M. Riede, N. Banerji, *J. Phys. Chem. Lett.,* **2018,** 9, 1885-1892.

[18] N. Moazezi, M. Baghdadi, M. A. Hickner, M. A. Moosavian, *J. Chem. Eng. Data,* **2018**, 63, 741−750.

[19] L. Cademartiri, G. A. Ozin, *Concepts of Nanochemistry,* Wiley-VCH publisher, **2010**, ISBN-978-3-527-32597-9.

[20] C. Kuttner, M. Mayer, M. Dulle, A. Moscoso, J. M. López-Romero, S. Förster, A. Fery, J. Pérez-Juste, R. Contreras-Cáceres, *ACS Appl. Mater. Interfaces,* **2018**, 10, 11152-11163.

[21] Q. Shi, S. Murcia-López, P. Tang, C. Flox, J. R. Morante, Z. Bian, H. Wang, T. Andreu, *ACS Catal.,* **2018**, 8, 3331−3342.

[22] X. Zhang, J. Qin, Y. Xue, P. Yu, B. Zhang, L. Wang, R. Liu, *Sci. Rep,* **2014**, 4596 (4).

[23] P. M. Shafi, A. C. Bose, *AIP Adv.*, **2015**, 5, 057137.

[24] B. Liu, K. Nakata, X. Zhao, T. Ochiai, T. Murakami, A. Fujishima, *J. Phys. Chem. C*, **2011**, 115, 16037–16042.

[25] F. E. Osterloh, *Chem. Mater.*, **2008**, 20, 35–54.

[26] H. Ma, W. Ma, J-F. Chen, X-Y. Liu, Y-Y. Peng, Z-Y. Yang, H. Tian, Y-T. Long, *J. Am. Chem. Soc.*, **2018**, 140, 5272-5279.

[27] I. Azzouz1, Y. G. Habba, M. Capochichi-Gnambodoe, F. Marty, J. Vial, Y. Leprince-Wang, T. Bourouina, *Microsystems & Nanoengineering*, **2018**, 4, 17093.

[28] V. L. Solozhenko, O. O. Kurakevych, P. S. Sokolov, A. N. Baranov, *J. Phys. Chem. A*, **2011**, 115, 4354–4358.

[29] R. S. Koster, C. M. Fang, M. Dijkstra, A. van Blaaderen, M. A. van Huis, *J. Phys. Chem. C*, **2015**, 119, 5648−5656.

[30] J. Li, J. Z. Zhang, Coord. *Chem. Rev*, 253, **2009**, 3015–3041.

[31] M. D. Ventra, S. Evoy, J. R. Heflin, *Introduction to Nanoscale Science and Technology*, Kluwer Academic Publishers, **2004**, ISBN-1-4020-7720-3.

[32] R. Gangopadhyay, A. De, *Chem. Mater*., **2000**, 12, 608-622.

[33] N. Raman, S. Sudharsan, K. Pothiraj, *J. Saudi Chem. Soc*., **2012**, 16, 339–352.

[34] S. K. M. Saad, A. A. Umar, M. I. A. Umar, M. Tomitori, M. Y. A. Rahman, M. M. Salleh, M. Oyama, *ACS Omega*, **2018**, 3, 2579−2587.

[35] Elisha. B. Babatunde, *Solar Radiation*, InTech publications, **2014**, ISBN-978-953-51-0384-4.

[36] H. Kisch, *Acc. Chem. Res.,* **2017**, 50, 1002−1010.

[37] W. Wang, Z. Li, J. Chen, C. Li, *J. Phys. Chem. C*, **2017**, 121, 2605−2612.

[38] P. V. Kamat, S. Jin, *ACS Energy Lett.*, **2018**, 3, 622−623.

[39] F. Wang, W. Ge, T. Shen, B. Ye, Z. Fu, Y. Lu, *Appl. Surf. Sci.*, **2017**, 410, 513–518.

[40] Y. Liu, J. Lou, M. Ni, C. Song, J. Wu, N. P. Dasgupta, P. Tao, W. Shang, T. Deng, *ACS Appl. Mater. Interfaces*, **2016**, 8, 772−779.

[41] C. Zhou, H. Li, J. Lin, K. Hou, Z. Yang, P. Pi, S. Xu, X. Wen, J. Cheng, *J. Phys. Chem. C*, **2017**, 121, 19716−19726.

[42] M. S. Johal, *Understanding nanomaterials*, CRC press, Taylor and Francis group, **2011**, ISBN-978-1-4200-7310-2.

[43] S. Özcan, G. Acıkbas¸ N. C. Acıkbas, *Appl. Surf. Sci.*, **2018**, 438,136–146.

[44] N. Abidi, L. Cabrales, E. Hequet, *ACS appl. Mater. Interfaces*, **2009**, 1(10), 2141–2146.

[45] K. Qi, B. Cheng, J. Yu, W. Ho, *J. Alloys Compd*, **2017**, 727, 792-820.

[46] V. L. Prasanna, R. Vijayaraghavan, *Langmuir,* **2015**, 31, 9155−9162.

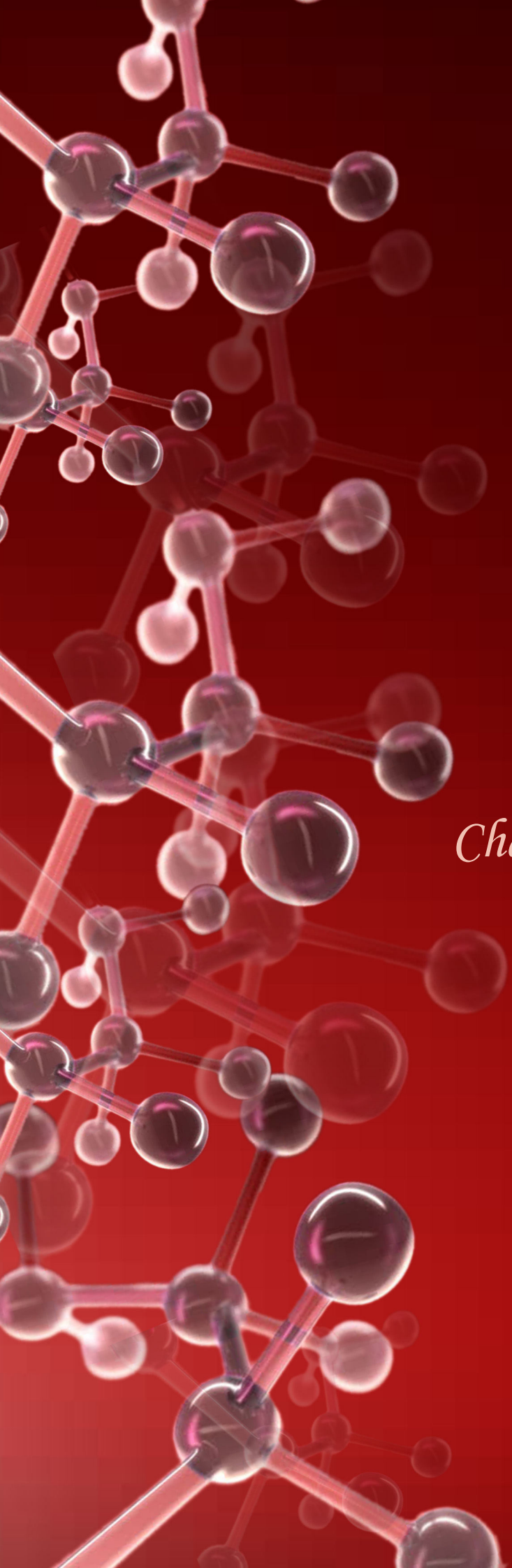

Chapter 2

Materials, Methods & Characterization Techniques

2 Materials, Methods and Characterization Techniques

2.1 MATERIALS USED FOR SYNTHESIS

2.1.1 Zinc acetate dihydrate ($Zn(Ac)_2.2H_2O$)

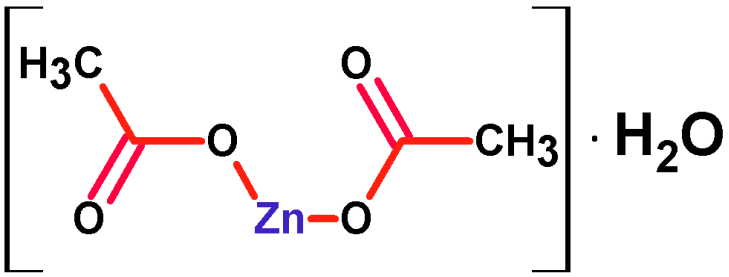

Figure 2.1 Chemical structure of zinc acetate dihydrate

Zinc acetate dehydrate is a widely accepted precursor for numerous chemical synthesis because of its easy solubility in water and low decomposition temperature[1, 2]. Most of the sol-gel methods involve treating zinc acetate solution with an alkali[3]. During the sol-gel process, hydrolysis of zinc acetate removes intercalated acetate ions and forms colloidal gel of zinc hydroxides. With the assistance of mild temperature, these zinc hydroxides split into Zn^{2+} and OH^- ions followed by the polymerization of hydroxyl complex leading to the formation of ZnO[4, 5]. M. K Liang *et al* made a detailed investigation of precursor effect on ZnO formation. According to him, by using zinc acetate precursor ZnO growth happens via dissolution/reprecipitation[6]. Zinc oxides with varied crystallinity, sizes and shapes were also synthesized exclusively by direct pyrolysis of zinc acetate[7]. L. Svoboda *et al* recently reported an interesting method for the synthesis of ZnO nanocoating over silica by the decomposition of zinc acetate and this decomposition was done with the help of electrons

emitted from the UV irradiated indium plate[8]. Figure 2.1 depicts chemical structure of zinc acetate dihydrate.

2.1.2 beta-Aminoethylamine ($C_2H_8N_2$)

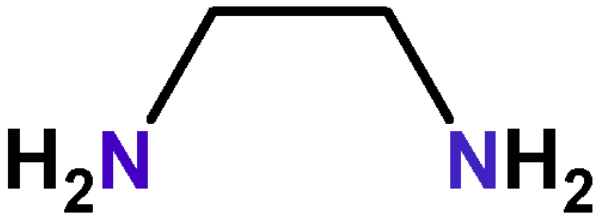

Figure 2.2 Chemical structure of beta-Aminoethylamine

Beta-Aminoethylamine (Figure 2.2) is a water soluble colourless liquid with strong alkaline nature[9]. It is highly viscous and makes fumes by reacting with moisture in the humid air conditions. The strong bidenting chelating character could make to form a complex with Zn^{2+} with high stability constant[10]. Because of its versatile performances such as capping, stabilizing and structure directing it is considered as a building block for the chemical synthesis processes[11,12]. Other names of beta-Aminoethylamine are 1, 2-Ethanediamine, Dimethylene diamine, Ethylendiamine, Edamine etc.

2.1.3 Polyvinylpyrrolidone (PVP)

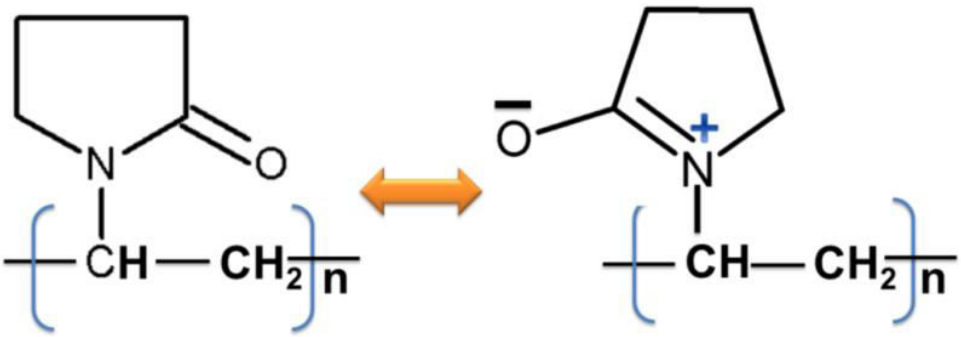

Figure 2.3 Resonance structures of polyvinylpyrrolidone

Polyvinylpyrrolidone is a water soluble biocompatible polymer which appears as white coloured powder[13]. Two resonating structures are possible in PVP with the presence of a hydrophilic $=N^{+}$-C-O^{-} group in its pyrene ring structure[14]. Amphiphilic PVP exhibit multiple roles in the synthesis process such as stabilizing against aggregation of nanoparticles, tune the nanoparticle oxide interfacial energy, interfering with oxide crystal formation, effective capping etc.[15, 16]. Very recently Z. J. Yu *et al* described the crucial role of PVP as surfactant in the formation of novel hierarchical heterostructured photocatalyst[17]. Figure 2.3 presents chemical structure of polyvinylpyrrolidone.

2.1.4 Emeraldine salt of polyaniline

The green colored emeraldine salt is an intrinsically conducting organic polymer due to its polaron and bipolaron form[18].

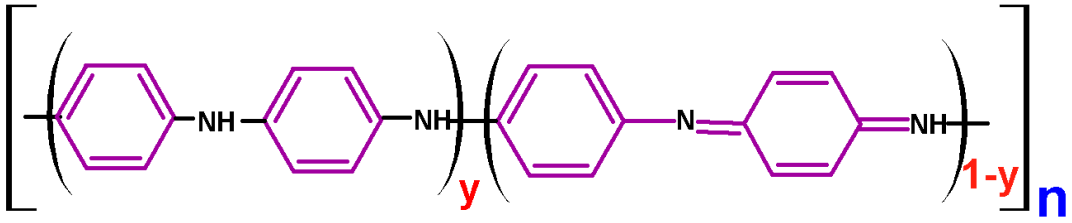

Figure 2.4 Chemical structure of polyaniline (y=0: Pernigraniline, y=0.5: Emeraldine, y=1: Leucoemeraldine)

Depending upon the oxidation states, it can chemically or electrochemically switch in to various forms such as leucoemeraldine, emeraldine, pernigraniline etc[19] as shown in Figure 2.4 and Figure 2.5. Emeraldine salt structure consist of only benzenoid groups (amine nitrogens) whereas emeraldine base has both benzenoid and quinoid groups (imine nitrogens). Characteristic switching property of polyanilne between a conductor and an insulator, make it a promising material for various practical applications[20].

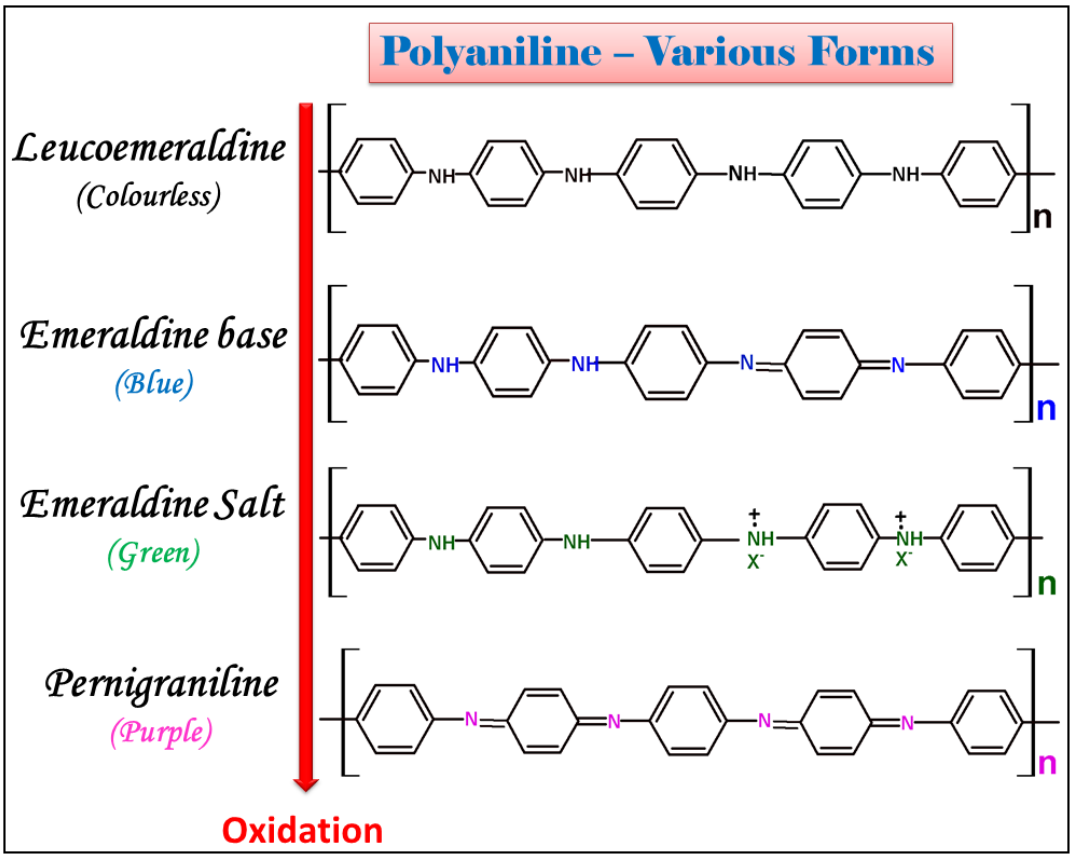

Figure 2.5 Different forms of polyaniline depending upon the oxidation states

2.1.5 Potassium Bromide (KBr)

Figure 2.6 Chemical structure of KBr

Potassium bromide is a water soluble crystalline ionic salt (Figure 2.6) widely used in various chemical synthesis processes and for the doping purposes in various single crystals[21-24]. It serves as a source of bromide ions for various synthesis (synthesis of silver bromide) and applications[25].

2.1.6 Tellurium Powder (Te)

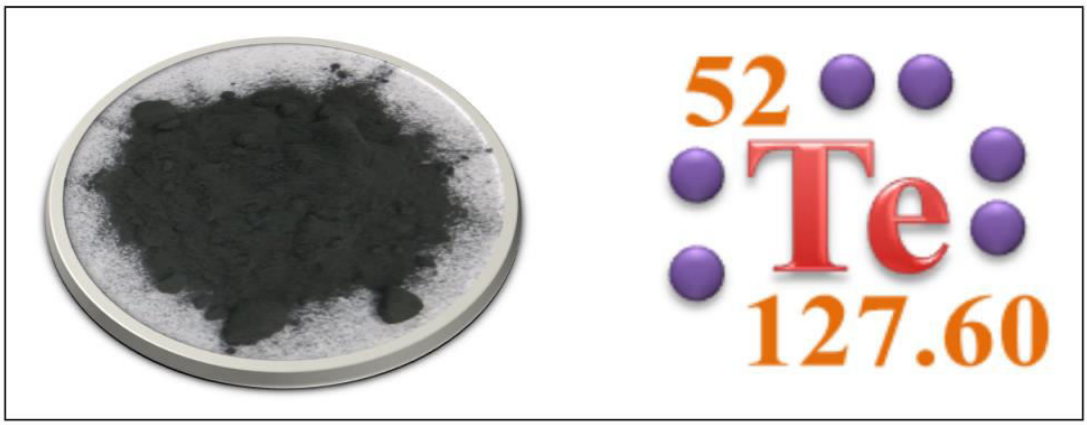

Figure 2.7 Tellurium powder and its chemical symbol

Tellurium is a metalloid in the chalcogen family usually appears as dark grey in colour as shown in Figure 2.7. Six electrons are occupying in the valence shell of tellurium with $5s^2 5p^4$ configuration and are chemically related to selenium and sulphur. Tellurium is used in various functional devices because of its intriguing properties[26]. In most of the synthesis high temperature is given to compromise the solubility problem of Te as the melting point of tellurium is 450 °C[27]. However it has excellent redox reaction chemistry which helps to improve the performance of devices[28].

2.2 METHODS

2.2.1 Sol-gel method

In the sol-gel process, a sol (colloidal suspension) formed from metal oxide precursors through hydrolysis and condensation is converted into gel network structure[29]. Actually a chemical transformation happens from liquid to gel state and subsequently converted in to metal oxide systems. The formed sol can be converted in to gel and finally in to different products depending upon the way of processing of the Gel. In addition, fibers and uniform

powders also can be formed by spinning of sol or precipitated from the sol directly[30].

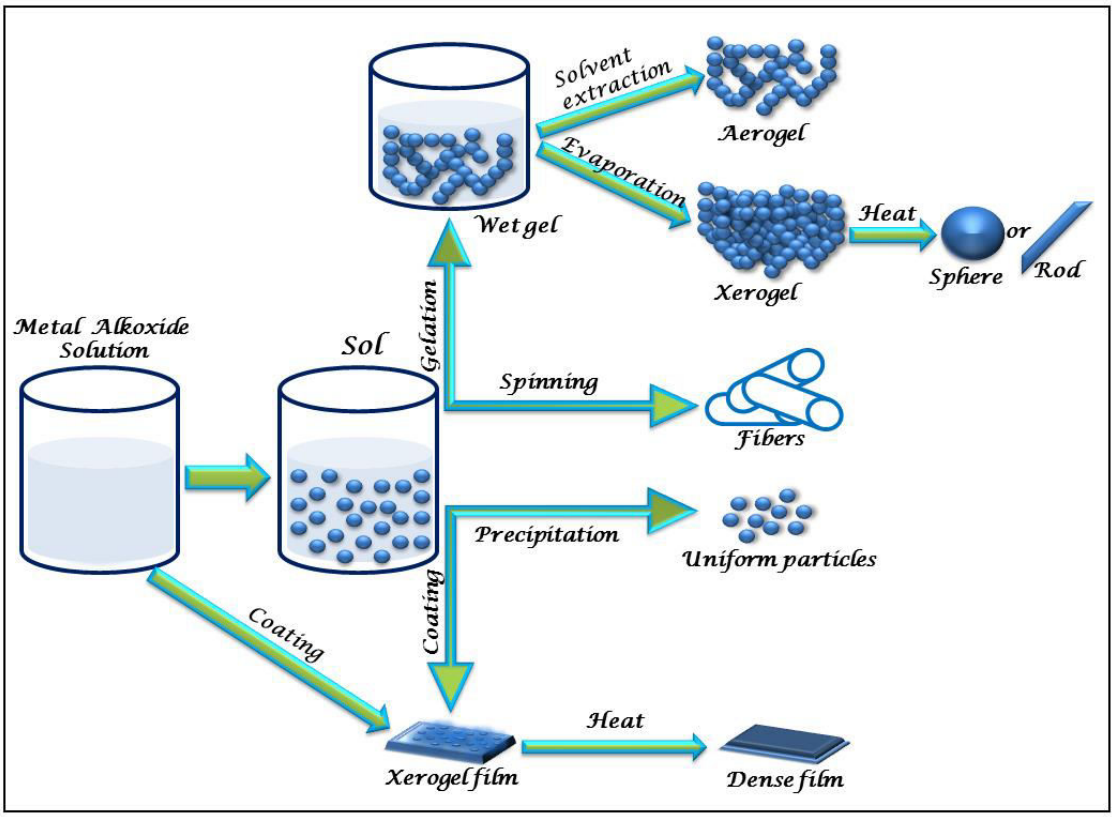

Figure 2.8 Schematic of Sol-gel synthesis methods and their products

The solvent evaporation of the gel results shrinkage accompanied with the capillary forces and form xerogels by the collapsing of the gel network[31]. Besides, when the gel is subjected to super critical drying, then aerogel is formed by retaining the gel network structure. Aerogels are seems to be as gel with large pores[32]. Schematic of various sol-gel synthesis processes and their corresponding products are given in Figure 2.8. Among numerous methods reported for the synthesis of nanomaterials, sol-gel method has got special attention because of the following reasons:

- ✓ Different structures of the materials can be prepared using same precursors by slightly changing the experimental conditions
- ✓ Low cost and simplicity of the synthesis procedures
- ✓ Reliability and repeatability of the materials production because of the

involvement of liquid phase synthesis chemistry

- ✓ Simple experimental set up and mild temperature conditions
- ✓ Precise control on doping is possible

2.2.2 Solvothermal method

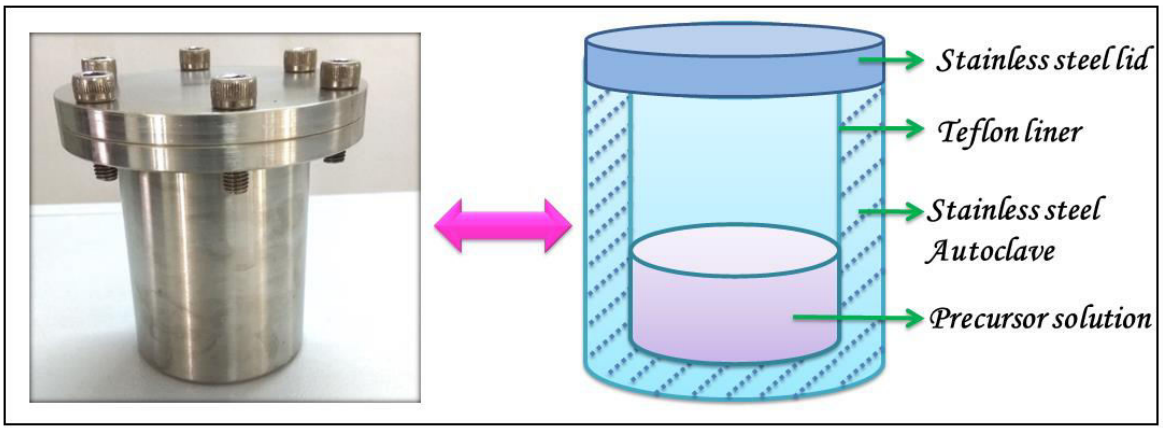

Figure 2.9 Solvothermal set up in an autoclave

Solvothermal synthesis is widely used for the preparation of nanomaterials. In this approach the chemical reactions in organic solvents around their critical temperature are carried out in a closed system under self-induced pressure [33]. If the solvent used is water, then the synthesis normally performed below super critical temperature of water (374 °C) and known as hydrothermal synthesis. A sealed reactor set up used for the solvothermal reaction is called autoclave as given in Figure 2.9. The outer cover of the autoclave usually made of stainless steel and a teflon or alloy liner is placed inside to carried out the reaction thereby protecting the autoclave body from the highly corrosive solvents[34].

Two main parameters (chemical and thermodynamic) control the solvothermal synthesis. Chemical parameters include selection of the solvent and nature of the reagents whereas the thermodynamic parameters include temperature, pressure and reaction time. Shape of the nanocrystals (dot, rod, tube etc.) can be tuned by optimizing the concentration of the precursors. The polarity and reducing / complexation capability of the solvents are

relevant for the synthesis of nanomaterials in solvothermal approach. Thermodynamic parameters like temperature and pressure increases the solubility of the precursors favoring supersaturation and subsequent growth.

The reaction mechanism involved during the solvothermal/hydrothermal synthesis proceeds through two steps. They are crystal nucleation and subsequent growth. The sizes and morphologies of the final particles can be tuned by varying temperature, pH, precursor concentrations, solvents etc. Nucleation occurs reversibly when the precursor solution attains supersaturation and results precipitation of the solutes in the medium. Following nucleation, growth occurs simultaneously with the attachment of growth units. The schematic of the mechanism is depicted in Fig 2.10.

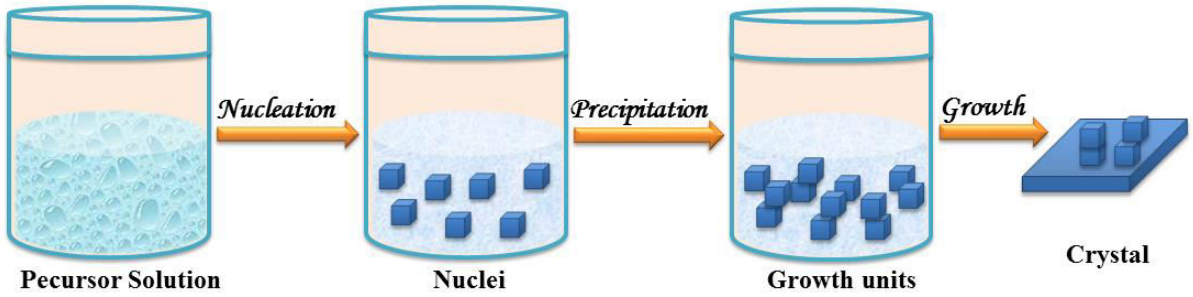

Figure 2.10 Schematic of the mechanism of crystal growth under solvothermal condition

Solvothermal route is an attractive method for the synthesis of nanocrystals and is now being considered as a promising synthesis strategy for novel functional nanomaterials because of the following advantages:

- ✓ Compromise solubility problem of precursors
- ✓ High product purity and homogeneity
- ✓ Unique pressure-temp interaction during synthesis
- ✓ Single step synthesis of highly crystalline materials
- ✓ Fast reaction time
- ✓ Narrow particle size distribution

- ✓ Precise control on the size, shape and crystallinity
- ✓ Mass quantity of yield in low cost single step

2.3 CHARACTERIZATION TECHNIQUES

2.3.1 Structural Characterizations

2.3.1.1 X-ray Diffraction (XRD)

X-ray diffraction analysis can be used for the quantitative as well as qualitative analysis of the crystals. Crystals are considered as three-dimensional array of oscillators separated at a distance or three-dimensional diffraction grating. The interaction of the monochromatic X-rays with the atomic planes of a crystal gives the structural information about the phase and unit cell dimensions of the nanomaterials[35]. The schematic of the XRD procedure is depicted in Figure 2.11(a).

When high energy particles (eg: electrons) falls on matter, ejection of electrons takes place from various atomic shells. Characteristic X-rays are emitted due to these electron ejections from the core orbitals. When an electron is ejected from 1s orbital, simultaneously electron from 2p or 3p orbital will fall into empty 1s orbitals emitting K_α radiations. Actually K_α will be doublet ($K_{\alpha1}$ and $K_{\alpha2}$) as 2p electron has two spin states ($2p_{3/2}$ and $2p_{1/2}$). Thus $K_{\alpha1}$ and $K_{\alpha2}$ are corresponds to the electronic transitions from two spin states of 2p electron. But in most of the diffractometers statistically weighted average of the two are measured. Normally characteristic X-rays of copper K_α radiations having wavelength 1.54 Å is used for the diffraction of crystals[36].

Powder diffraction method is normally used for the structural and phase identification of nano/micro crystals based on Bragg's law (Figure 2.11(b)). When light falls on the crystals, it will be radiated in all directions from the lattice planes and occur constructive or destructive interferences over several ways.

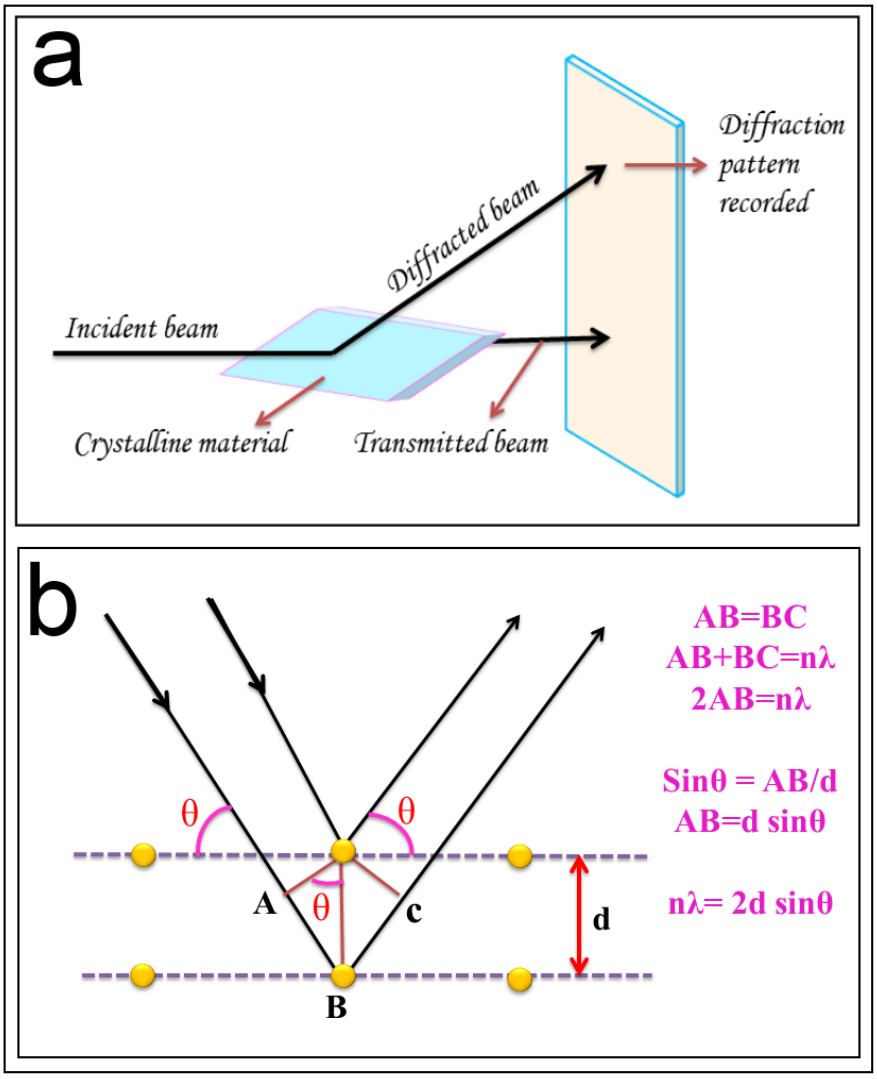

Figure 2.11 (a) X-ray diffraction procedure and (b) derivation of Bragg's law

Reflections are also takes place with angle of incidence equal to angle of reflections. The path length between the crystal planes becomes an integral multiple of wavelength of incoming radiations when the reflected beams are in phase and that resulted in constructive interference. For first order diffraction, equation $\lambda=2d \sin \theta$, when $\theta = 90^{o}$, $\sin \theta$ get the maximum value 1. If θ is less than 90° and d value less than λ, then zero order diffraction beams observed. If d value is much higher than λ value, then a diffraction continuum is obtained by the combination of the diffracted beams of different orders.

The essential components of a diffractometer are a radiation source, a sample of any

kind such as powder, film or a solid piece and a detector such as a photographic plate or a sophisticated counter. In Debye-Scherrer method, monochromatic X-ray is fallen on to the finely grounded powder sample and measured the intensity of the diffracted beam as a function of intensity. To collect all the reflections from the various planes of the nanocrystals, the detector is rotated in a circle. The positions of the diffracted peaks are compared with standard values for phase and plane identifications. In addition to the plane and phase identifications, intensity of the diffracted peaks gives information about the unknown crystal structure and quantitative phase analysis. X-rays causes a vibration in electrons of materials through elastic or inelastic collisions. Elastic collisions generate coherent scattering (in phase with the incident X-rays) and inelastic collisions leads to Compton scattering of electromagnetic radiations from the vibrating charge of the electrons. The total scattering intensity is measured as the sum of the scattered intensities occurs from each electron. Convergent beam of X-rays always improve the sensitivity and resolution of the diffraction patterns when placing both source and detector at the circumference of same circle.

In Bragg's condition diffraction from one plane occur exactly one wavelength later from the previous plane results constructive interference. Therefore number of planes present in the crystallites constitutes the width of the diffraction peak. The crystallites sizes are obtained by the Scherrer formula, $t = \frac{0.9\lambda}{\beta cos\theta}$, where 't' is the thickness of the crystallite in Å, λ is the wavelength of incident rays, β is the full width at half maximum of the most intense peak in radians and θ is the Bragg's angle[37]. For smaller crystallites, the diffracted lines become broadened and the size of the particles up to 200 nm can be calculated using this equation. A non-uniform stress present in the crystallites also constitutes the broadening of the pattern. X-ray diffraction is one of the most useful techniques to obtain the information given below:

- ✓ Identification of the phases of the compounds (amorphous/crystalline)
- ✓ Measurement of degree of crystallinity
- ✓ Determination of crystal structures (cubic, monoclinic etc)
- ✓ Determination of lattice parameters
- ✓ Measurement of crystallite sizes
- ✓ Orientation of single crystals
- ✓ Quantitative analysis of phases
- ✓ Determination of residual stress in the crystals

2.3.1.2 Spectroscopy for structural characterizations

Spectroscopy analysis deals with the interaction of electromagnetic radiations with atoms and molecules of the materials. Electromagnetic radiations constitute mass less particles having wave like nature which travel with the speed of light called photons. These photons associate with discrete packets of energy. Normally in spectroscopic techniques, the electromagnetic radiations strikes on the sample and the intensity of the emitted radiations are analyzed at respective frequencies[38].

2.3.1.2.1 Fourier transform infrared spectroscopy (FTIR)

The interactions of infrared radiations with the materials can cause a vibrational transition in its molecules and those vibrational transitions accompanying with a change in dipole moment is detected. Homo diatomic molecules (eg: H_2, O_2) cannot produce change in dipole moment thereby it do not detected by IR spectroscopy. The inherent vibrations of atoms and bonds in molecules or in crystals are in the range of 3-300µm range (IR region in electromagnetic spectrum). When these vibrational frequencies come in resonance with IR frequency results vibrational transitions in the molecules. The intensity of IR radiations before and after interactions with materials is measured and the relative intensity is plotted against frequency in an FTIR spectrum[39].

The interferometer part of the FTIR consists of a light source, beam splitter, two

mirrors and a detector as shown in Figure 2.12. Beam splitter is an optically transparent material (Eg: KBr) coated plate so that it can reflect and transmit 50% of the light. The reflection from two mirrors recombined by beam splitter into a single beam and it is collected by the detector. The detected interferogram signal is interpreted by a mathematical Fourier transformation technique. The following information obtained from FTIR making it a useful tool for the nanomaterials characterization:

- ✓ Information about chemical bonding
- ✓ Information about molecular structure
- ✓ Identification of organic and inorganic nature
- ✓ Identification of materials
- ✓ Information about the degradation of organic compounds

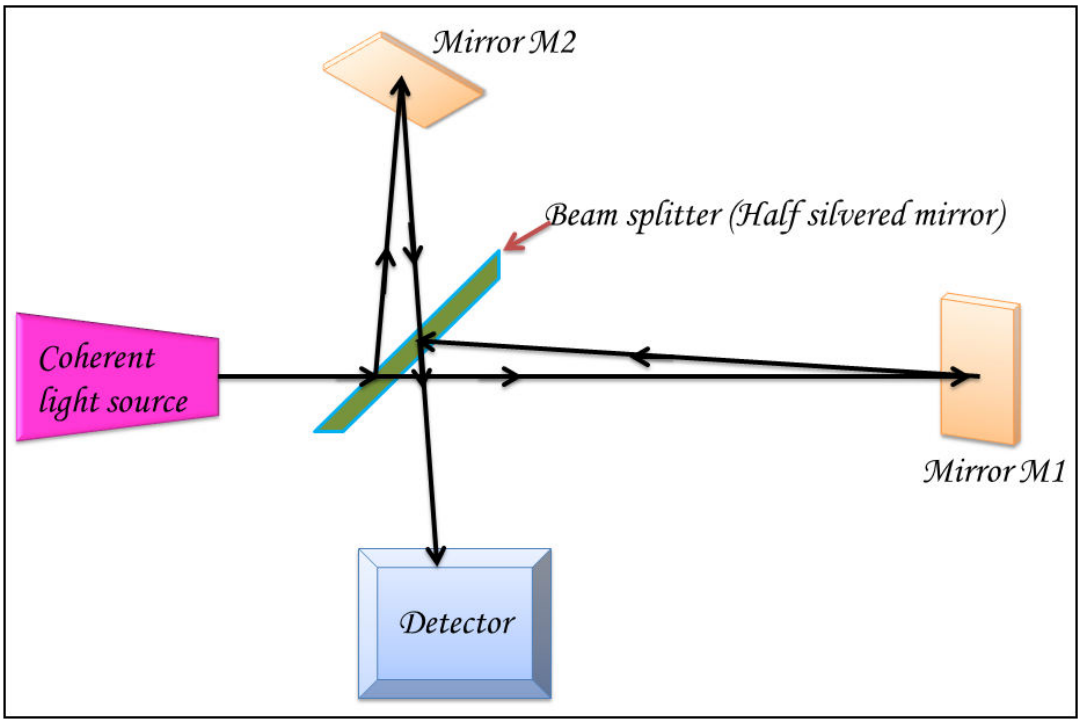

Figure 2.12 Working of interferometer unit in an FTIR instrument

The characteristic vibrational motions of molecules are normally found in the region below 1500 cm^{-1}. In this finger print region, lower frequency bending vibrations are occurring. In 3700-2500 cm^{-1} region, hydrogen stretching vibrations have seen. The region

2500-2000 cm^{-1} is triple bond region since these bonds have large force constant. 2000-1600 cm^{-1} is the double bond region and 500-1700 cm^{-1} is the single bond stretching and bending region[40].

2.3.1.2.2 Raman spectroscopy

Figure 2.13 (a) presents instrumental set up in a Raman spectrometer. Raman spectroscopy analyses the frequency variations in the scattering of visible light radiations when passed through transparent materials. The scattered radiations have either same frequency as that of the incident frequency (Rayleigh scattering) or certain discrete frequencies vary from that of incident radiations (Raman scattering) [41]. This altering in frequency corresponds to change in vibrational energy states of the molecules. The intensity of these lines are in the order Rayleigh scattering > Stokes lines > Anti-stokes lines (Figure 2.13 (b)). A Raman shift is observed in the range of 100-4000 cm^{-1}due to the vibrational energy changes. If λ_{in} is the incident wavelength of light and λ_R is the wavelength of Raman lines, then Raman shift in $cm^{-1}$is given by the expression $\Delta\bar{\upsilon} = \frac{10^8}{\lambda_{in}(in\ Å)} - \frac{10^8}{\lambda_R(in\ Å)}$.

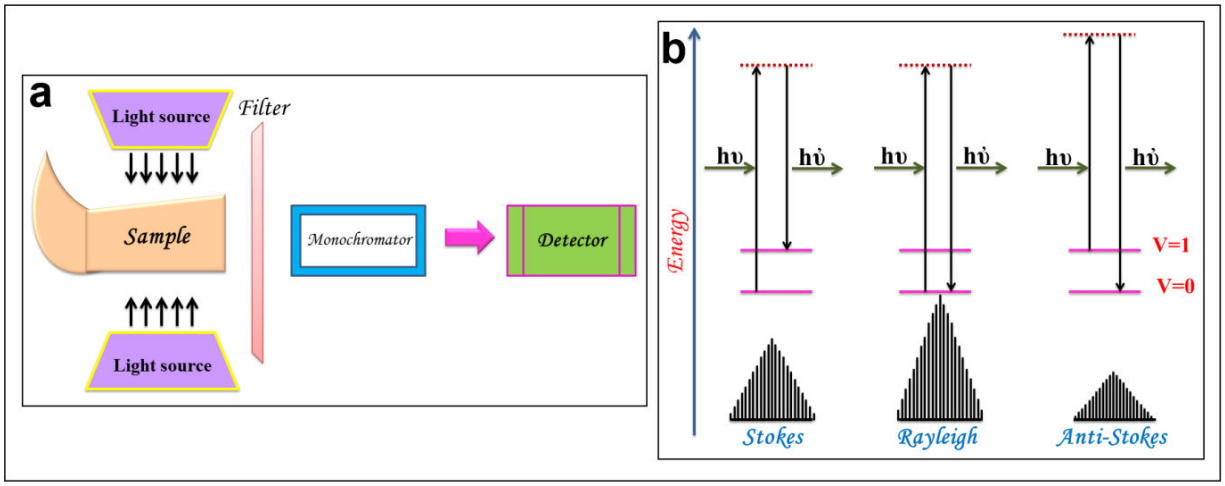

Figure 2.13 (a) Raman spectroscopy instrumental set up and (b) Raman and Rayleigh scattering

The source used in Raman is coherent monochromatic LASER. To reduce the direct

reflections from the source, horn shaped sample holder is used. The detector used is either a photomultiplier or a photographic plate. The importance of Raman spectroscopy is described below:

- ✓ Information of molecular vibrations which are inactive in IR
- ✓ Gives idea about the composition of the materials
- ✓ Detection of impurities
- ✓ Detection of surface bond vibrations
- ✓ Information about crystallinity

2.3.1.2.3 Energy dispersive spectroscopy (EDS)

EDS spectrum gives information about the composition of the materials and the electronic structure of atoms. A beam of electrons when falls on materials, number of processes occurs such as scattering, transmission, secondary electron emission, X-ray emission, cathodoluminescence and back scattered electrons emissions. Out of these variable processes, characteristic X-ray emission gives EDS spectrum. With the influence of the incident electrons, a core level electron is ejected from the excited atom. Simultaneously an electron from the outer shell relaxes and occupied at the vacant core site along with transient generation of a local photon. Next relaxation occurs through either of the two processes in which one is accompanying with the ejection of an Auger electron and other is with the emission of X-ray quantum. The electrons transfer processes occur during EDS analysis are depicted in Figure 2.14 (a). Actually these emitted X-rays are functions of atomic number with characteristic energy which are used in EDS for analysis (Figure 2.14 (b)).

EDS analysis is based on Moseley's law which states that the energy of X-rays (E) is directly proportional to the atomic number (Z) of elements. The corresponding equation is $= C_1(Z - C_2)^2$, Where C_1 and C_2 are constants[42].

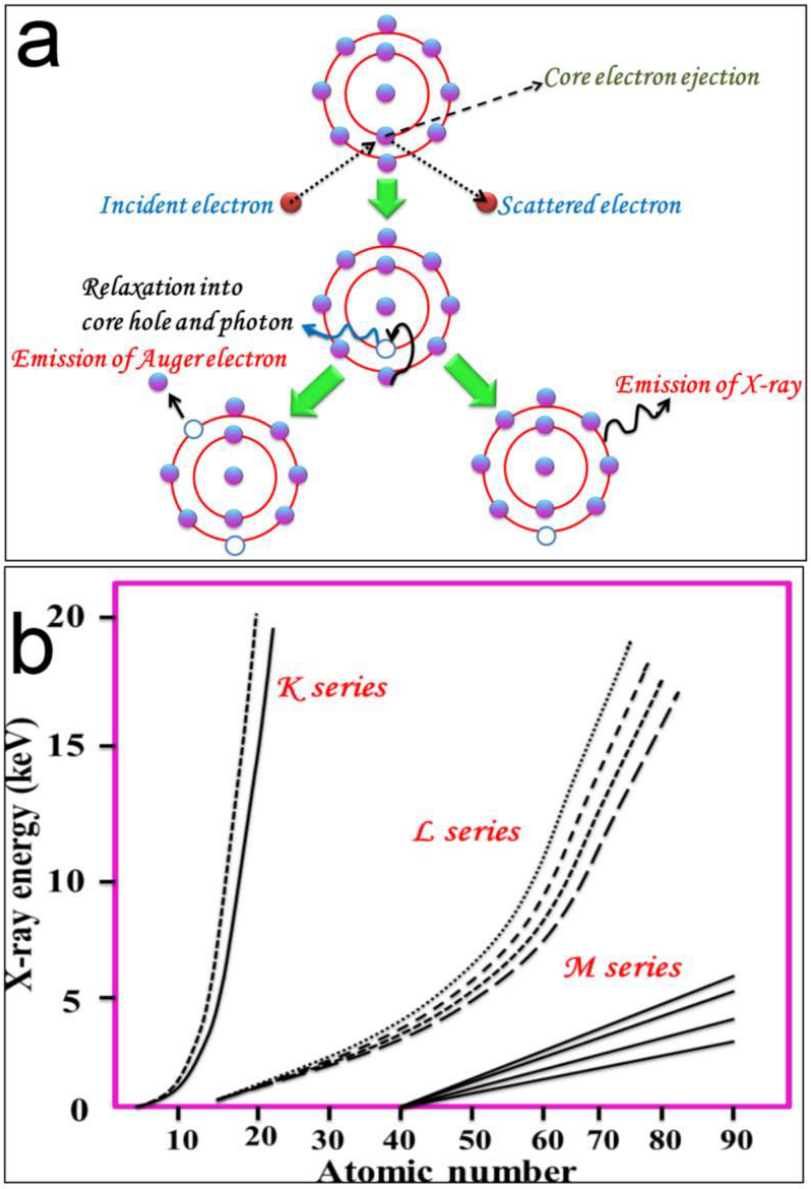

Figure 2.14 (a) Schematic of the process occurring during EDS analysis and (b) Graph depicts dependence of X-ray energy and atomic number

2.3.1.2.4 X-ray photoelectron spectroscopy (XPS)

Photoelectron spectroscopy works based on Einstein's photoelectric equation[43],$h\nu = KE + \phi$, Where hν is the energy of photon, KE is the kinetic energy of ejected electrons and ϕ is the work function. XPS technique is also known as electronic spectroscopy for chemical analysis (ESCA)[44].

In XPS, monochromatic X-rays are falling on the samples (solid, liquid or gas) and the kinetic energy of the emitted photoelectrons are analysed using a detector. The intensity of photoelectrons is plotted against kinetic energy of the photoelectrons. The kinetic energy of the electrons is related to binding energy by the following relation

$$E_{KE} = h\nu - \phi - E_V$$

Where, Ev is the binding energy of the photoelectron

During this kinetic energy measurement, the maximum electrons coming from the materials are found to be from the top of surface of the materials. So that surface mapping of nanomaterials is possible by this spectroscopic technique, where the irradiation area is found to be of the order of mm^2. Ultra high vacuum is needed during the surface analysis (greater than 10^{-9} torr) to avoid scattering of electrons with air. The core level electrons having energy of the order of 1000 eV or below can be concerned with photoelectron spectroscopy. The binding energies of the core electrons are very specific so that from the binding energy data the atoms can be predicted[45]. Actually the binding energy of electrons depend the energy of the shell where they occupy and also the magnetic interactions between the orbital angular momentum and the intrinsic spin of the electrons.

The essential part of a modern XPS instrument involves a monochromatic X-ray source. These X-ray photons when hit on a sample surface, photoelectrons are emitted and the emitted photoelectron passed through a velocity analyzer and finally falls on the detector. The detector can analyze the intensity of emitted electrons with their respective kinetic energies[46]. The working procedure in modern XPS instruments is schematically shown in Figure 2.15.

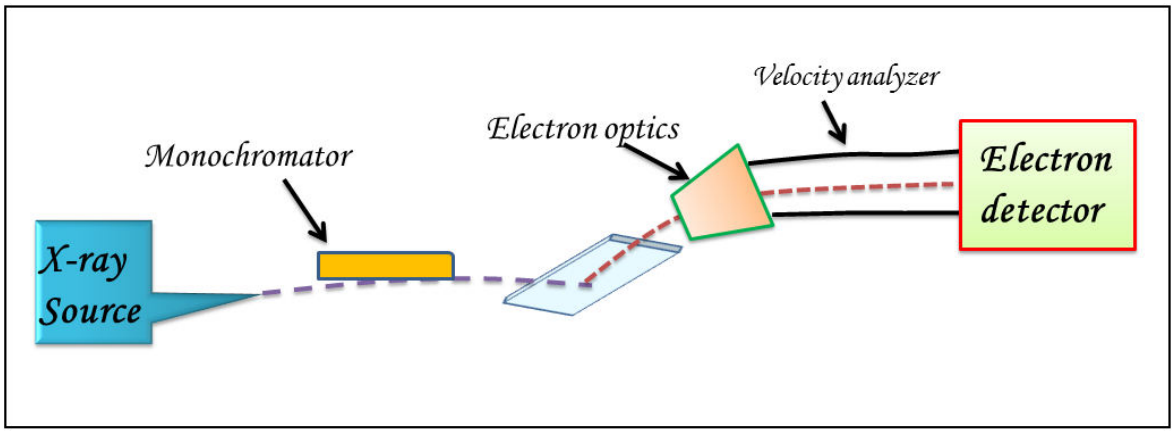

Figure 2.15 Working procedures in a modern XPS instrument

XPS is widely used for the characterization of nanosystems as it helps to get the information listed below:

- ✓ Elemental characterization of the material is possible
- ✓ Quantitative analysis of the surface of nanomaterials
- ✓ Ionization potential/ binding energies of core electrons
- ✓ Information about the chemical composition except H and He
- ✓ Information about chemical environment
- ✓ Get idea about the electronic states of the elements

2.3.2 Optical Characterizations: Spectroscopic techniques

2.3.2.2 Diffuse reflectance spectroscopy (DRS)

Diffuse reflectance spectroscopy, also called elastic scattering spectroscopy is used to estimate the band gaps of the powder nanomaterials[47]. When a semiconductor nanomaterial is subjected to electromagnetic radiations with wavelength range from UV to NIR, these radiations can be absorbed, reflected or transmitted from the material depends upon the wavelength of the photon and band gap of the nanomaterials. Diffusive reflections are multiple reflections occurring from the surfaces of smaller particles (Figure 2.16(a)). 'Reflectance' is the power of diffusive reflections which is the ratio of the reflected radiant flux to the incident radiant flux.

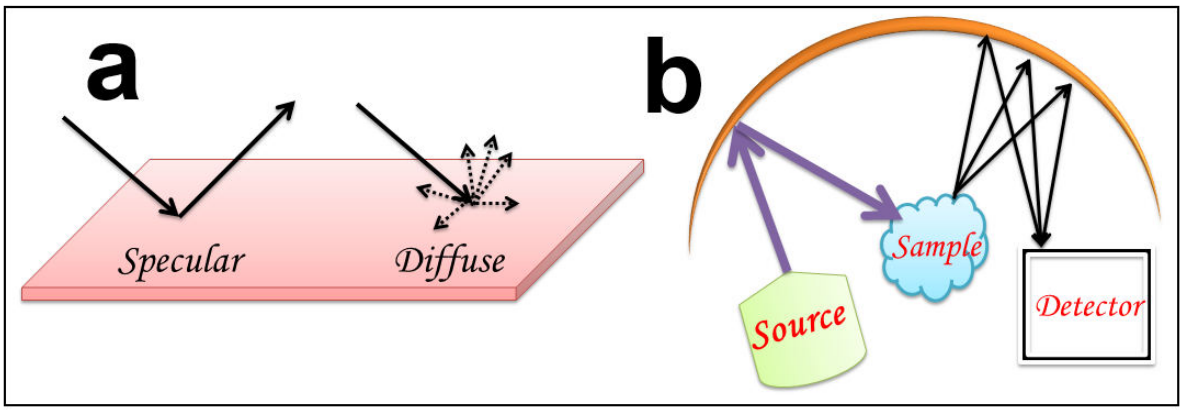

Figure 2.16 (a) Specular and diffuse reflectance and (b) DRS instrumental set up

The instrumental set up in a DRS is displayed in Figure 2.16 (b). When light radiations falls on powder surface, scattering happens in all dimensions and the measurement of this diffuse reflected light gives a DRS spectrum. Kubelka-Munk function converts the measured spectrum into absorption spectrum[48]. According to Kubelka-Munk model, the diffuse reflectance

$$R_\infty = 1 + \frac{K}{S} - \sqrt{(K}/S(2 + \frac{K}{S}))$$

Where, K is the absorption coefficient ($K = 4\Pi k/\lambda$) and S is the scattering coefficient.

The absorption coefficient is a function of photon energy. For indirect band gap and direct band gap semiconductors, the absorption coefficient is given by the equations $A(hv - Eg)^2$ and $A(hv - Eg)^{1/2}$ respectively where A is the material dependant constant. In the case of in-direct bandgap semiconductors (eg: TiO_2), a change in momentum is associated with the absorption whereas in direct bandgap semiconductors (eg: ZnO) no such momentum change happens. The absorption coefficients of indirect band gap semiconductors are smaller compared to direct band gap semiconductors[49]. The scattering coefficient S depends on the particle size and refractive index and does not depend on the wavelength and absorption coefficient. On simplifying the above equation becomes, $\frac{K}{S} = (1 - R_\infty)^2/2R_\infty$.

2.3.2.3 Photoluminescence spectroscopy (PL)

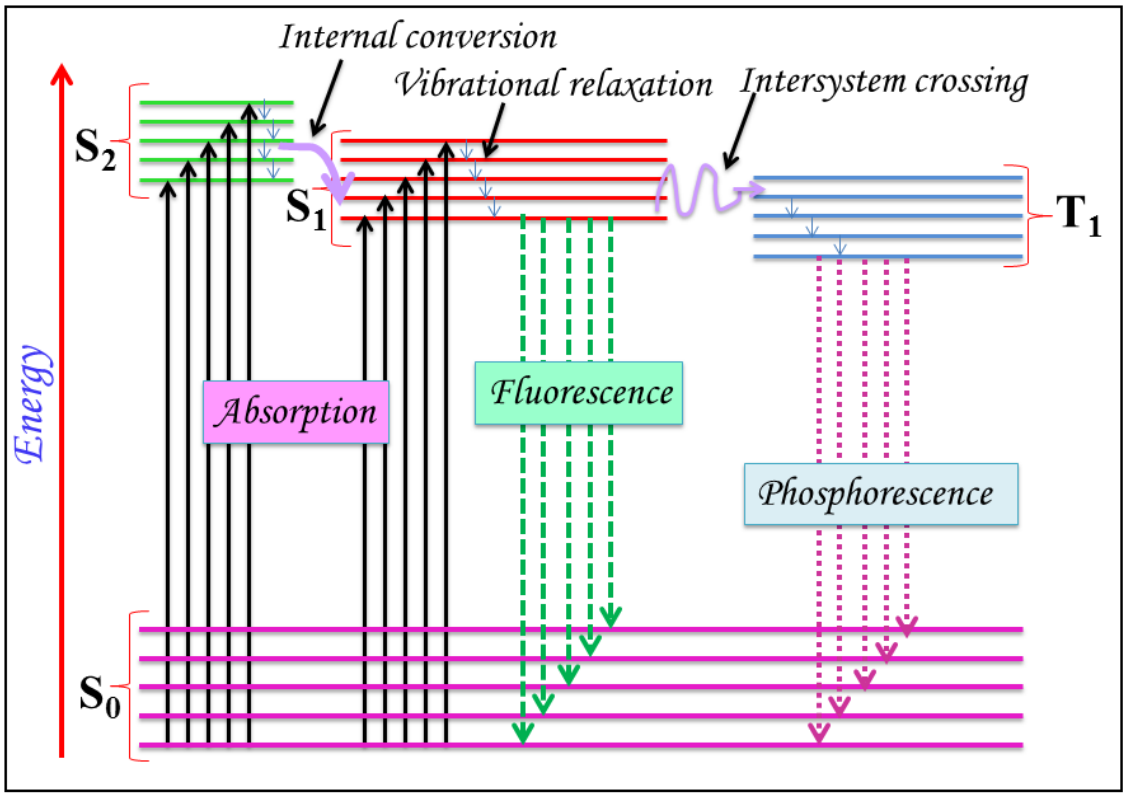

Figure 2.17 Jablonski diagram explaining photoluminescence

Light incidence on materials causes photo-excitations and excess energy dissipated in the form of luminescence is called photo-luminescence[50]. The photo-excited electrons when returns to its equilibrium states, the emission of energy happen either radiatively (with emission of light) or non-radiatively. In addition, resonant radiation within an order of 10 nanoseconds may also happen when incident photon and emitted photon have same energy[39]. Depending upon the lifetime of light emission, radiative emissions are of two, fluorescence and phosphorescence which can be explained on the basis of Jablonski diagram[51] as shown in Figure 2.17.

In fluorescence, the light emission happens within 10^{-8} to 10^{-4} seconds and the emission ceases with the removal of source. The lifetime of phosphorescence is 10^{-4} to 10^{-2}

seconds thereby it exists even after the removal of the source. Non-radiative transition (No emission of radiations) takes at about 10^{-11} seconds which include internal conversion (emission from excited state to ground state of same multiplicity) and intersystem crossing (emission from excited state to ground state of different multiplicity). The intensity of PL emission is the relative amount of the radiative and non-radiative recombinations. PL spectroscopy is of having great significance as it gives following informations:

- ✓ Determination of band gaps
- ✓ Identification of defect levels
- ✓ Information about surface structure
- ✓ Information about recombination mechanism

2.3.3 Morphological analysis

2.3.3.1 Electron Microscopy : Scanning electron microscopy (SEM) & Transmission electron microscopy (TEM)

Electron microscopy is equivalent to light microscopy where electron beams are used instead of light for the imaging of nanomaterials. The used electron beams have shorter wavelength thereby obtain clear image with high resolution than light. Also the electrons can interact with matter very strongly compared to X-rays or neutrons.

When a beam of electrons hit on a surface of a material (powder or film), collisions happens with the atoms of the material and emit X-rays, secondary electrons or backscattered electrons. In addition, some electrons are directly transmitted through the material or by scattered due to the collisions from the atoms (Figure 2.18)[52]. These scattered electrons may be elastic (without change in energy) or inelastic which lead the auger or transmitted electrons. Figure 2.19 presents images of SEM, TEM and SAEED pattern.

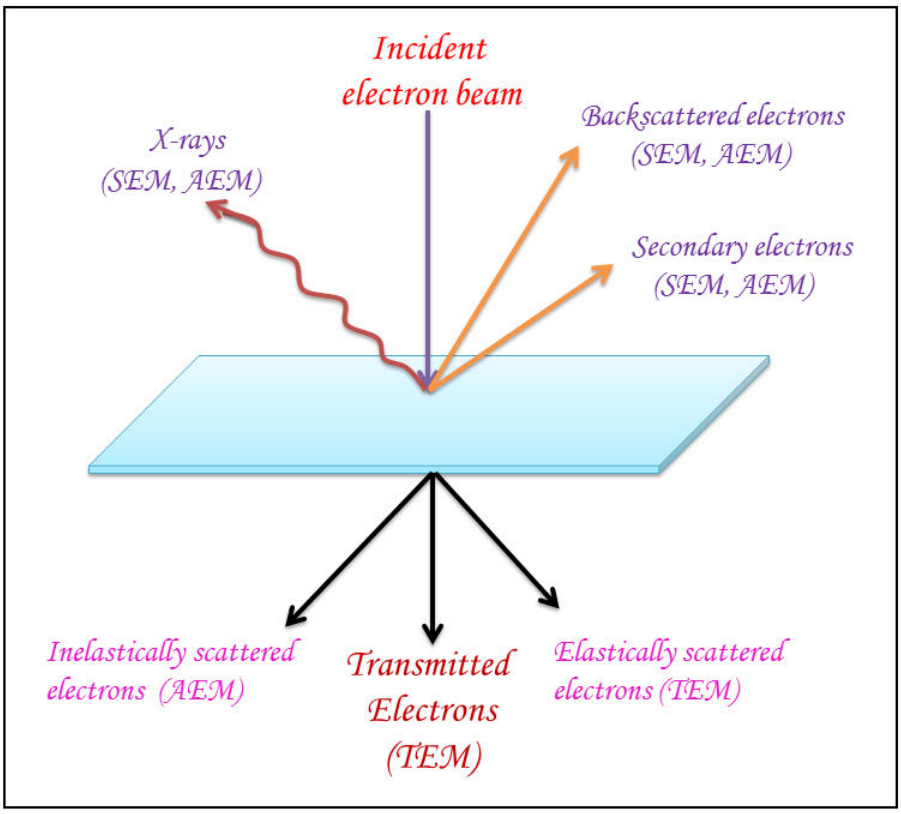

Figure 2.18 Electron microscopy processes

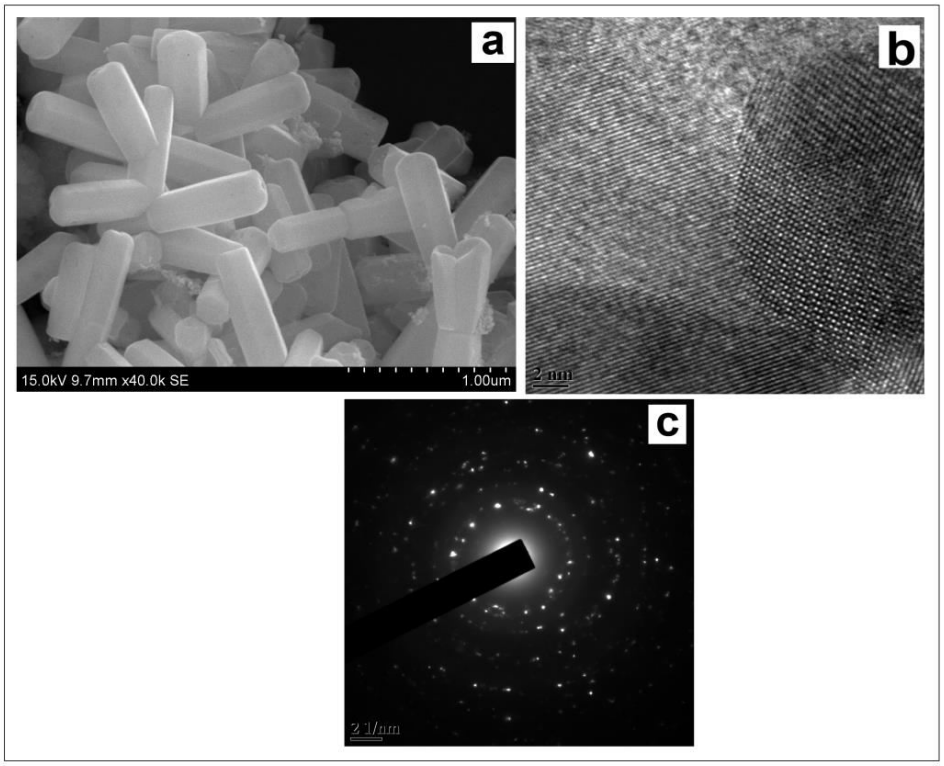

Figure 2.19 Typical image of (a) SEM, (b) TEM and (c) SAEED pattern

Working principle of electron microscopy

In electron microscopy, the source of electrons is a cathode made up of hot tungsten (W) filament and these electrons are accelerated by anode to high velocity beam. The lenses used are electromagnetic and vacuum is maintained inside the set up. The accelerated electron beam is converted in to a fine beam when passed through condensing magnetic lenses (a series of current carrying coils producing magnetic field) and this fine beam is passed through the object. The absorbed/scattered/transmitted electrons are focused and enlarged on a fluorescent screen by objective magnetic lens and projector magnetic lens arranged one after other[53]. From the SEM analysis of the nanomaterials we get a clear picture of three dimensional topographic image, size and shape of the material, surface features etc whereas TEM gives a two dimensional image of the particle by projecting the transmitted electrons on to a fluorescent screen. TEM can provide informations about the crystallinity of the materials, size and shape of the nanoparticles with resolution less than 0.1 nm.

Selected Area Electron Diffraction (SAED) is performed inside the TEM and small bright spots appear due to Bragg's reflection from individual crystallites. Amorphous materials produce diffuse rings whereas crystalline nanomaterials give rise to 2-10 nm sized small spots. By measuring the distance between the spots interplanar distance (d) of the crystal can be calculated easily[54].

2.4 REFERENCES

[1] S. J. Malthus, S. A. Cameron, S. Brooker, *Inorg. Chem.* **2018**, 57, 2480−2488.

[2] S. Josephine G. A, S. Arumugam, *ACS Omega* **2018**, 3, 1090−1101.

[3] B. N, Meethal, N. Pullanjiyot, S. Swaminathan, *Mater. Des.***2017**, 130, 426–432.

[4] A. Kołodziejczak-Radzimska, T. Jesionowski, *Materials,* **2014**, 7, 2833-288.

[5] M. S. Tokumoto, S. H. Pulcinelli, C. V. Santilli, V. Briois, *J. Phys. Chem. B* **2003**, 107, 568-574.

[6] M-K. Liang, M. J. Limo, A. Sola-Rabada, M. J. Roe, C. C. Perry, *Chem. Mater.* **2014**, 26, 4119−4129

[7] K. Rahimi, A. Yazdani, *Mater. Sci. Semicond. Process.,* **2018**, 80, 38-43.

[8] L. Svoboda, R. Dvorsky, P. Praus, D. Matysek, J. Bednar, *Appl. Surf. Sci.***2016**, 388, 491‑496.

[9] S. B. Seenivasagaperumal, S. Shanmugam, *New J. Chem.,* **2018**, 42, 3394.

[10] M. Skompska, K. Zarebska, *Electrochim. Acta,* **2014**, 127, 467–488.

[11] M-Q. Dai, L-Y. L. Yung, *Chem. Mater.* **2013**, 25, 2193−2201.

[12] S. A. Acharya, N. Maheshwari, L. Tatikondewar, A. Kshirsagar, S. K. Kulkarni, *Cryst. Growth Des.* **2013**, 13, 1369−1376.

[13] J. Szczurek, M. Rams-Baron, J. Knapik-Kowalczuk, A. Antosik, J. Szafraniec, W. Jamroz, M. Dulski, R. Jachowicz, M. Paluch, *Mol. Pharmaceutics,* **2017**, 14, 1071−1081.

[14] J. Wang, T. Tsuzuki, B. Tang, P. Cizek, L. Sun, X. Wang, *Colloid Polym Sci*, **2010**, 288, 1705–1711.

[15] H. Sun, J. He, J. Wang, S-Y. Zhang, C. Liu, T. Sritharan, S. Mhaisalkar, M-Y. Han, D. Wang, H. Chen, *J. Am. Chem. Soc*. **2013**, 135, 9099−9110.

[16] Z. Bao, Y. Yuan, C. Leng, L. Li, K. Zhao, Z. Sun, *ACS Appl. Mater. Interfaces,* **2017**, 9, 16417−16425.

[17] Z.J. Yu, M. R. Kumar, Y. Chu, H.X. Hao, Q.Y. Wu, H.D. Xie, *ACS Sustainable Chem. Eng.* **2018**, 6, 155−164.

[18] G. Ciric –Marjanovic, *Synth. Met.* **2013**, 177, 1– 47.

[19] N. R. Tanguy, M. Thompson, N. Yan, *Sens. Actuators, B* 257, **2018**, 1044‑1064.

[20] G. Xiong, P. He, Z. Lyu, T. Chen, B. Huang, L. Chen, T. S. Fisher, *Nat. Commun.,* **2018**, 9, 790.

[21] S. Kumar, S. L. Jain, *Ind. Eng. Chem. Res.* **2014**, 53, 15798−15801.

[22] D. Barpuzary, A. Banik, A. N. Panda, M. Qureshi, *J. Phys. Chem. C* **2015**, 119, 3892−3902.

[23] A. Bensouici, J.L. Plaza, E. Dieguez, O. Halimi, L. Guerbous, M. Sebais, *J. Lumin,* **2010**, 130, 688‑691.

[24] N. Reddeppa, A.K. Sharma, V.V.R. N. Rao, W. Chen, *Microelectron. Eng.*, **2013**, 112, 57–62.

[25] Z. Kaili, D. Yongguo, C. Shimin, *Org. Electron.*, **2015**, 26, 380–385.

[26] W. Cao, L. Wang, H. Xu, *Nano today*, **2015**, 10, 717-736.

[27] C. Han, G. Tan, T. Varghese, M. G. Kanatzidis, Y. Zhang, *ACS Energy Lett.*, **2018**, 3, 818−822.

[28] K. Xu, X. Liu, J. Liang, J. Cai, K. Zhang, Y. Lu, X. Wu, M. Zhu, Y. Liu, Y. Zhu,

G. Wang, Y. Qian, *ACS Energy Lett.* **2018**, 3, 420−427.

[29] L. Armelao, G. Bottaro, M. Pascolini, M. Sessolo, E. Tondello, M. Bettinelli, A. Speghini, *J. Phys. Chem. C* **2008**, 112, 4049-4054.

[30] B. Tyagi, K. Sidhpuria, B. Shaik, R. V. Jasra, *Ind. Eng. Chem. Res.* **2006**, 45, 8643-8650.

[31] K. K. Chattopadhyay, A. N. Banerjee, *Introduction to Nanoscience and Nanotechnology*, PHI learning private limited, **2009**, ISBN-978-81-203-3608-7.

[32] W. Han, L. Ren, L. Gong, X. Qi, Y. Liu, L. Yang, X. Wei, J. Zhong, *ACS Sustainable Chem. Eng*. **2014**, 2, 741−748.

[33] S. Yue, J. Li, L. Wang, B. Haider, E. A. Stach, X. Tong, S. S. Wong, *Cryst. Growth Des*. **2018**, 18, 2055−2066.

[34] J. Li, Q. Wu, J. Wu, *Handbook of nanoparticles*, Springer international publishing Switzerland **2015,** ISBN- 978-3-319-15338-4.

[35] T. Pradeep, *Nano the essentials*, Tata Mc Graw-Hill publications, **2007**, ISBN-13:978-0-07-061788-9.

[36] N. Stojilovic, *J. Chem. Educ.*, **2018**, 95 (4), 598–600.

[37] D. Dzhigaev, T. Stankevic, Z. Bi, S. Lazarev, M. Rose, A. Shabalin, J. Reinhardt, A. Mikkelsen, L. Samuelson, G. Falkenberg, R. Feidenhans'l, I. A. Vartanyants, *ACS Nano* **2017**, 11, 6605−6611.

[38] V.S. muralidharan, A. Subramania, *Nanoscience and Technology*, Ane Books Pvt.Ltd, **2009**, ISBN-13: 978-81-8052-201-7.

[39] B. R. Puri, L. R. Sharma, M. S. Pathania, *Principles of physical chemistry*, Vishal Publishing Co., 2007, ISBN-81-88646-00-8.

[40] F. Huth, A. Govyadinov, S. Amarie, W. Nuansing, F. Keilmann, R. Hillenbrand, *Nano Lett.* **2012**, 12, 3973−3978.

[41] S. Entani, S. Sakai, Y. Matsumoto, H. Naramoto, T. Hao, Y. Maeda, *J. Phys. Chem. C* **2010**, 114, 20042–20048.

[42] S. Myhra, J. C. Riviere, *Characterization of Nanostructures,* **2013**, Taylor and Francis, CRC press, ISBN: 978-1-4398-5415-0.

[43] P. Wang, J. Lei, M. Su, Y. Liu, Q. Hao, H. Ju, *Anal. Chem*. **2013**, 85, 8735−8740.

[44] R. S. Swingle, *Anal. Chem.*, **1975**, 47, 1, 21-24.

[45] K. W. Nebesny, B. L. Maschhoff, N. R. Armstrong, *Anal. Chem.,* **1989**, 61, 7, 469.

[46] H. Sezen, A. A. Rockett, Sefik Suzer, *Anal. Chem*., **2012**, 84, 2990−2994.

[47] J. Klaas, G. Schulz-Ekloff, N. I. Jaeger, *J. Phys. Chem. B* **1997**, 101, 1305-1311.

[48] N. K. Shah, R. K. Pati, A. Ray, I. Mukhopadhyay, *Langmuir*, **2017**, 33, 1599−1604.

[49] T. Soga, *Nanostructured materials for solar energy conversion*, **2007**, Elsevier publications, ISBN-13:978-0-444-52844-5.

[50] A. Stevanovic, J. T. Yates, *J. Phys. Chem. C* **2013**, 117, 24189−24195.

[51] R. N. Sampaio, W. R. Gomes, D. M. S. Araujo, A. E. H. Machado, R. A. Silva, A. Marletta, I. E. Borissevitch, A. S. Ito, L. R. Dinelli, A. A. Batista, S. C. Zílio, P. J. Gonc-alves, N. M. B. Neto, *J. Phys. Chem. A* **2012**, 116, 18–26.

[52] K. sellers, C. Mackay, L. L. Bergeson, S. R Clough, M. Hoyt, J. Chen, K. Henry, J. hamblen, *Nanotechnology and the environment*, CRC press, **2009**, ISBN-978-1-4200-6019-5.

[53] J. Sun, A. Adhikari, B. S. Shaheen, H. Yang, O. F. Mohammed, *J. Phys. Chem. Lett*. **2016**, 7, 985−994.

[54] C. M. Silva, T. M. Rosseel, M. C. Kirkegaard, *Inorg. Chem.* **2018**, 57, 3329−3338.

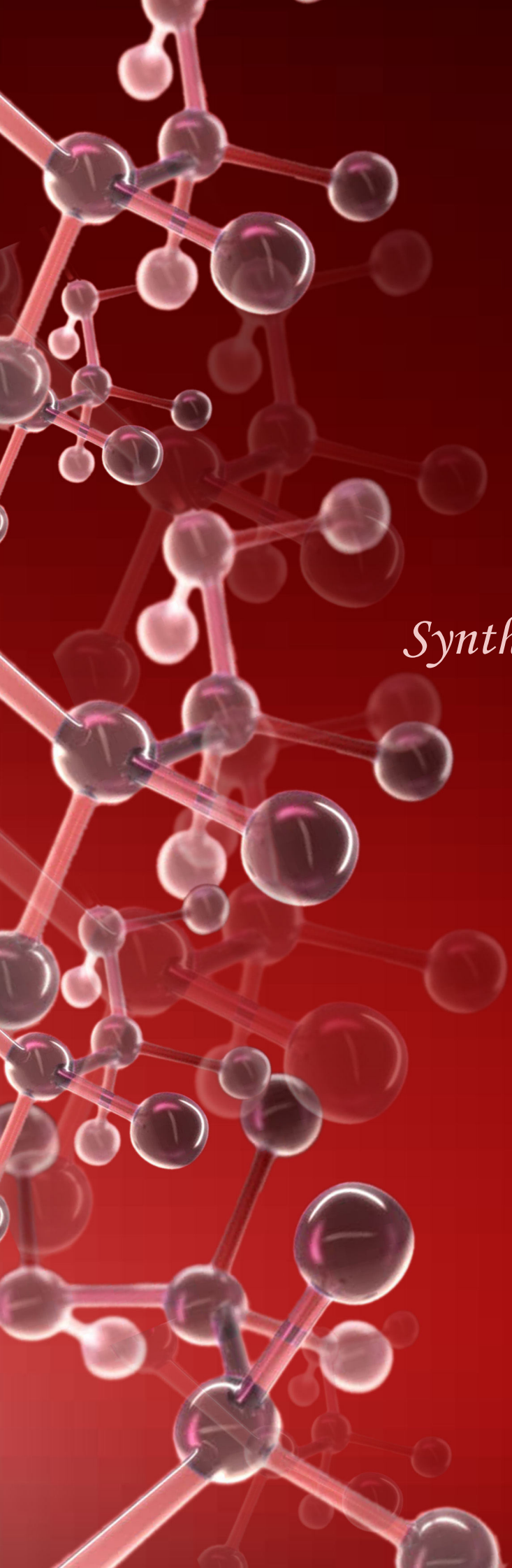

Chapter 3

Synthesis, Characterizations & Applications of ZnO Nanotubes

3 Synthesis, Characterizations & Applications of ZnO Nanotubes

Research in improving the photocatalytic activity of zinc oxide, either by doping or making nanocomposites[1] has been occupying the centre stage for quite a long time. In recent times, studies tend to focus on novel applications of ZnO in solar cell[2], biological labeling[3], LED[4] and in varistors[5] etc, due to its economically viable production methods and eco-friendly nature. Another area that has gained fresh momentum is the application of pure ZnO nanomaterials as photocatalyst[6]. Abdullah *et al.* report that powdered pure ZnO is better for the degradation of broad range of pollutants than it's composite with Ag_2O[7]. A plethora of morphological variants of ZnO nanomaterials such as, nanoflowers[8], nanosheets[9], nanorods[10], nanospheres[11], nanoplates[12], nanowires[13], nanoflakes[14] etc. are being extensively explored as photocatalyst in recent times. However, nanotubes have carved a niche for themselves due to their favourable energy band alignments for efficient trapping of solar energy leading to high photocurrent and photocatalytic activity[15]. Acharyya *et al.* report that, among different morphology of ZnO nanomaterials, nanotubes with better carrier transport have an advantage over other morphologies[16].

A host of comprehensive studies have been conducted on the electrochemical synthesis of ZnO nanotubes[15, 16] to establish the advantage of short time production, but the use of conducting substrate is the flipside of this process. Most of the reports show templated synthesis of nanorods prior to the synthesis of etched nanotubes[17]. However, expensive templates and multiple steps involved in their removal make those methods more difficult. Hence, template-free sol-gel synthesis with minimal usage of cost effective precursors with

one-step surface etched nanotube formation, commencing from nucleation without the assistance of other reagents, is of prime significance[18]. In such cases one precursor can play multiple roles during the formation by eliminating multiple steps and other byproducts during synthesis.

The photocatalytic activity of ZnO finds wider application in the recycling of polluted water, a major public health challenge across the globe[7, 9-11]. Textile industry contributes enormously to the pollutants by way of harmful dyes like Rhodamine B[9], Methylene blue[11] etc. Radical changes are possible in the field of textile dye degradation process with nano zinc oxide photocatalysts due to the small quantity needed for broad range of degradation[19]. It is found that these toxic, refractory, carcinogenic and non-biodegradable textile dyes can be completely decomposed into CO_2, water and mineral acids under room temperature and atmospheric pressure by ZnO nanotubes.

Here, an attempt is made to explore the photocatalytic activities of zinc oxide nanotubes for the degradation of methylene blue (MB), a textile dye. For this, ZnO nanotubes have been prepared in an easier and economical way through sol-gel approach using zinc acetate dihydrate and beta-aminoethylamine (edamine) with water as the medium for synthesis. A slight manipulation in the concentration of the polymeric precursor in reaction medium results in ZnO nanotubes with varying degrees of surface roughness. A template-free single step sol-gel method, which has not been reported previously, is used for the synthesis of ZnO nanotubes in powder form in water medium. The formation mechanism illustrates that, precipitation, co-ordination, dissolution and etching happen in a single stretch within 6 h at mild and constant temperature. A systematic study on the effect of edamine in the surface etching of ZnO nanotubes and the role of etched surface in the degradation of methylene blue dye is discussed in detail in this chapter. Previous reports by Wang *et al* explain the degradation of dye by ZnO nano sheets with an efficiency of 9.4%[20]. Chang carried out MB

degradation under UV light by ZnO/ZnS nanocable and nanotube arrays and got a rate constant (k) value of 0.025 min^{-1} within 2.30 h[21]. Chang *et al.* report, 11% MB degradation under visible light by pure ZnO and maximum 71% degradation by Ag-ZnO-RGO composite within 2 h exposure[22]. Here, the synthesized surface etched nanotubes give 66% dye degradation under visible light within 1.30 h with a k value of 0.012 min^{-1}. The photocatalytic activity of ZnO nanotubes with their varying degrees of surface roughness is correlated with dye degradation studies.

Apart from dye degradation, this synthesized surface modified (roughness) nanotubes are found suitable for self-cleaning applications which has gained significant attention in the commercial use of goggles, wind shields and rear view mirrors. The self-cleaning property of these nanotubes has been confirmed through contact angle measurements. The photocatalytic mechanism is elucidated to highlight its antifogging applications.

3.1. MATERIALS AND METHODS

3.1.1. Sol-gel ZnO nanotubes

All the reagents were used as received, without further purification. Zinc acetate dihydrate, edamine and methanol were from Merck. Double distilled water used for the synthesis was collected from Heal force super easy series ultrapure water purification system. ZnO nanotubes with varying surface roughness were synthesized by changing the molar ratio of zinc acetate and edamine gradually to 1:0.5, 1:1 and 1:2. For the synthesis of ZnO nanotubes with equimolar ratio (1:1), 0.015 M zinc acetate solution was prepared in double distilled water and kept in a water bath at 60 °C. 0.015 M edamine was injected into this solution with micro pipette and the beaker was kept for 6 h of aging at the same temperature. The white powder formed was washed thrice in water and extracted with the help of a high speed centrifuge at 12000 rpm for ten minutes. The precipitate thus synthesized with equimolar

concentration of precursors was named as 11ZE. The same procedure was repeated with changed molar concentrations of the precursors for the preparation of two more samples named 21ZE and 12ZE respectively for 1:0.5 and 1: 2 ratio of zinc acetate to edamine. The synthesized samples were sintered at 400 °C for 1 h and stored for further characterizations.

3.2 MECHANISM

Nucleation and growth of ZnO nanotubes

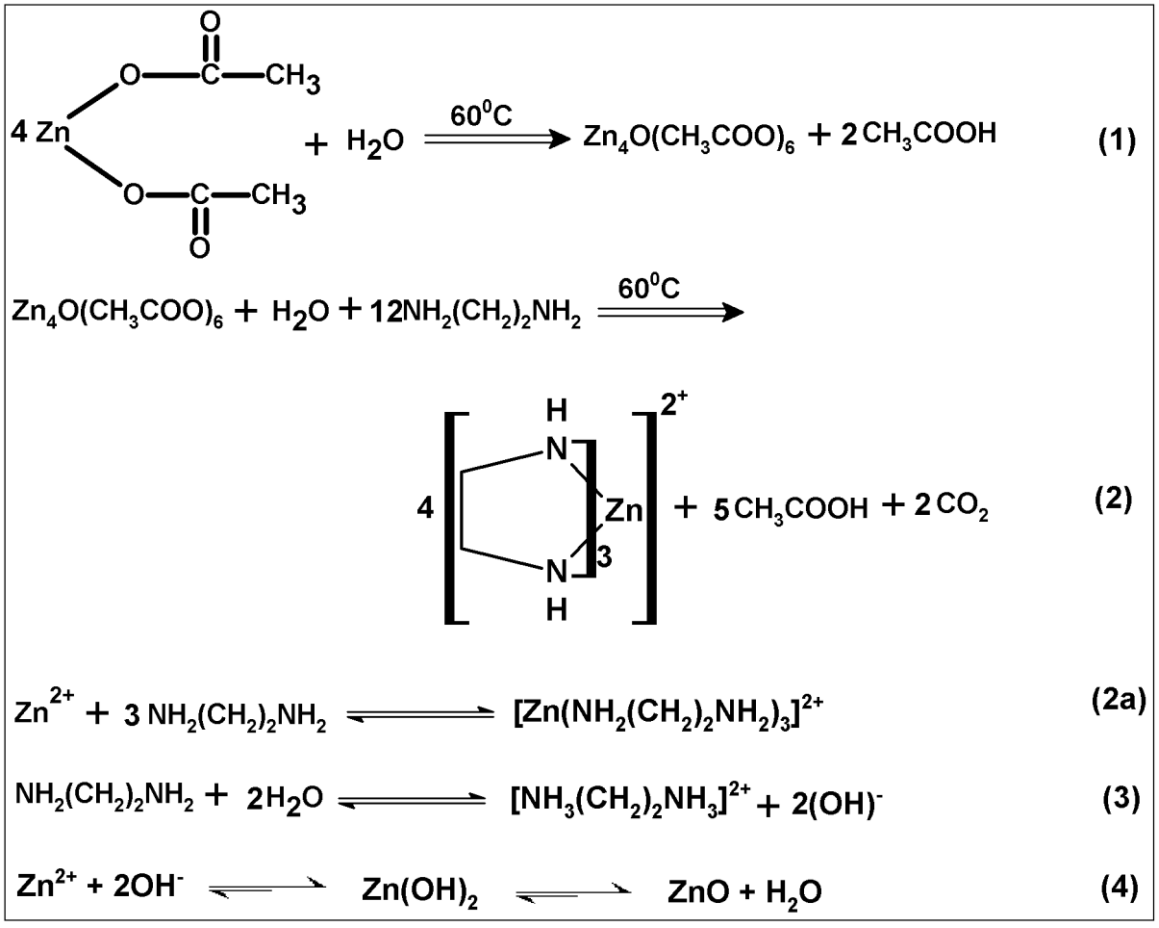

Figure 3.1 Proposed mechanism of the sol-gel synthesis of ZnO nanotubes

Sol gel synthesis involves hydrolysis of the precursors. When zinc acetate dissolves in water, the resultant temporary complex (step (1) of Figure 3.1) retains a solution pH of 5[23]. On addition of alkaline precursor, edamine, to the medium the pH shoots up suddenly to 7.5, 6.5

and 5.5 for 12ZE, 11ZE and 21ZE respectively. The increase in pH lead to immediate Zn^{2+} precipitation followed by the formation of Zn^{2+}-edamine complex (step 2 of Figure 3.1)[24]. At the same time edamine gets hydrolysed and helps the formation of hydroxyl ions (Step 3 of Figure 3.1). The Zn^{2+} from step (2) and OH^- from step (3) combine to form $Zn(OH)_2$ leading to the formation of ZnO. In the case of 12ZE, the increase in pH helps to increase the nucleation excessively because of the higher edamine concentration. Here growth starts only after completion of the heterogeneous nucleation[25] as pH of the solution spirals down from 7.5 to 5 in the final stage of the synthesis. Fast consumption of growth species and inhibition of further growth leads to undefined crystal growth in 12ZE. At low edamine concentration (21ZE), the reversible reaction (step (3) in Figure 3.1) predominates and reduces the availability of OH^- in the solution. Here, the pH of the solution observed was 5.5 after addition of edamine and this pH gets maintained throughout the process without fluctuations. This facilitates the occurrence of heterogeneous nucleation, growth and dissolution process simultaneously. Here, water and acetate helps to accelerate the growth process[23, 26] to compensate the shortage of edamine. Zinc oxide is formed directly from the complex $Zn_4O(CH_3COO)_6$ without undergoing co-ordination with edamine, *i.e* in such cases steps (2) and (3) of Figure 3.1 takes place scarcely. The precursor concentration was optimized in 11ZE for the synthesis of surface etched ZnO nanotubes for efficient photocatalysis. In the case of 11ZE the initial pH drops from 6.5 to 5.5 in the early stages of the growth process and surface etched nanotube formation takes place by the dissolution and etching along with growth process at a stable solution pH of 5.5[27].

Wurtzite ZnO crystal structure is formed by the alternate stacking of Zn^{2+} and O^{2-} enriched polar surfaces. Zn^{2+} polar surfaces {0001} are of two types; O-atom terminated and Zn-atom terminated. The growth occurs along oxygen atom terminated zinc polar surfaces; as the double layer formed from solution contain fewer number of OH^-. Here, the fewer number

of OH^- can be attributed to the oxygen atom termination in zinc polar surface which occurs through hydroxyl groups. When pH reaches 5.5, the unstable O^{2-} rich polar surfaces undergo dissolution[28] at a comparatively faster pace. Nonpolar surfaces {1010} in presence of edamine become relatively stable because these {1010} planes are covered by nonpolar chains of edamine. The dissolution of oxygen rich polar surfaces is inferred from the PL spectra by the presence of emission peaks due to oxygen vacancies along with bandedge emission and no peak due to zinc vacancies are detected. From our experimental observation it was found that the pH 5.5 trigger the formation of nanotubes with chelation assisted combined growth-dissolution-etching mechanism. The schematic illustration of the synthesis procedure adopted for the nanotube formation is shown in Figure 3.2.

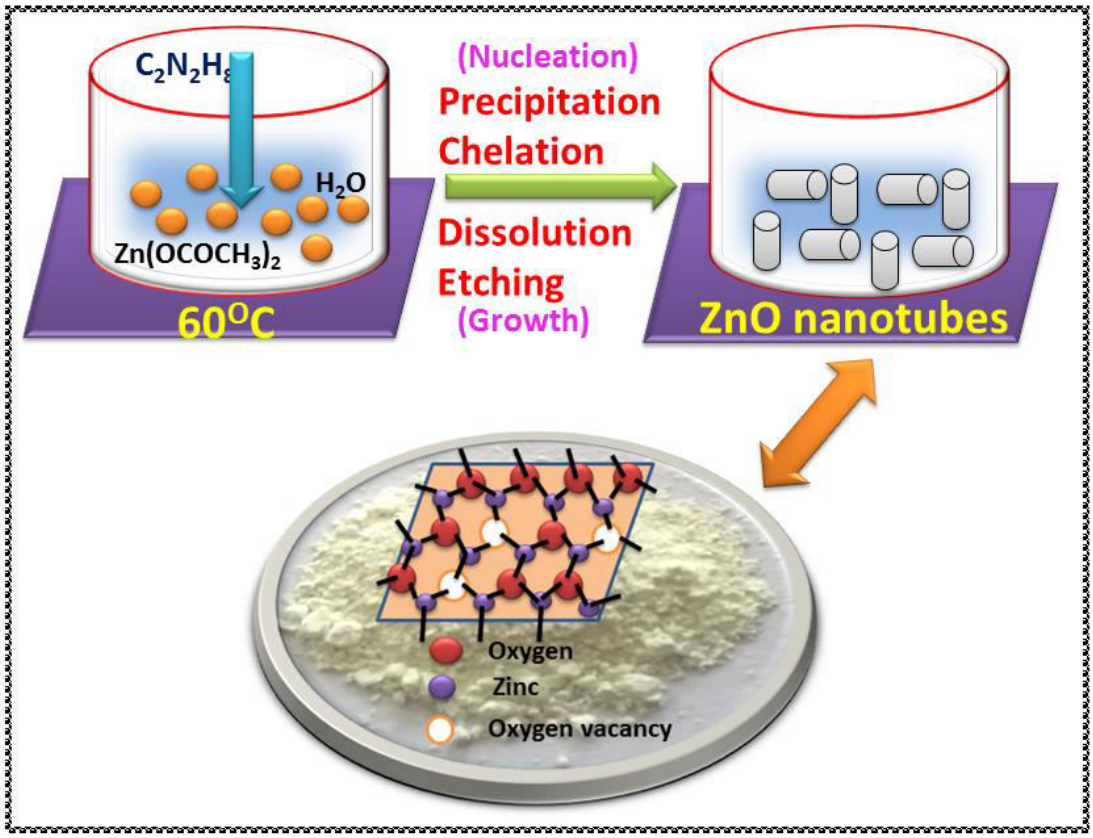

Figure 3.2 Schematic diagram of the synthesis procedure of ZnO nanotubes

The multitasking characteristics of edamine during ZnO nanotube synthesis and

optimization of its concentration for efficient photocatalyst are evident from the points listed. (1) The presence of edamine rapidly brings up the alkalinity of the precursor solution to facilitate nucleation by precipitating Zn^{2+}cations. (2) The bi-dentate chelating effect helps to control the supersaturation for the nucleation and growth of ZnO nanotubes. (3) Capping property of edamine helps to hinder agglomeration of nanocrystals and assist anisotropic growth. (4) A particular concentration level of edamine promotes etching of nanotubes along with growth of particles. (5) Edamine also plays a role in concentration dependent selective dissolution of polar planes to accelerate ZnO nanotube formation.

3.3 CHARACTERIZATIONS

3.3.1 Instrumentation used

The crystal structure was elucidated from X-Ray powder diffraction (XRD) studies using Rigaku miniplex X-Ray diffractometer (Cu Kα, λ= 0.15496 nm), scanned between 10 to 80°. Morphology and size of the ZnO nanoparticles were investigated using Hitachi SU 6600 field emission scanning electron microscope. The elemental composition of the sample was confirmed from EDAX analysis using Oxford instruments. Absorption spectra of the samples were recorded by means of Shimadzu 3600 plus spectrometer. Photoluminescence (PL) spectra were taken by using Perkin Elmer LS 55 luminescence spectrometer with Xenon discharge lamp at room temperature. Percentage of transmittance of the samples was analyzed from Fourier Transform Infrared Spectra (FTIR) by using PerkinElmer FTIR Spectrum Two instrument with a resolution of 4 cm^{-1}. Raman spectra were taken with JASCO instrument with 532 nm laser wavelength.

3.3.2 Morphology and structural analysis

3.3.2.1 Scanning Electron Microscopy (SEM)

From SEM analysis it is evident that the edamine concentration has a significant role in the shape, size and surface etching of the formed nanotubes. The SEM micrographs of 12ZE, 21ZE, and 11ZE show nanotube morphology with different tube size and surface roughness as seen in Figure 3.3 (a-c).

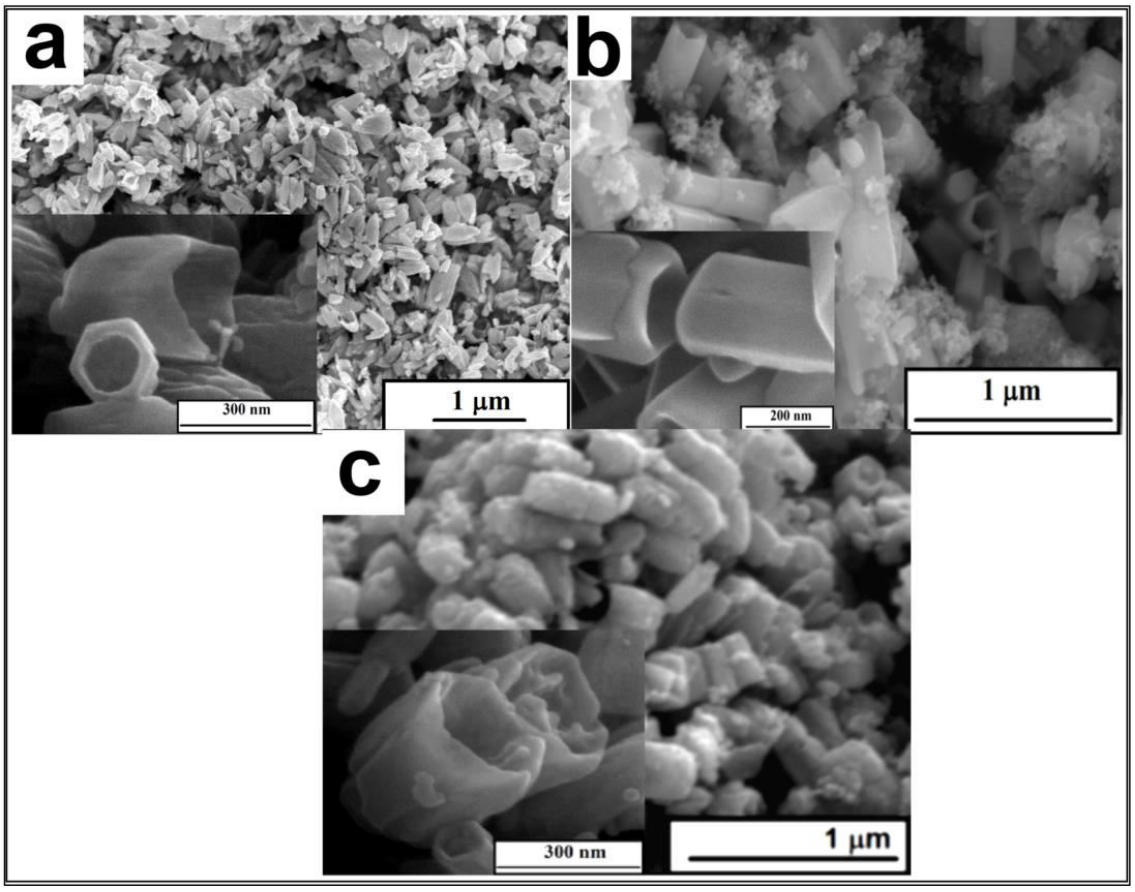

Figure 3.3 SEM images of calcined (a) 12ZE, (b) 21ZE, (c) 11ZE

Edamine concentration increases gradually from 21ZE, 11ZE and 12ZE. 21ZE shows slightly elongated nanotubes with smooth surface with hexagonal edge, but for 11ZE, the tube surface becomes etched due to the increased concentration of edamine and loses definite edge shape. Further increase on the concentration of edamine leads to the destruction of nanotube structure and uncertain particle dimension for 12ZE samples. It is presumed here that, the presence of edamine in the reaction medium acts as an etching agent and gradually

destroys ZnO nanotubes with increased concentration. The formation of non-tubular structure along with the nanotubes seen in the case of 21ZE (Figure 3.3b) may be an outcome of lesser concentration of edamine, which in turn results in the formation of zinc oxides directly from the complex $Zn_4O(CH_3COO)_6$ without undergoing co-ordination with edamine[23].

3.3.2.2 Energy Dispersive Spectrum (EDS)

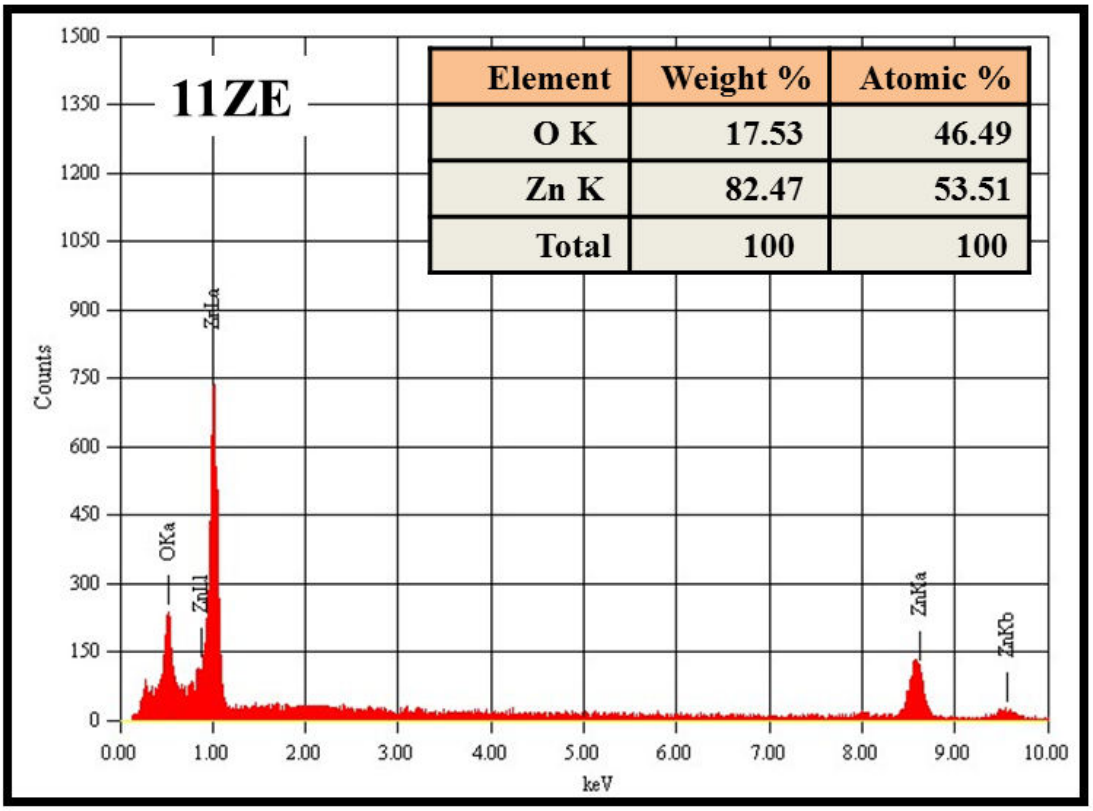

Figure 3.4 EDS spectra of 11ZE

Figure 3.4 shows the EDAX spectrum of 11ZE confirming the elemental composition of the sample. The EDAX result shows only zinc and oxygen in the sample. The richness of Zn atom seen in the EDAX spectrum of ZnO crystals indicates oxygen deficiency present in the sample[29].

3.3.2.3 X-ray Diffraction Analysis (XRD)

X-Ray powder diffraction (XRD) method is conducted to study the crystalline structure and phase of ZnO before and after calcination and the diffractograms are shown in Figure 3.5. Sample before calcination (BC-11ZE) do not undergo any phase changes but shows extra peaks (marked by * in figure 3.5). After calcination, all impurity peaks disappeared and the purity of the ZnO samples is ensured. The data is compared with JCPDS File No: 89-0510 to confirm the anisotropic growth of wurtzite ZnO with hexagonal geometry[22]. The maximum intense peak is observed at a 2θ value of 36.4° (101) and other peaks are at 31.8°(100), 34.6°(002), 47.6°(102), 56.6°(110), 63° (103) and 68° (112) for all three samples. From the XRD pattern the crystallite size is calculated using Scherrer equation[23] and is found to be 26.04, 27.94 and 28.03 nm for 11ZE, 12ZE and 21ZE respectively.

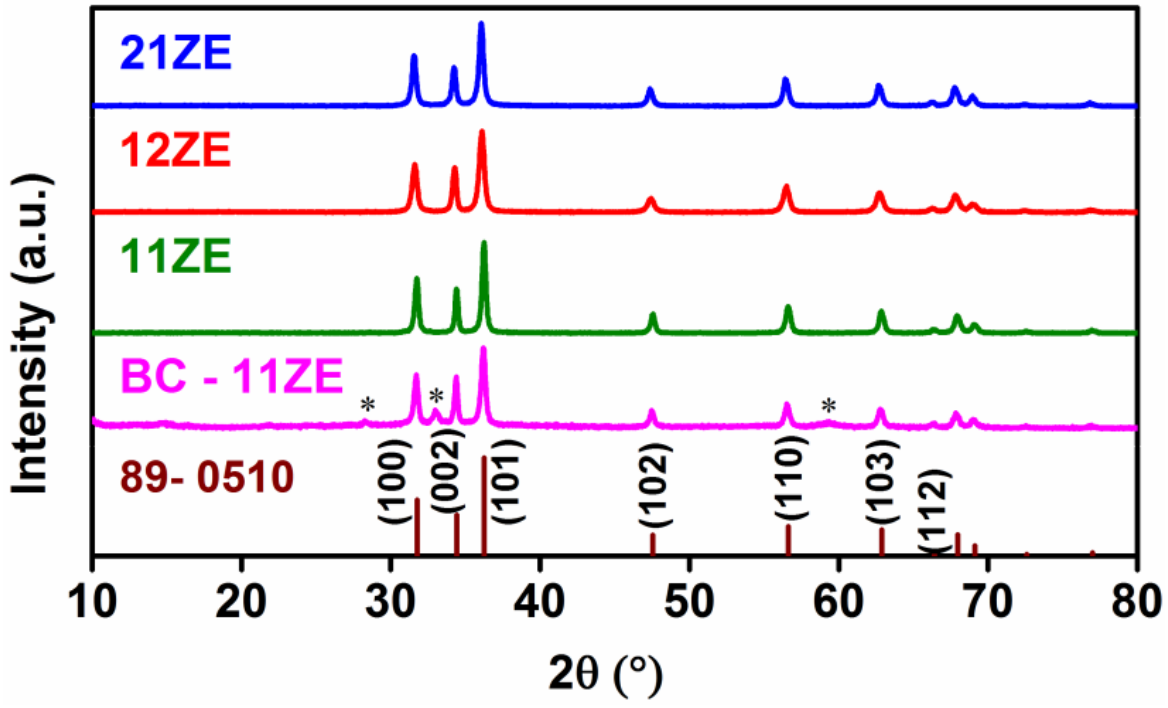

Figure 3.5 XRD of ZnO samples before and after calcination compared with JCPDS

3.3.2.4 Raman Spectroscopy

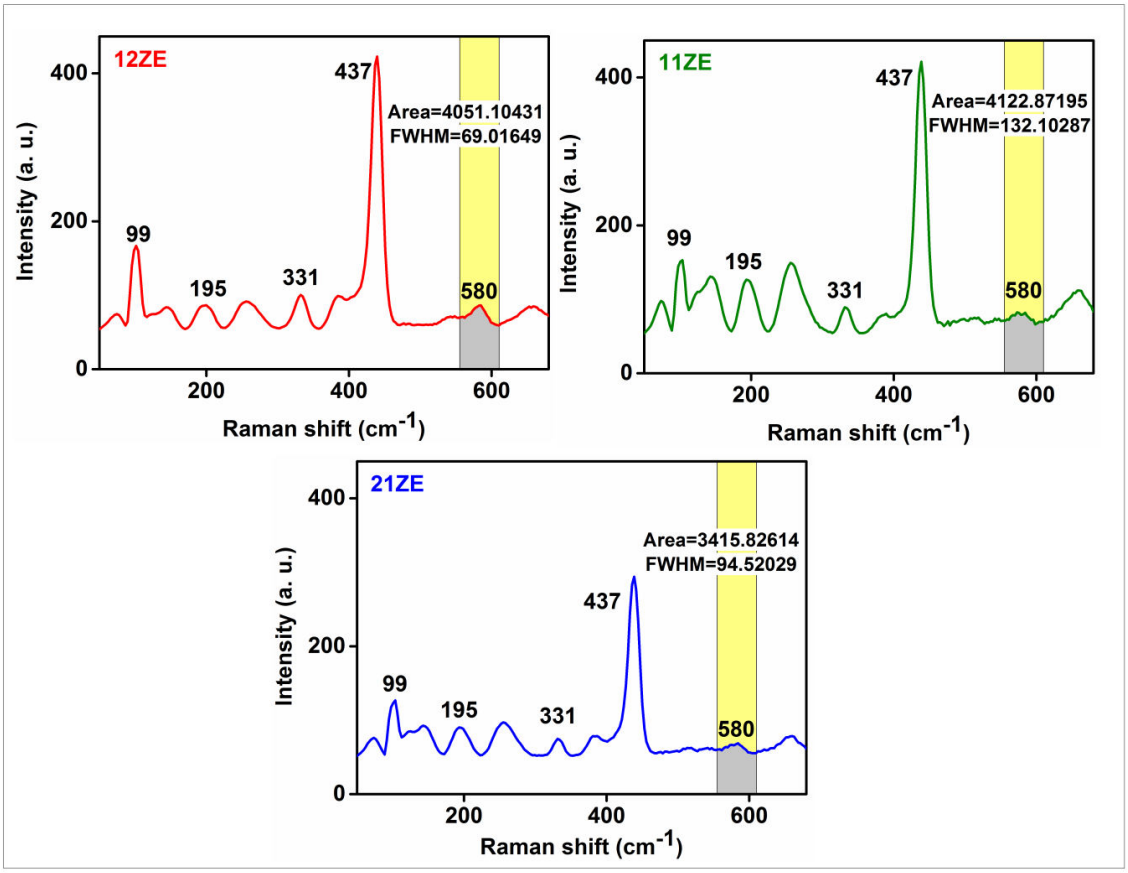

Figure 3.6 Raman spectra of 12ZE, 11ZE and 21ZE

The difference in surface oxygen vacancies are demonstrated in Raman spectra of the samples. The analysis was done with laser wavelength 532 nm. The spectra are shown in Figure 3.6. Vibrational bands in Raman spectra are due to the active phonon modes of wurtzite ZnO with C_{6V} symmetry. Bands at 99 cm^{-1}(E_2 low) and 437 cm^{-1} (E_2 high) are characteristic peaks of wurtzite ZnO structure[30]. Strong high intense E_2 (high) mode indicates good crystallinity of the samples. Peaks at 144 cm^{-1} and 195 cm^{-1} are attributed to lattice vibrations and TO (Transverse and Optical) overtone respectively[31]. The vibrational mode at 256 cm^{-1} corresponds to laser plasma lines[32]. The peak at 331cm^{-1} corresponds to phonon scattering peak overlap of E_2 (high) and E_2 (low) and the one observed at 660 cm^{-1} represents an intrinsic mode of ZnO (TO+LO). The peaks at 560 cm^{-1} and 580 cm^{-1} represents zinc and oxygen deficiencies[30, 33]. Here, the peak at 560 cm^{-1} is absent in all three samples indicates

absence of zinc deficiencies. The area ratio at 580 cm^{-1} are calculated and found to be 1.19:1.21:1.0 for 12ZE, 11ZE and 21ZE respectively.

3.3.2.5 Fourier Transform Infrared Spectroscopy (FTIR)

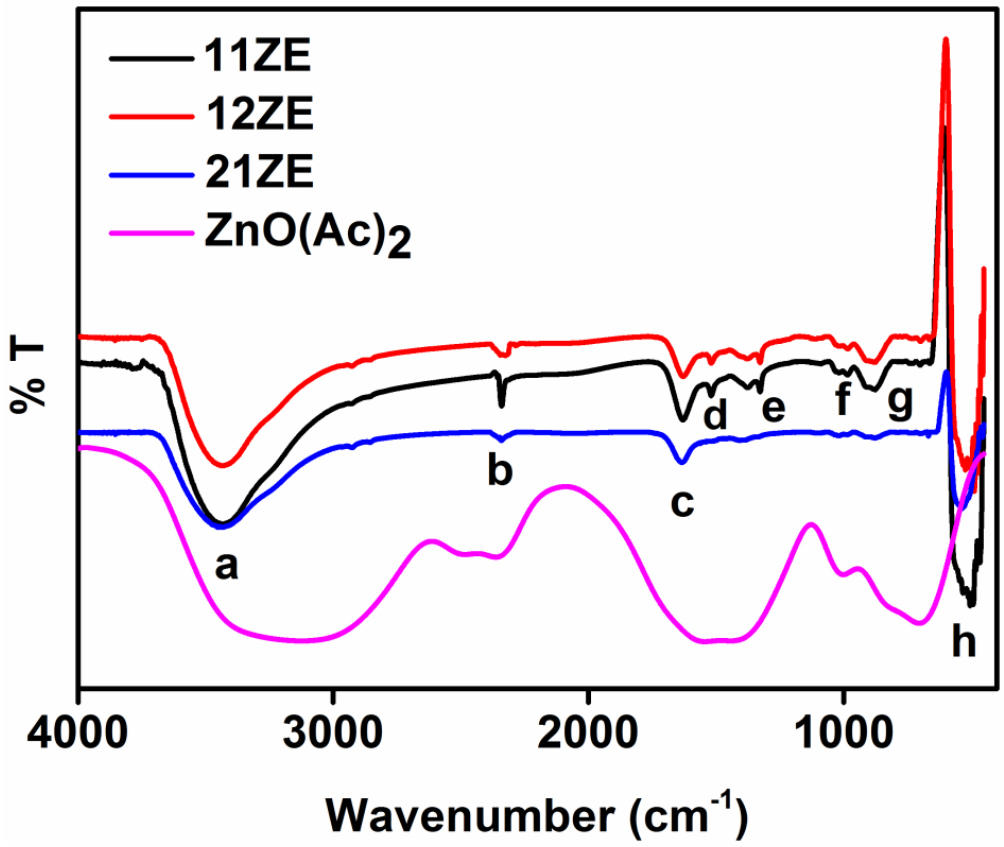

Figure 3.7 FTIR spectra of 11ZE, 12ZE, 21ZE and zinc acetate

The formation of ZnO nanostructures is further confirmed using FTIR analysis and the spectra obtained are shown as Figure 3.7. All the three samples except the precursor zinc acetate show an intense peak at 480 cm^{-1} (h) due to the stretching vibrations of Zn-O bond confirming the formation of zinc oxide. Peak at 3435 cm^{-1} (a) indicates the presence of O-H stretching vibration[34] which is conspicuously broadened in zinc acetate dihydrate. All samples give almost the same intense peak at 1626 cm^{-1} (c) because of O-H bending vibrations[35]. The C=O stretching mode is observed at 2340 cm^{-1} (b) [36]. Other peaks present at 1515 cm^{-1}(d), 1330 cm^{-1} (e), 990 cm^{-1} (f) and 875 cm^{-1} (g) are of negligible intensity in

smooth surfaced 21ZE. The broad band (c) in zinc acetate allocates symmetric and asymmetric stretching vibrations of COO^- group[37].

3.3.2.6 Transmission Electron Microscopy (TEM)

The TEM image of 11ZE is shown in Figure 3.8. Stalking faults of the crystal lattice fringes is clearly visible from the HRTEM image. The deviations in the lattice fringe continuum can be due to the defects present in the crystal[38]. The Selected Area Electron Diffraction (SAED) pattern reveals the polycrystalline nature of 11ZE.

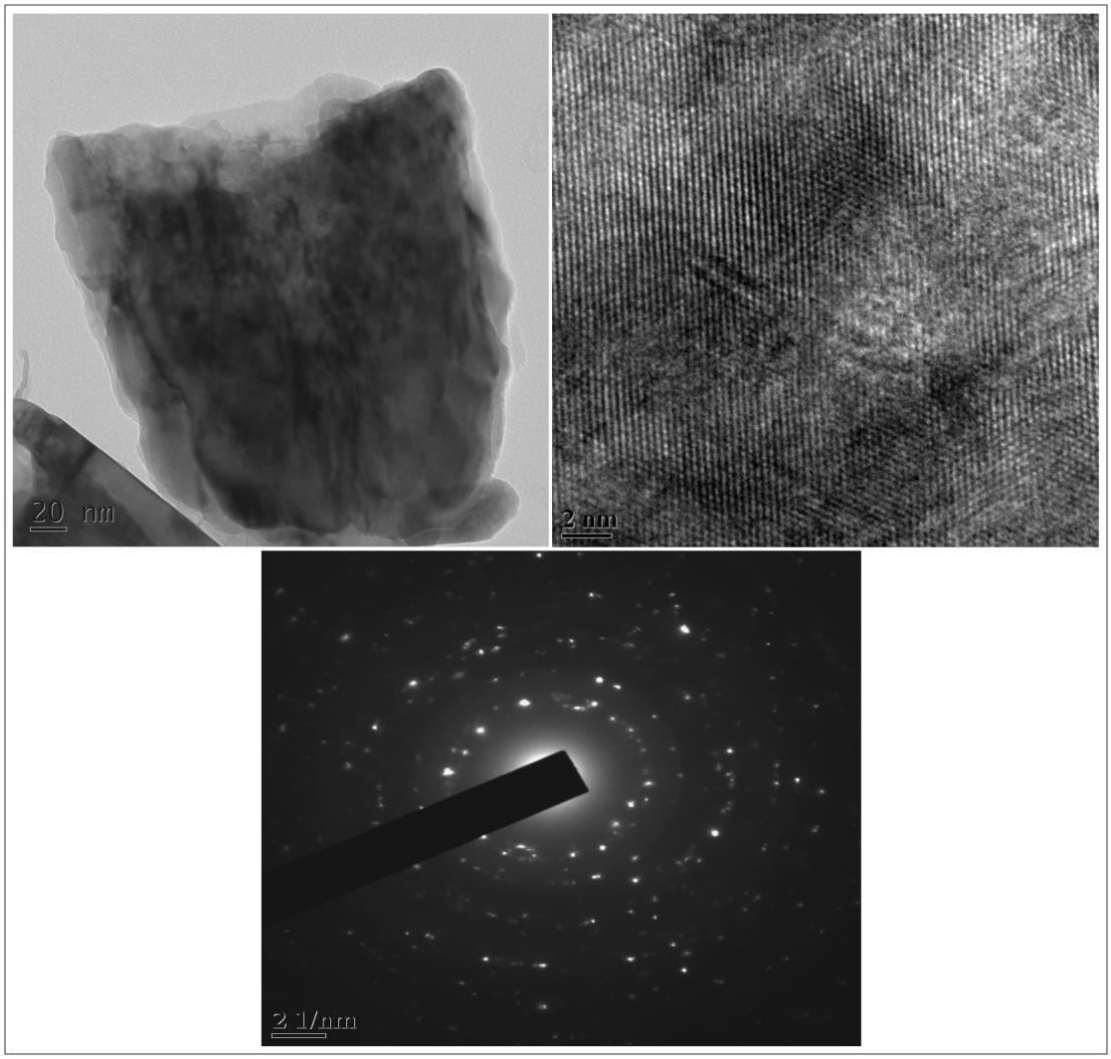

Figure 3.8 TEM, HRTEM images and SAED pattern of 11ZE

3.3.3 Optical properties

3.3.3.1 Diffuse Reflectance Spectroscopy (DRS)

Diffuse reflectance spectra of the samples taken before and after calcination are shown in Figure 3.9. All samples show almost similar absorption in both cases with a band edge absorption is observed around 369 nm.

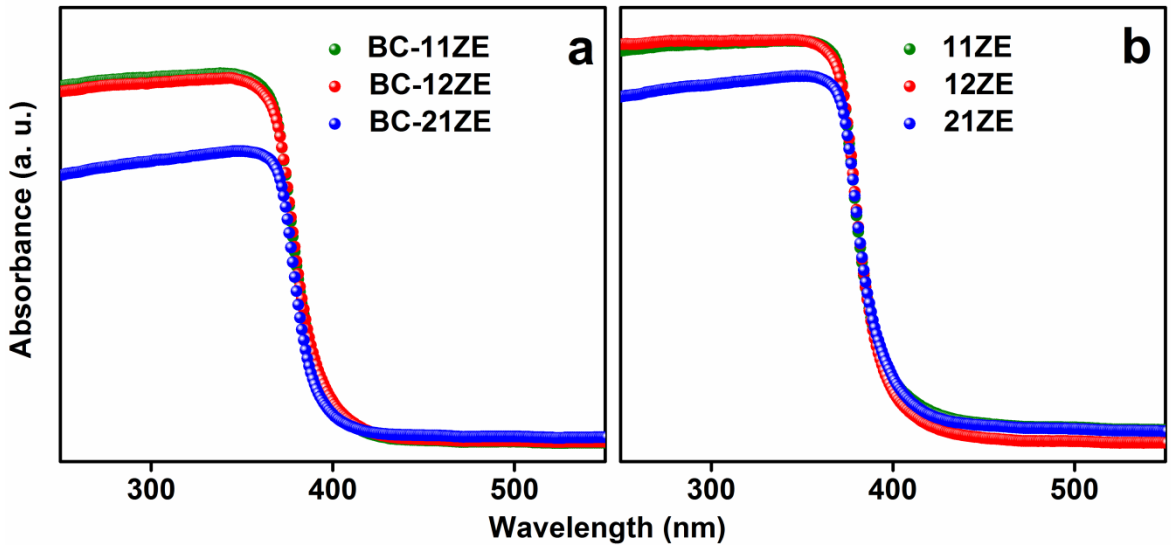

Figure 3.9 Diffuse reflectance spectra of ZnO (a) pre-calcination and (b) post- calcination

3.3.3.2 Tauc Plot

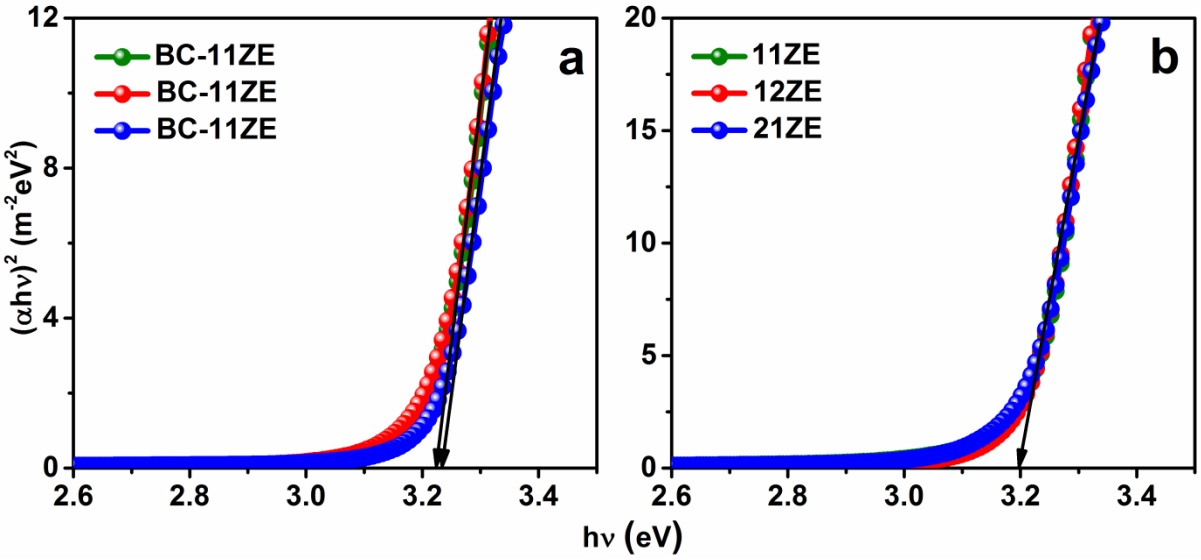

Figure 3.10 Tauc plots of ZnO samples (a) pre-calcination and (b) post-calcination

The bandgap of ZnO samples before and after calcination is determined by means of Tauc plot and is found to be ~3.3 and 3.1 eV respectively. This narrowing of bandgap after temperature treatment may be due to self-doping arises in the crystal lattice[39] or increased oxygen deficiency[40]. The corresponding Tauc plot is given in Figure 3.10.

3.3.3.3 Photoluminescence Spectroscopy (PL)

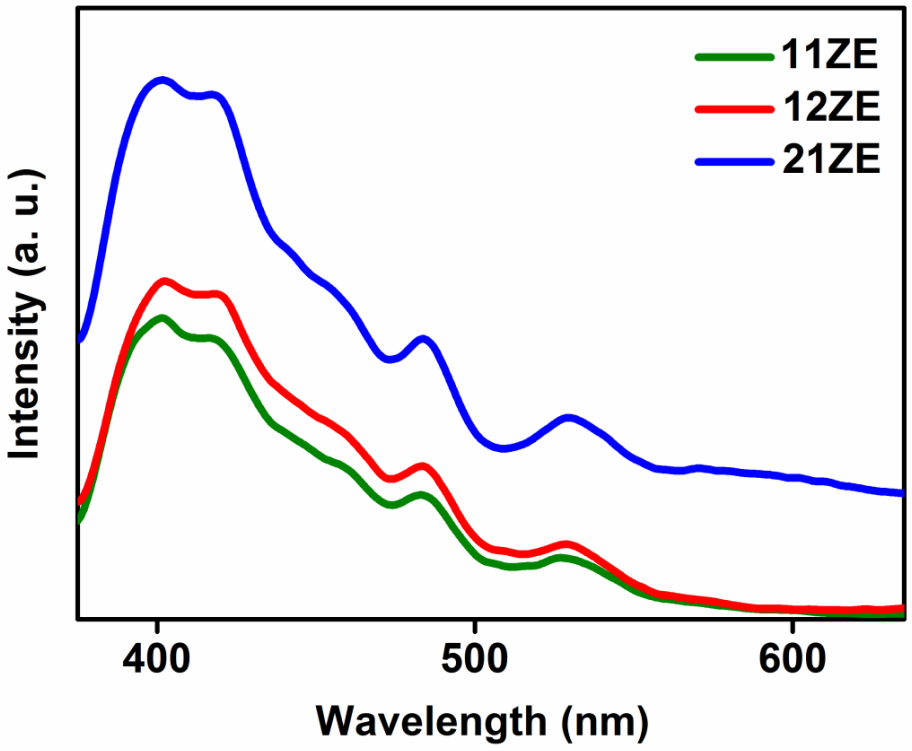

Figure 3.11 PL spectra of 11ZE, 12ZE, 21ZE

Emission behaviour of the ZnO nanostructures was checked by recording the photoluminescence spectrum of the calcined samples at room temperature. All the samples are excited at 340 nm and the resultant band edge emission is observed around 400 nm as shown in Figure 3.11.

The emissions, observed at 420, 485 and 528 nm are due to defect emissions from the ZnO nanocrystals[41]. The blue emission observed at 420 nm can be assigned to the transition between the conduction/valence bands and trap states near the valence or conduction band[42].

The emission at 485 nm may arise due to oxygen vacancy (V_o) or singly ionised oxygen vacancy (V_o-) in ZnO lattice[43]. The green emission observed at 528 nm in ZnO can be attributed to the transition of electrons from the conduction band to the defect states due to oxygen vacancies[41- 44].

3.3.4 Photoactivity study

Chronoamperometric analyses were done to study the photoactivity of 11ZE, 12ZE and 21ZE by measuring the photocurrent density. Photocurrent was measured under 1 sun illumination (100 mW/cm^2) using a solar simulator interfaced with Biologic SP-150 potentiostat instrument. A three electrode system was used with Ag/AgCl as reference electrode, Pt wire as counter electrode, evenly distributed ZnO film (with a fixed area of 0.25 cm^2) on FTO as working electrode and 0.1 M Na_2SO_4 as electrolyte. Chronoamperograms were recorded after ten cycles of periodic illuminations with intervals of 60 s.

3.3.4.1 Chronoamperometric analysis

Photoactivity of ZnO nanostructures has been studied by using chronoamperometry under illumination and the corresponding time dependent current behaviour is shown in Figure. 3.12. Photoconductivity being surface related, the ZnO samples with different surface roughness show different photocurrents. When ZnO is illuminated, the excitons generated are proportional to the photocurrent generated from the sample[45, 46]. The stability and degradation of photocurrent are different for the three samples and 11ZE is found to be more stable (0.056 mA/Cm^2) with minimum rate of photocurrent degradation. It is presumed here that, more oxygen species from the electrolyte is chemisorbed on the etched surface of 11ZE and converted to superoxides (O_2^-) by accepting the excited electrons (reaction 1). Photocurrent is contributed by the electrons generated as a result of oxygen desorption by the reaction of holes with the superoxides (reaction 2)[47].

$$O_2 + e^* \rightarrow O_2^- \qquad (1)$$

$$O_2^- + h^+ \rightarrow O_2 \qquad (2)$$

The stable photocurrent observed for 11ZE can be attributed to the increased trap states arise from the etched surface. These defect states due to oxygen increases the carrier lifetime and prevent recombination resulting in a steady photocurrent formation by desorption of chemisorbed oxygen on the surface of the ZnO nanotube. For 12ZE and 21ZE, under illumination, initially photocurrent attains a maximum value then slowly decays to a steady state[48]. It is presumed here that both the chemisorbed oxygen and oxygen related defects are less for these two samples, showing photocurrent decay. The photocurrent stability after many cycles of illumination denotes the photocatalytic stability of the sample maintained by means of continuous charge transport at the electrode-electrolyte interface[49].

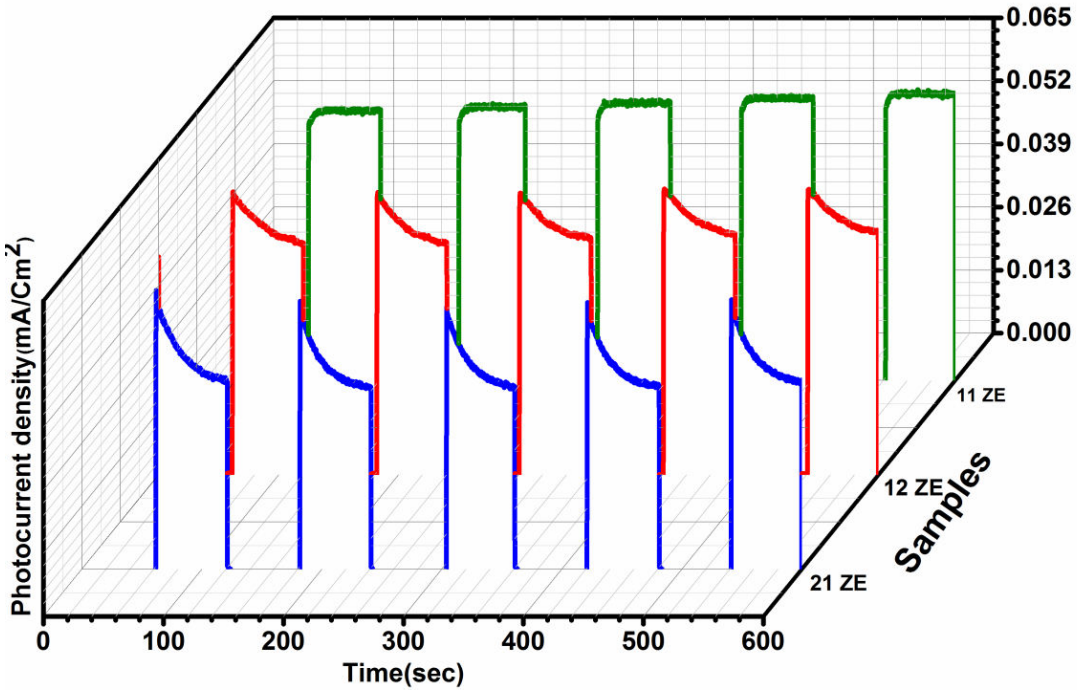

Figure 3.12 Chronoamperogram of 11ZE, 12ZE and 21ZE

3.4 APPLICATIONS - PHOTOCATALYSIS

3.4.1 Water treatment - Dye degradation

Photocatalytic activity of ZnO nanostructures with tuned morphology and surface was studied by checking the degradation of a textile dye, methylene blue, in aqueous solution. Methylene blue was supplied by Spectrochem. A weighed amount of 0.05 g of each sample was taken in a beaker. 50 mL methylene blue solution in distilled water (0.002 wt %) was added to the beaker containing ZnO nanotubes and was stirred in dark for 30 minutes. Then, the beaker was placed under 300 W Xenon lamp with stirring continuing. At 15 minutes of periodic intervals of exposure, small volumes of the solution mixture were taken to study the dye degradation by recording the absorption spectra.

During photocatalysis, the degradation process is activated by the excitons generated by ZnO and the degradation rate of dye is influenced by the exciton recombination rate[50]. Being a direct bandgap semiconductor, radiative recombination occurs faster for ZnO. However, the defect density controls the exciton recombination behaviour by triggering Shockley-Read-Hall (SRH) recombination[51]. The oxygen related defect states are capable of controlling the photocatalytic degradation of organic dyes[50].

In the process of dye degradation the excitons generated in ZnO on illumination produce highly reactive hydroxyl free radicals (OH^0) and superoxide species (O_2^-) by reacting with water present in the MB solution. These hydroxyl free radicals and superoxides decompose methylene blue to CO_2, H_2O and volatile organic compounds (VOC), leading to decolourisation of the dye solution. During photocatalysis of dye, the light illumination is done after stirring the dye solution with ZnO nanostructures for 30 minutes in dark to establish adsorption-desorption equilibrium between ZnO and dye. To eradicate any error due to initial adsorption of methylene blue on the surface of zinc oxide samples, the mixture was stirred in dark for 30 minutes before being placed under light source. According to the data obtained after 30 minutes, dark adsorption analysis, 21ZE shows very weak adsorption

compared to other two samples to establish adsorption-desorption equilibrium. The heat dispersed due to illumination is considered to be insignificant as it doesn't play any role in photocatalysis[52]. A time dependent concentration study of the dye in the presence of 11ZE, 12ZE and 21ZE is done under illumination and is graphically represented in Figure 3.13.

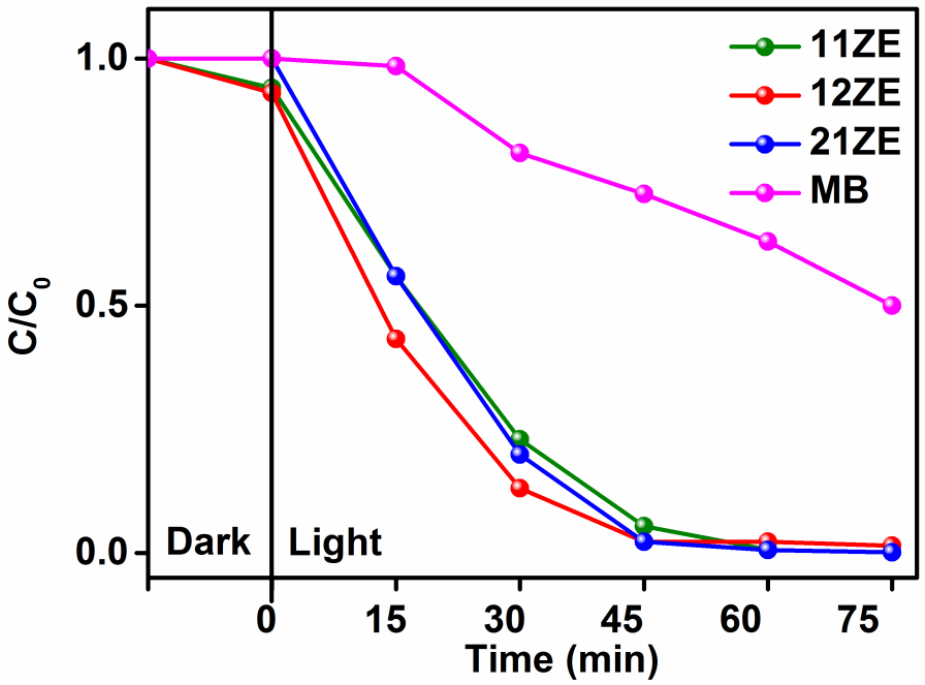

Figure 3.13 Photocatalytic MB degradation in the presence of zinc oxide samples

Pure methylene blue is found to be degraded in the absence of photocatalyst at about 35 percent. This may be attributed to the presence of dissolved oxygen present in the water[53]. The degradation of methylene blue in presence of ZnO follows a pseudo first order kinetics with rate constant $k=1/t \ln (C_0/C)$[50], where, C_0 is the initial and C is the final concentration of the dye. 11ZE with its etched surface produces high and stable photocurrent which translates in to increased photocatalytic activity. In this process the degradation of dye and regeneration of hydroxyl and superoxide species occur simultaneously. The chemisorbed oxygen on the surface of ZnO nanostructure has a significant role in the regeneration mechanism of hydroxyl and superoxide species for the degradation of dye and the same can be represented as follows[54].

$$O_2 + e^- \rightarrow O_2^- \quad (3)$$

$$O_2^- + H^+ \rightarrow HO_2^\circ (Free\ radical) \quad (4)$$

$$HO_2^\circ + O_2^- + H^+ \rightarrow H_2O_2 + O_2 \quad (5)$$

$$H_2O_2 + hv \rightarrow 2OH^\circ \quad (6)$$

The schematic illustration of the mechanism of dye degradation is shown in Figure 3. 14. Among the three oxygen deficient zinc oxide nanotubes, surface etched 11ZE shows better degradation efficiency towards methylene blue[50]. Here, the photocatalytic degradation rate is influenced by the rate of formation of superoxides and hydroxyl free radicals that correlate with the exciton lifetime.

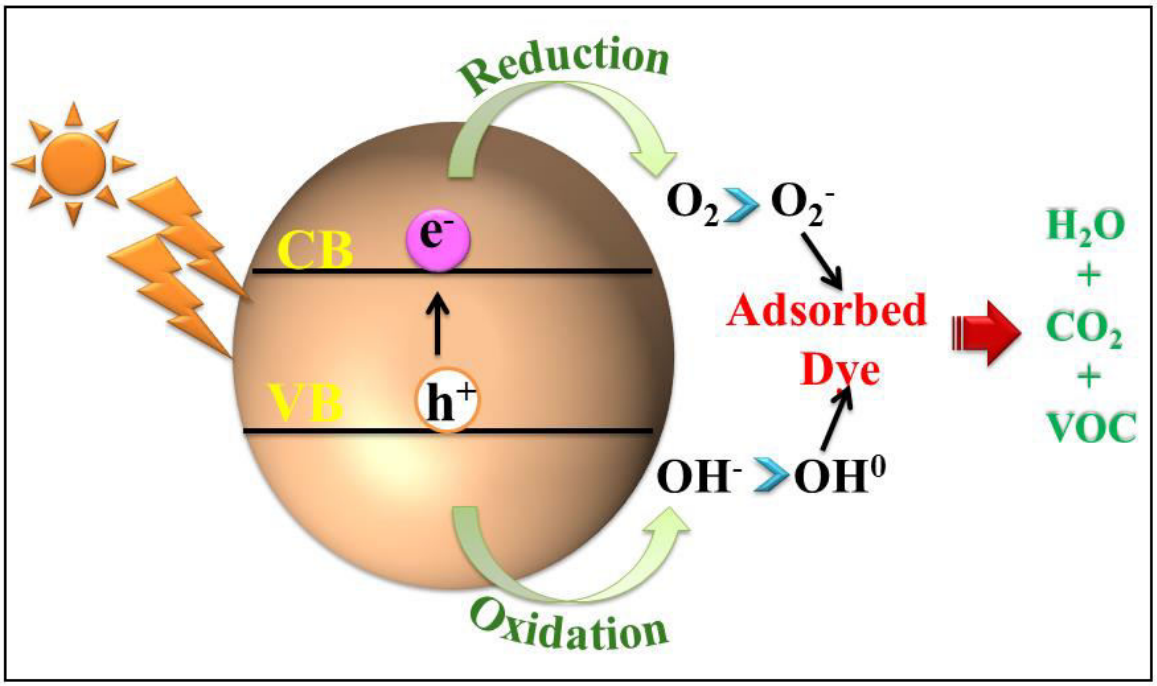

Figure 3.14 Plausible mechanism of Photocatalytic dye degradation

Recombination of excitons eliminates the formation of superoxides and hydroxyl free radicals and thus affects the photocatalytic reaction rate. PL data support this argument by showing minimum bandedge emission for 11ZE samples. 21ZE shows high intense bandedge emission indicating high recombination rate of photogenerated carriers, leading to low photocatalytic activity[45]. The surface defect sites present near valence and conduction bands

minimizes the bandedge recombination rate by trapping these photo-excited carriers and enhances the photocatalytic activity.

The recyclability of the photocatalyst is an essential pre-requisite for the practical industrial applications[55]. The recyclability and performance stability put to test by the recurrent use of the powder in five consecutive cycles for degrading fresh dye and the results are shown in Figure 3.15.

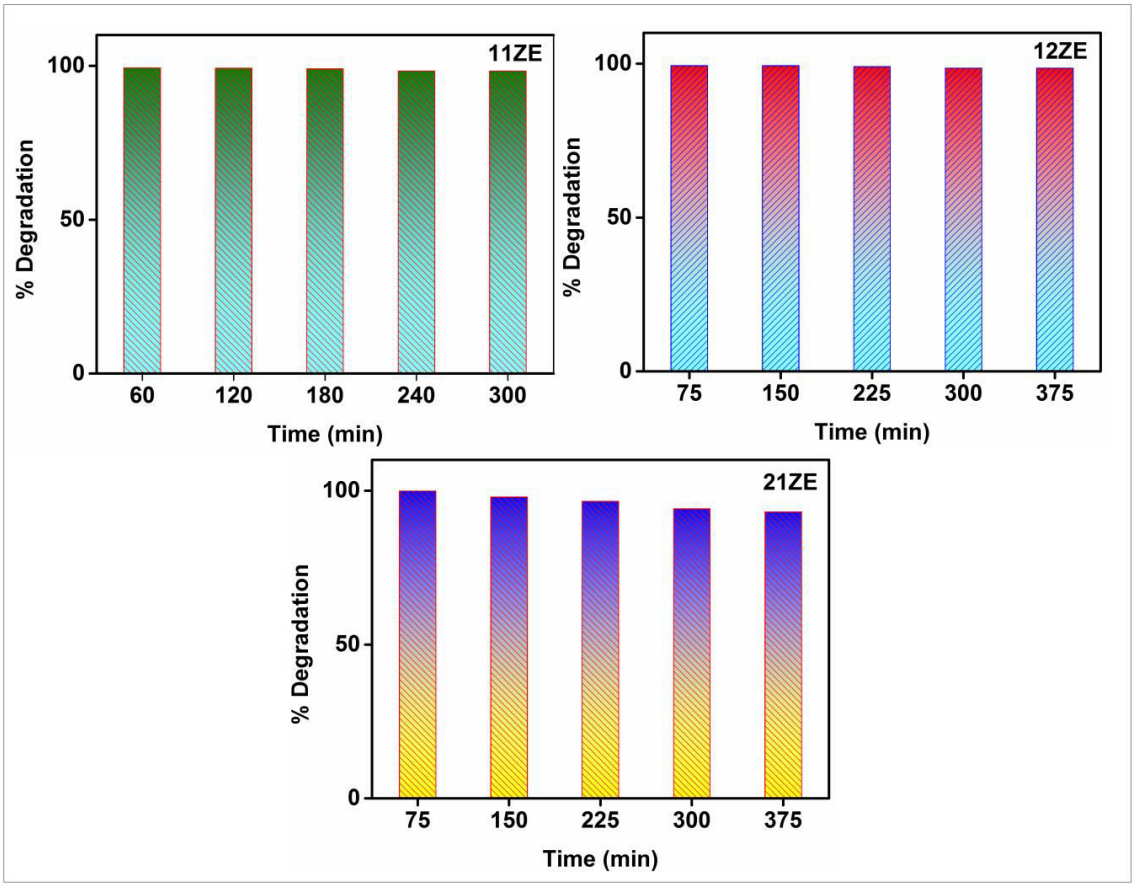

Figure 3.15 Cyclic stability of 11ZE, 12ZE and 21ZE

11ZE and 12ZE exhibit good stability and recyclability as well for five consecutive cycles whereas 21ZE exhibit a gradual decrease of stability. Out of these three samples 11ZE shows excellent overall activity compared to 12ZE and 21ZE.

3.4.2 Estimation of reactive oxygen species

The photocatalytic activity of the nanomaterials is generally attributed with the generation of reactive oxygen species as shown in equation (6) (in page 71). The hydroxyl free radicals released is quantified using terephthalic acid (TTA) probe molecule[56]. The hydroxyl radicals released by the semiconductor photocatalyst, on illumination, convert terephthalic acid in to a fluorescent 2-hydroxylterephthalic acid (HTTA) as shown in Figure 3.16. The intensity of nonflourescent TTA and fluorescent HTTA is compared in Figure 3.17.

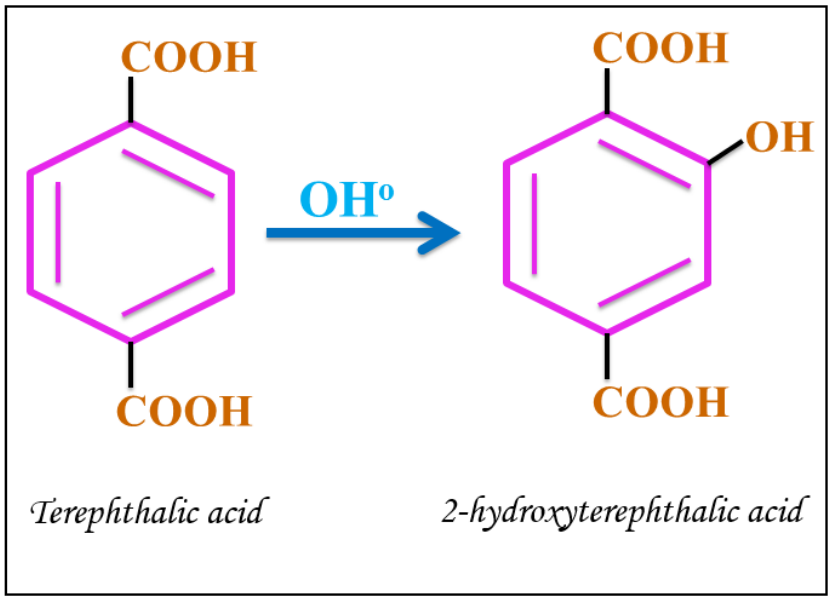

Figure 3.16 Chemical structures of terephthalic acid and 2-hydroxyterephthalic acid

Terephthalic acid solution ($5x10^{-4}$ M) is prepared in water and its pH is adjusted with NaOH[57]. Then, 0.005 g of the photocatalyst was dispersed in 50 ml of the prepared terephthalic acid solution and placed under light irradiation with continuous stirring for 10 minutes. After light exposure, the solution was centrifuged and recorded the photoluminescence spectra of the solution to measure the intensity of the fluorescence.

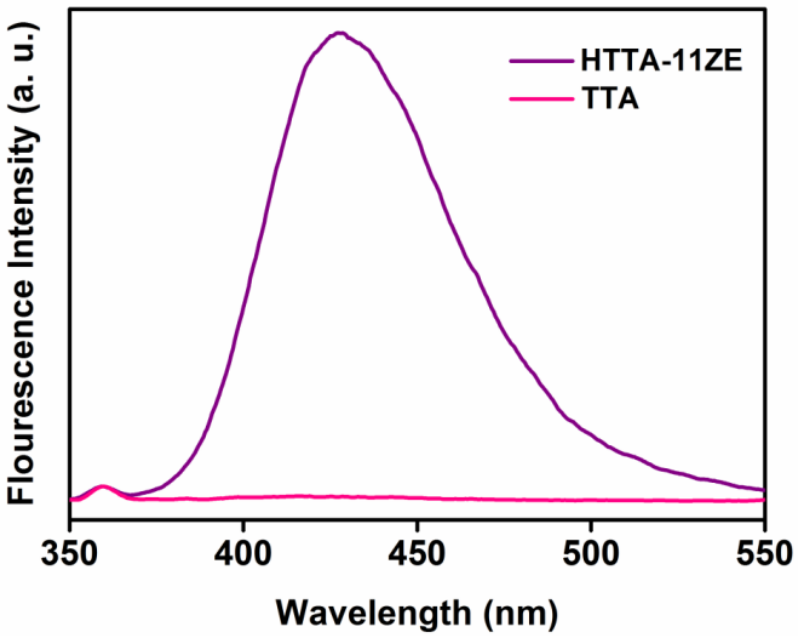

Figure 3.17 Flourescence spectra of TTA and HTTA

3.4.3 Surface treatment – Contact angle measurements

The self-cleaning performance and surface wettability of 11ZE photocatalyst was analyzed from contact angle measurements. A paste of 11ZE was made in methanol and doctor bladed on a thin glass substrate. Each coated glass plate was dried at room temperature and subjected to measure contact angle with water. Water contact angle photographs of ZnO film on glass substrate are shown in Figure 3.18.

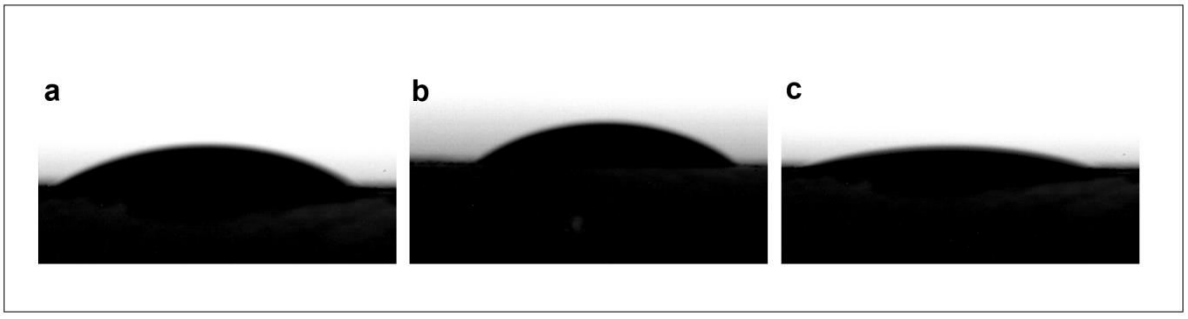

Figure 3.18 Photographs of water contact angle measurements on ZnO surface (a) initial angle (b) After 100 seconds (c) After 120 seconds

The contact angle was found to be 36.1^{o} initially and within hundred seconds the

angle reaches to 31.2°. After 2 min the angle was 29.9° indicating the hydrophilic nature of the film. The synergetic action of polar hydroxyl groups at the surface of ZnO nanotubes along with the wettability induced by the capillary forces helps for achieving this hydrophilicity[58]. According to Kenanakis *et al,* surface roughness and crystallinity promotes water absorption of a material considerably[59]. The hydrophilic nature of 11ZE helps in absorbing water and subsequently its photocatalytic property comes handy in cleaning the surface by degrading the surface adsorbed dust.

3.5 CONCLUSIONS

Oxygen deficient morphologically tuned ZnO nanostructures with varying photocatalytic activities were obtained by changing the concentration of polymeric precursor in the reaction medium. One dimensional ZnO with three different samples were obtained by changing the zinc to beta-Aminoethylamine ratio 2:1, 1:2 and 1:1 (21ZE, 12ZE and 11ZE). A detailed study on the photocatalytic activity of these ZnO nanostructures shows that 11ZE gives stable photocurrent behaviour with better photocatalytic performance by showing hundred percentage degradation of methylene blue. Performances of these three ZnO nanostructures on methylene blue degradation were correlated with the surface chemisorbed oxygen, oxygen related defect density and excitonic recombinations. Compared to 11ZE, 21ZE shows smooth surfaced nanotubes whereas; 12ZE shows completely distorted nanotube structure because of high etching rate. Among the three samples, 11ZE surface accommodates more chemisorbed oxygen and the photoluminescence studies indicate that the excitons life time is high in 11ZE. All these factors indirectly affect the photocatalytic degradation of methylene blue by producing more superoxides and enhancing the carrier lifetime in the oxide structure under illumination. The hydrophilic nature of 11ZE also put promising material for antifogging applications.

3.6 REFERENCES

[1] R. Cai, J.-g. Wu, L. Sun, Y.-j. Liu, T. Fang, S. Zhu, S.-y. Li, Y. Wang, L.-f. Guo, C.-e Zhao, A. Wei, *Mater. Des.* **2016**, 90, 839-844.

[2] Z. Zang, A. Nakamura, J. Temmyo, *Opt. Express,* **2013***,* 21(9), 11448-11456.

[3] Z. Zang, X. Tang, *J. Alloys Compd.* **2014**, 619, 98-101.

[4] Z. Zang, X. Zeng, J. Du, M. Wang, X. Tang, *Opt. Lett.* **2016**, 41, 3463-3466.

[5] M. S. Samuel, J. Koshy, A. Chandran, K. C. George, *Curr. Appl. Phys.* **2011**, 11, 1094-1099.

[6] A. Phuruangrat, S. Thongtem, T. Thongtem, *Mater. Des.* **2016***,* 107, 250-256.

[7] H. Abdullah, D-H. Kuo, Y-R. Kuo, F-A. Yu, K-B. Cheng, *J. Phys. Chem. C,* **2016***,* 120 (13), 7144-7154.

[8] S-L. Zhou, S. Zhang, F. Liu, J-J. Liu, J-J. Xue, D-J. Yang, C-T. Chang, *J. Photoch. Photobiol., A: Chemistry,* **2016**, 328, 97–104.

[9] F. Peng, Q. Zhou, C. Lu, Y. Ni, J. Kou, Z. Xu, *Appl. Surf. Sci.* **2017**, 394, 115–124.

[10] M. Yu, Y. Ma, J. Liu, X. Li, S. Li, S. Liu, *Appl. Surf. Sci.* **2016**, 390, 266–272.

[11] H. Shima, M. M. Hossain, I. Lee, S. Son, J. R. Hahn, *Mater. Chem. Phys.* **2017**, 185, 73-82.

[12] N. Güy, S. Çakar, M. Özacar, *J. Colloid Interface Sci.* **2016**, 466, 128–137.

[13] J. D. Major, R. Tena-Zaera, E. Azaceta, L. Bowen, K. Durose, *Sol. Energy Mater. Sol. Cells,* **2017,** 160, 107–115.

[14] S-C. Huang, K. M. Hsieh, T. W. Chang, Y. C. Chen, C-T. R. Yu, T-C. Lu, C. F. Lin, T-Y. Yu, T-T. Wang, H. Chen, *Ceram. Int.* **2016**, 42, 7848–7851.

[15] F. Xu, J. Chen, L. Guo, S. Lei, Y. Ni, *Appl. Surf. Sci.* **2012**, 258, 8160– 8165.

[16] D. Acharyya, P. Bhattacharrya, *Sens. Actuators B,* **2016**, 228, 373–386.

[17] T. Kong, Y. Chen, Y. Ye, K. Zhang, Z. Wang, X. Wang, *Sens. Actuators B*, **2009**, 138, 344–350.

[18] X. Li, J. Wang, J. Yang, J. Lang, M. Wei, X. Meng, S. Lü, Y. Sui, *J. Mol. Catal. A: Chem.* **2013**, 378, 1– 6.

[19] A.K. Yetisen, H. Qu, A. Manbachi, H. Butt, M.R. Dokmeci, J.P. Hinestroza, M. Skorobogatiy, A. Khademhosseini, S.H. Yun, *ACS Nano,* **2016***,* 10, 3042−3068.

[20] J. Wang, Y. Xia, Y. Dong, R. Chen, L. Xiang, S. Komarneni, *Appl. Catal., B: Environ.* **2016**, 192, 8–16.

[21] Y-C. Chang, *J. Alloys Compd.* **2016**, 664, 538-546.

[22] X. Chang, Z. Li, X. Zhai, S. Sun, D. Gu, L. Dong, Y. Yin, Y. Zhu, *Mater. Des.* **2016**, 98, 324–332.

[23] A. Londono-Calderon, F. F. Jurado-Lasso, J. D. Romero-Salazar, N. Jurado-Lasso, J. F. Jurado, *J. Nanomater.* **2014**, 2014, 1- 6.

[24] Y. Zhang, M. K. Ram, E. K. Stefanakos, D. Y. Goswami, *J Nanomater.* **2012**, 2012, 1-22.

[25] X. Y. Liu, *J. Chem. Phys.* **2000**, 112, 9949-9955.

[26] L. Znaidi, Mater. *Sci. Eng., B* **2010**, 174, 18–30.

[27] Y. Sun, D. J. Riley, M. N. R. Ashfold, *J. Phys. Chem. B.* **2006**, 110, 15186-15192.

[28] K-W. Chae, Q. Zhang, J. S. Kim, Y-Ha. Jeong, G. Cao, Beilstein *J. Nanotechnol.* **2010**, 1, 128–134.

[29] F. Tsin, A. Venerosy, J. Vidal, S. Collin, J. Clatot, L. Lombez, M. Paire, S. Borensztajn, C. Broussillou, P. P. Grand, S. Jaime, D. Lincot, J. Rousset, *Sci. Rep.* **2015**, 5 : 8961, 1-8.

[30] D. Chen, Z. Wang, T. Ren, H. Ding, W. Yao, R. Zong, Y. Zhu, *J. Phys. Chem. C*

2014, 118, 15300−15307.

[31] R. Djemour, A. Redinger, M. Mousel, L. Gütay, X. Fontané, V. Izquierdo-Roca, A. Pérez-Rodríguez, S. Siebentritt, *Opt. Express* **2013**, 21(S4), A695-A703.

[32] M. S. Samuel , J. Koshy, A. Chandran, K. C. George, *Indian J. Pure Appl. Phys.* **2010**, 48, 703-708.

[33] T. Ngo-Duc, K. Singh, M. Meyyappan, M. M Oye, *Nanotechnology* **2012**, 23,194015.

[34] J. Singh, P. Kumar, K. S. Hui, K. N. Hui, K. Ramam, R. S. Tiwari, O. N. Srivastava, *CrystEngComm* **2012**, 14, 5898–5904.

[35] M. H. Habibi, B. Karimi, *J. Ind. Eng. Chem* **2014**, 20, 1566–1570.

[36] C. Xu, Z. Bacsik, N. Hedin, *J. Mater. Chem A* **2015**, 3, 16229–16234.

[37] Y. Wang, Y. Li, Z. Zhou, X. Zu, Y. Deng, *J Nano part Res* **2011**, 13, 5193–5202.

[38] S. G. Ullatil, P. Periyat, *J. Mater. Chem. A* **2016**, 4, 5854.

[39] P. Zhan, Z. Xie, Z. Li, W. Wang, Z. Zhang, Z. Li, G. Cheng, P. Zhang, B. Wang, X. Cao, *Appl. Phys. Lett.* **2013**, 102, 071914 (1-5).

[40] X. Li, J. Song, Y. Liu, H. Zeng, *Curr. Appl. Phys* **2014**, 14, 521-527.

[41] M. Willander, O. Nur, J. R. Sadaf, M. I. Qadir, S. Zaman, A. Zainelabdin, NargisBano, I. Hussain, *Materials* **2010**, 3, 2643-2667.

[42] E. J. Guidelli, O. Baffa, D. R. Clarke, *Sci. Rep.* **2015**, 5:14004, 1-11.

[43] C. H. Ahn, Y. Y. Kim, D. C. Kim, S. K. Mohanta, H. K. Cho, *J. Appl. Phys.* **2009**, 105, 013502 (1-5).

[44] K. Bandopadhyay, J. Mitra, *RSC Adv.* **2015**, 5, 23540–23547.

[45] C. Liu, Z. Qiu, W. Yue, X. Zhou, M. Wang, *J. Phys. Chem. C,* **2014**, 118, 28462−28473.

[46] Y-P. Zhu, M. Li, Y-L. Liu, T-Z. Ren, Z-Y. Yuan, *J. Phys. Chem. C.* **2014**, 118, 10963−10971.

[47] V. K. Dwivedi, P. Srivastava, G. V. Prakash, *J. Semicond.* **2013**, 34(3), 033001 (1-5).

[48] F. Spadavecchia, S. Ardizzone, G. Cappelletti, L. Falciola, M. Ceotto, D. Lotti, *J Appl. Electrochem.* **2013**, 43, 217–225.

[49] A. Irshad, N. Munichandraiah, *J. Electrochem. Soc.* **2015**, 162 (4), H235-H243.

[50] X. Xin, T. Xu, J. Yin, L. Wang, C. Wang, *Appl. Catal., B.* **2015**, 176-177, 354-362.

[51] W. Shocklev, W.T. Read, *Phys. Rev.* **1952**, 87 (5), 835-842.

[52] B. Liu, X. Zhao, C. Terashima, A. Fujishima, K. Nakata, *Phys. Chem. Chem. Phys.* **2014**, 16, 8751-8760.

[53] S. G. Ullattil, P. Periyat, *Nanoscale* **2015**, 7, 19184-19192.

[54] S. Zhuang, X. Xu, B. Feng, J. Hu, Y. Pang, G. Zhou, L. Tong, Y. Zhou, *ACS Appl. Mater. Interfaces* **2014**, 6, 613−621.

[55] S. Y. Sawant, M. H. Cho, *Rsc Adv.* **2016**, 6, 70644-70652.

[56] Y. Nosaka, A. Y. Nosaka, *Chem. Rev.* **2017**, 117, 11302−11336.

[57] M. Sahni, B. R. Locke, *Ind. Eng. Chem. Res.* **2006**, 45, 5819-5825.

[58] Y. Gao, I. Gereige, A. E. Labban, D. Cha, T. T. Isimjan, P. M. Beaujuge, *ACS Appl. Mater. Interfaces* **2014**, 6, 2219−2223.

[59] G. Kenanakis, E. Stratakis, K. Vlachou, D. Vernardou, E. Koudoumas, N. Katsarakis, *Appl. Surf. Sci* **2008**, 254, 5695–5699.

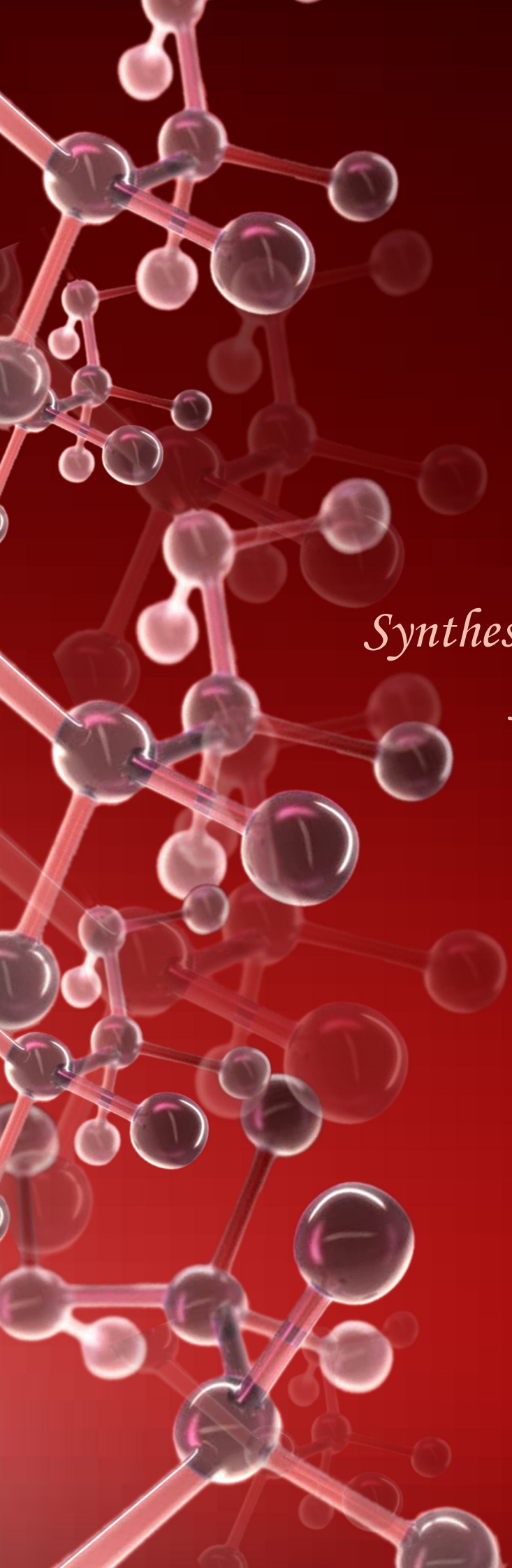

Chapter 4

Synthesis, Characterizations & Applications of Hybrid Nanocomposites

4 Synthesis, Characterizations and Applications of Hybrid Nanocomposites

The efforts of scientific community in developing hybrid nanocomposites augur well for implementing nanotechnology in innovative applications[1]. The many parameters that can be varied and different material components which can be chosen play a pivotal role in developing these composite materials. Hybrid nanocomposites either exhibit new properties or a mixup of individual component characteristics. Wide band gap metal oxides, like zinc oxide and their hybrid nanocomposites with polymers have extensively improved in their applications in sensor[2], batteries[3], photovoltaics[4], supercapacitor[5] and photocatalysis[6] with effect of their surface properties[7], bandgaps[8], interface[9] and shapes[10]. One of the most effective surface treatments of ZnO can be achieved through the incorporation of a polymer shell[11]. The synergetic and complimentary performance between conducting /non conducting polymers and inorganic metal oxides makes a significant improvement in properties of these hybrids. When these nanocomposites supported by polymers, the agglomeration of nanoparticles can be prevented to a certain extent. In addition, the synthesis protocol of polymer based semiconductor nanocomposites is simple due to the ease in bonding between them[12] and the use of a less expensive aqueous medium for the synthesis.

Over the past few decades polyaniline is very much attractive with its intrinsic conduction for various catalytic and photocatalytic processes[13]. According to Zhang *et al*, the photocorrosion of ZnO can be inhibited through polyaniline coating[14]. Conductivity of polyaniline (PANI) and biocompatibility of polyvinylpyrrolidone (PVP) make the polymer zinc oxide nanocomposite an economically viable efficient system for photocatalytic and photovoltaic applications by the potential utilization of solar energy. Reports on PANI-ZnO

and PVP-ZnO composites are available with highlights on their properties and photoactive applications. However, bi-functional nanocomposites with PANI-PVP-ZnO combination are hardly seen in literature. Ming yang *et al* reported bifunctional PANI/Fe_3O_4/PVP composite nanofiber from electrospinning synthesis[15]. Recently Jihai Tang *et al* studied the electromagnetic properties of PANI/PVP /carbonyl iron powder[16]. But to the best of our knowledge this could be the first sol-gel synthesis of hybrid nanocomposite of zinc oxide with both the polymers PANI and PVP (the composite is coded as PPZ). In addition to this, the incorporation of carbon in to the ZnO lattice through polymer assisted approach is not so common in the literature.

The present work reports a facile and effective protocol for the synthesis of polymer wrapped zinc oxide nanotubes in aqueous medium. Nanocomposite combinations of PANI/ZnO (PNZ), PVP/ZnO (PVZ), PANI/PVP/ZnO (PPZ) and PANI/PVP blend (PP) are successfully fabricated with a well-controlled and cost effective procedure. The synthesized composite samples (PNZ, PVZ and PPZ) were subjected to post thermal treatment and formed carbon incorporated ZnO. According to Tseng *et al*, carbon atoms can replace both zinc and oxygen atoms[17] in ZnO lattice. The above mentioned composites are systematically characterized structurally, optically and morphologically. The photocatalytic stability of the synthesized hybrids analyzed in detail and the sample shows good photocatalytic stability and recyclability, even after using for five cycles.

4.1 Carbon incorporated ZnO derived from Polyvinylpyrrolidone assistance

Polyvinylpyrrolidone-zinc oxide hybrid nanocomposite (PVZ) was prepared by one – pot sol precipitation method with water as the medium. The polymer, polyvinylpyrrolidone (PVP), used for the incorporation of carbon into ZnO lattice is highly biocompatible and environment friendly[18]. The obtained PVZ was calcined at 400 ^{o}C for one hour in muffle

furnace to obtain carbon incorporated ZnO and the sample is coded as CPVZ.

4.1.1 SYNTHESIS

4.1.1.1 Synthesis of PVZ and CPVZ

Zinc acetate dihydrate $(CH_3COO)_2$ Zn. $2H_2O$, Ethane-1, 2-diamine $(C_2H_4(NH_2))$ and methanol (CH_3OH) were purchased from Merck. Double distilled water filtered from Heal force super easy series purification system was used throughout for synthesis and washing process. Polyvinylpyrrolidone (PVP with average Mol. wt > 40,000 g/mol) was purchased from SRL.

ZnO - PVP polymer nanocomposite was prepared by one – pot sol precipitation method with water as the medium. A homogeneous precursor solution of zinc acetate (0.015 M) was heated to 60^{o}C followed by the injection of 0.015 M ethane-1, 2-diamine under continuous heating and stirring at 900 rpm. Aqueous solution of PVP (0.1 g in 50 mL water) was added to the reaction medium after 75 minutes and the whole reaction was continued up to six hours. The precipitate obtained after washing the reaction mixture with water using ultra centrifuge, air-dried and stored in vials for further characterizations and is coded as PVZ. Pristine zinc oxide nanotubes were also synthesized with same procedure without addition of polymer solution[19]. The obtained PVZ was calcined at 400 ^{o}C for one hour in muffle furnace to obtain carbon incorporated ZnO named as CPVZ. Addition of PVP during the formation of white cloudy precipitate of zinc oxide results in the hydrolyzation of PVP followed by the wrapping on ZnO surface[20]. The COO^- groups in the polymer are attached to the Zinc atom of Zn-O through electrostatic interactions. After calcination of these polymer wrapped ZnO, carbon is entering in to ZnO lattice. The schematic of the synthesis is shown in Figure 4.1.

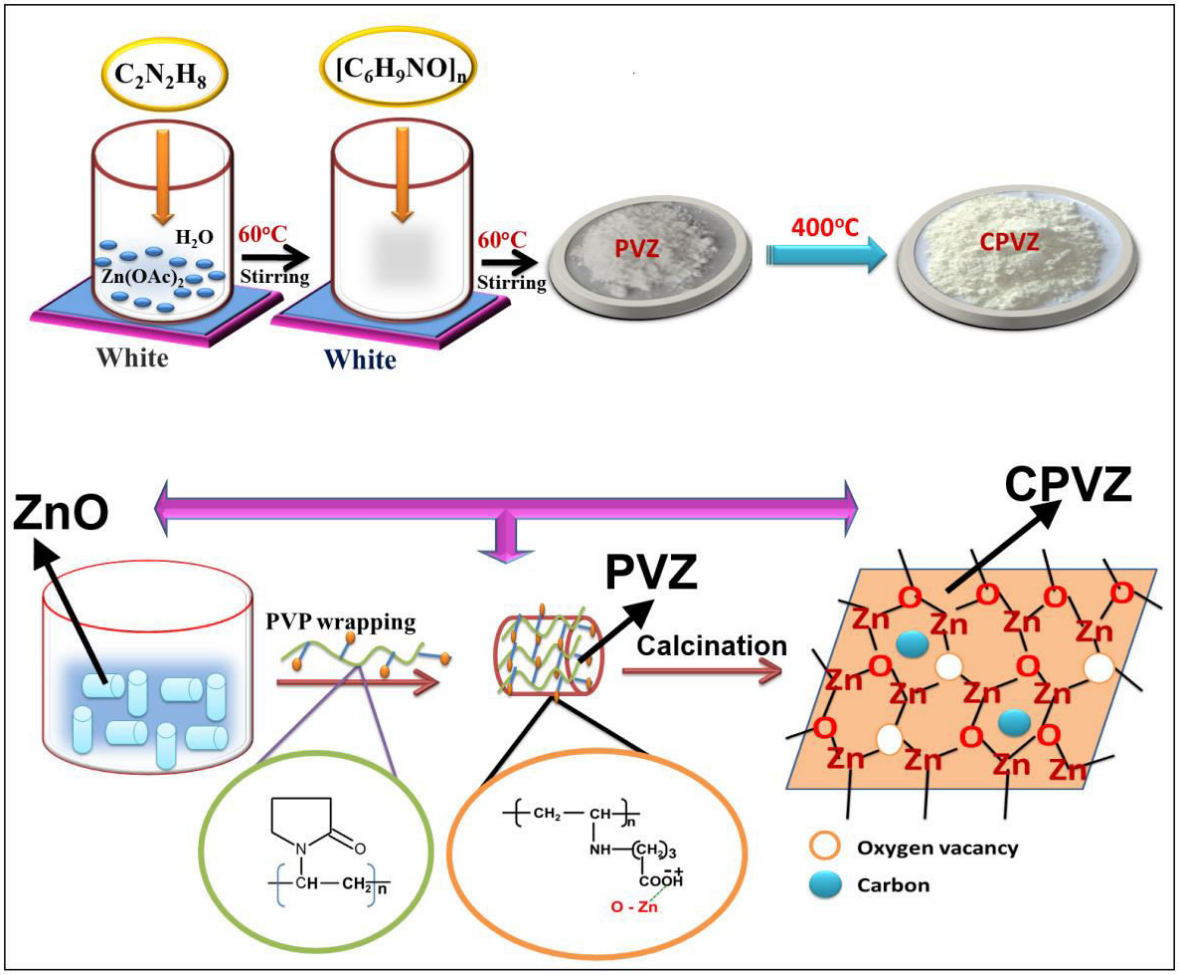

Figure 4.1 Schematic of the synthesis procedure of CPVZ

4.1.2 CHARACTERIZATIONS

4.1.2.1 Morphology and structural analysis

4.1.2.1.1 Scanning Electron Microscopy (SEM)

Morphology obtained from FESEM (Zeiss Gemini SEM 300) reveals short nanotube structure for both PVZ and CPVZ as shown in Figure 4.2.b and c.

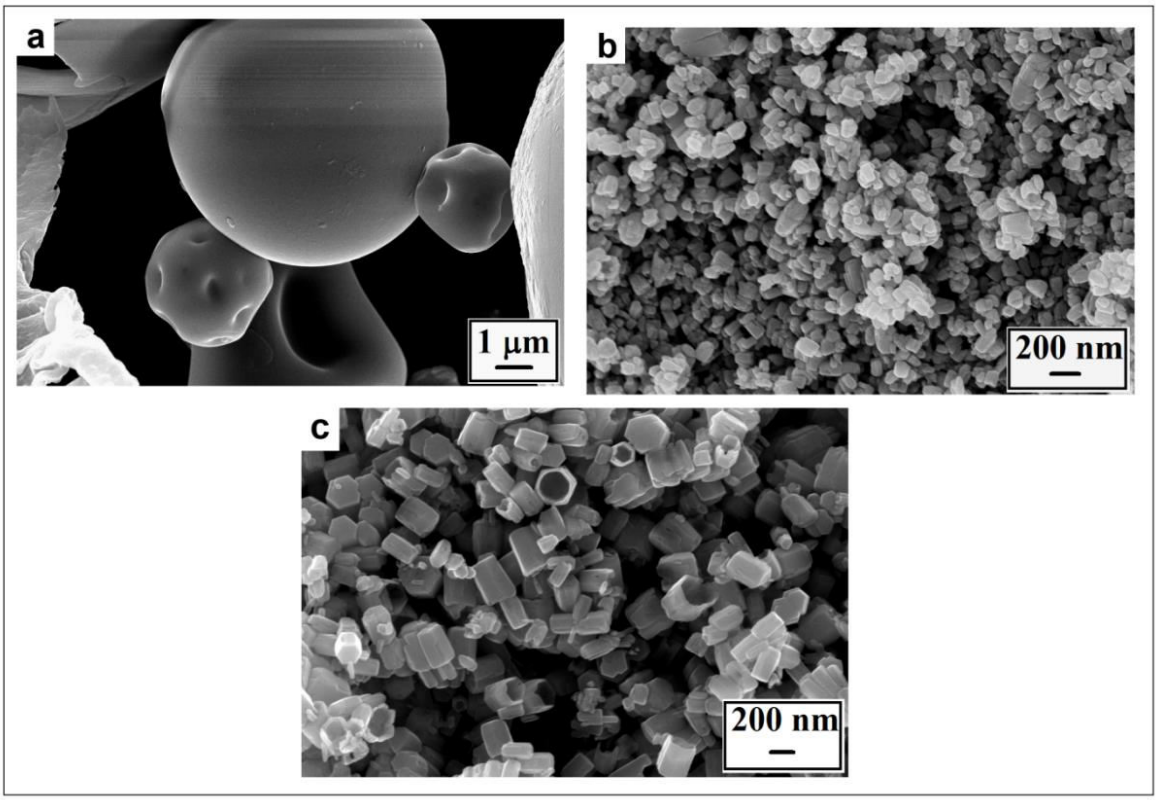

Figure 4.2 FESEM images of (a) PVP, (b) PVZ and (c) CPVZ

4.1.2.1.2 Energy Dispersive Spectrum (EDS)

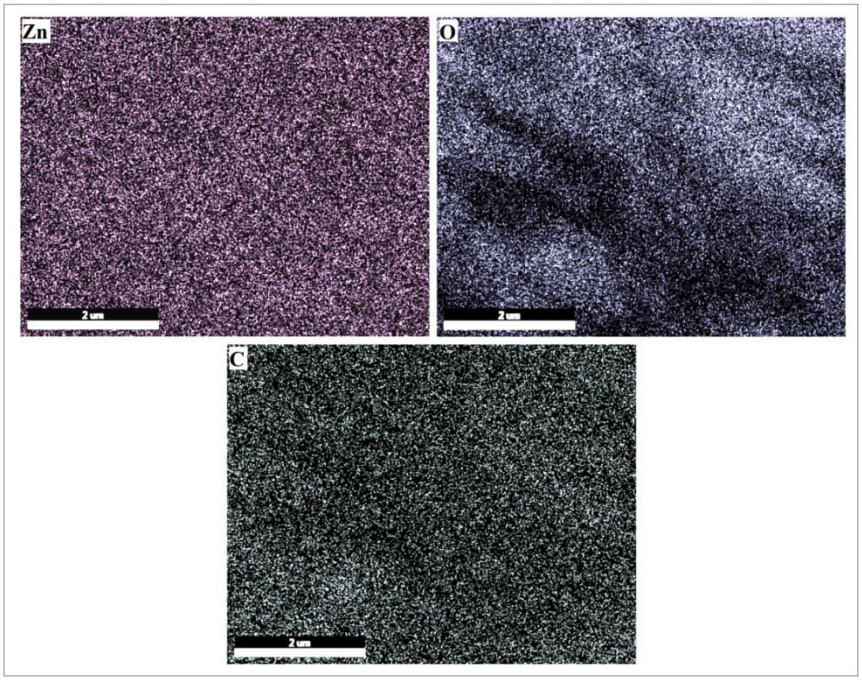

Figure 4.3 EDAX mapping of elements Zn, O and C in CPVZ

EDAX mapping shows non-uniformity of the elements in the prepared samples. The slight darkness (absence of blue colour) observed at the left side of oxygen mapping can be attributed to the randomly located oxygen vacancies present in the CPVZ crystals. The atomic percentage of elements obtained from the EDAX spectrum of CPVZ is 40.58, 34.54 and 24.87 for zinc, oxygen and carbon respectively (Figure 4.3).

4.1.2.1.3 X-ray Diffraction Analysis

Crystallinity and phase purity of the synthesized samples were ensured from X-ray diffraction pattern. The XRD pattern of PVZ, CPVZ, commercially available PVP and pure ZnO are shown in Figure 4.4(a). PVZ and CPVZ are in good agreement with the wurtzite zinc oxide structure (JCPDS-89-0510) and the absence of impurity peaks approves the purity of the samples. Crystallinity shown by PVZ resembles that of ZnO and it indicates nanotube-polymer fusion[21]. In CPVZ, the presence of carbon does not produce a new phase or impurity peaks. However the presence of carbon makes an increase in the intensity of the CPVZ along with a shift towards lower 2 theta values compared to PVZ and ZnO as illustrated in Figure 4.4(b). This shift observed in CPVZ compared to PVZ and ZnO indicates the expansion of crystal lattice of ZnO by carbon incorporation[22].

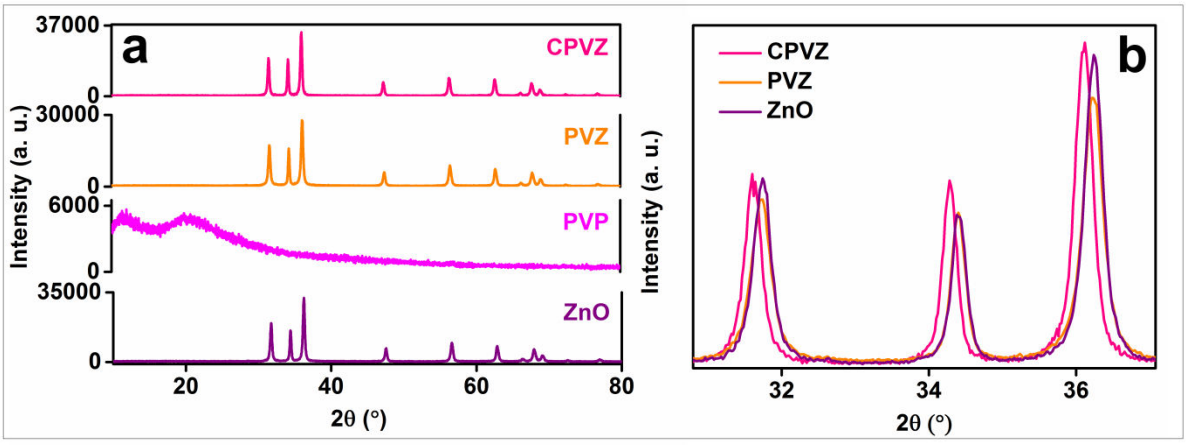

Figure 4.4 XRD patterns of (a) CPVZ, PVZ, PVP and ZnO (b) Enlarged XRD image

4.1.2.1.4 Fourier Transform Infrared Spectroscopy (FTIR)

FTIR analysis gives information on the structural features of PVP, PVZ and CPVZ as illustrated in Figure 4.5. Both PVP and PVZ show broad peak at ~3300-3500 cm^{-1} arise from O-H stretching vibrations of inter-molecular hydrogen bonding[23]. In PVZ this broad peak is more intense as N-H stretching in 2° amine shows peak at the same area. CPVZ also shows association of the adventitious intermolecular bonded O-H groups. PVP shows characteristic peaks at 2933 cm^{-1} due to the presence of intra-molecular O-H stretching from the resonance structure[24]. This peak is absent in PVZ because of the hydrolysis of the amide group in presence of edamine that destroys the cyclic nature. A broad peak at 2170 cm^{-1} in PVP may be attributed the presence of N=C=O bond in the ring which is absent in PVZ. Two sharp peaks present in PVP at 1724 cm^{-1}, 1680 cm^{-1} represent C=O stretching in 3° amide group which is found to be absent in PVZ confirms the destruction of cyclic structure. Presence of 1400 cm^{-1} peak in PVZ attributes the carboxylate anion stretching[25]. 1280 cm^{-1} peak in PVP implies C-N stretching in aromatic amine[26]. In the resonance structure of PVP carbon-nitrogen bond is similar to aromatic amine. C-H bending in tri-substituted alkene at 835 cm^{-1} is shifted to 895 cm^{-1} because of the conversion of aliphatic to linear chain form of the polymer. Strong peak at 690 cm^{-1} represent C=C di-substituted alkene out of plane bending in PVP ring. This is absent in PVZ due to the change in chemical environment. The incorporation of ZnO in PVZ and CPVZ is clear by the presence of peak at 500 cm^{-1}. Peak at 2348 cm^{-1} and 1639 cm^{-1} in CPVZ are the indication of C-O vibrations[27].

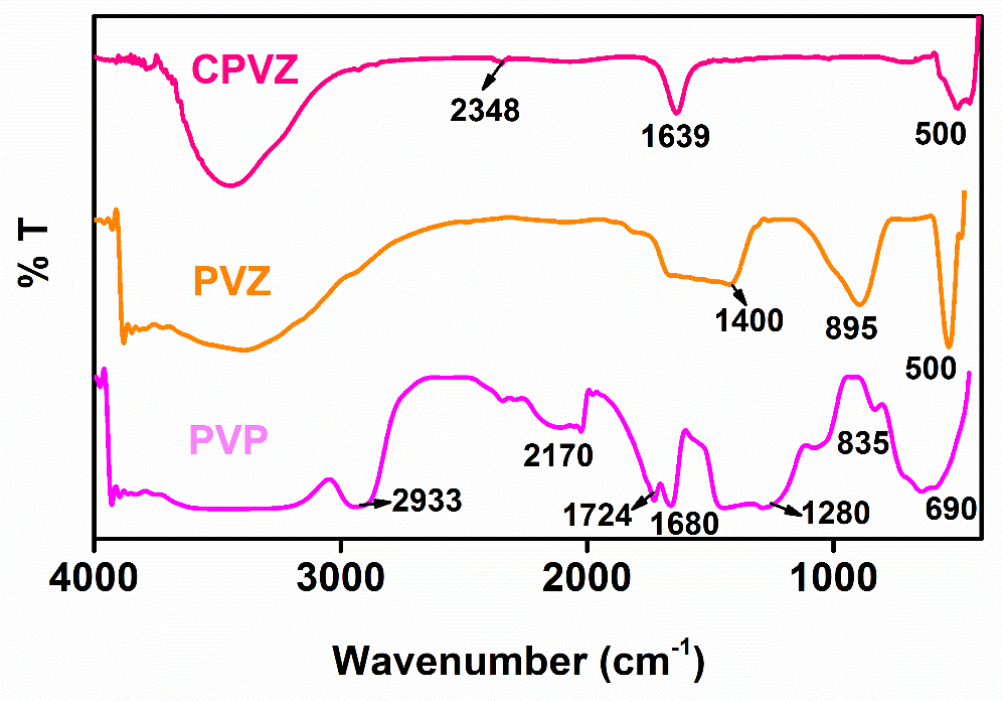

Figure 4.5 FTIR spectra of PVP, PVZ and CPVZ

4.1.2.1.5 X-ray Photoelectron Spectroscopy

The X-ray photoelectron spectroscopy (XPS) spectra of the samples were taken from Axis supra instrument with Monochromatic (AlKα) 600 W X-ray source. XPS data helps to interpret the electronic structure, chemical composition and defect chemistry of CPVZ. The absence of nitrogen in CPVZ is confirmed from XPS as seen in the N1s spectrum given in Figure 4.6. In order to investigate the carbon bonding, the Carbon 1s spectrum is deconvoluted in to three peaks by Gaussian peak fitting. Two major peaks observed at 285.8 eV and at 289.6 eV are arising due to Zn-O-C bonds and C-O bonds respectively[28, 29]. One satellite peak appears at 287.1 eV is assigned to C=O/O-C-O bonds respectively[30]. In the case of Zinc 2p spectrum two peaks are observed at 1022.2 eV for Zn $2p_{3/2}$ and at 1045.2 eV for Zn $2p_{1/2}$. The distance between these two peaks is 23 eV which is matching well with the standard reference value of ZnO[31, 32]. The oxygen 1s peak centered at 532.1 eV[33] is deconvoluted to three peaks at 530.6 eV, 531.5 eV and 532.6 eV. Peak at 530.6 eV indicate

O^{2-} ions on the wurtzite structure of ZnO[34]. Peaks at 531.5 eV and 532.6 eV represent oxygen defects and O-C bonds respectively[35, 36]. N 1s spectrum confirms the absence of nitrogen in the samples.

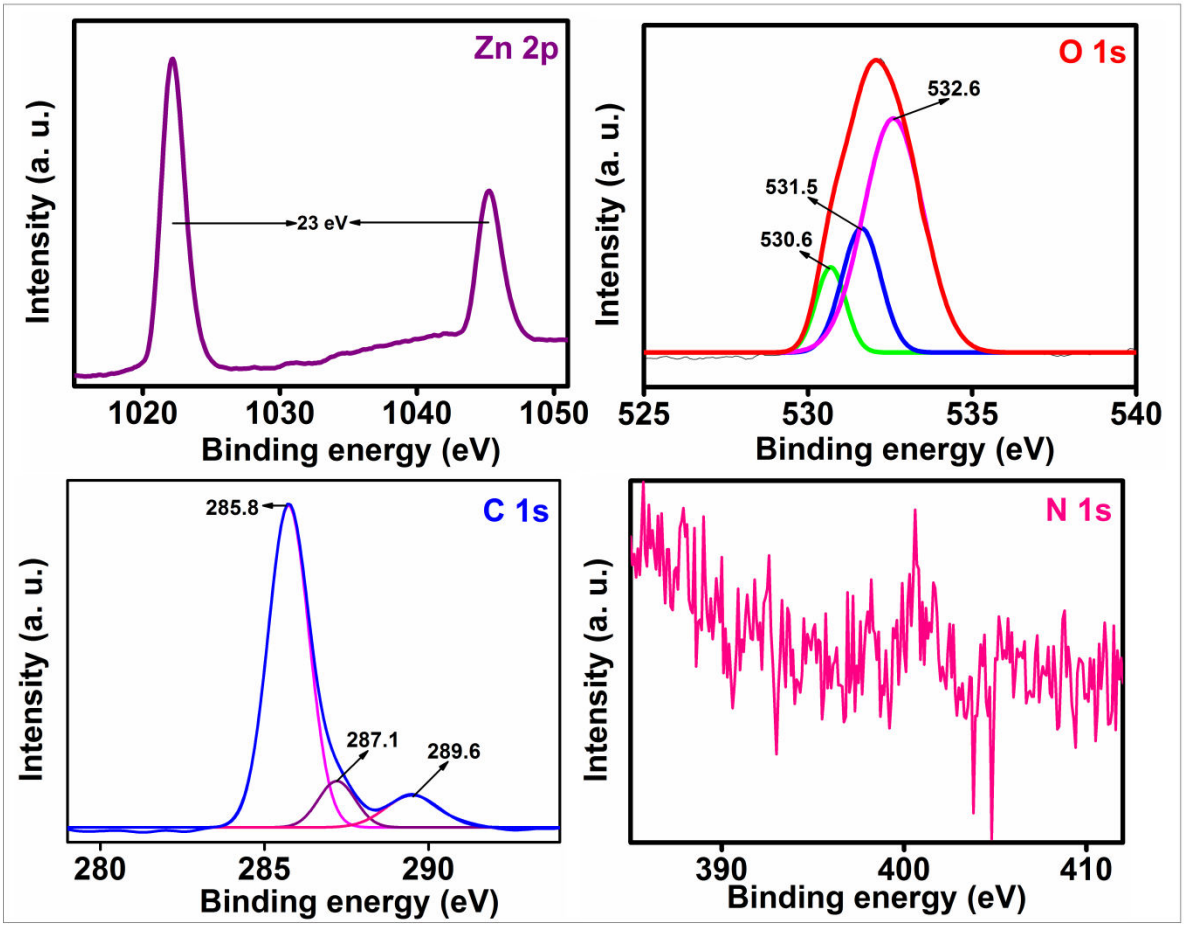

Figure 4.6 XPS elemental profiles of Zn 2p, O 1s, C 1s and N 1s of CPVZ

4.1.2.1.6 Raman spectroscopy

Raman spectra of PVZ and CPVZ were compared with that of ZnO as given in Figure 4.7. The characteristic peaks of wurtzite ZnO are observed in all three samples. The peak at 580 cm^{-1} is integrated to compare the oxygen deficiency in the samples [19]. Pure ZnO have sufficient oxygen vacancies which are suppressed by PVP adsorption in PVZ. However calcination further increases the surface oxygen vacancies in CPVZ.

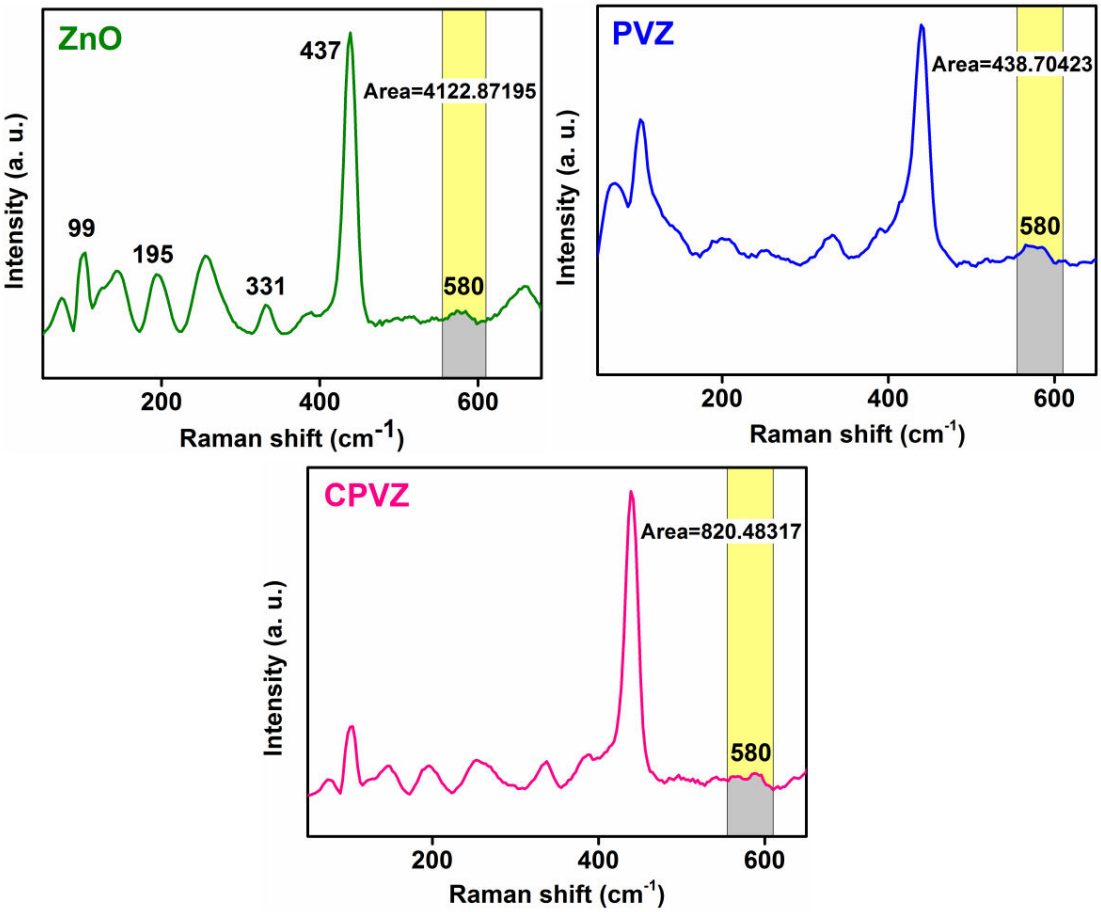

Figure 4.7 Raman spectra of pure ZnO, PVZ and CPVZ

4.1.2.2 Optical properties

4.1.2.2.1 Absorption Spectra (Uv-Vis-NIR)

The photophysical properties of PVP, PVZ and CPVZ are studied and presented in Figure 4.8. In PVP, the absorption at 200-320 nm attributed to pi-pi* and n-pi* transitions in C=O group whereas in PVZ the absorption at 200-400 nm is due to ZnO[37, 38]. Both PVZ and CPVZ show an increase in absorption intensity. It is anticipated here that the hydrolysis of polymer leads highly exposed chromophores and after thermal treatment these chromophores get decomposed and carbon enters the ZnO lattice.

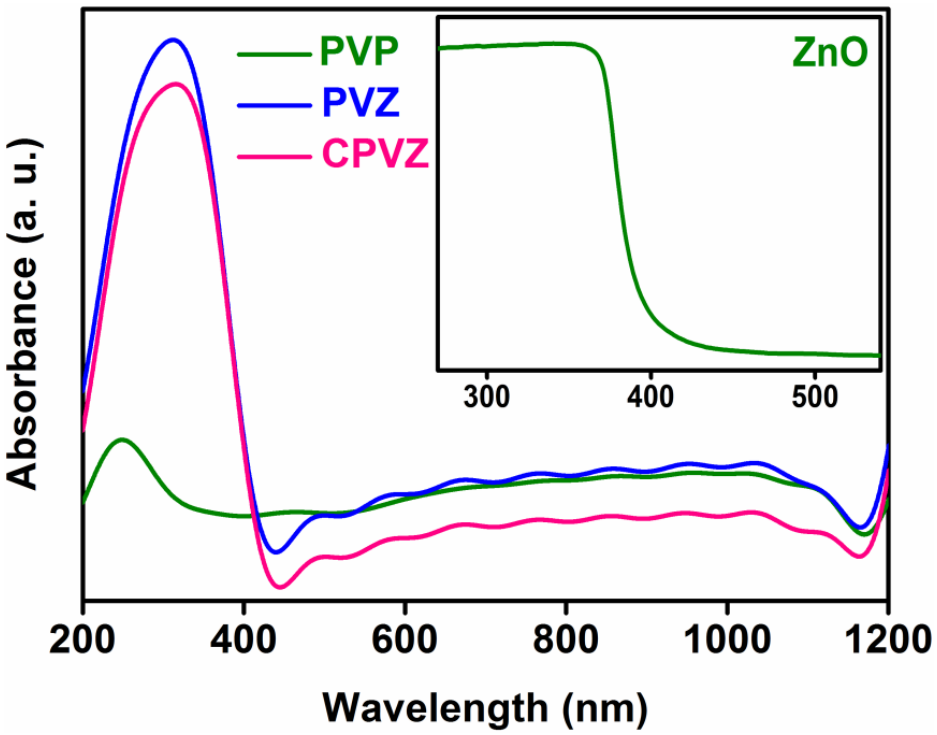

Figure 4.8 Absorbance spectra of PVP, PVZ, and CPVZ

4.1.2.2.2 Photoluminescence Spectroscopy (PL)

PL spectra were taken with equally weighed samples, by exciting at 340 nm to understand emission behavior of CPVZ. The emission spectra of PVZ, CPVZ and PVP are shown in Figure 4.9. The band edge emission was observed at 400 nm and other peaks present at 420 nm and 485 nm are related to defect emissions from the crystal[19, 39]. The green emission at 528 nm is associated with oxygen vacancies of the samples. The quenching of bandedge emission in ZnO and CPVZ could be due to decrease in excitonic recombination favourable for pholtocatalysis[40]. Oxygen vacancies and the presence of mid gap energy levels from carbon facilitate trapping of photoelectrons and holes and thereby decreasing the recombination of excitons. These trapped electrons and holes play a major role for enhanced photoactivity.

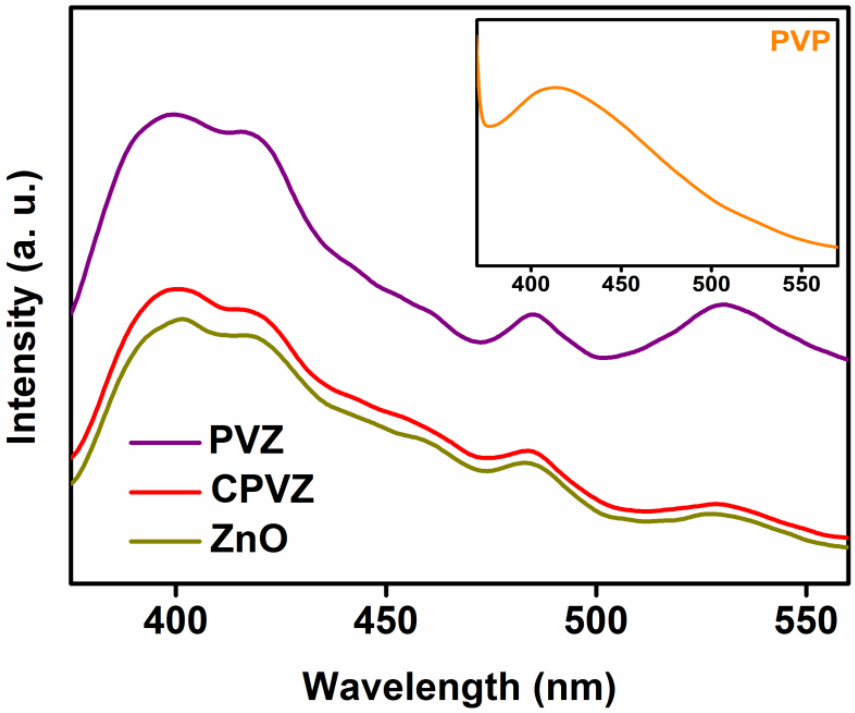

Figure 4.9 Photoluminescence emission of PVP, CPVZ, and PVP (inset)

4.1.2.3 Tauc plot, Valence band spectra and Density of states

Density of states of CPVZ is determined from optical bandgap and valence band XPS spectra as shown in Figure 4.9. The optical bandgap of CPVZ obtained from Tauc plot is 3.15 eV as depicted in Figure 4.10 (a). According to Lavand *et al*, the existence of midgap bands or trap states (arise due to C1s orbitals) in between the valence and conduction band in carbon doped ZnO channelize the photoexcited electrons and thereby reduce the recombination rate of photogenerated excitons[40]. The valence band spectrum obtained for CPVZ shows a band tail with a band edge maximum of 2.9 eV (Figure 4.10 (b)). The energy level shift due to band tail is estimated from the spectrum and is -0.71 eV. Considering the band tail, the conduction band minimum is calculated from the optical bandgap and is observed at -3.86 eV. Existence of conduction band tail, like valence band tail, due to crystal defects[41] is expected here. Schematic representation of the density of states of CPVZ is shown in Figure 4.10 (c).

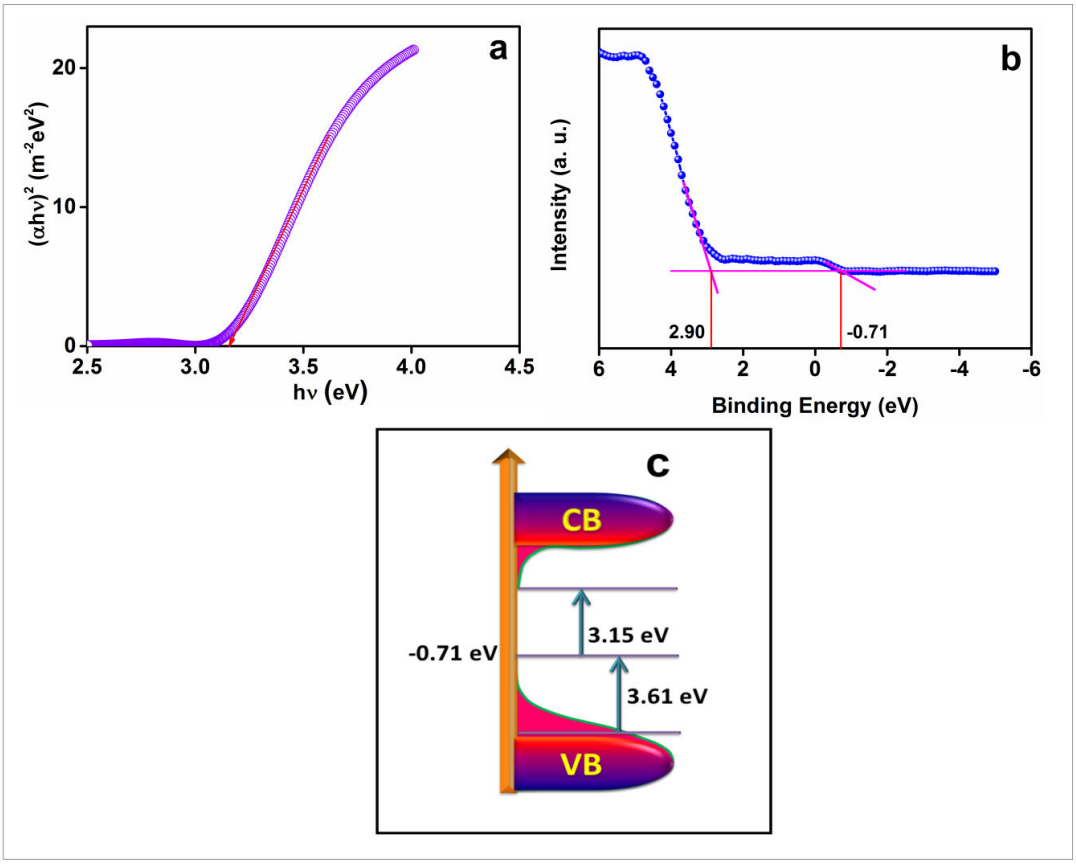

Figure 4.10 (a) Tauc plot of CPVZ, (b) Valence band XPS of CPVZ and (c) Schematic illustration of DOS of CPVZ

Generally amphoteric carbon can either substitute oxygen/ zinc or be present at interstitial sites of ZnO crystal lattice, as the carbon atom's size (0.070 nm) is smaller than that of oxygen (0.136 nm) and zinc (0.086 nm). Carbon-oxygen complex ($C_{Zn} + 2O_i$) defects and C_{zn} (zinc substituted by carbon) defects are energetically favorable but defects due to oxygen substituted by carbon (C_0) are not energetically viable[36]. From our investigation we propose predominantly two chances associated with the defect chemistry of CPVZ (i) carbon present interstitially (evident from lattice expansion and shifting of XRD peaks of CPVZ) forming midband gap energy levels and (ii) the presence of oxygen vacancies (evident from XPS and PL). These crystal defects of CPVZ boost its photocatalytic performance compared to pristine ZnO sample.

4.1.3 APPLICATIONS – PHOTOCATALYSIS

4.1.3.1 Water treatment – Dye degradation

The photocatalytic dye degradation of MB $2x10^{-3}$ wt% in presence of CPVZ is checked inside a photocatalytic reactor under 300 W Xe lamp (Figure 4.10(a)) and the results are compared with the degradation profile of pristine ZnO and pure MB (inset of Figure 4.11 (a). The self-degradation observed in pure MB under illumination (~30% within 60 minutes) can be attributed to the presence of dissolved oxygen in water[42]. CPVZ degraded MB completely within 34 minutes where as pure ZnO took 60 minutes for the same process.

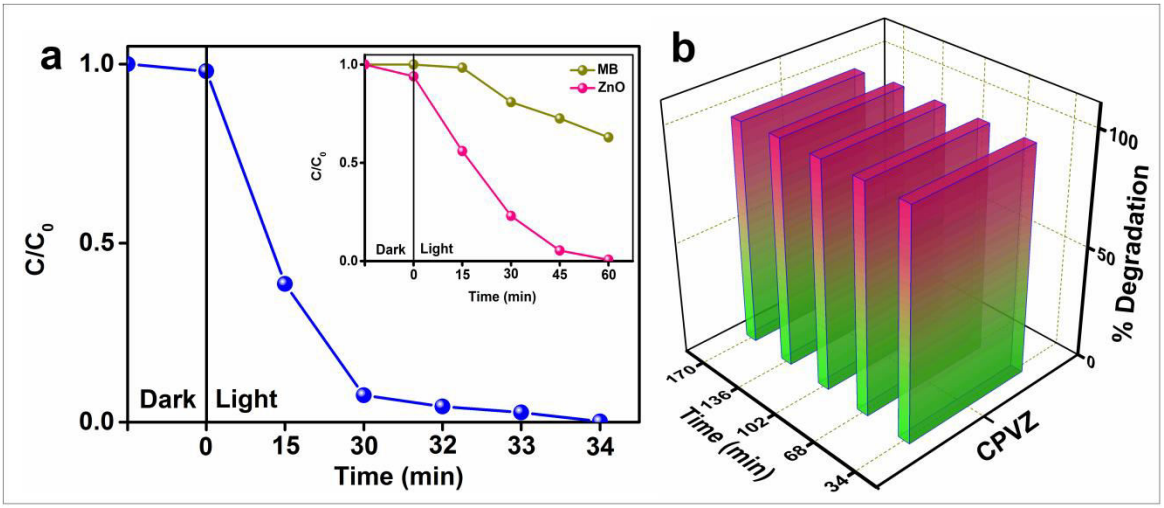

Figure 4.11 (a) Photodegradation of MB in presence of CPVZ, (inset) pure MB and ZnO and (b) photocatalytic stability of CPVZ

The carbon incorporation greatly enhances the photocatalytic activity of CPVZ. Shen *et al* reported that only 66% of $1x10^{-5}$ M methylene blue degraded within 60 minutes in the presence of carbon doped ZnO[43]. Similarly Zhang *et al* studied various percentage of carbon doped ZnO and the highest activity towards MB degradation observed was 90% after 2 hrs of exposure[21]. Whereas in our case within 34 minutes a complete degradation of MB ($2x10^{-3}$ wt%) is observed hinting the superior photoresponse of CPVZ.

The stability of the photocatalyst is a vital parameter in determining its utility in commercial applications[44]. The time dependent stability studies conducted on the samples show evidence of repeated photocatalytic behavior of CPVZ without remarkable variation in degradation efficiency in five consecutive runs indicating excellent stability of the photocatalyst (Figure 4.11 (b)).

4.1.3.2 Estimation of reactive oxygen species

The reactive oxygen species generated from the photocatalysts were experimentally confirmed and quantified with respect to its photocatalytic properties. Hydroxyl radicals generated from CPVZ is measured and compared with that of pure ZnO. Terephthalic acid (TTA) probe molecules were used to estimate the OH^{o} released by the photocatalysts experimentally. For the analysis, $5x10^{-4}$ M TTA solution was prepared in presence of NaOH for the complete dissolution of TTA. Then, 0.005 g of photocatalysts were dispersed in 50 ml of the prepared TTA solution and placed under light irradiation with continuous stirring for 10 minutes. After light exposure, the solution was centrifuged and the photoluminescence spectrum was taken to measure the intensity of the fluorescence.

Terephthalic acid (TTA) is a non-fluorescent probe molecule normally used to estimate the formation of hydroxyl radicals. In presence of hydroxyl radicals these TTA converted into 2-hydroxy terephthalate (HTTA) which exhibit fluorescence. The fluorescence intensity of the TTA solution in presence of CPVZ and ZnO under illumination is compared and found that the fluorescence intensity is higher in presence of CPVZ compared to pristine ZnO (Figure 4.12). The ratio of fluorescence intensity of pure ZnO to that of CPVZ is found to be 1:1.7. The carbon induced defects in CPVZ increases the ROS generation thereby improving photocatalytic activity.

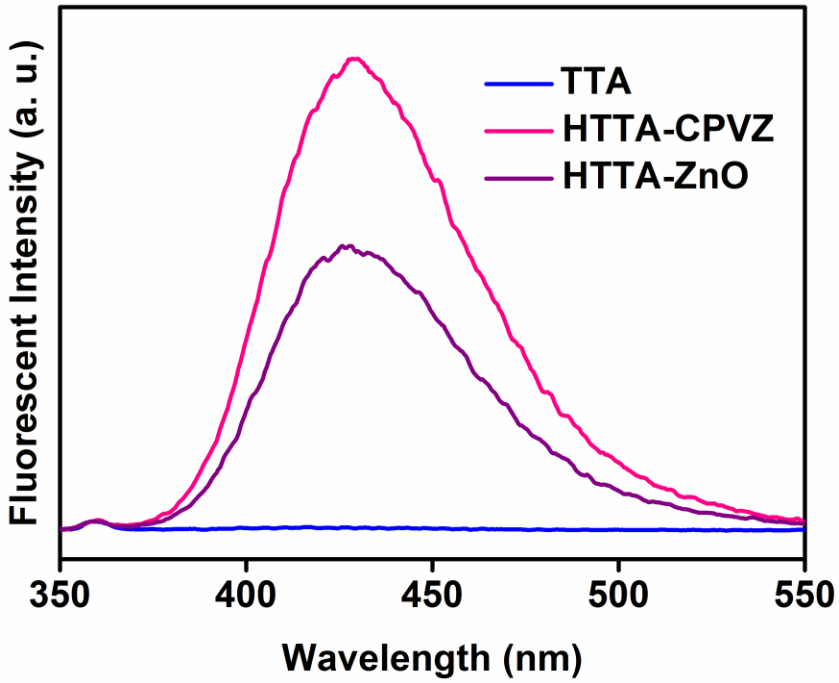

Figure 4.12 Fluorescence spectra of TTA before light exposure and HTTA after light exposure in presence of pure ZnO and CPVZ

4.1.3.3 Surface treatment – Contact angle measurements

The self-cleaning performance and surface wettability of CPVZ photocatalyst is analyzed from contact angle measurements. To prevent fogging, super hydrophobic/hydrophilic surfaces have been extensively reported over the past decades. However, super hydrophobicity is not favorable to extreme humid condition because of its high static contact angles. Super hydrophilic surfaces with low contact angles (less than 10) are significant in this regard as they prevent fogging by the formation of a continuous optically clear film of water and subsequently cleaning the surface[45]. Here, CPVZ coated glass substrate is subjected to dynamic contact angle measurements and achieved super hydrophilicity within two minutes by the formation of thin film. Initially the contact angle found to be 19.3^{o} and within 100 seconds the angle reaches to 14.5^{o}. After completion of 120 seconds the contact angle becomes almost zero proving the super hydrophilic nature of the prepared sample. The

wettability images obtained from dynamic contact angle measurements are displayed in Figure 4.13. Here the photocatalytic activity of CPVZ films degrade the contaminants from the atmosphere present on the surface of the film under illumination thus clean the surface.

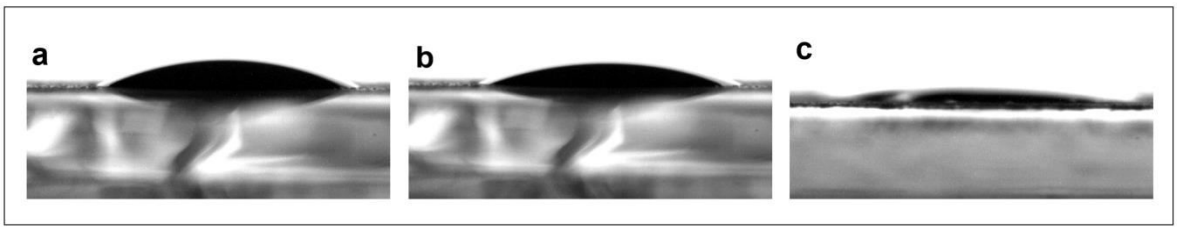

Figure 4.13 Photographs of water contact angle measurements on CPVZ surface (a) initial (b) after 100 seconds (c) after 120 seconds with illumination

4.1.3.4 Mechanism of photocatalysis

The mechanism involved in the fast photodegradation of methylene blue in the presence of CPVZ has been presented schematically in Figure 4.14. In CPVZ, carbon placed at the interstitial sites create new mid bandgap energy levels (evident from DOS of CPVZ) and act as trap states for the photogenerated carriers thereby suppress the exciton recombination[46, 47]. The presence of oxygen vacancies augments the separation efficiency of excitons through electron trapping. The PL intensity dip observed for CPVZ further support this argument by showing a decrease in carrier recombination. Suppression of carrier recombination results in the accumulation of photoexcited electrons and holes on the surface of CPVZ and induces the formation of highly reactive hydroxyl free radicals through concurrent oxidation and reduction process with the dissolved oxygen molecules from the dye solution leading to dye degradation. The same photocatalytic mechanism works on super hydrophilic surfaces, where the degradation of particulate contaminants from the atmosphere results the cleansing of surface[48]. This synergetic effect of oxygen vacancies and carbon induced tarp levels attributes the remarkable photocatalytic activity of CPVZ than pure ZnO. Here both oxygen deficiency and carbon incorporation leads a decrease in electron density of CPVZ and thus increases its

Lewis acidity. Being a Lewis base MB has an increased adsorption on the catalyst and that contributes to higher photocatalytic activity.

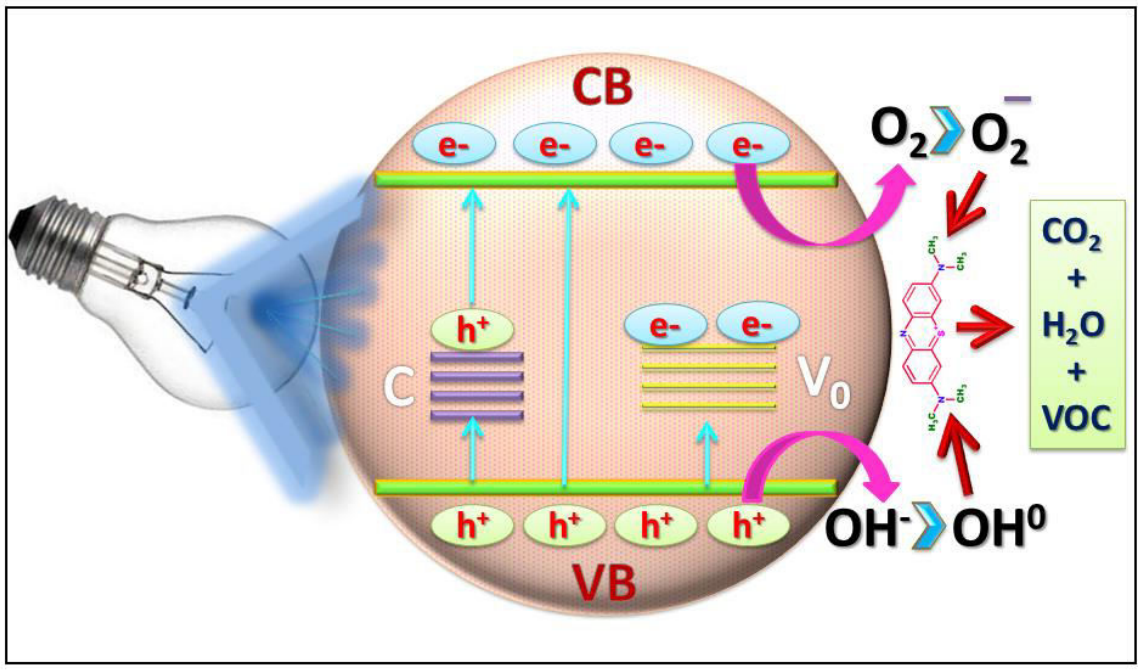

Figure 4.14 Plausible photocatalytic MB degradation mechanism in presence of CPVZ

4.1.4 CONCLUSIONS

Phase pure carbon embedded short nanotubes of ZnO (CPVZ) were prepared by post thermal treatment of PVP wrapped ZnO nanomaterials. The presence of carbon and absence of nitrogen were verified from various characterization techniques. X-ray photoelectron spectroscopy confirms the presence of enormous surface oxygen defects and carbon incorporation in CPVZ. Carbon incorporation introduces mid bandgap energy levels acting as traps for the photogenerated electrons and holes. The photocatalytic activity of these nanotubes was evaluated through the degradation of a textile dye. Super hydrophilicity of CPVZ films on glass substrate was checked from dynamic mode contact angle measurements and confirms its self-cleaning and surface wettability nature. These carbon doped ZnO nanotubes become more Lewis acidic and found to be 16% more photoactive than pure ZnO.

Presence of carbon induced mid-gap energy levels and presence of oxygen vacancies suppress the exciton recombination rate and shows better photocatalytic activity. Estimation of reactive oxygen species ratified the results obtained from photocatalytic performances.

4.2 *Carbon incorporated ZnO derived from Polyaniline assistance*

Polyaniline-zinc oxide hybrid nanocomposite (PNZ) was successfully prepared in water medium. The emeraldine salt of polyaniline (ES) was taken as the polymer matrix but in the composite, polyaniline exists as emeraldine base form. The post thermal treatment at 400 ^{o}C of PNZ leads to the formation of carbon incorporated ZnO (coded as CPNZ). The photocatalytic activity and stability of CPNZ was discussed in detail.

4.2.1 SYNTHESIS

4.2.1.1 Synthesis of PNZ and CPNZ

The hybrid nanocomposite PNZ was synthesized by taking ZnO and polyaniline. A precursor solution of zinc acetate was mixed in double distilled water (0.015M) with heating and stirring. When the temperature reached 60 °C, Ethane-1, 2-diamine with same molar concentration was injected into the solution using micropipette. After an hour, 0.1 wt% polyaniline emeraldine salts (Average mol.wt > 15,000 g/mol and particle size 3-100µm) in dimethyl sulfoxide was added to the reaction mixture, followed by six hours of continuous heating at 60 °C and stirring at 900 rpm, gives a dark blue hybrid precipitate. The precipitate was collected after centrifuged at 12000 rpm. Washed sample then dried and kept for analyzes. The schematic of the synthesis procedure is represented below in Figure 4.15. Polyaniline is completely soluble in DMSO through the formation of hydrogen bonding[49]. This polyaniline-DMSO solution when added to zinc acetate- Ethane-1, 2-diamine mixture, the alkaline mixture deprotonates ES to emeraldine base. With the assistance of mild

temperature, polyaniline in its emeraldine base structure interact with ZnO and lead the formation of hybrid nanocomposite PNZ. The composite PNZ, after heat treatment at 400 °C for one hour resulted in the formation of carbon incorporated PNZ and the sample is coded as CPNZ.

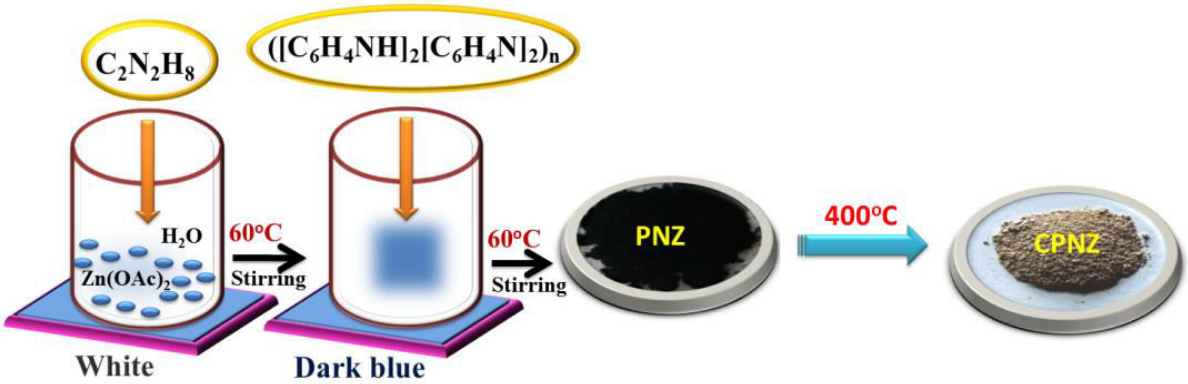

Figure 4.15 Schematic showing the synthesis procedure of CPNZ

4.2.2 CHARACTERIZATIONS

4.2.2.1 Morphology and structural analysis

4.2.2.1.1 Scanning Electron Microscopy (SEM)

Field emission scanning electron microscope was used to obtain images of the air dried PNZ, CPNZ and commercially available emeraldine salt of polyaniline (ES) as shown in Figure 4.16. ES resembles extended fibers. The images of hybrid, PNZ clearly point out the coverage of polymer on zinc oxide nanostructures. The smaller size of PNZ is also obvious from the SEM images. CPNZ are found to have destructive tubular structure with high rate of etching on surface. On temperature treatment, the surface of CPNZ becomes rough because the organic polymer (polyaniline) is detached from its surface.

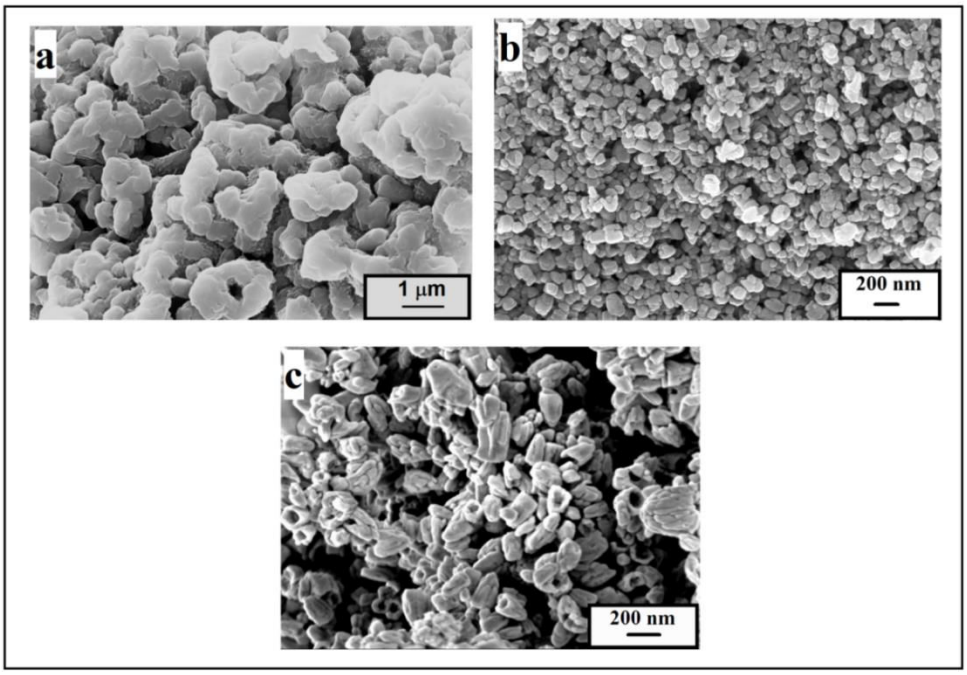

Figure 4.16 FESEM images of (a) ES, (b) PNZ and (c) CPNZ

4.2.2.1.2 Energy Dispersive Spectrum (EDS)

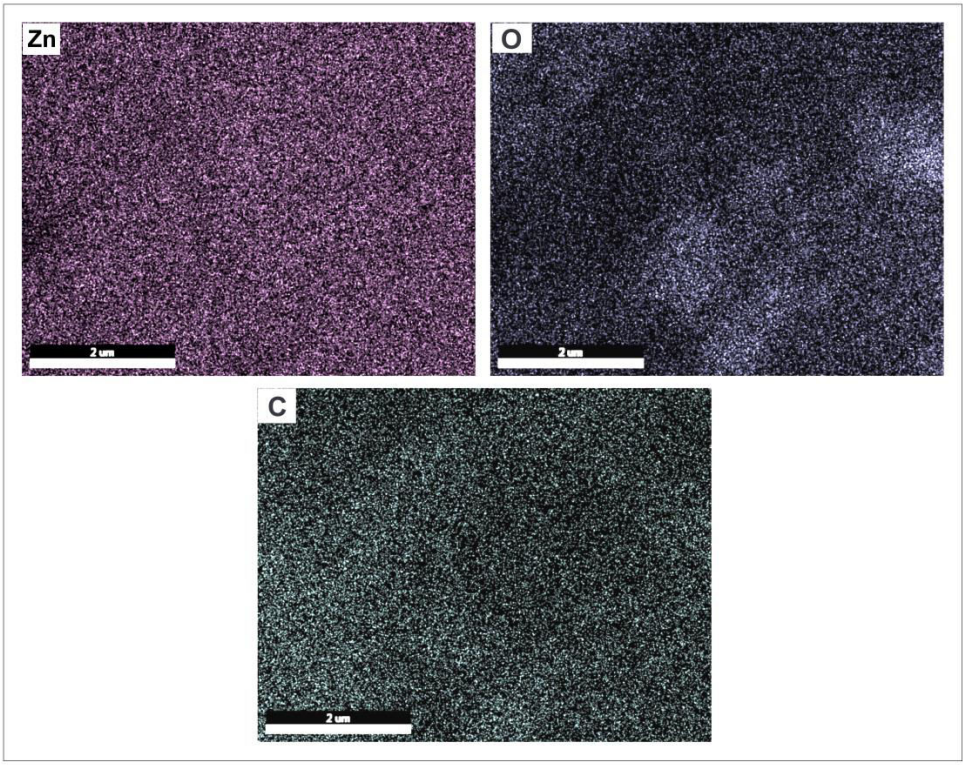

Figure 4.17 Elemental mapping of Zinc, Oxygen, and Carbon of CPNZ

The mapping of constituent elements (Zn, O and C) is as shown in Figure 4.17. The three elements are uniformly distributed in the CPNZ.

4.2.2.1.3 X-ray Diffraction Analysis (XRD)

The crystallinity and phase purity of the nanocomposites were analyzed from XRD pattern (Figure 4.18). Commercially available green colored emeraldine salt of polyaniline (ES) is in fully amorphous form whereas PNZ is crystalline and similar to pure ZnO (JCPDS - 89-0510), indicating that the crystal structure of ZnO is well maintained its wurtzite structure even after the polyaniline coating[50]. The diffraction peaks of CPNZ are also well matched with wurtzite ZnO. A gradual shift in the peaks towards lower two theta value with decrease in peak intensity is observed for PNZ and CPNZ with respect to pure ZnO as seen in Figure 4.18 b. The incorporation of carbon increased in the intensity of the CPNZ than PNZ.

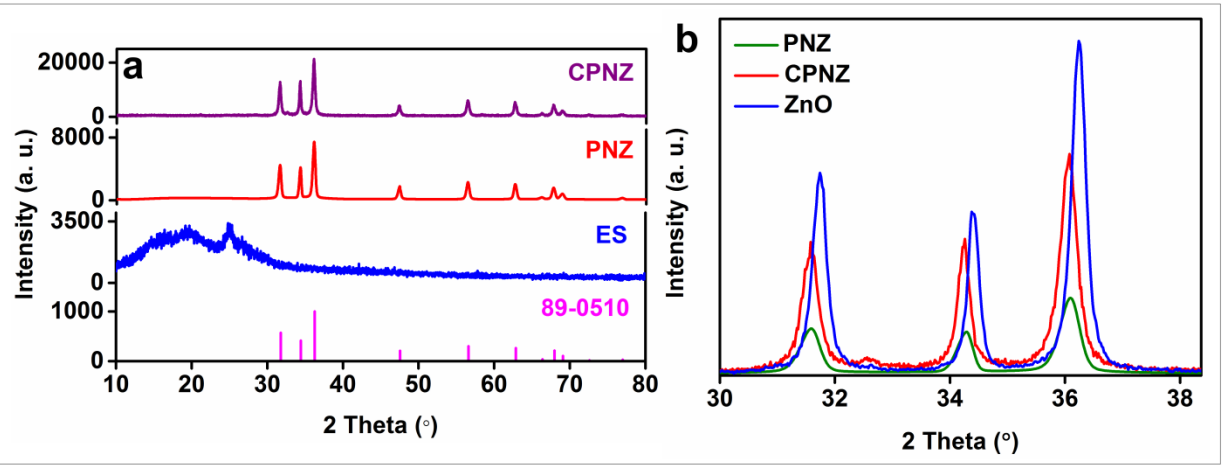

Figure 4.18 (a) XRD pattern of ES, PNZ and CPNZ compared with standard JCPDS (b) Enlarged image of XRD peaks

4.2.2.1.4 Fourier Transform Infrared Spectroscopy (FTIR)

FTIR spectra (Figure 4.19) provide ample evidence about the formation of hybrids compared to their polymer matrix. Intermolecular (3450 cm^{-1} / 3406 cm^{-1}) and intramolecular (2933 cm^{-}

[1]) hydrogen bondings are present in ES, PNZ and CPNZ[51]. The formed PNZ attains an emeraldine base structrure in the presence of alkali during synthesis[52].

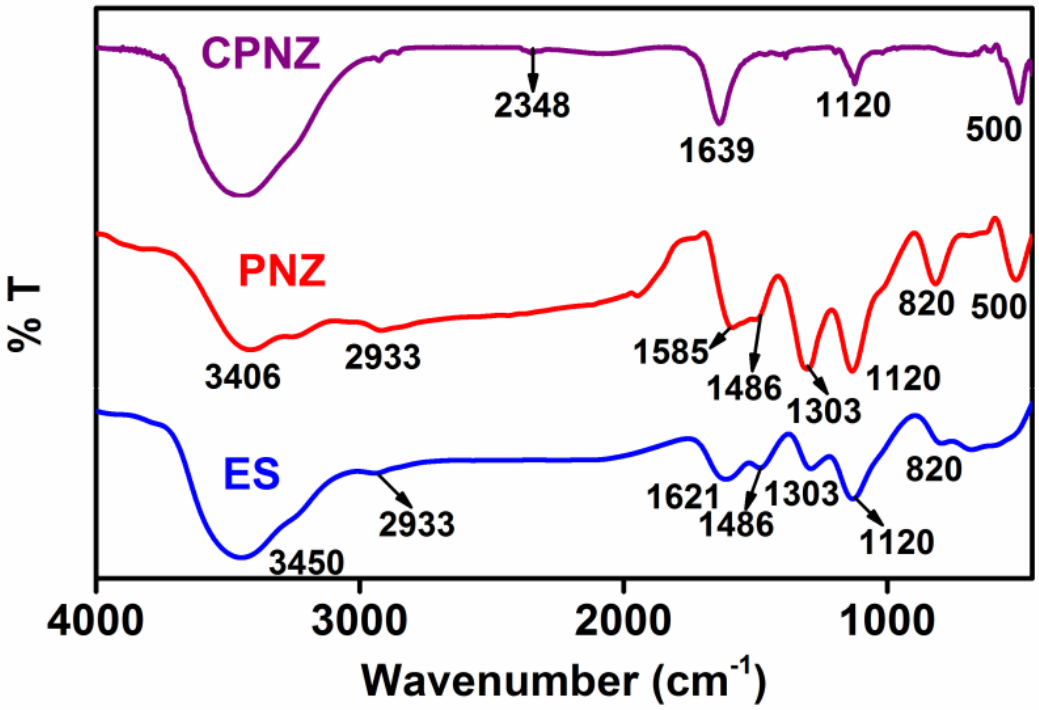

Figure 4.19 FTIR spectra of ES, PNZ and CPNZ

The structure of emeraldine salts depicts only benzenoid rings whereas that of emeraldine base features both benzenoid and quinoid rings. C=C stretching band in both quinoid (1585 cm^{-1})[53] and benzenoid (1486 cm^{-1})[54] are present in PNZ. Zn-O stretching (500 cm^{-1}) is also seen in PNZ[55]. As vibrational frequency increases in accordance with the bond order, C-N stretching frequency in quinoid (1303 cm^{-1})[56] is found to be higher in PNZ and that attributes the formation of EB. The peaks at 1120 cm^{-1} and 820 cm^{-1} in PNZ attributes aromatic C-H group in plane and the out of plane deformation for the 1,4-disubsituted benzene. These two peaks are more intense in PNZ than ES due to the change of chemical environment[57]. These observations indicate that the ZnO crystals are associated with the polyaniline by strong coulombic interaction with positively charged backbone[58]. Besides,a hydrogen bonding between imine group of polyaniline and surface hydroxyl grops of ZnO

nanomaterials is observed[59]. In CPNZ, a small peak at 2348 cm^{-1} indicate O=C=O asymmetric stretching[60] and peak at 1639 cm^{-1} indicate C=O stretching mode[61]. Peak at 1120 cm^{-1} is also an evidence for the presence of carbon in CPNZ[62]. The peak at 500 cm^{-1} indicates ZnO.

4.2.2.1.5 X-ray photoelectron spectroscopy (XPS)

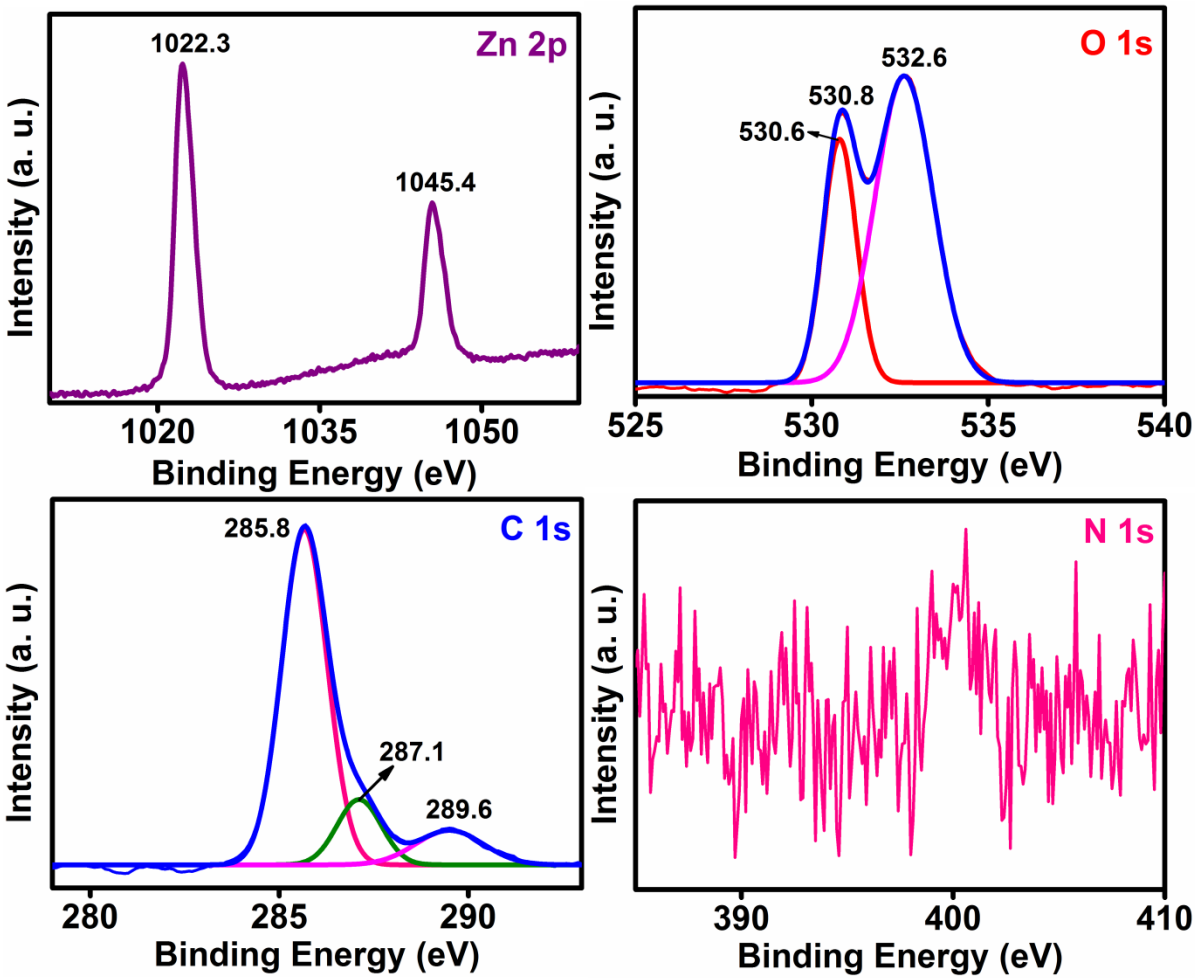

Figure 4.20 XPS spectra of Zn 2p, O 1s, C 1s and N 1s in CPNZ

A detailed study on the surface composition of CPNZ was predicted from binding energies derived from X-ray photoelectron spectroscopy, the spectra corresponding to Zn 2p, O 1s, C 1s and N 1s are shown in Figure 4.20. Valence and conduction band alignment are also determined using this spectroscopic technique. Oxygen 1s peak appears as doublet due to the

presence of surface oxygen defects[63]. Gaussian fitted peak at 532.6 eV indicate presence of C-OH groups corresponds to oxygen vacancies or defects[64]. Peaks at 530.8 eV and 530.6 eV are attributed to Zn-O binding and lattice oxygen respectively[65, 66]. In the case of Zn 2p, the result shows two main peaks centered at 1022.3 eV and 1045.4 eV corresponds to Zn $2p_{3/2}$ and Zn $2p_{1/2}$ in the ZnO phase respectively. Spin separation of 23.1 eV is same as the previously reported value in the literature[67]. Carbon 1s peaks are located at 285.8 eV, 289.6 eV and 287.1 eV and these peaks are corresponds to Zn-O-C, C-O and O-C-O bonds [28, 68]. The absence of nitrogen in the sample also confirmed from the spectral information.

4.2.2.2 Optical properties

4.2.2.2.1 Absorption spectra (Uv-Vis-NIR)

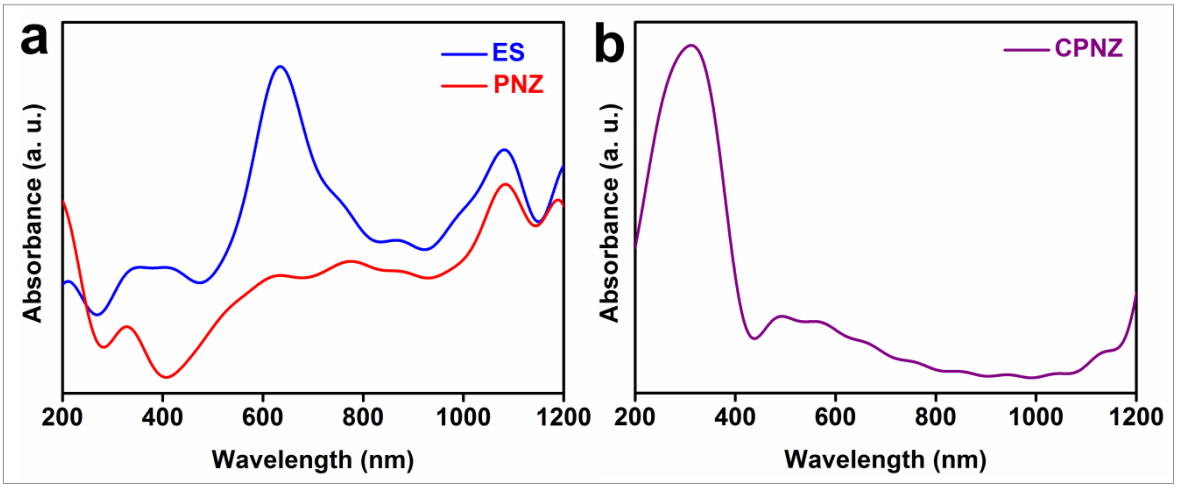

Figure 4.21Absorption spectra of (a) ES, PNZ and (b) CPNZ

The absorption spectra of ES, PNZ and CPNZ are depicted in Figure 4.21. Both ES and PNZ shows a peak at 330 nm attributed to the pi-pi* transition of benzenoid ring[69] and in ES this band appeared broad between 280 to 460 nm as it contain only benzenoid rings. In PNZ, the broad peak at 280-400 nm gives the indication of the incorporation of ZnO. The absorption spectra of ES show high intensity absorption at 635 nm, due to the delocalization of

polarons[69]. Polarons are conduction electrons present in polar organic semiconductors. Presence of polarons helps for the conduction of ES. But in PNZ this absorption peak is fully diminished indicating the conversion of ES to EB. During the formation of EB, ES combine with ZnO-1, 2-diaminoethane resulted in the destruction of amine associated polarons. The near IR peak at 1082 nm present in ES and PNZ attribute to the existence of polarons in amine and imine nitrogens respectively[70]. In CPNZ the band edge slightly shifted towards visible region. According to Sandesh *et al*, the red shift observed in absorbance is the indication of oxygen vacancies present in the sample[71].

4.2.2.2.2 Photoluminescence spectroscopy

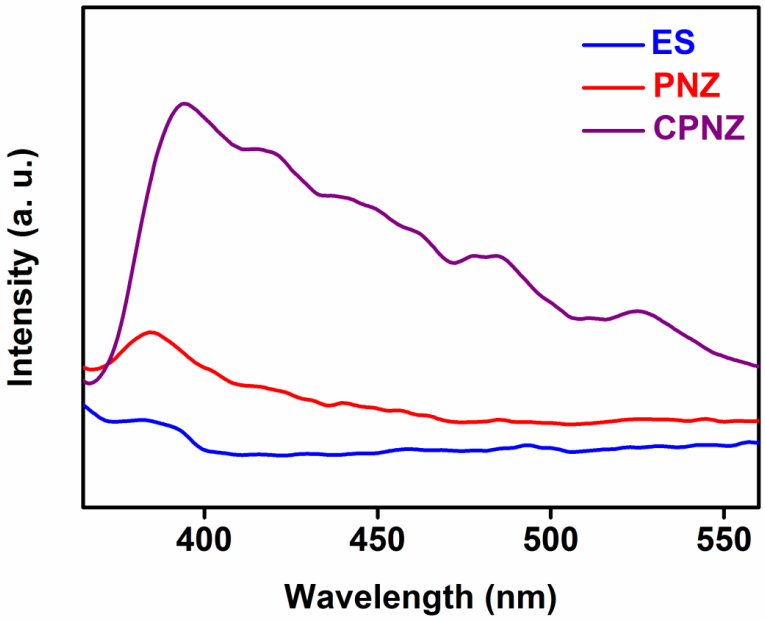

Figure 4.22 Photoluminescence spectra of ES, PNZ and CPNZ

The photoluminescence spectra are depicted in Figure 4.22. The PL spectra are taken by exciting the samples at 320 nm. Emission peaks of CPNZ spans over ES and PNZ. Incorporation of ZnO intensifies emission of PNZ compared to ES attributes extended conjugation present along benzenoid and quinoid rings, which helps delocalization of excitons[56]. The emission peaks in CPNZ mainly attributes to band edge emission and defect

emissions[72, 73].

4.2.2.3 Tauc plot, Valence band spectra and Density of states

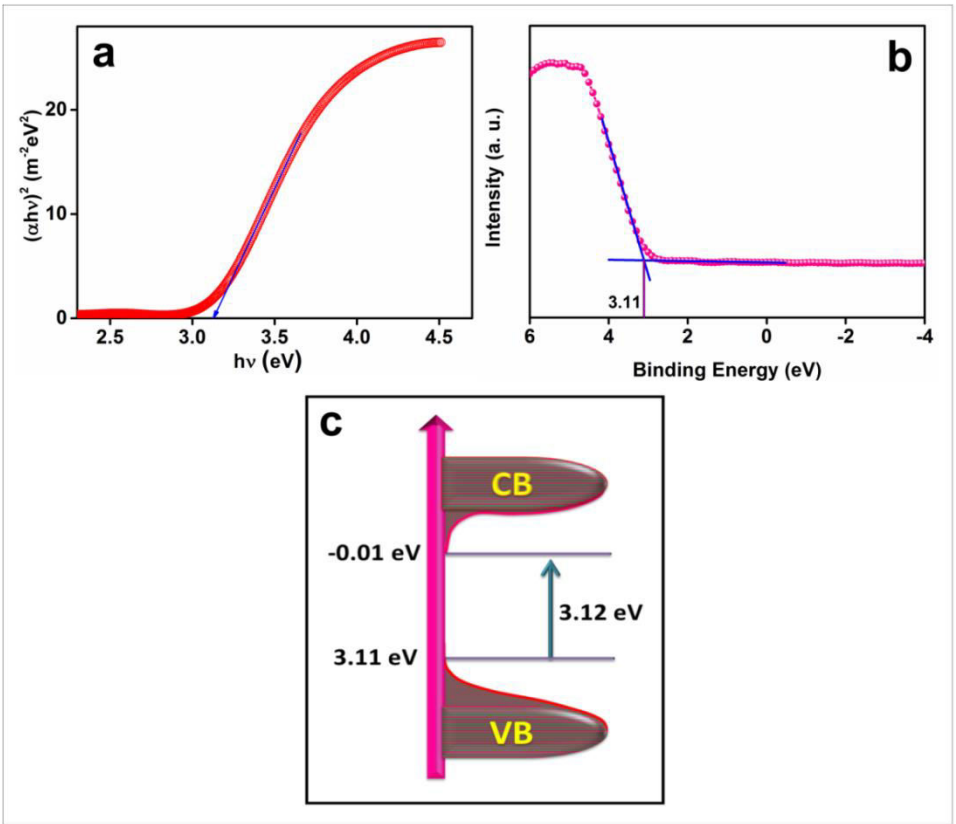

Figure 4.23 Tauc plot (a) Valence band XPS (b) and Density of states (c) of CPNZ

The band gap observed for CPNZ is 3.12 eV. The valence band maximum is found to be at 3.11 eV from valence band spectra. By considering these two values, the density of states of CPNZ is being predicted as shown in Figure 4.23. There will be an existence of midgap states due to the incorporation of carbon in the nanotubes and this will influence the density of states by generating a small tailing effect in valence band[74]. The conduction band minimum was calculated as -0.01 eV. Conduction band tail can be anticipated just like valence band tail because of the presence of crystal defects[75].

4.2.3 APPLICATIONS - PHOTOCATALYSIS

4.2.3.1 Water treatment - Dye degradation

To examine the activity of CPNZ photocatalyst, 0.002 wt% aqueous methylene blue dye solution was taken as the model system and the degradation of the dye was monitored within a time frame of 57 minutes. 0.05 g photocatalyst was added in to 50 mL of dye solution. This suspension was kept under dark for 30 minutes with stirring to avoid any error due to initial adsorption effect. The stirring in darkness also helps dye adsorption on the surface of the photocatalyst to establish adsorption-desorption equilibrium. After dark analysis, the dye solution was placed inside a photocatalytic reactor under 300W Xenon lamp. After 15 minutes of periodic exposure, 5 mL aliquots were taken to monitor the dye degradation. The Uv-visible absorption spectra were recorded after centrifuging at 10000 rpm for 10 minutes to avoid any scattering effect. The degradation of methylene blue in presence of CPNZ is shown in Figure 4.24 (a).

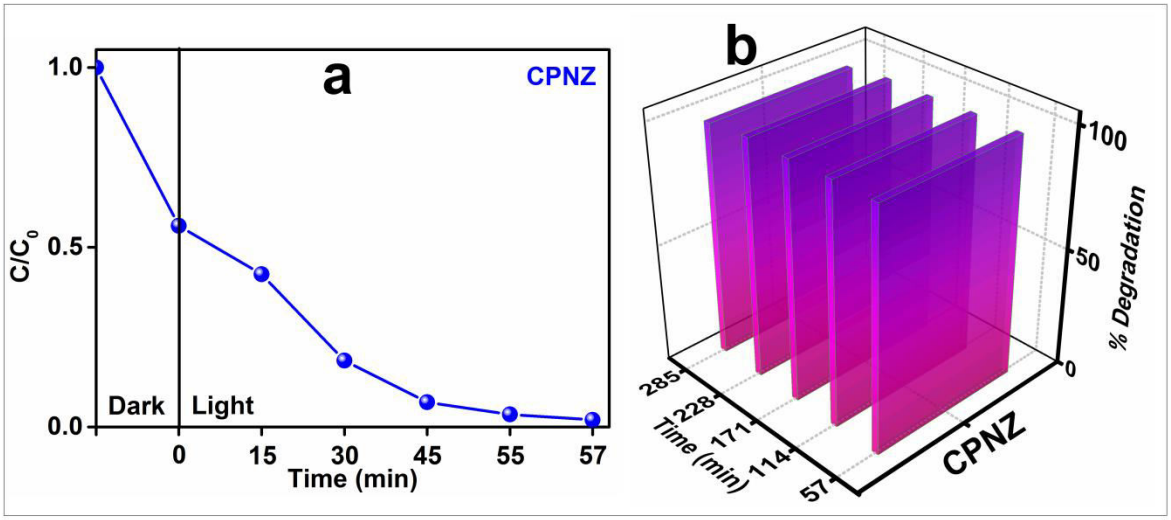

Figure 4.24 (a) Photodegradation of MB in presence of CPNZ and (b) Photocatalytic stability of CPNZ.

The recyclability and stability performances of CPNZ were also studied for five

consecutive steps and the material exhibit stability and recyclability very well. The graph showing stability performance of CPNZ is as depicted in Figure 4.24(b).

4.2.3.2 Estimation of reactive oxygen species

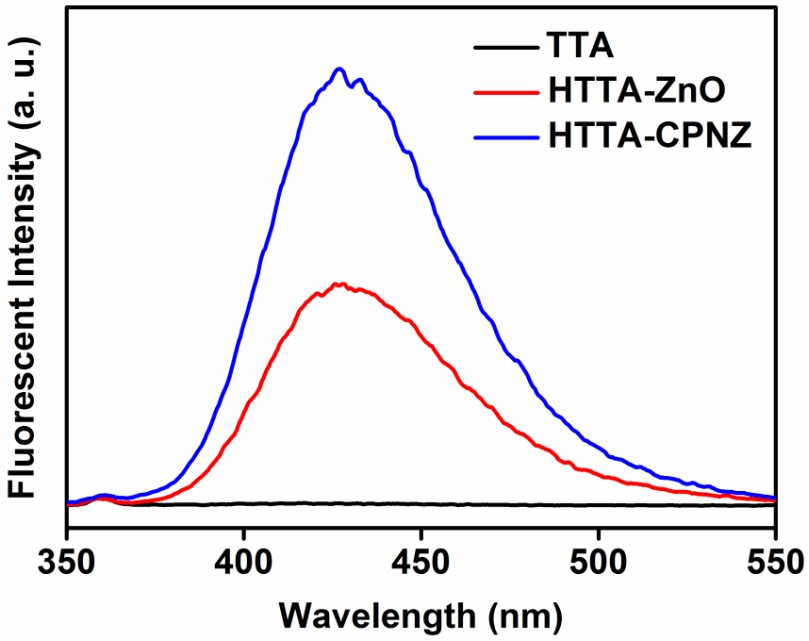

Figure 4.25 Photoluminescence spectra of TTA before light exposure and HTTA after light exposure in presence of pristine ZnO and CPNZ

The generation of hydroxyl radicals is mainly responsible for the photocatalytic activity of CPNZ. Hydroxyl radicals generated from CPNZ is estimated using terephthalic acid (TTA) probe. The fluorescent intensity obtained from hydroxyl terephthalic acid (HTTA) is depicted in Figure 4.25. CPNZ releases more reactive oxygen species compared to pure ZnO which are responsible for the higher photocatalytic activity of CPNZ.

4.2.3.3 Surface treatment - Contact angle measurements

The wettability images obtained from dynamic contact angle measurements are displayed in Figure 4.26. Antifogging activity of CPNZ coated glass surface is checked from contact angle measurements. When subjected to CPNZ coated glass substrate for dynamic contact angle

measurements, water was making 19.9^{o} contact angle with the surface. Within hundred seconds the film attains super hydrophilicity and the angle reaches to almost zero.

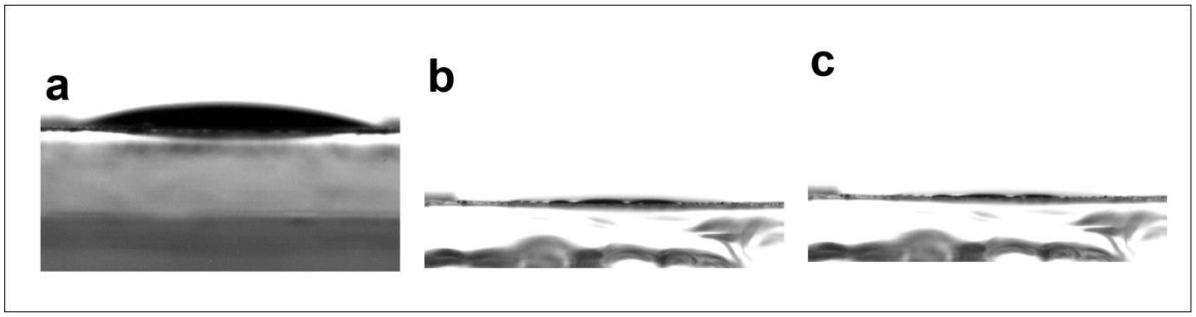

Figure 4.26 Photographs of water contact angle measurements on CPNZ surface (a) initial (b) after 100 seconds (c) after 120 seconds with illumination

4.2.4 CONCLUSIONS

Carbon incorporated ZnO nanostructure with the assistance of polyaniline was synthesized by a template free sol-precipitation method. The carbon embedded system shows better photocatalytic performance than pure zinc oxide. The formation of mid-gap levels combined with oxygen deficiency in carbon incorporated ZnO attributes better photocatalytic activity and can be considered as a promising material for effective water and surface treatments.

4.3 Carbon incorporated ZnO derived from both polyaniline and polyvinylpyrrolidone

Polymer wrapped ZnO nanotubes were synthesized using two polymers polyaniline and polyvinylpyrrolidone and a polymeric precursor ethane-1, 2-diamine from aqueous medium. The synthesized hybrid material named as PPZ. In addition to that a polymer blend containing polyaniline and polyvinylpyrrolidone was also synthesised parallely. The as prepared PPZ when heated at 400 °C obtained a black coloured powder and named as CPPZ. Characterizations and applications of PPZ and CPPZ are discussed in detail.

4.3.1 SYNTHESIS

4.3.1.1 Synthesis of PPZ and CPPZ

0.015 M zinc acetate in 150 ml water was taken as the zinc precursor. Two polymer solutions were set aside for timely addition in to the reaction mixture. When temperature of the precursor solution reached at 60 °C, 0.015 M ethylene diamine was added as the reducing and capping agent. After one hour, added 0.1 wt% polyaniline in dimethyl sulfoxide and after half an hour added 0.2 wt% polyvinylpyrrolidone in water to the reaction mixture. The presence of white precipitate confirmed that the zinc oxide nanotubes formed slowly. Total reaction time was fixed as 6 hours. After six hours, the solution was set aside to filter out the PPZ precipitate. The precipitate was washed with water and calcined at 400 °C for 1h using a muffle furnace and got CPPZ.

4.3.1.2 Synthesis of polymer blend (PP)

The schematic illustration of the synthesis procedure of CPPZ and PP are as shown in Figure 4.27. For this synthesis of PP, 0.1 wt% polyaniline in DMSO was added to double distilled water at 60 °C, After 30 minutes, 0.2 wt% PVP in water was added to the polyaniline/DMSO/water mixture. After reaction was stopped after 6 hours and the precipitate was centrifuged, washed and collected for further analysis.

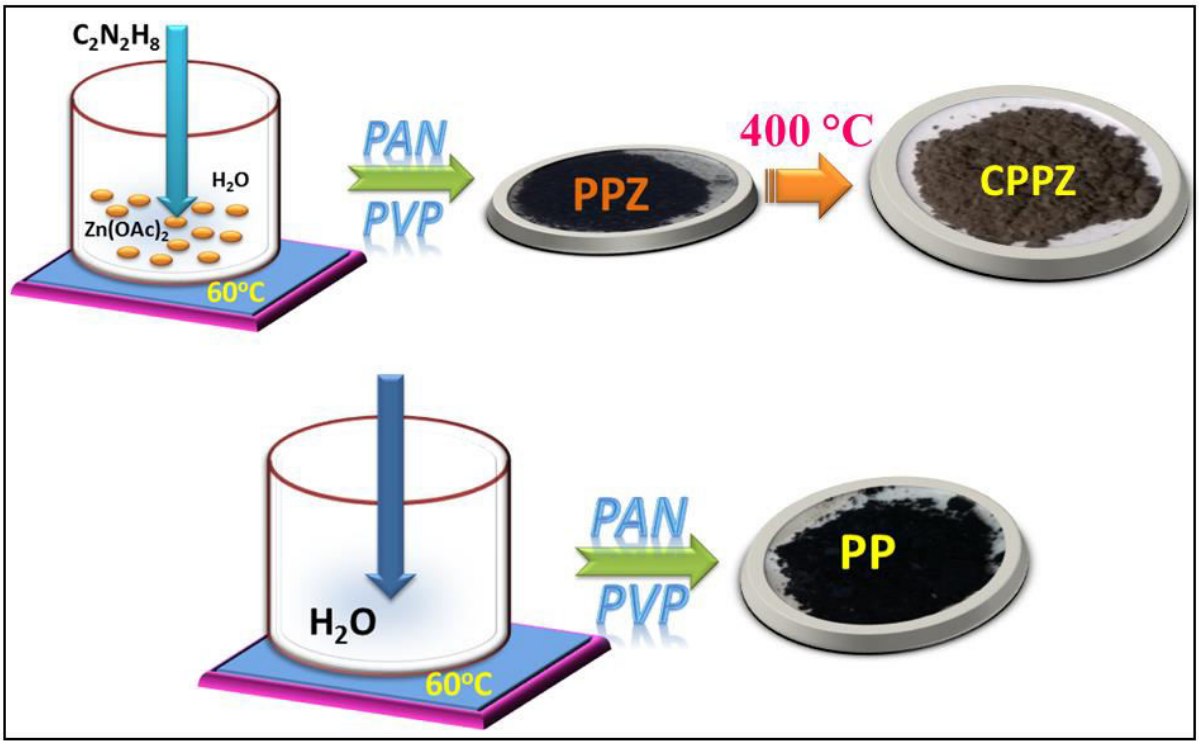

Figure 4.27 Schematic of synthesis procedure of CPPZ and PP

4.3.2 CHARACTERIZATIONS

4.3.2.1 Morphology and structural analysis

4.3.2.1.1 *Scanning electron microscopy (SEM)*

The scanning electron microscopy images of PP, PPZ and CPPZ are depicted in Fig 4.28. Polymers polyaniline and polyvinylpyrrolidone are completely blended and formed a continuous network structure whereas PPZ and CPPZ are similar to distorted short nanotubular structure.

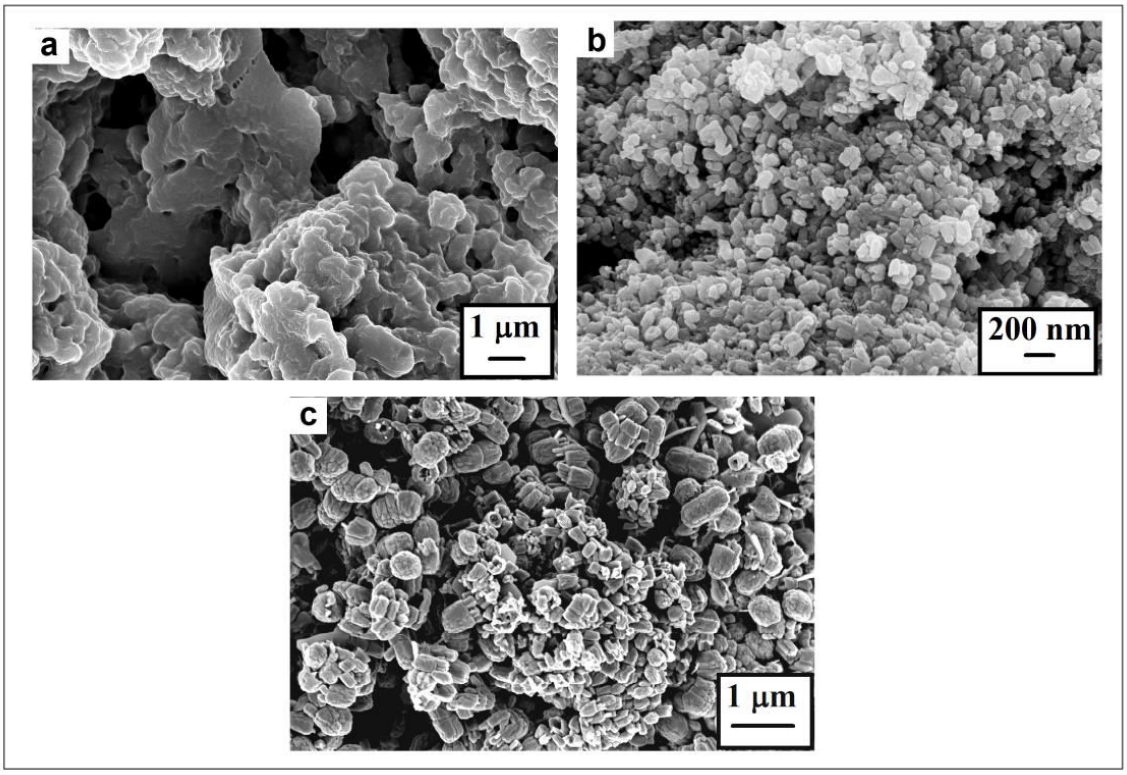

Figure 4.28 SEM images of (a) PP, (b) PPZ and (c) CPPZ

4.3.2.1.2 X-ray Diffraction Analysis (XRD)

XRD patterns of PP, PPZ and CPPZ are as shown in Figure 4.29. It can be seen that the samples PPZ and CPPZ have the similar XRD patterns of ZnO and incorporation of polymer decreases the intensity of peaks with a shift towards lower 2theta value. This indicates that the surface coverage of polymer or incorporation of carbon does not change the wurtzite structure of ZnO but make some sort of lattice expansions with increase of the interplanar spacing[76, 77]. This lattice expansion resembles with that of PNZ and CPNZ indicating the influence of polyaniline characterstics in PPZ and CPPZ than polyvinylpyrrolidone. The crystallite size of CPPZ was calculated from Scherrer equation and found to be 29.15 nm.

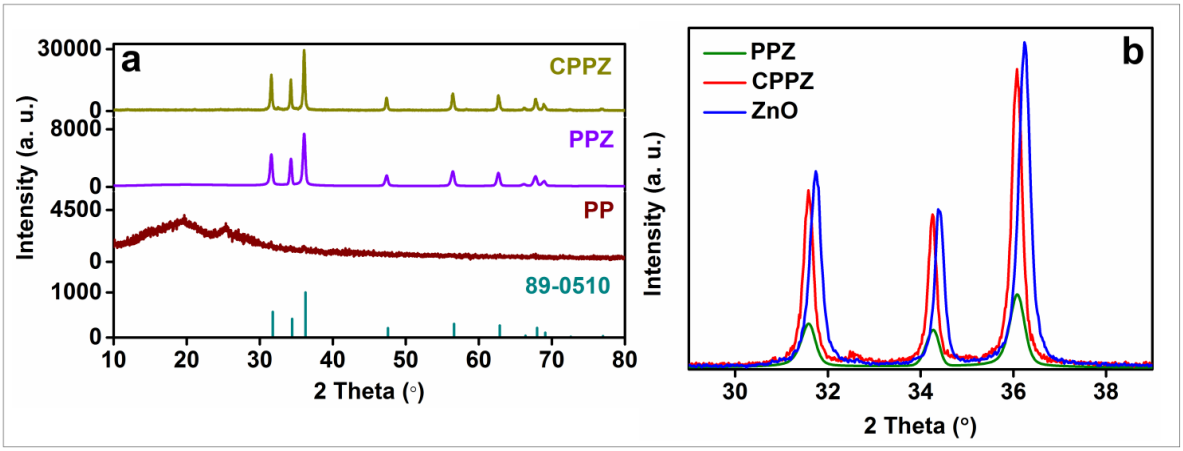

Figure 4.29 (a) XRD patterns of PP, PPZ and CPPZ compared with standard JCPDS (b) Enlarged image of XRD

4.3.2.1.3 Fourier Transform Infrared Spectroscopy (FTIR)

Figure 4.30 represents FTIR spectra of PP, PPZ and CPPZ. Inter and intra molecular hydrogen bonding was recorded at 3406 cm^{-1}/3436 cm^{-1} and 2933 cm^{-1} respectively. There exists hydrogen bonding between hydrogen atom (from OH group due to ring distuction) of the polyvinylpyrrolidone and nitrogen atom of polyaniline benzenoid group or between the N-H groups of PVP and PANI. The characteristic peaks of polyaniline (1585 cm^{-1}, 1120 cm^{-1} and 820 cm^{-1}) and polyvinylpyrrolidone (1280 cm^{-1}) are observed in PP. Peak at 500 cm^{-1} is due to the stretching of Zn-O bond and it is present in both PPZ and CPPZ. Peaks at 1303 cm^{-1}, 1120 cm^{-1} and 820 cm^{-1} in PPZ are same as peaks in PNZ. The C=C stretching in benzenoid and quinoid (1550 cm^{-1} and 1480 cm^{-1}) are slightly shifted in PPZ to lower wavenumber region compared to PNZ. This relative exposition may be due to the strong interaction present between PANI and PVP through benzenoid part[78]. In addition to the hydrogen bonding interaction, there exists coulombic as well as electrostatic interaction between polyaniline and polyvinylpyrolidone. The peak at 1303 cm^{-1} present in ES is shifted to 1280 cm^{-1} in PP and also peak at 1486 cm^{-1} is absent in PP. The strong interaction of PVP affects the structure of polyniline by extending or stretching the polyaniline backbone

through intramolecular hydrogen bonds breaking[79]. Peak at 1639 cm-1 indicate C=O stretching mode.

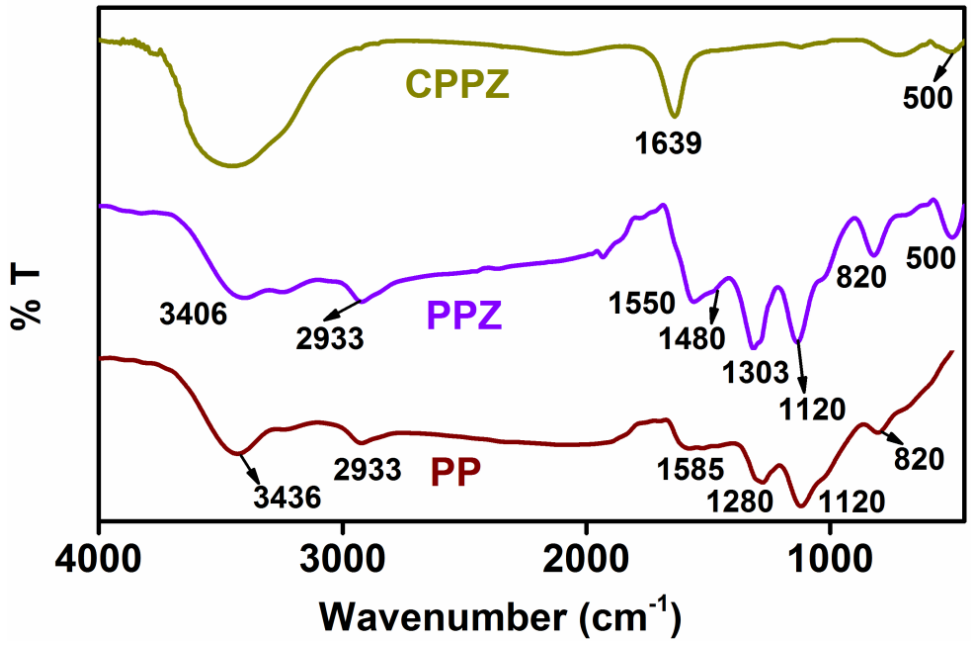

Figure 4.30 FTIR spectra of PP, PPZ and CPPZ

4.3.2.2 Optical properties

4.3.2.2.1 Absorption spectra (Uv-Vis-NIR)

In PP, the absorption in the range 280-460 nm indicates the Π-Π* transitions in both PANI and PVP[80].Characteristic peaks of polyaniline (635 nm and 1082 nm) are also observed in PP. Similarly PPZ exhibit both ZnO and PP peaks (330 nm and 1082 nm). Cross linking of these two polymers give rise to absorption at 765 nm. The absorption spectra are depicted in Figure 4.31.

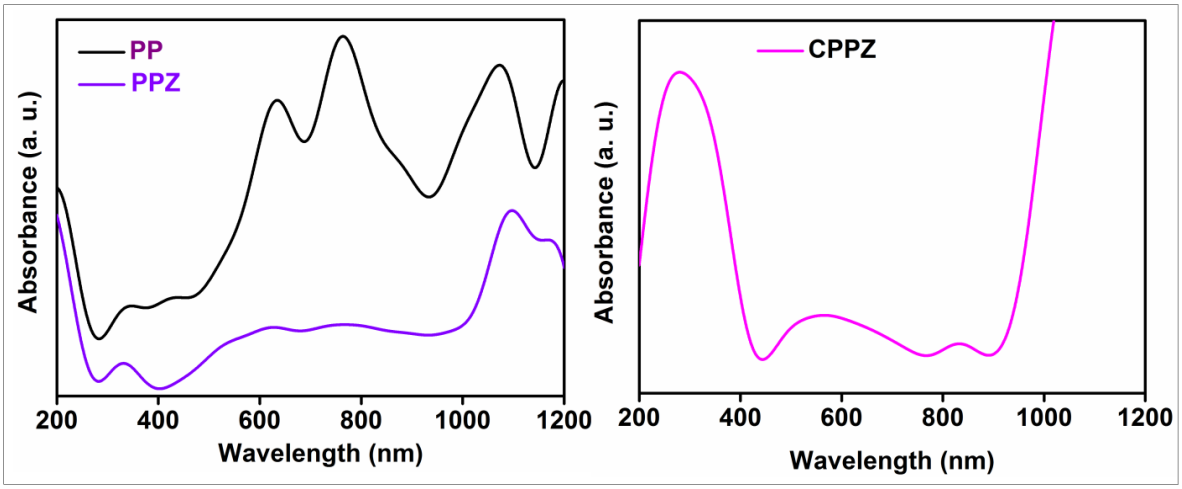

Figure 4.31 Absorption spectra of PP, PPZ and CPPZ

4.3.2.2.2 Photoluminescence Spectroscopy (PL)

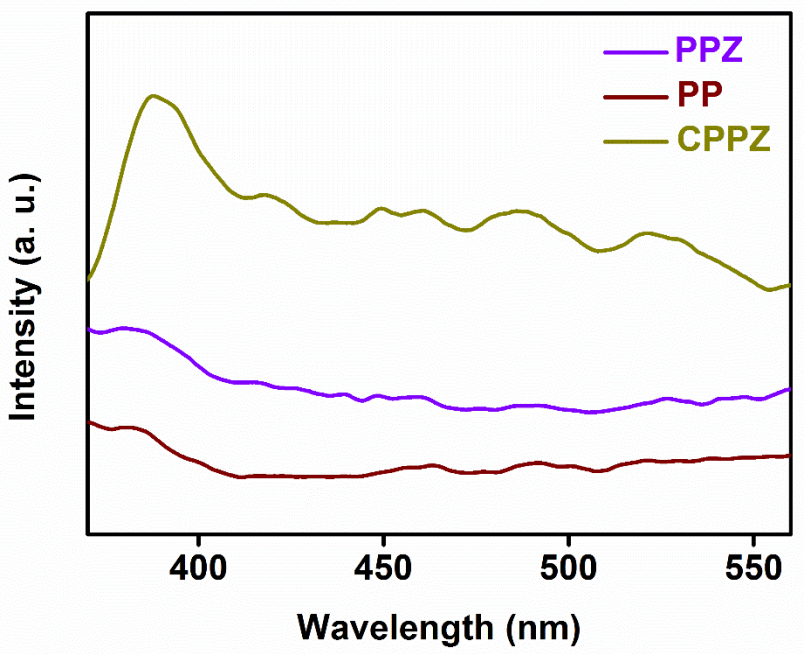

Figure 4.32 Photoluminescence spectra of PP, PPZ and CPPZ

The emission spectra of PP, PPZ and CPPZ were taken by equally weighed samples with excitation wavelength 320 nm and the results are depicted in Figure 4.32. The emission peaks in PP and PPZ were not clearly observed due to the polymer whereas in CPPZ the bandedge emissions as well as defect emissions were cleared similar to that of ZnO. It is generally

accepted that the calcination process intensify the PL emission with the improvement in the crystallinity[81, 82].

4.3.3 APPLICATIONS –PHOTOCATALYSIS

4.3.3.1 Water treatment - Dye degradation

The photocatalytic activity of CPPZ was evaluated by monitoring the decomposition of methylene blue. The graph showing the degradation was depicted in Figure. 4.33.

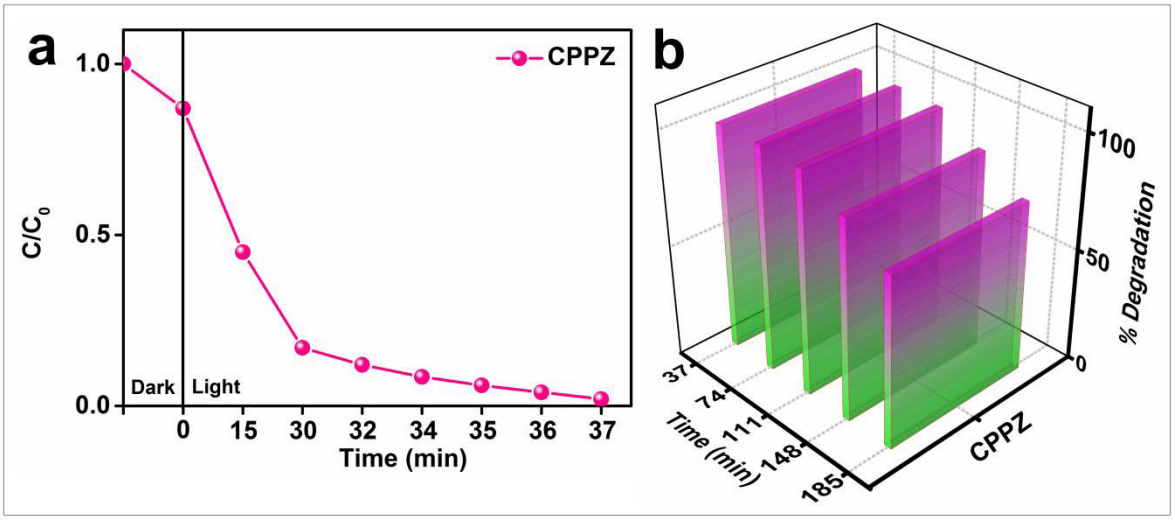

Figure 4.33 (a) Photodegradation of MB in presence of CPPZ and (b) photocatalytic stability of CPPZ

0.05 g of CPPZ was added to 50 ml 0.002 wt% methylene blue aqueous solutions. Dark adsorption analysis study was carried out for 30 minutes with continuous stirring in dark and established adsorption-desorption equilibrium. After 30 minutes of stirring 4 mL suspended dye solution was withdrawn and monitored the extinction of intensity by taking the Uv-Vis spectrum. After the illumination of light, the methylene blue was degraded completely within 37 minutes. The stability performance of the CPPZ photocatalyst towards dye degradation was also performed in five consecutive runs. The photocatalyst after one usage washed for next run with fresh 50 mL methylene blue solution and this cyclic process

repeated for five times. After four consecutive runs the stability was found decreased. This decrease in stability after five runs can be assign to the synergetic effect of lower adsorption and lower reactive oxygen species generation in CPPZ. Higher carbon content above a certain limit can suppress the availability of ROS for the degradation process

4.3.3.2 Estimation of reactive oxygen species

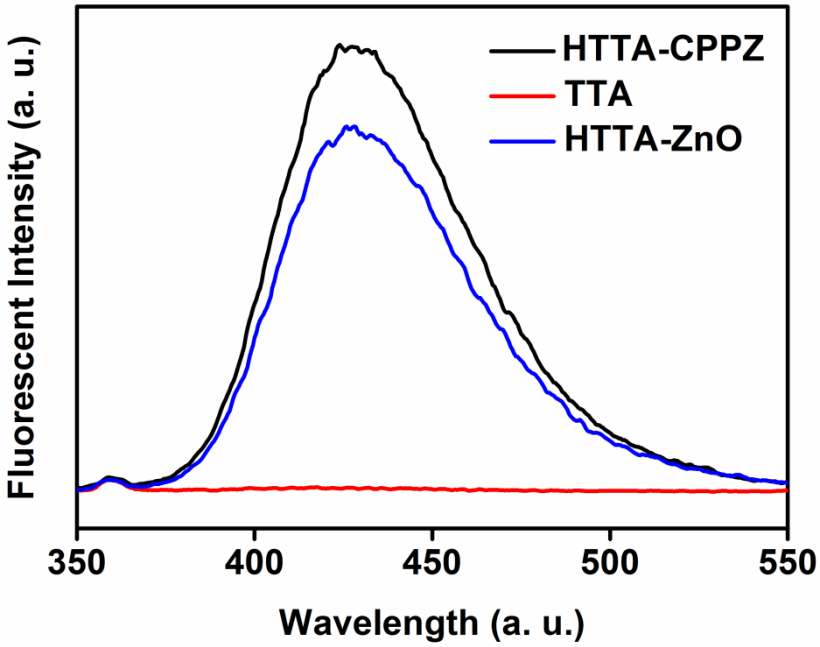

Figure 4.34 Graph depicts fluorescent intensity of TTA and HTTA in presence of CPPZ and pure ZnO

The hydroxyl radicals generated from CPPZ are detected using terephthalic acid probe method and the spectrum obtained is depicted in Figure 4.34. CPPZ released comparatively higher reactive oxygen species than pure ZnO and exhibit excellent photocatalytic activity.

4.3.3.3 Surface treatment - Contact angle measurements

The surface treatment of CPPZ was analysed from its antifogging ability measured by contact

angles with water. The photographs of the water droplets on the surface of CPPZ coated glass film was as shown in Figure 4.35. For the study, CPPZ powder was made paste with methanol and evenly doctor bladed on the glass substrate. The air dried sample then used for taking dynamic contact angle measurements. The initial angle was found to be 31.2° and within hundred seconds the angle was found to decrease attain the value 21.75° ·After two minutes, the contact angle reaches to 18.5°.

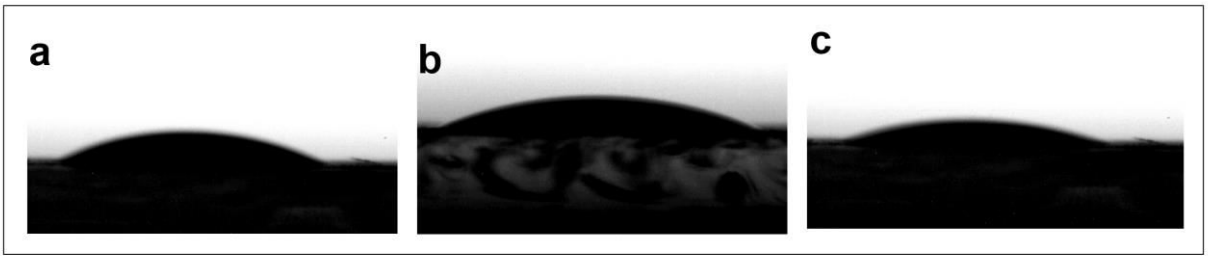

Figure 4.35 Photographs of water contact angle measurements on CPPZ surface (a) initial (b) after 100 seconds (c) after 2 min with illumination

4.3.4 CONCLUSIONS

Synthesised carbon decorated ZnO nanotubes by using both the polymers simultaneously and analysed its performance towards photocatalysis. When comparing the activity of CPPZ with CPVZ and CPNZ, it was observed that it works better than CPNZ but lesser than CPVZ.

4.4 SUMMARY

Hybrid nanocomposites of zinc oxide were prepared by an easy and scalable sol-gel approach. A conducting polymer (polyaniline), a non-conducting polymer (polyvinylpyrrolidone) and a blend of these two polymers were chosen for the synthesis of nanocomposites of ZnO. The synthesized nanocomposites were named as PVZ, PNZ and PPZ. Calcination of these products enables the incorporation of carbon in to the ZnO lattice which is confirmed from various characterization techniques and the calcined products are

named as CPVZ, CPNZ and CPPZ. Among these three carbon incorporated samples, the dye adsorption is found in the order CPVZ < CPPZ < CPNZ and the ROS generation is in the order CPPZ < CPVZ < CPNZ. But the photocatalytic activity is exhibited in the order CPVZ > CPPZ > CPNZ. Combined effect of particle size, adsorption capability, generation of ROS and presence of crystal defects support CPVZ to become an efficient photocatalyst. Moreover all three samples exhibit super hydrophilic behavior so that they can be used as anti-fogging coatings.

4.5 REFERENCES

[1] Malafronte, F. Auriemma, R. Di Girolamo, C. Sasso, C. Diletto, A.E. Di Mauro, E. Fanizza, P. Morvillo, A.M. Rodriguez, A.B. Munoz-Garcia, M. Pavone, C. De Rosa, *J. Phys. Chem. C* **2017**, 121, 16617-16628.

[2] J. Wang, X. Li, Y. Xia, S. Komarneni, H. Chen, J. Xu, L. Xiang, D. Xie, ACS Appl. *Mater. Interfaces* **2016**, 8, 8600−8607.

[3] H. Zhang, Y. Wang, W. Zhao, M. Zuo, Y. Chen, L. Yang, L. Xu, H. Wu, A. Cao, *ACS Appl. Mater. Interfaces* **2017**, 9, 37813-37822.

[4] V. Saadattalab, A. Shakeri, H. Gholami, *Prog. Nat. Sci : Mater. Int.* **2017**, 26, 517–522.

[5] X. Xiao, B. han, G. Chen, L. Wang, Y. Wang, *Sci. rep.*, **2017**, 7:40167.

[6] R. Ahmad, I. Hasan*, J. Chem. Eng. Data* **2017**, 62, 1594-1607.

[7] A. Mostafaei, A. Zolriasatein, *Prog. Nat. Sci. Mater. Int.* **2012**, 22, 273–280.

[8] R. Kandulna, R. B. Choudhary, *Optik,* **2017**, 144, 40–48.

[9] J. R. Aggas, W. Harrell, J. Lutkenhaus, A. G-Elie, *Nanoscale,* **2018**, 10, 672-682.

[10] I. Y. Kim, Y. K. Jo, J. M. Lee, L. Wang, S. Hwang, *J. Phys. Chem. Lett.* **2014**, 5, 4149-4161.

[11] N. Saurakhiya, S. K. Sharma, R. Kumar, A. Sharma, *Ind. Eng. Chem. Res.* **2014**, 53, 18884-18890.

[12] M. A. Barakat, *Arab. J. Chem*, **2010**, 4, 361-377.

[13] Y. Bu, Z. Chen, *ACS Appl. Mater. Interfaces,* **2014,** 6, 17589-17598.

[14] H. Zhang, R. Zong, Y. Zhu, *J. Phys. Chem. C.,* **2009**, 113, 4605–4611.

[15] M. Yang, S. Sheng, Q. Ma, N. Lv, W. Yu, J. Wang, X. Donga, G. Liu, *Mat. Res*, **2016**, 19(2), 308-313.

[16] J. Tang, L. Ma, N. Tian, M. Gan, F. Xu, J. Zeng, Y. Tu, Materials Science and Engineering B, **2014**, 186, 26–32.

[17] L. T. Tseng, J. B. Yi, X. Y. Zhang, G. Z. Xing, H. M. Fan, T. S. Herng, X. Luo, M. Ionescu, J. Ding, S. Li, *Aip Adv.*, **2014**, 067117.

[18] R. Hariharana, S. Senthilkumara, A. Suganthib, M. Rajarajan, *J. Photochem. Photobiol., A: Chemistry,* **2013**, 252, 107– 115.

[19] B. N. Meethal, N. pullanjiyot, S. Swaminathan, *Mater. Des.,* **2017,** 130, 426–432.

[20] A. E. Danks, S. R. Hall, Z. Schnepp, *Mater. Horiz.,* **2016**, 3, 91-112.

[21] H. Yang, Q. Ye, R. Zeng, J. Zhang, L. Yue, M. Xu, *Sensors,* **2017**, 17, 2415, 1-11.

[22] X. Yan, Y. Gu, X. Zhang, Y. Huang, J. Qi, Y. Zhang, T. Fujita, M. Chen, *J. Phys. Chem. C,* **2009***,* 113 (4), 1164-1167.

[23] H. M. Pouran, V. Llabjani, F. L. Martin, H. Zhang, *Environ. Sci. Technol.,* **2013**, 47, 11115−11121.

[24] B. N. Roy, G. P. Singh, H. M. Godbole, S. P. Nehate, *Indian J. Pharm. Sci.,*

2009, 71(4), 395-405.

[25] M. L. S. Mello, B. C. Vidal, *Plos one*, **2012**, 7(8), 43169 (1-12).

[26] S. Gunasekaran, E. Sailatha, S. Seshadri, S. Kumaresan, *Indian J. Pure Appl. Phys.,* **2009***,* 47, 12-18.

[27] M. Vetter, A. Brodyanski, H.-J. Jodl, *Fizika Nizkikh Temperatur*, **2007**, 33, 1383–1392.

[28] X. Zhang, J. Qin, R. Hao, L. Wang, X. Shen, R. Yu, S. Limpanart, M. Ma, R. Liu, *J. Phys. Chem. C,* **2015**, 119, 20544−20554.

[29] L. Óvári, S. K. Calderon, Y. Lykhach, J. Libuda, A. Erdohelyi, C. Papp, J. Kiss, H.-P. Steinrück, *J. Catal.,* **2013**, 307, 132–139.

[30] K. Dave, K. H. Park, M. Dhayal, *RSC Adv.,* **2015**, 5, 107348-107354.

[31] V.V. Titov, A.A. Lisachenko, I. K. Akopyan, M.E. Labzowskaya, B.V. Novikov, *J. Lumin.*, **2018**, 195, 153–158.

[32] V. Sharma, P. Kumar, A. Kumar, Surbhi, K. Asokan, K. Sachdev, *Sol. Energy Mater. Sol. Cells*, **2017**, 169, 122–131.

[33] R. Madhu, V. Veeramani, S-M Chen, P. Veerakumar, S-B Liu, N. Miyamoto, *Phys. Chem. Chem. Phys.,* **2016**, 18, 16466-16475.

[34] S. Iaiche, A. Djelloul, *J. Spectrosc.* **2015**, 836859, 2015, 1-9.

[35] S. N. Q. A. A. Aziz, S-Y. Pung, N. N. Ramli, Z. Lockman, *Sci. World J,* **2014***,* 252851, 1-9.

[36] G. Patrinoiu, J. M. Calderon-Moreno, R. Birjega, D. C. Culita, S. Somacescu, A.

M. Musuc, T. Spataru, O. Carp, *Phys. Chem. Chem. Phys.,***2016***,* 18, 30794-30807.

[37] S. Chall, A. Saha, S. K. Biswas, A. Datta, S. C. Bhattacharya, *J. Mater. Chem.* **2012***,* 22, 12538-12546.

[38] B. Kumar, G. Kaur, S.B. Rai, *Spectrochim. Acta, Part A: Mol. Biol. Spectrosc.*, **2017**, 187, 75–81.

[39] E. J. Guidelli, O. Baffa, D. R. Clarke, *Sci. Rep*., **2015**, 5:14004, 1-11.

[40] A. B. Lavand, Y. S. Malghe, *J. Saudi Chem. Soc.*, **2015**, 19, 471–478.

[41] X. Chen, L. Liu, P. Y. Yu, S. S. Mao, *Science,* **2011***,* 331, 746-750.

[42] H. Huang, F. Li, H. Wang, X. Zheng, *RSC Adv.* **2017**, 7, 50056-50063.

[43] Z. Shen, P. Liang, S. Wang, L. Liu, S. Liu, *ACS Sustainable Chem. Eng.* **2015**, 3, 1010−1016.

[44] D. He, Y. Li, I. Wang, J. Wu, Y. Yang, Q. An, *Appl. Surf. Sci.,* **2017***,* 391, 318–325.

[45] P. Chevallier, S. Turgeon, C. S-Bournet, R. Turcotte, G. Laroche, *ACS Appl. Mater. Interfaces,* **2011***,* 3, 750–758.

[46] X. Liu, H. Du, X. W. Sun, *RSC Adv.*, **2014**, 4, 5136-5140.

[47] R. Atchudan, T. N. J. I. Edison, Sugun, S. Perumal, N. Karthik, D. Karthikeyan, M. Shanmugam, Y. R. Lee, *J. Photochem. Photobiol., A: Chemistry,* **2018***,* 350, 75–85.

[48] M. W. England, C. Urata, G. J. Dunderdale, A. Hozumi, *ACS Appl. Mater.*

Interfaces, **2016**, 8, 4318−4322.

[49] S-J. Su, N. Kuramoto, *Macromolecules* **2001**, 34, 7249-7256.

[50] S. Chaturvedi, R. Das, P. Poddar, S. Kulkarni, *RSC Adv.,* **2015**, 5, 23563–23568.

[51] N. Parveen, M. O. Ansari, M. H. Cho, *Ind. Eng. Chem. Res.,* **2016**, 55, 116–124.

[52] T. Ogoshi, Y. Hasegawa, T. Aoki, Y. Ishimori, S. Inagi, T. Yamagishi, *Macromolecules,* **2011**, 44, 7639–7644.

[53] K. Mallick, M. Witcomb, M. Scurrell, Platin. *Met. Rev.,* **2007**, 51, 3–15.

[54] N-A. Rangel-Vazquez, C. Sánchez-lópez, F.R. Felix, *Polímeros,* **2014**, 24, 453–463.

[55] C. Pholnak, C. Sirisathitkul, S. Suwanboon, D.J. Harding, *Mater. Res.,* **2014**, 17, 405–411.

[56] V.J. Babu, S. Vempati, S. Ramakrishna, *Mater Sci Appl,* **2013,** 4, 1–10.

[57] Z. Tang, J. Wu, M. Zheng, Q. Tang, Q. Liu, J. Lin, J. Wang, *RSC Adv.,* **2012**, 2, 4062-4064.

[58] P. Rajakani, C. Vedhi, *Int. J. Ind. Chem*., **2015**, 6, 247–259.

[59] S. Ameen, M. S. Akhtar, Y. S. Kim, O. B. Yang, H. S. Shin, *Colloid Polym. Sci.,* **2011**, 289, 415–421.

[60] D. Sharabi, Y. Paz, *Appl. Catal. B: Environmental*, **2010**, 95,169–178.

[61] P. Muthukumar, C. Rangasami, S. Ganesan, *Chalcogenide Letters*, **2013**, 10 (3), 113 – 119.

[62] V. Ţucureanu, A. Matei, A. M. Avram, *Critical reviews in analytical chemistry*, **2016**, 46 (6), 502–520.

[63] H. Huang, F. Li, H. Wang, X. Zheng, *RSC Adv.*,**2017**, 7, 50056.

[64] D. H. Wang, Y. Hu, J. J. Zhao, L. L. Zeng, X. M. Tao, W. Chen, *J. Mater. Chem. A,* **2014**, 2, 17415.

[65] M. T. Uddin, Y. Nicolas, C. Olivier, T. Toupance, L. Servant, M. M. Muller, H-J. Kleebe, J. Ziegler, W. Jaegermann, *Inorg. Chem.,* **2012**, 51, 7764−7773.

[66] V. L. prasanna, R. Vijayaraghavan, *Langmuir,* **2015**, 31, 9155−9162.

[67] G-H. An, D-Y. Lee, H-J. Ahn, *ACS Appl. Mater. Interfaces,* **2017**, 9, 12478−12485.

[68] D. H. Wang, Y. Hu, J. J. Zhao, L. L. Zeng, X. M. Tao, W. Chen, *J. Mater. Chem. A,* **2014**, 2, 17415.

[69] J. Gu, S. Kan, Q. Shen, J. Kan, *Int. J. Electrochem. Sci.,* **2014**, 9, 6858 – 6869.

[70] J. Laska, *Mater. Sci. Eng., B,* **1999**, 68, 76–79.

[71] S. Y. Sawant, M. H. Cho, *RSC Adv.,* **2016**, 6, 70644-70652.

[72] M. Willander, O. Nur, J.R. Sadaf, M.I. Qadir, S. Zaman, A. Zainelabdin, N. Bano, I. Hussain, *Materials,* **2010**, 3, 2643-2667.

[73] H.G. Chen, J.L. Shi, H.R. Chen, J.N. Yan, Y.S. Li, Z.L. Hua, Y. Yang, D.S. Yan, *Opt. Mater.,* **2004**, 25, 79–84.

[74] X. Zhang, J. Qin, R. Hao, L. Wang, X. Shen, R. Yu, S. Limpanart, M. Ma, R. Liu, *J. Phys. Chem. C,* **2015**, 119, 20544−20554.

[75] X. Chen, L. Liu, P. Y. Yu, S. S. Mao, *Science*, **2011**, 331,746-750.

[76] X. Xiao, B. Han, G. Chen, L. Wang, Y. Wang, *Sci. Rep.,* **2017**, 7, 40167 (1-13).

[77] Y. Wu, L. Fan, Q. Liu, S. Chen, W. Huang, F. Chen, G. Liao, C. Zou, Z. Wu, *Sci. Rep.,* **2015**, 5, 9328 (1-8).

[78] P. R. A. Selvan, E. Subramanian, R. Murugesan, *Int. J.Res. Chem. Environ.,* **2017**, 7(4), 13-22.

[79] R. A. Selvan, Subramanian, Murugesan, *RJPBCS,* **2017**, 8 (4), 871.

[80] A. R. Prasad, A. Joseph, *RSC Adv.,* **2017**, 7, 20960.

[81] M. Ahmad, H. Sun, J. Zhu, *ACS Appl. Mater. Interfaces,* **2011**, 3, 1299–1305.

[82] J. Ungula, B.F. Dejene, H.C. Swart, *Results in Physics,* **2017**, 7, 2022–2027.

Chapter 5

Synthesis, Characterizations & Applications of Br-ZnO Nanocomposites

5 Synthesis, Characterizations & Applications of Br-ZnO Nanocomposites

In recent times, scientists have put in tremendous efforts to explore zinc oxide with fine tuning of each and every physicochemical and electronic property encouraged by its fascinating applications especially in photocatalysis[1]. Through new applications and property enhancements they have made considerable advances in this direction[2]. Here, defect chemistry gains prominence while a plethora of metal, non-metal and metalloids are being explored as dopants in ZnO. The molecular and atomic level doping found drastically altering the performances during the application of surface modified zinc oxide[3]. Doping can be carried out through various synthesis strategies by introducing solid, liquid or gaseous precursors containing desired foreign atoms[4, 5]. Economically viable mass production of desired products can be achieved through aqueous methods[6]. Among the elements of halogen family, the impact of bromine doped surface modification in zinc oxide is not well studied experimentally despite plentiful computational soundings[7].

An impurity can induce defects either on the surface or in the bulk of the host crystals and the defects due to both types have different impact on photocatalysis[8]. According to Daimei Chen et al, surface defects on ZnO are beneficial for enhanced photocatalytic activity than that on bulk defects[9]. When the size of the foreign dopant is considerably larger than the host crystal atoms, it makes excess surface defects and these surface defects are able to trap electrons and holes[10]. These trapped electrons and holes undergo interfacial transfer and surface recombination. The contention among recombination, trapping and transfer of photogenerated excitons decides the overall

photocatalytic activity. When the trapping and transfer transcend the recombinations, the result is an improved photocatalytic activity according to band bending approximation[11]. The photogenerated holes are easily trapped by surface bound hydroxyl groups (a type of defect) and transferred to adsorbants through oxidation. Similarly the photogenerated electrons are trapped by shallow defects (oxygen vacancies or interstitial defects) on the surface and then transferred to O_2 molecules to channelize the formation of reactive oxygen species. Gorichok *et al* investigated the point intrinsic and replacement defects induced by bromine in cadmium telluride single crystals apart from the shallow donor level in the bandgap created by bromine[12].

Surface doping of ZnO by bromine, a non-metal, is being demonstrated and their proficiency in photocatalysis for the water purification process is investigated. Bromine doped ZnO short nanotubes are being synthesized through sol-gel aqueous mediated route at ambient conditions. The photocatalytic performance of doped samples is analysed by examining the decomposition of methylene blue under visible light in the presence of photocatalyst. It is observed that, bromine doped samples disrupt ZnO surface predominantly by inducing defects along with shottky defects at the anion sublattices and exhibit good photocatalytic performance compared to pure ZnO.

5.1 SYNTHESIS

Four samples with compositional formula of $Zn_{1-x}Br_xO$ of 2, 4, 6 and 8 wt% bromine doped ZnO nanocomposites and pristine ZnO were prepared by aqueous mediated one–pot sol precipitation method. Precursor solution was made with different percentage of zinc acetate and potassium bromide (KBr) in 50 mL water and the details of weights taken were given in the table 5.T1. KBr were purchased from Merck. For the synthesis of pure ZnO, 50 mL of

0.015 M (0.1646 g) zinc acetate solution was prepared and kept in a water bath at 60 °C. 0.015 M beta-Aminoethylamine was injected in to the zinc acetate solution using a micropipette and the beaker was kept for 6 h of aging at the same temperature inside the water bath. The precipitate obtained after ultracentrifugation, was washed with water and dried for further analyses. For the synthesis of bromine doped ZnO, 2, 4, 6 and 8 percentages of KBr were initially mixed with 98, 96, 94 and 92 wt % of zinc acetate dihydrate. The obtained pristine and doped zinc oxides were calcined at 400 $^{\circ}$C for one hour inside a muffle furnace. The samples were coded as 2DZ, 4DZ, 6DZ and 8DZ respectively for 2, 4, 6 and 8 % of bromine doping.

Sample Name	Weight of zinc acetate (g) in 100 ml	Weight of potassium bromide (g) in 100 ml
ZnO	0.329	0
2DZ	0.323	0.0066
4DZ	0.316	0.0132
6DZ	0.309	0.0197
8DZ	0.303	0.0263

Table 5.T1. Details of the weights of precursors taken for synthesis

The strategy for synthesizing bromine doped short nanotubes of ZnO is schematically presented in Figure 5.1. As reported in our previous work, the versatile performances of beta-aminoethylamine precursor direct the formation of ZnO nanotubes with sufficient oxygen vacancies[13]. Here, we focus on bromine incorporation in ZnO which can alter the physico-chemical properties without changing the crystal structure of ZnO to increase the photocatalytic activity. The zinc and oxygen atoms have electronic configurations [Ar] $3d^{10}4s^2$ and $1s^2 2s^2 2p^4$ respectively. Zinc atoms occupy at the tetrahedral sites with sp^3 covalent bonding with the surrounding oxygen atoms in ZnO hexagonal wurtzite crystals[14]. Doping by bromine having electronic configuration [Ar] $3d^{10}4s^2 4p^5$ invariably alters the ionicity and disturbs the hybridization of ZnO.

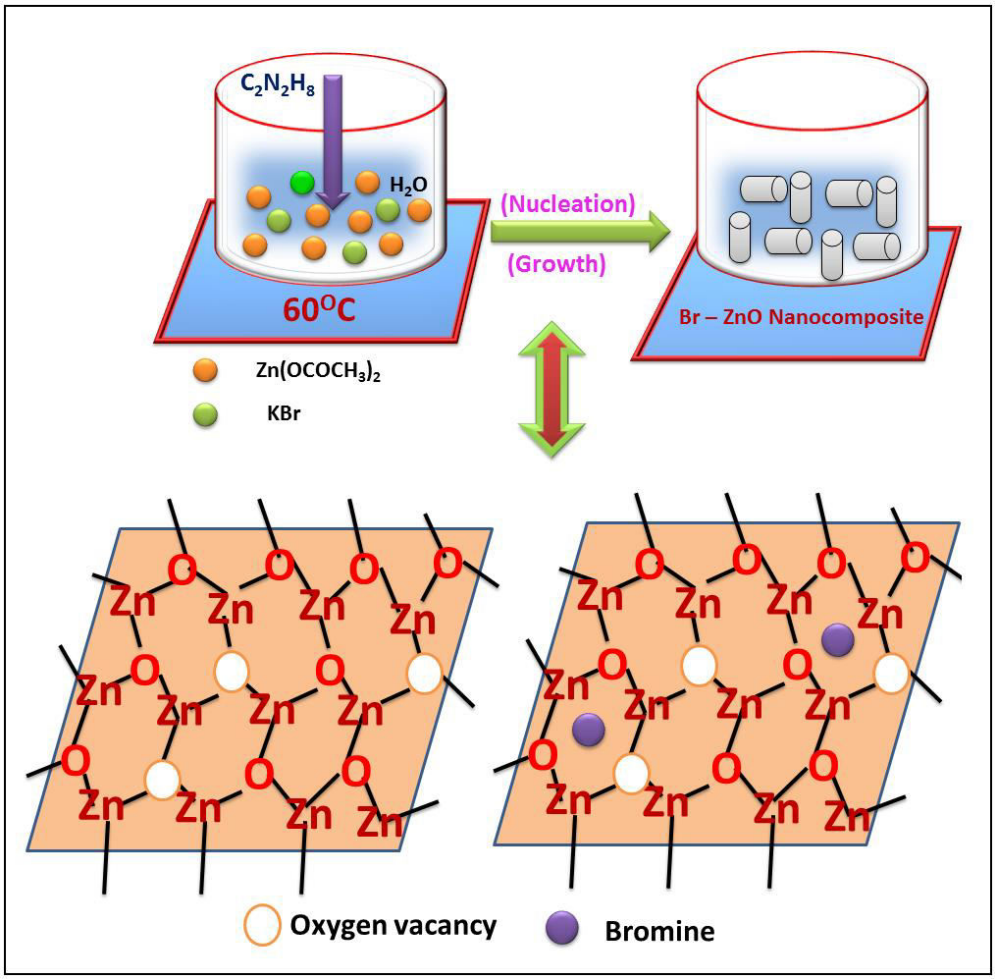

Figure 5.1 Pictorial representation of synthesis procedure

In the initial stages on the formation of bromine doped ZnO, the sufficient OH^- ions present in the solution by the hydrolysis of beta-aminoethylamine combine with the Zn^{2+} and K^+ ions to form $Zn(OH)_2$ and KOH. At the same time Br^- ions diffuse through the solution and occupy the $Zn(OH)_2$ surface resulting in an intermediate temporary complex $Zn(OH)_xBr_y^{(x+y-2)-}$[15]. The reaction temperature supports to retain the bromine ions in the ZnO surface lattice. KOH has been removed during the washing of the precipitate.

5.2 CHARACTERIZATIONS

5.2.1 Structural and Morphological analysis

5.2.1.1 X-ray Diffraction Analysis (XRD)

The crystal nature of the synthesized samples was studied by X-ray diffraction pattern as shown in Figure 5.2. The doped samples exhibit negligible shifts compared to the XRD pattern of pure ZnO and retain the hexagonal wurtzite structure with no extra peaks of bromine or trace impurities. The dopants can induce lattice defects or lattice disorder, which exhibit a positive contribution on the photocatalytic performances of the doped systems compared to pristine samples.

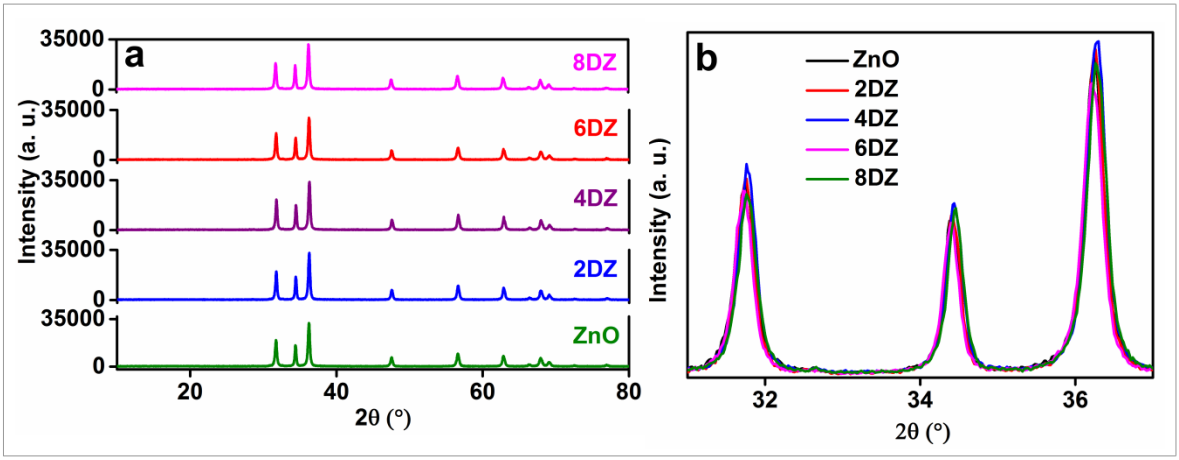

Figure 5.2 XRD pattern of ZnO, 2, 4, 6 and 8DZ (a) Enlarged XRD pattern (b)

Normally larger size of the dopants and increased dopant concentrations make considerable lattice defects enabling the doped system to act as free electron reservoirs[16]. Accumulation of these free electrons on the surfaces of ZnO enhances the photocatalytic activity due to the production of increased reactive oxygen species. Since, the ionic radius of bromine (0.193 nm) is larger than zinc (0.074 nm) and oxygen (0.140 nm), it may not replace zinc or oxygen atoms in the lattice and hence placed in interstitial sites[15]. The crystallite sizes were calculated using Scherrer equation $D = \frac{0.9\lambda}{\beta \cos\theta}$ and the details are given in Table 5.T2. Where D = crystallite size, λ = wavelength of the X-ray used (1.54), β = full width at half maximum and θ = angle of incidence. The crystallite sizes were found to be between 26.04

nm to 27.52 nm and the details are given in table 5.T2.

Sample name	Crystallite size (nm)
2DZ	27.52
4DZ	27.00
6DZ	26.04
8DZ	26.04
ZnO	26.04

Table 5.T2 Crystallite sizes of doped samples

5.2.1.2 X-ray Photoelectron Spectroscopy (XPS)

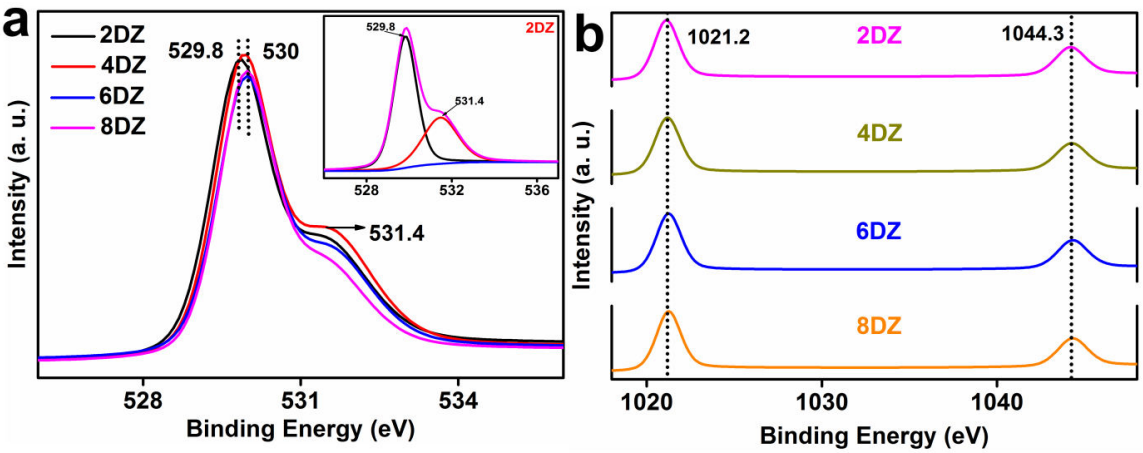

Figure 5.3 XPS spectra of (a) O 1s and (b) Zn 2p of 2DZ, 4DZ, 6DZ and 8DZ

The chemical states of the elements in the doped samples were investigated by X-ray photoelectron spectroscopy (XPS). The XPS spectra of oxygen 1s and zinc 2p are depicted in Figure 5.3a and 5.3b respectively. The peaks representing the presence of oxygen in the oxide lattices are at 529.8 eV for 2% doped sample and at 530 eV for the other doped samples[17, 18]. The deconvoluted spectrum given in the inset of figure 3a shows an additional peak at 531.4 eV, arise due to oxygen defects[19]. The Zn 2p core level doublets due to spin-orbit coupling are separated by 23 eV in ZnO samples[20]. Here

the separation value 23.1 eV in the Zn 2p (Figure 5.3b) explicitly reveal the effect of bromine interstitials. The incompletely filled p orbitals possessed by atomic bromine will disturb electron density around ZnO while retaining in the crystal[21].

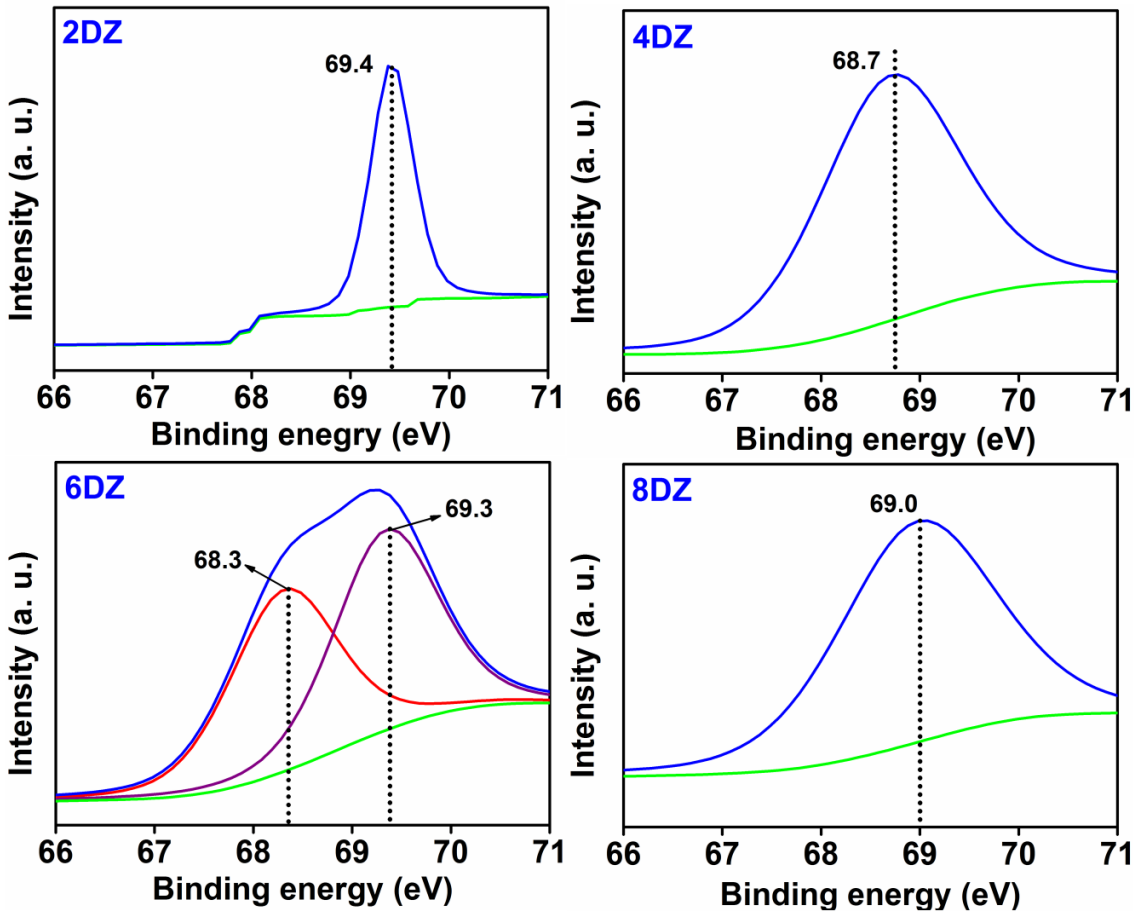

Figure 5.4 XPS spectra of Br 3d of 2DZ, 4DZ, 6DZ and 8DZ

The XPS spectra of bromine show considerable shift in the $3d_{5/2}$ peak with peak positions at 69.4, 68.7, 69.3 and 69.0 eV[22] respectively for 2DZ, 4DZ, 6DZ and 8DZ (Figure 5.4). A change in chemical environment due to different doping percentage and anion vacancy may cause this shift in peak observed. The deconvoluted spectrum of bromine in 6DZ shows an additional peak at 68.3 eV[23], which may arise from the physisorbed bromine[24], indicating the presence of surface bounded bromine in the crystals[25, 26]. The absence of potassium in the doped samples is also confirmed from XPS and the corresponding spectrum is given as Figure 5.5.

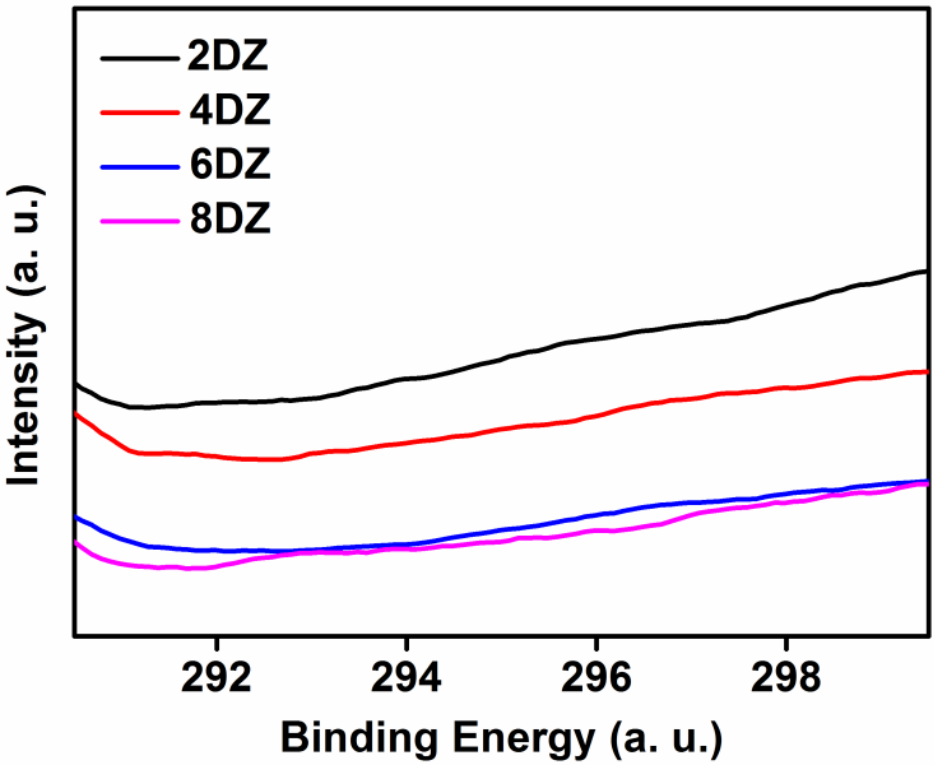

Figure 5.5 XPS spectra of K 2p of 2DZ, 4DZ, 6DZ and 8DZ

5.2.1.3 Raman spectra

For further confirmation of the oxygen vacancies, Raman spectroscopy were carried out and area of 580 cm^{-1} peak was estimated as in Figure. 5.6. Here, the entire donor doped samples exhibit oxygen vacancies in additions with the characteristic peaks of ZnO[27]. Both XPS and Raman supports that the density of oxygen defects is sufficient in 6DZ among doped samples. In addition to this Br induces other defects to satisfy the charge compensation mechanism within the crystal[28].

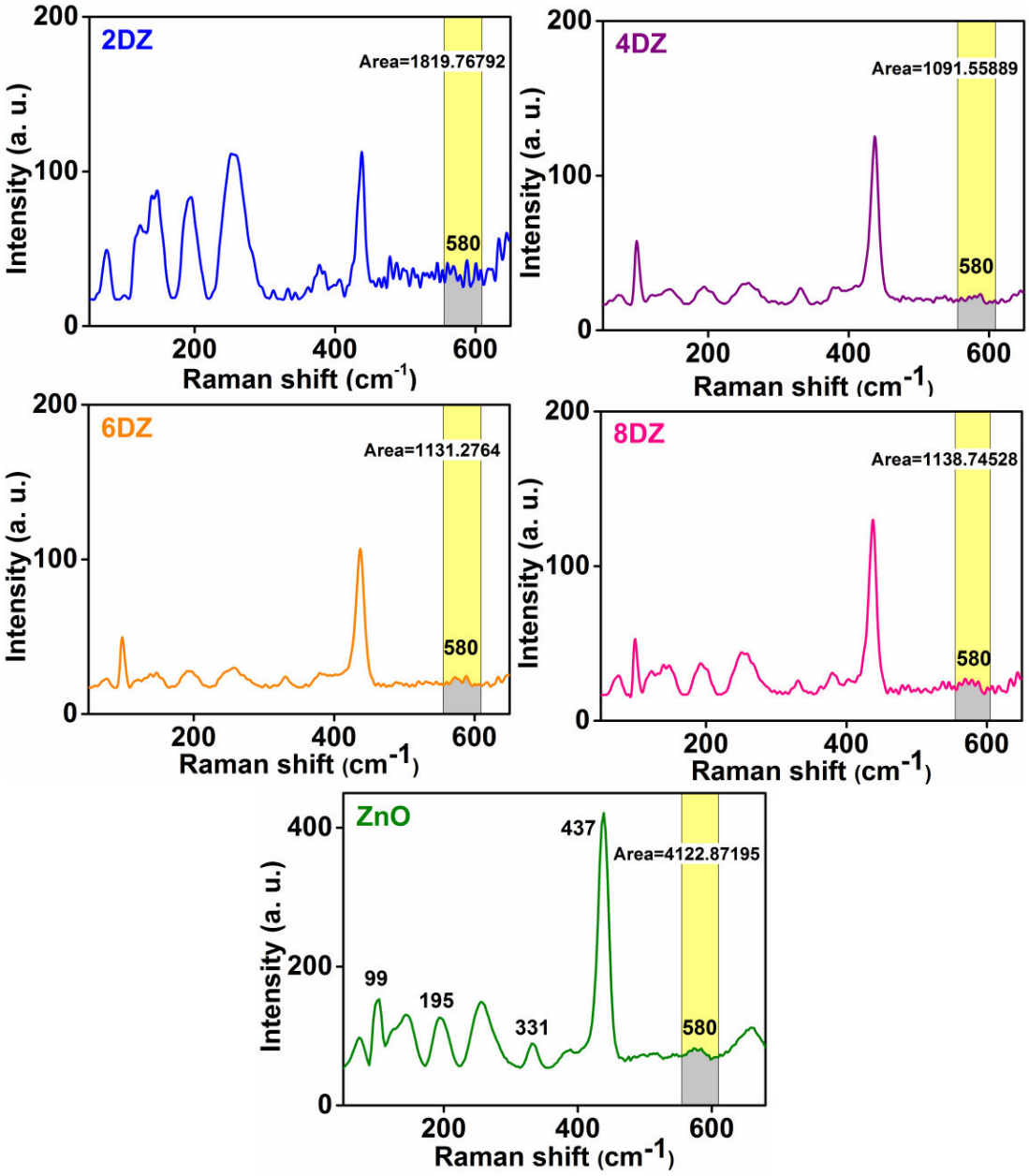

Figure 5.6 Raman spectra of 2DZ, 4DZ, 6DZ, 8DZ compared with pure ZnO

5.2.1.4 Energy Dispersive Spectra (EDS)

The EDAX analysis of the samples shows a little increase in bromine with the percentage of doping and the details are given in Table 5. T3. The low doping level estimated from the EDAX analysis, irrespective of the percentage of doping, can be attributed to the low chemical reactivity, low electronegativity and large size of bromine ions[29].

SAMPLES	ELEMENTS	Wt%	At%
2DZ	Zn	85.00	63.40
	O	11.24	34.28
	Br	3.72	2.27
4DZ	Zn	83.61	60.57
	O	12.55	37.16
	Br	3.84	2.28
6DZ	Zn	81.4	56.87
	O	14.22	40.60
	Br	4.33	2.48
8DZ	Zn	83.63	60.35
	O	12.71	37.49
	Br	3.65	2.16

Table 5.T3 EDAX data of elements in samples

5.2.1.5 Scanning electron microscopy

Morphology of the samples was obtained from SEM images and all the doped samples exhibit tubular morphology with short length as seen in Figure 5.7.

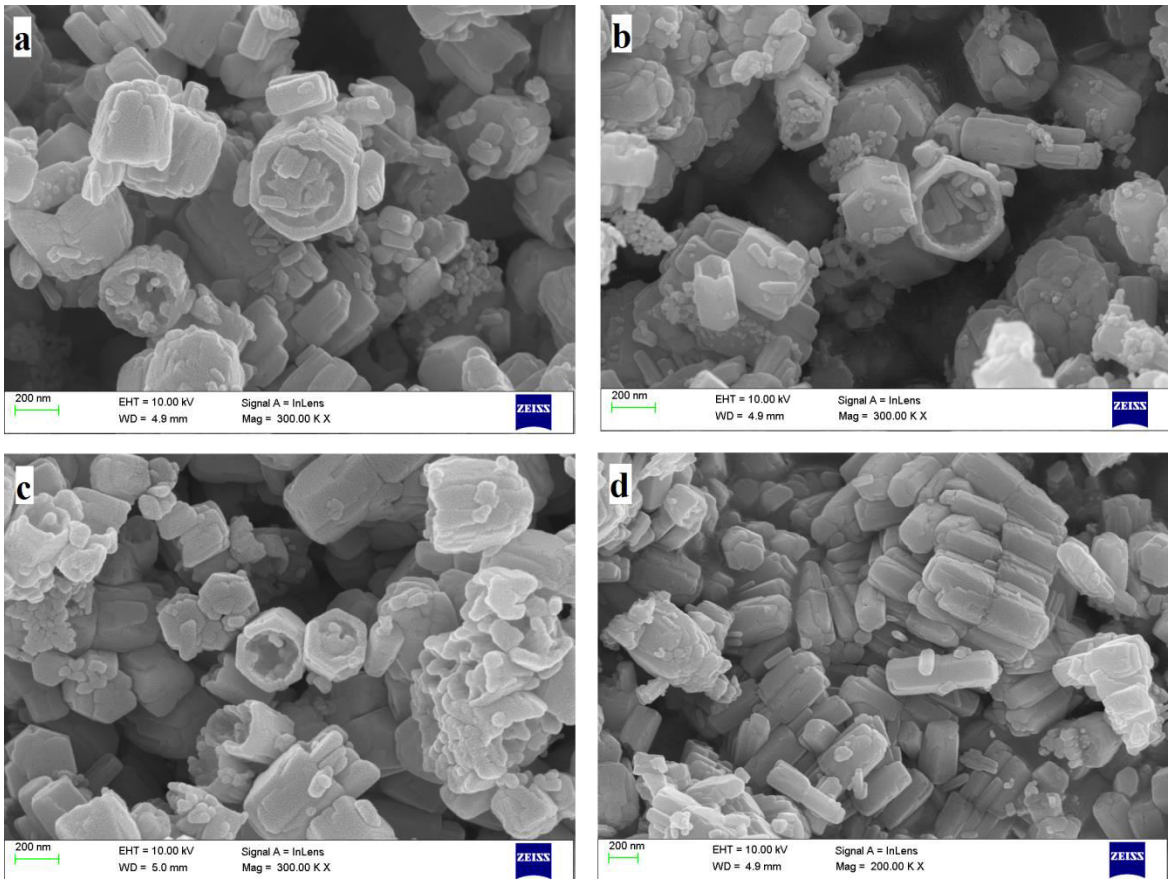

Figure 5.7 SEM images of (a) 2DZ, (b) 4DZ, (c) 6DZ and (d) 8DZ

5.2.2 Optical Properties

5.2.2.1 Diffuse Reflectance Spectroscopy (DRS) and Tauc plot

Figure 5.8 (a) depicts optical absorption spectra of the samples. All doped samples show same absorption edge with a slight shift towards lower wavelength compared to pure ZnO. This can be attributed to the doping level consistency, irrespective of percentage of doping, observed from EDAX analysis. The emission spectra are recorded by taking equal amount of the samples and are depicted in Figure 5.8b. The Tauc plots of the samples are analysed using Kubelka Munk function[30, 31] and the estimated bandgap energy is in the range of 3.18 to 3.2 eV for the doped samples. According to Burstein-Moss effect, doping can introduce defects and thus modifies the energy levels, leading to drastic change in their properties and performances[32]. In the doped systems, electrons are populated in conduction

band and push the Fermi-level towards conduction band for enabling energy gap expansion. In contrast, when doping concentration come above critical Mott value, renormalization results and bandgap narrowing occurs[33].

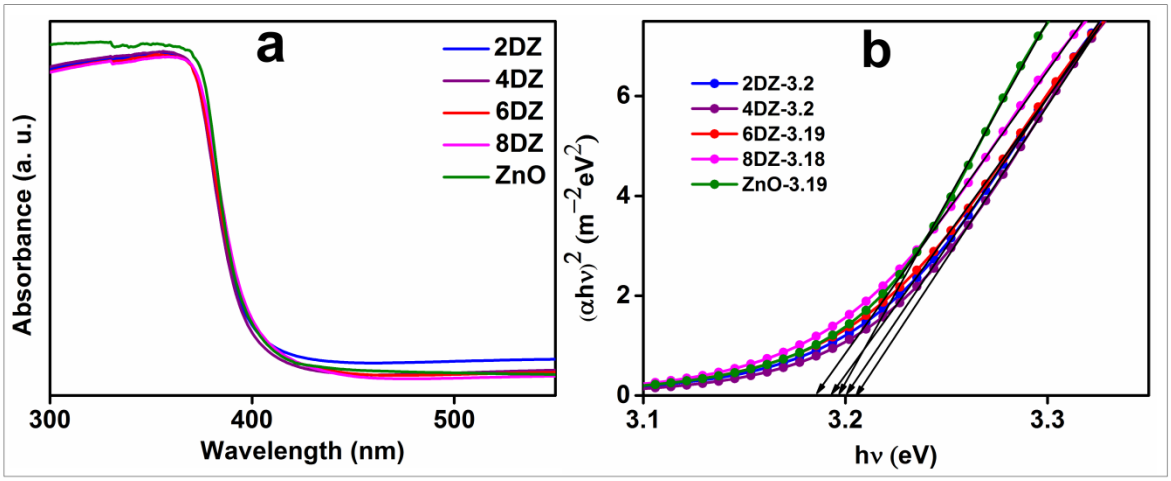

Figure 5.8 DRS spectra (a) and tauc plot (b) of doped samples compared with pure ZnO

5.2.2.2 Photoluminescence Spectroscopy (PL)

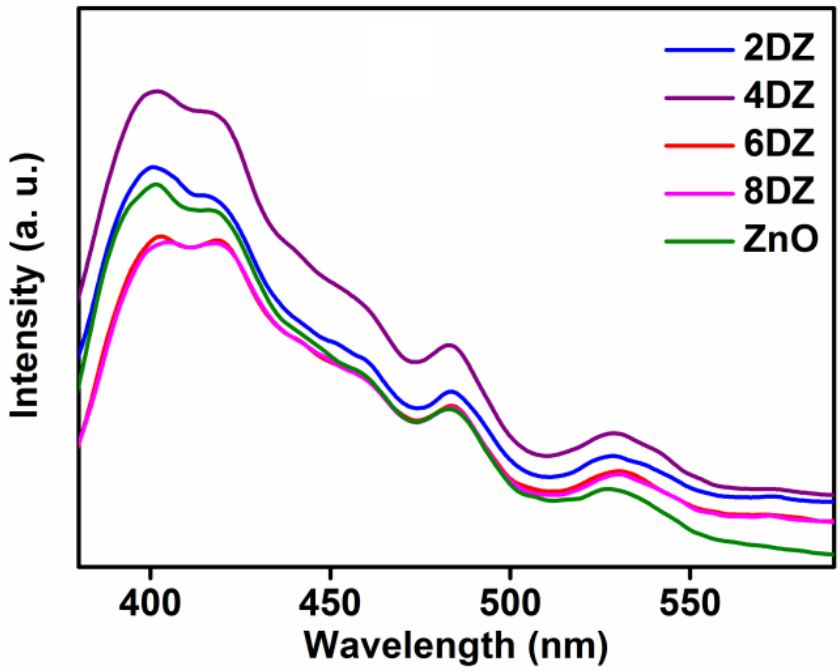

Figure 5.9 Photoluminescence spectra of pure and bromine doped ZnO

The emission spectra were analysed by taking equal weights of the samples and were

depicted in Figure 5.9. The PL emission depends predominantly on surface defects and exhibits emission intensity variations in the doped samples[34]. Relatively low band edge emission shown by 6DZ and 8DZ can be assigned to the effect of lattice strain and generation of more defects due to bromine incorporation in ZnO lattice[35]. The emission peaks at 485 and 528 nm are assigned to oxygen vacancies and crystal defects in the prepared nanosystems[13].

5.2.3 Valence band spectra and density of states

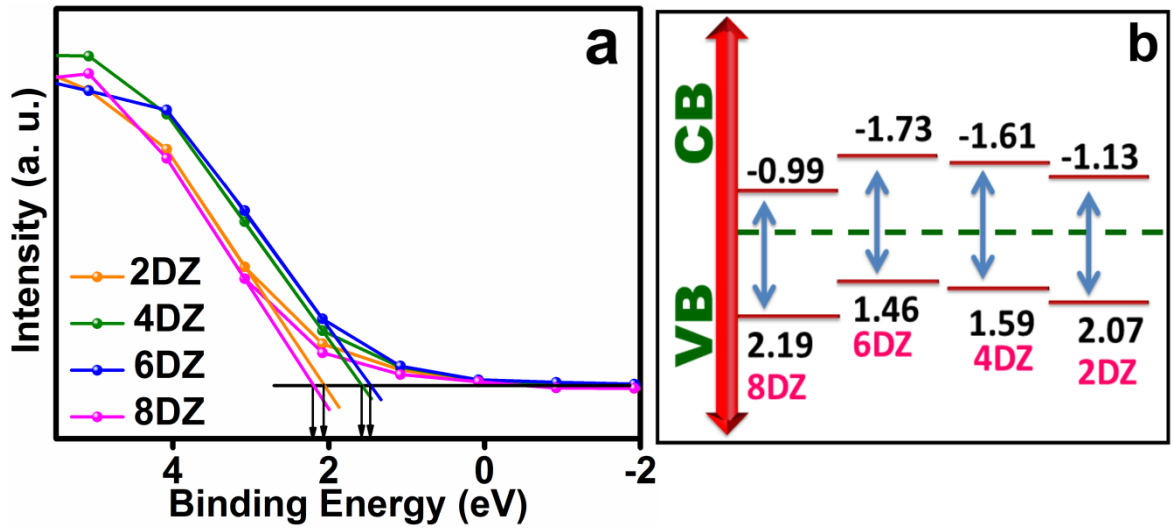

Figure 5.10 (a) Valence band XPS and (b) Band edge positions of 2DZ, 4DZ, 6DZ and 8DZ

Figure 5.10 (a and b) shows the valence band XPS and band edge positions of 2DZ, 4DZ, 6DZ and 8DZ. The main absorption onset with valence band maximum of 6DZ is found to be closer to that of 4DZ and the valence band maximum of 8DZ and 2DZ are very close to each other. The valence band maximums obtained are 2.19 eV, 1.46 eV, 1.59 eV and 2.07 eV for 8DZ, 6DZ, 4DZ and 2DZ respectively. Combined with the optical bandgap, the conduction band minimum of 8DZ, 6DZ, 4DZ and 2DZ are estimated to be at -0.99 eV, -1.73 eV, -1.61 eV and -1.13 eV respectively. There may be a chance of conduction band tail existence just like the presence of valence band tail due to the presence of defects. According to Sanjay *et al,* surface oxygen vacancy states were generated above the valence band as forbidden states,

which give rise to tailing of the valence band towards Fermi level[36].

5.3 APPLICATIONS – PHOTOCATALYSIS

5.3.1 Water treatment – Dye degradation

The photocatalytic activity of all samples was checked by monitoring the degradation of a water contaminant dye, Methylene blue[37]. The photocatalyst (0.05 g) was well dispersed in 50 mL, 20 ppm methylene blue aqueous solution. During the analysis inside a photocatalytic reactor, the degraded dye solution was collected at regular intervals of time and examined the degradation by observing the change in absorption intensity of a characteristic band at a wavelength of 664 nm. Without photocatalyst, only 35% of methylene blue was photobleached after 60 minutes of irradiation. In presence of un-doped ZnO, a complete decomposition of MB was observed within 60 minutes of exposure. The bromine doped ZnO exhibits excellent photocatalytic activity compared to undoped ZnO. The degradation results are depicted in Figure 5.11.

Methylene blue was completely decomposed after 42, 40, 38 and 42 minutes of visible light exposure in presence of photocatalysts 2DZ, 4DZ, 6DZ and 8DZ respectively. Very recently Wang *et al* reports dye degradation using Br doped titania within 50 minutes of light exposure[38]. Though 2 to 8 percentage doping was introduced into ZnO, a significant increase in doping level was not visible in our system (EDAX data Table 5.T3). This may be due to the larger size of the bromine and ease of formation of diatomic bromine in the solution. The maximum doping percentage experimentally estimated is 2.5 at% in 6DZ.

The undoped ZnO contains enormous oxygen vacancies which have been reported already[13]. In doped samples, bromine induced surface defects supplemented by this oxygen vacancies exhibit improved photocatalytic activity. The synergetic effect contributed by

oxygen vacancy and bromine induced interstitials gives an impact on higher photocatalytic activity shown by bromine doped ZnO. The experimental evidences (XPS and EDAX) supports that the magnitude of bromine induced defects is high in 6DZ sample and that may be the reason for the high photocatalytic activity shown by 6DZ among the doped samples[28].

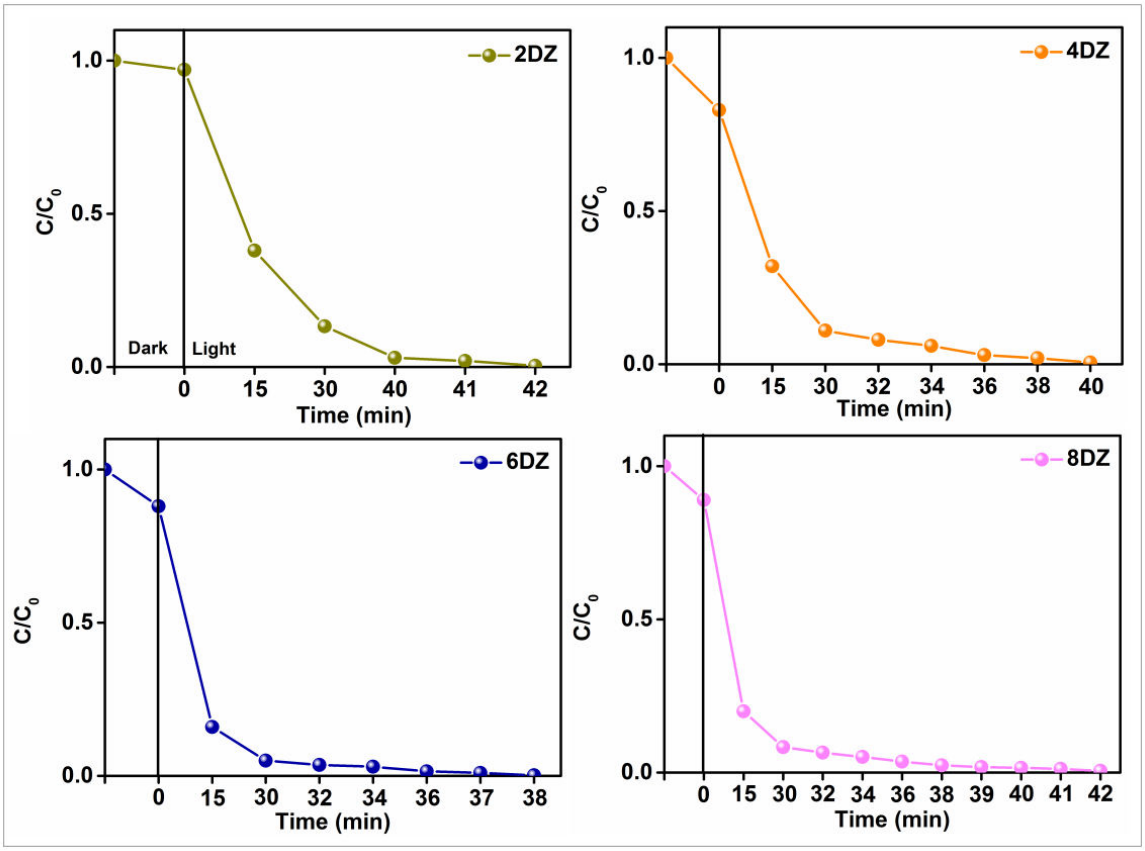

Figure 5.11 Photodegradation of MB in presence of bromine doped samples

The stability and recyclability are highly significant for commercial and industrial applications of photocatalysts. The stability study of the photocatalysts was performed by repeated use of the catalyst powder for five consecutive runs with fresh dye solution. All samples exhibit good stability as well as recyclability within the stipulated time. The stability studies are demonstrated in Figure 5.12.

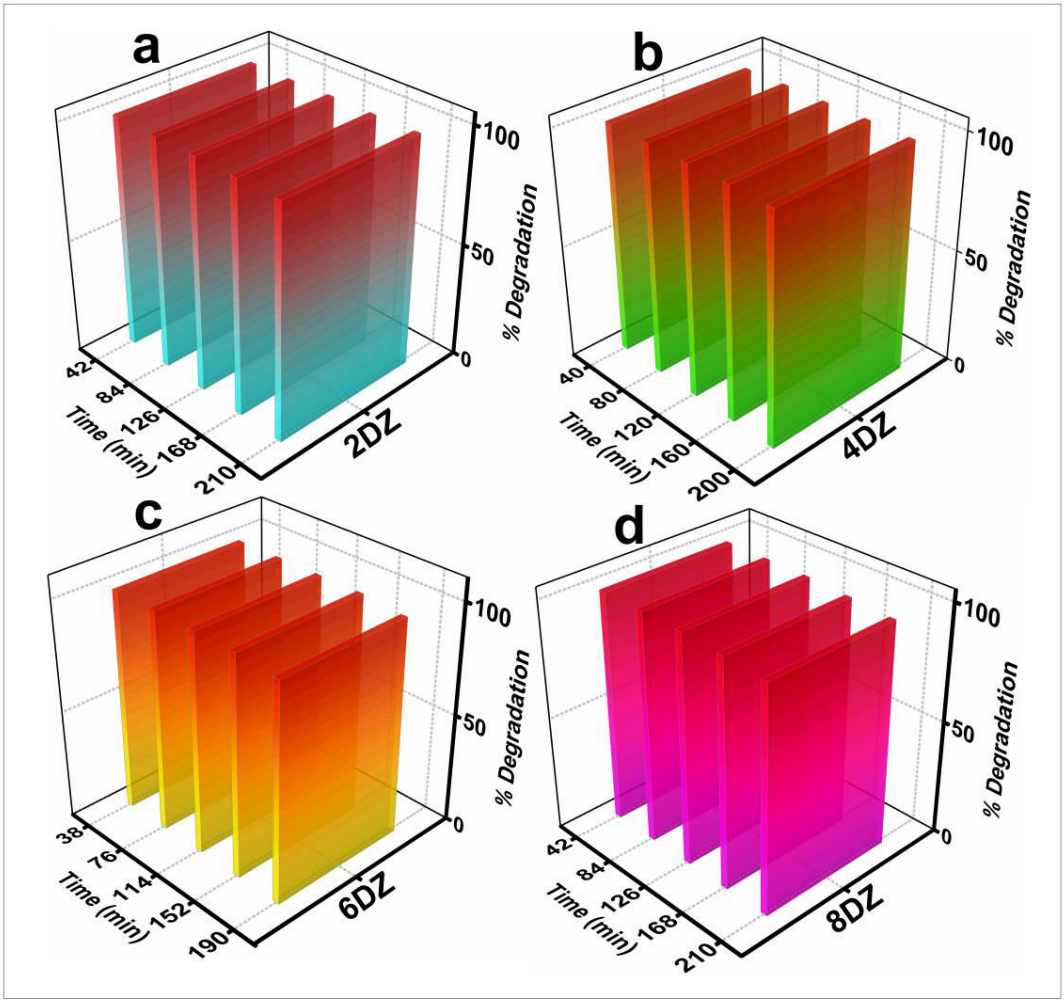

Figure 5.12 Stability of photocatalysts (a) 2DZ, (b) 4DZ, (c) 6DZ and (d) 8DZ

The mechanism involved in the photocatalytic decomposition of textile dyes in the presence of undoped ZnO is well studied[39]. When Br doped ZnO was excited with visible light, the generated photo electrons excited to conduction band and leaving behind the holes in valence band. These photo generated carriers must be separated effectively to avoid recombination for efficient photocatalysis. Both interstitial bromine and oxygen vacancies present on the surface of the samples turn as electron trapping centres and facilitate transfer of these electrons to the ZnO surface. This surface reached electrons promotes the degradation of surface adsorbed MB dye by redox catalytic reactions. Here, bromine doped ZnO possess donor and acceptor levels within the bandgap due to interstitial bromine and

anion vacancies respectively. The donor levels act as trap centers for the photogenerated electrons and thus prevent the exciton recombination. In addition to this the valence band broadening due to surface oxygen vacancy may produce photogenerated carriers via interband transitions. As a whole, the synergetic effect due to bromine interstitials and surface oxygen vacancies results in high photocarrier generation with low recombination possibilities leading to improved degradation of MB[40, 41]. MB fastly degraded in to CO_2, water and volatile organic compounds by OH free radicals at the surface of the photocatalysts.

5.3.2 Estimation of hydroxyl radicals

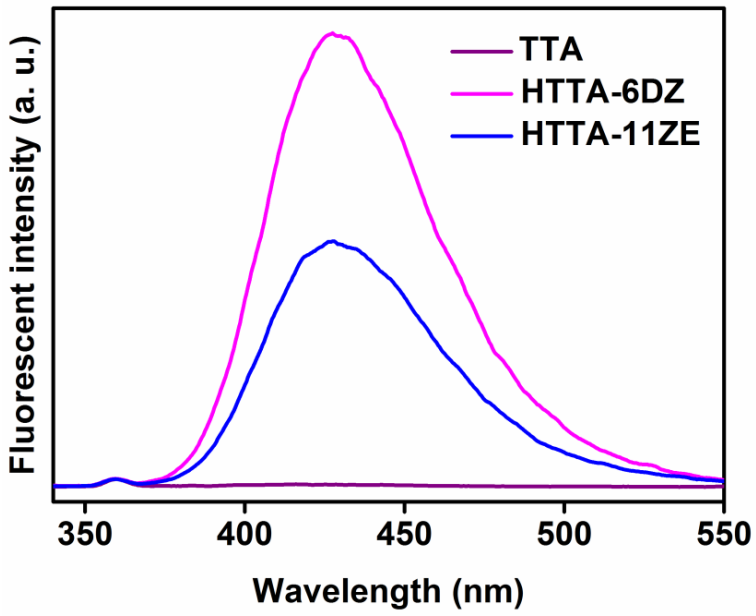

Figure 5.13 Comparison of fluorescent spectra of HTTA in presence of 6DZ and ZnO

Hydroxyl radicals released from 6DZ is monitored experimentally by using terephthalic acid as a probe molecule. The intensity of 2-hydroxy terephthalic acid (HTTA) is found to be very much higher than pure ZnO. The photoluminescence spectrum of terephthalic acid before and after light exposure is depicted in Figure 5.13.

5.3.3 Surface treatment – Contact angle measurements

The hydrophilic nature of most active photocatalyst, 6DZ, was checked by coating the material on a glass plate by doctor blading method. The contact angle measurements were performed statically. The images of the water droplet on material surface are depicted in Figure 5.14.

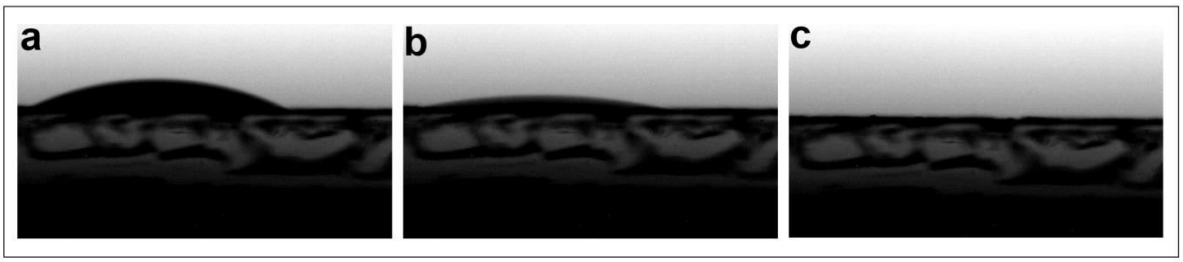

Figure 5.14 (a) Image of the water droplet on the surface of 6DZ coated glass initially, (b) Spreading of the drop on surface within 100 seconds and (c) After 120 seconds

A motor driven syringe is used to pump a liquid drop steadily on the glass surface and the maximum contact angle was measured by averaging from left and right side of the water drop with the material coated glass surface. The angle thus measured is found to be 25.5^{o}. It has been found that within 100 seconds the contact angle becomes 6.1^{o}. After 120 seconds, the angle completely turned to zero. The material exhibit super hydrophilicity compared to pure ZnO.

5.3.4 Antibacterial activity

The antimicrobial inhibition of 6DZ was evaluated against standard and multiple drug resistant gram negative bacterium of *Escherichia. Coli* by the agar well diffusion method. For the study, seed culture was swabbed on the agar dishes for 12 h using sterile cotton. Required numbers of wells were punched into the nutrient agar dishes of having diameter 8 mm. These wells were filled with water dispersed 6DZ sample. Clinical disc of Tetracycline (30

mcg/disc- positive control) is used as standard and distilled water as negative control for evaluation. In the presence of fluorescent lamp (18 W) the plates were incubated for 24 h at 37 °C in a temperature controlled incubator. The zone of inhibition observed after 24 h was measured using a zone reader.

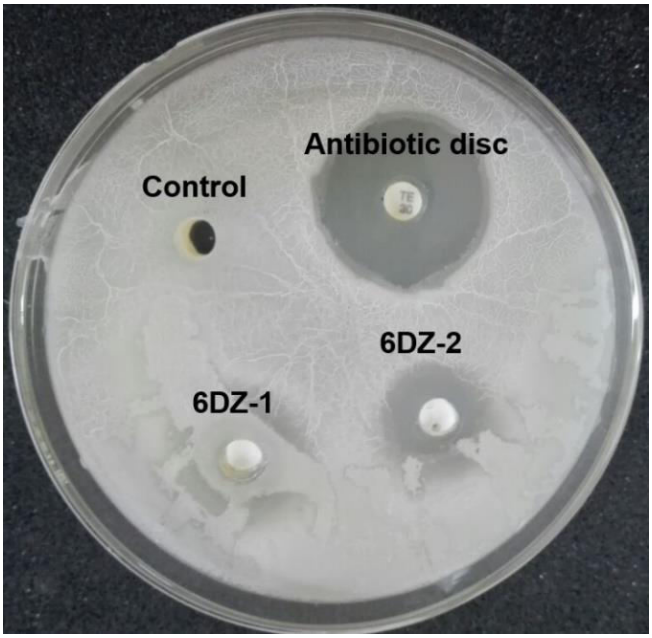

Figure 5.15 Antibacterial inhibition of 6DZ against *E. Coli*

Result shows that 6DZ inhibit the bacterial growth with zone of 24 mm diameter whereas standard tetracycline exhibit 33 mm as shown in Figure 5.15. This antibacterial function of 6DZ can be utilized for self-cleaning process in ceramic tiles. When 6DZ is incorporated during the manufacture of ceramic tiles, it self- cleans the surface with the assistance of photocatalysis.

Normally gram negative bacteria contain an outer cell wall with a thin layer of peptidoglycan. 6DZ have the ability to destroy its cell wall by charge misbalancing and penetrate to the cell completely. The ROS generation also facilitates an easy destruction of bacteria completely[42].

5.4 CONCLUSIONS

Bromine doped ZnO short nanotubes were developed systematically through aqueous mediated template-free sol precipitation synthesis route. The doping of bromine at the interstitial sites of ZnO nanocrystal surface creates additional trap states along with already existing oxygen vacancies within the ZnO lattice. These crystal defects pave the way for the migration and separation of photogenerated electrons and holes and promote photocatalysis. Bromine induced defects efficiently support the photocatalytic activity of the doped samples than undoped ZnO. Mutual performances of both these defects exhibit superior photocatalysis in 6DZ towards dye degradation analysis. Complete degradation of methylene blue happens within 38 minutes of visible light exposure. Moreover, the prepared photocatalysts exhibit good recyclability and stability under ambient conditions. The sample, 6DZ exhibits super-hydrophilicity for the anti-fogging application and potential antibacterial activity. These new findings provide good insights about the defect chemistry in solution processed Br doped nanocrystals and achieved a platform to further develop and investigate the use of Br as dopant in metal oxide systems.

5.5 REFERENCES

[1] H. Parangusan, D. Ponnamma, M. A. A. A. Maadeed, *Sci. Rep*, **2018**, 8, 754, 1-11.

[2] B. K. Barnes, K. S. Das, *Sci. Rep*, **2018**, 8, 2184, 1-10.

[3] W. Zhang, W. Wang, H. Shi, Y. Liang, J. Fu, M. Zhu, *Sol. Energy Mater Sol.* Cells, **2018**, 180, 25-33.

[4] Y-N. Xue, J-Y. Zhang, S. Tang, J-K. Liu, Y-B. Yue, X-H. Yang, *New J. Chem.,* **2018**, 42, 4308.

[5] D. kathiravan, B. R. Huang, *J. Mater. Chem. C,* **2018**, 6, 2387.

[6] X. Chen, S. Chen, T. Xia, X. Su, Q. Ma, *J. lumin*, **2017**, 188, 162-167.

[7] C. Lin, S. Li, W. Zhang, C. Shao, Z. Yang, *ACS Appl. Energy Mater*, **2018**, 1, 3, 1374-1380.

[8] C. Supatutkul, S. Pramchu, A.P. Jaroenjittichai, Y. Laosiritaworn, *Surf. Coat. Technol*, **2016**, 3.6, 364–368.

[9] D. Chen, Z. Wang, T. Ren, H. Ding, W. Yao, R. Zong, Y. Zhu, *J. Phys. Chem. C*, **2014**, 118, 15300−15307.

[10] W. Lee, J. W. Han, Y. Chen, Z. Cai, B. Yildis, *J. Am. Chem. Soc.* **2013**, 135, 7909−7925.

[11] M. H. Huang, G. Naresh, H-S, Chen, *ACS Appl. Mater. Interfaces,* **2018**, 10, 4−15.

[12] I.V. Gorichok, P.M. Fochuk, Ye.V. Verzhak, T.O. Parashchuk, D.M. Freik, O.E. Panchuk, A.E. Bolotnikov, R.B. James, *J. Cryst. Growth*, **2015**, 415, 146–151.

[13] B. N. Meethal, N. Pullanjiyot, S. Sindhu, *Mater. Des*, **2017**, 130, 426-432.

[14] B. C. Lin, P. Shen, S. Y. Chen, *J. Phys. Chem. C,* **2011**, 115, 5003–5010.

[15] Y. Zhang, C. Liu, J. Liu, J. Xiong, J. Liu, K. Zhang, Y. Liu, M. Peng, A. Yu, A. Zhang, Y. Zhang, Z. Wang, J. Zhai, Z. L. Wang, *ACS Appl. Mater. Interfaces,* **2016**, 8, 1381−1387.

[16] E. Gilardi, E. Fabbri, L. Bi, J. L. M. Rupp, T. Lippert, D. Pergolesi, E. Traversa, *J. Phys. Chem. C,* **2017**, 121, 9739−9747.

[17] J. W. Park, Y. J. tak, J. W. Na, H. Lee, W-G. Kim, H. J. Kim, *ACS Appl. Mater. Interfaces,* **2018**, 10 (19), 16613-16622.

[18] S. Ramachandran, S. Arumugam, *ACS Omega,* **2018**, 3, 4798−4809.

[19] Y-Y. Kim, J-S. Hwang, J-K. Kim, S. K. Viswanath, J. Kim, K-B. Kim, J-M. Lee, *Ceram. Int.,* **2017**, 43, S506–S510.

[20] N. Kamarulzaman, M.F. Kasim, N.F. Chayed, *Results in Physics*, **2016**, 6, 217–230.

[21] R. Hamdan, A. F. Kemper, C. Cao, H. P. Cheng, *J. Chem. Phys,* **2013**, 138, 164702.

[22] A. E. Mansour, S. Dey, A. Amassian, *ACS Appl. Mater. Interfaces,* **2015**, 7, 17692−17699.

[23] C. Ehlert, W. E. S. Unger, P. Saalfrank, *Phys. Chem. Chem. Phys.*, **2014**, 16, 14083.

[24] O. Jankovsky, P. Simek, K. Klimova, D. Sedmidubsky, S. Matejkova, M. Pumera, Z. Sofer, *Nanoscale,* **2014**, 6, 6065.

[25] Z. Fu, T. Li, X. He, J. Liu, Y. Wu, *RSC Adv.,* **2014**, 4, 26413.

[26] N. D. Hutson, B. C. Attwood, Kirk. G. Scheckel, *Environ. Sci. Technol.,* **2007**, 41, 1747-1752.

[27] C. Slouka, T. Kainz, E. Navickas, G. Walch, H. Hutter, K. Reichmann, J. Fleig, *Materials*, **2016**, 9, 945.

[28] C. Gao, H. Song, L. Hu, G. Pan, R. Qin, F. Wang, Q. Dai, L. Fan, Lina Liu, H. Liu, *J. lumin.*, **2008**, 128, 559‑564.

[29] X. Wang, G. Sun, P. Routh, D-H Kim, W. Huang, P. Chen, *Chem. Soc. Rev.,* **2014**, 43, 7067.

[30] D. Wang, N. Liu, Z. Guo, W. Wang, L. Guo, W. Yuan, X. Chen, *Phys. Chem. Chem. Phys.*, **2018**, 20, 4787.

[31] K. Huang, Z. Tang, L. Zhang, J. Yu, J. Lv, X. Liu, F. Liu, *Appl. Surf. Sci*, **2012**, 258, 3710– 3713.

[32] A. Chanda, S. Gupta, M. Vasundhara, S. R. Joshi, G. R. Mutta, Jai Singh, *RSC Adv.*, **2017**, 7, 50527.

[33] F. Wang, J-H. Seo, Z. Li, A. V. Kvit, Z. Ma, X. Wang, *ACS Appl. Mater. Interfaces* **2014**, 6, 1288−1293.

[34] Q. Dou, Y. Zhang, *Langmuir,* **2011**, 27, 13236–13241.

[35] A. K. Munirathnappa, V. C. Petwal, J. Dwivedi, N. G. Sundaram, *New J. Chem.*, **2018**, 42, 2726.

[36] S. G. Ullatil, P. Periyat, B. Naufal, M. A. Lazar, *Ind. Eng. Chem. Res*. **2016**, 55(22), 6413-6421.

[37] K. Iqbal, A. Iqbal, A. M. Kirillov, C. Shan, W. Liu, Y. Tang, *J. Mater. Chem. A*, **2018**, 6, 4515.

[38] Q. Wang, S. Zhu, Y. Liang, Z. Cui, X. Yang, C. Liang, A. Inoue, *Mater. Res. Bull.*, **2017**, 86, 248-256.

[39] J-j. Ban, G-c. Xu, L. Zhang, H. Lin, Z-p. Sun, Y. Lv, D-z. Jia, *J. Solid State Chem.,* **2017,** 256, 151–157.

[40] A. M. Al-Hamdi, M. Sillanpaa, J. Dutta, *J. Alloys Compd.* **2015**, 618, 366-371.

[41] R. Marschall, L. Wang, *Catal. Today*, **2014**, 225, 111-135.

[42] T. Tian, X. Shi, L. Cheng, Y. Luo, Z. Dong, H. Gong, L. Xu, Z. Zhong, R. Peng, Z. Liu, *ACS Appl. Mater. Interfaces,* **2014,** 6, 8542−8548.

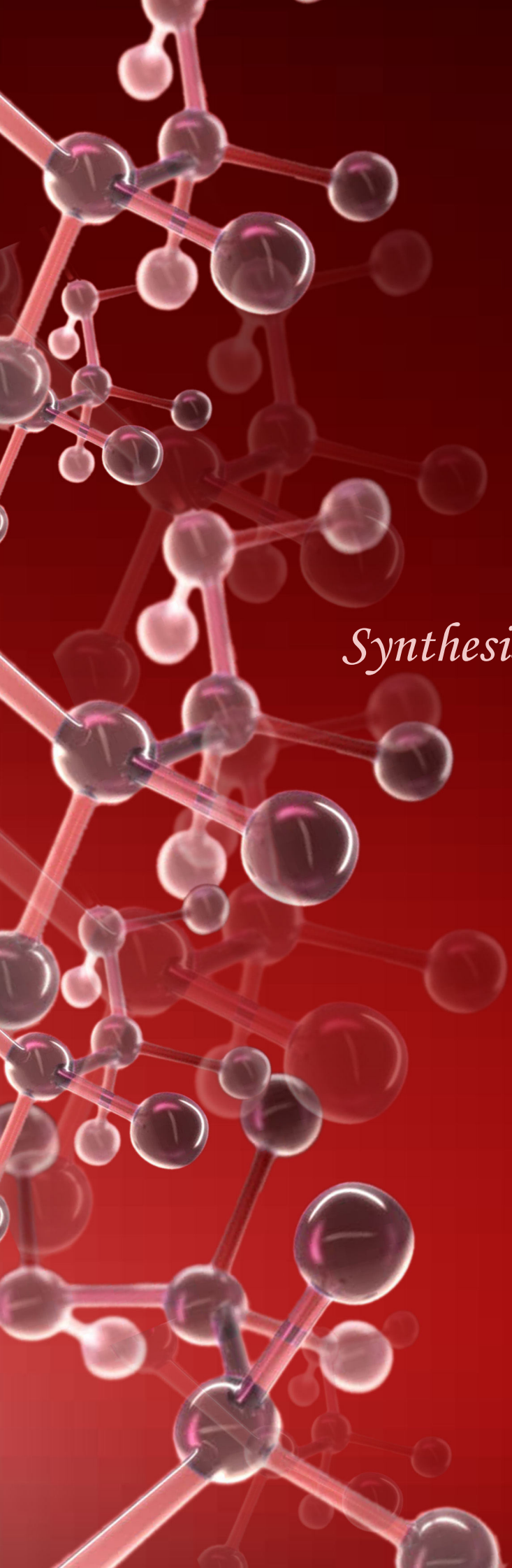

Chapter 6

Synthesis, Characterizations & Applications of Zinc Tellurium Oxide

6 Synthesis, Characterizations and Applications of Zinc Tellurium Oxide

Shift to renewable energy is crucial to life on the planet due to dwindling of fossil fuels and the looming threat of climate change. The efforts of scientific community to address the challenge by harnessing solar energy utilizing semiconductor nanomaterials become all the more important at this critical juncture[1]. Consequently researchers devote much of their energies on developing photocatalysts to address the manifold environmental concerns. A number of reports focus on ternary and quarternary nanomaterials with various combinations of metals/ non-metals/ semiconductor oxides/ RGO to expedite photocatalysis[2, 3]. Here the surface and interface interaction properties of these materials greatly influence the photocatalytic efficiency. Reports show that, RGO based photocatalyst performs better, but the presence of conspicuously higher levels of carbonaceous material turns in to an inevitable health hazard. Low toxicity, abundance of material, low cost and high environmental compatibility tempt researchers to explore the possibilities of varying combinations of oxides[4] and non-oxides[5] of zinc in ternary and quarternary form for various applications such as DSSC[6], optoelectronics[7], sensors[8] and photocatalysis[9]. The USA based Materials Genome Initiative spotlighted two elements, Tellurium and Platinum, for functional devices in 2011[10]. High conductivity is one of the attractive features of tellurium for thermoelectric materials[11]. In the case of $Zn_2Te_3O_8$ (ZTO), the glassy behaviour obtaining with temperature tuning is highly explored for its unique properties such as broad transmission and highly nonlinear optical properties[12]. The crystalline ZTO is not much explored for photocatalysis to the best of our knowledge.

Contemporary enquiries bring crystalline defects to the fore as these defects might

play a critical role in photocatalysis[13, 14]. According to Daimei Chen *et al*, surface defects can serve as active sites, which are favorable to the photocatalytic activity, while bulk defect is often regarded as the recombination sites, which adversely affect the photocatalytic activity[15]. Current study emphasizes the synthesis of crystalline ZTO nanomaterial with wide range of absorption and surface oxygen vacancies make it imperative to analyse the photocatalytic activity. A simple, well controlled, cost effective synthesis of crystalline black ZTO photocatalyst have not been observed hitherto. The critical antibacterial activity of ZTO towards *Escherichia coli* and also super hydrophilicity exhibited by the material are also being demonstrated here.

6.1 SYNTHESIS

Zinc tellurium oxide (ZTO) nanomaterial was synthesized by adopting solvothermal method. Minimum precursors were used for the synthesis and the details are as shown below. All the chemicals used were collected from Merck and Sigma and are used as received without further purification.

Materials used for synthesis

- ✓ Zinc acetate dihydrate
- ✓ Tellurium powder
- ✓ Ethylene diamine

Procedure for synthesis

For the synthesis of shining black ZTO photocatalyst, minimum precursors were used. 0.3M (0.1317 g) zinc acetate and 0.3M (0.0766 g) tellurium powder were taken into 20 mL edamine solvent in an autoclave. According to Yue Zhao *et al*, hydrothermal synthesis is a

better method for the synthesis of highly crystalline chemically stoichiometric materials in mild condition[16]. He also suggested that the solubility problem in synthesis can be effectively addressed by adopting this method. Solvothermal condition was chosen to dissolve the tellurium powder as solubility is the predominant hurdle during the synthesis of tellurium compounds. Recently David H. Webber *et al* reported that, 0.5 wt % tellurium would dissolve in ethylene diamine and glycerol mixture at 180 to 200 °C[17]. Therefore ZTO synthesis was carried out in edamine at 200 °C for six hours. A flowchart showing the synthesis procedure of ZTO nanomaterial is shown in Fig 6.1. The sheen is visible in the digital photographs of ZTO in Figure 6.1. After six hours, the obtained uniformly precipitated shining black material was washed with methanol and finally dried in room temperature for further usage. There was no white precipitate of pure ZnO or TeO_2 observed.

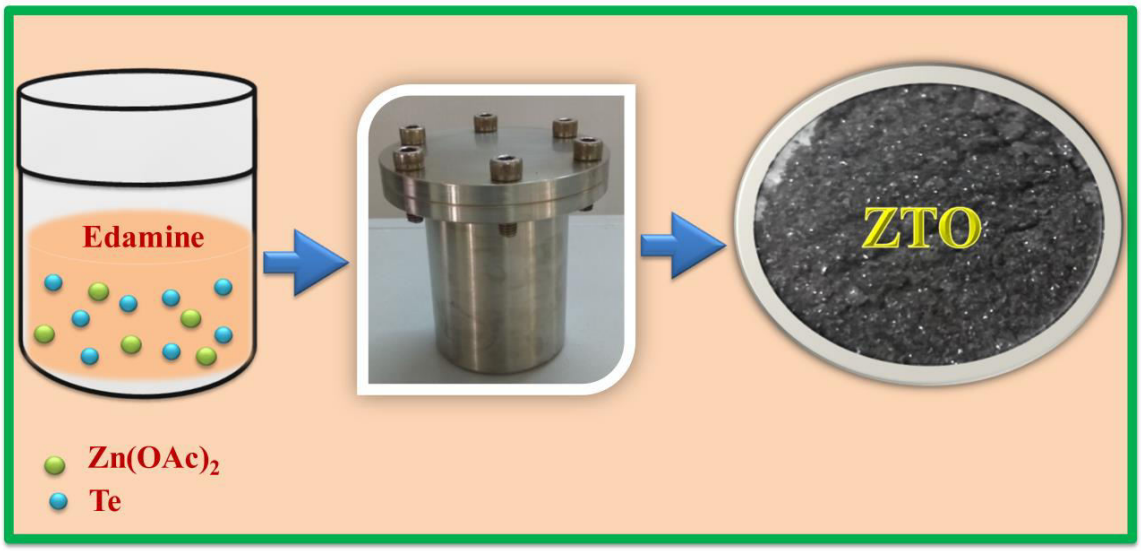

Figure 6.1 Flow chart of the synthesis of ZTO

The zinc precursor, $Zn(O_2CCH_3)_2$ when react with edamine results in the formation of zinc oxides as per the reported mechanism[18, 19]. Similarly when tellurium reacts with edamine will forms tellurium single crystals[10]. In most of the synthesis, capping agent addition was done separately for the size reduction of materials. Here comes the exceptional

advantage of edamine because of its versatile performances as a solvent for solubilizing the precursor material and a perfect medium for the growth of ZTO. Edamine also acts as an effective capping agent to reduce the size of ZTO into nano size regime[20]. In this work, zinc acetate dissolves in edamine immediately and forms a complex $Zn_5(OH)_8(CH_3COO)_2.xH_2O$[18]. Gradual heating in the presence of excess alkali leads to condensation of hydroxyl groups and decomposition of acetate groups make avail zinc for further reaction. When tellurium got sufficient temperature for dissolution, combines with zinc and oxygen to form ZTO nanomaterials.

6.2 CHARACTERIZATIONS

The synthesized sample was subjected to various characterizations to confirm its formation, purity, morphology and properties. The techniques adopted are listed below.

Structural analysis

- ✓ *X-ray diffraction analysis (XRD)*
- ✓ *Raman spectroscopy*
- ✓ *X-ray photoelectron spectroscopy (XPS)*
- ✓ *Energy dispersive spectrum (EDS)*

Morphological analysis

- ✓ *Scanning electron microscopy (SEM)*

Optical measurements

- ✓ *Diffuse reflectance spectrum (DRS)*
- ✓ *Tauc plot*

6.2.1 Structural and morphological analyses

6.2.1.1 X-ray diffraction analysis (XRD)

The formation of ZTO is confirmed from XRD pattern (Figure 6.2) and the formed material unambiguously matches with that of $Zn_2Te_3O_8$ with JCPDS card No. 72-1283. The presence of sharp peaks reflects the crystalline nature of ZTO with no detectable peaks for the presence of secondary crystalline phases such as ZnO and TeO_2. The JCPDS files for ZnO and TeO_2 are compared with that of ZTO as detailed in Figure 6.3. The peaks marked with asterisks (at 15.5°, 16.3°, 21.7° and 25.5°) are from the diamine precursor (Figure 6.4). Multiple washing eliminates the peaks due to diamine at 15.5° and 16.3° and diminish peaks at 21.7° and 25.5°, indicating removal of physisorbed solvent moieties from the samples. XRD pattern in figure 6.5 shows characteristic peaks of ZTO with much dimished diamine peak after multiple washing with methanol. The crystallite size of ZTO obtained from Sherrer's formula is found to be 47.97 nm.

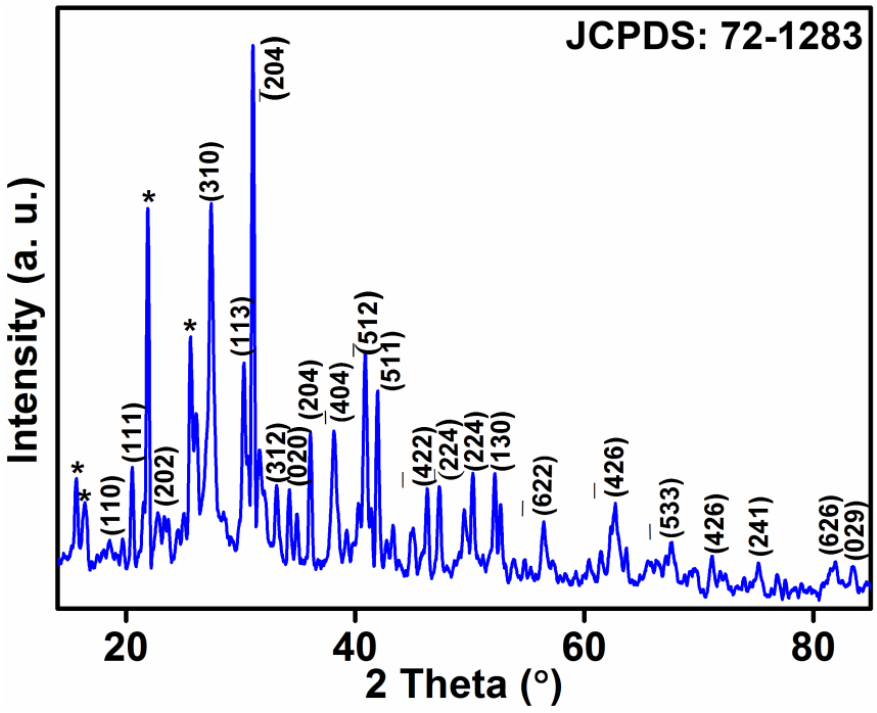

Figure 6.2 XRD pattern of ZTO

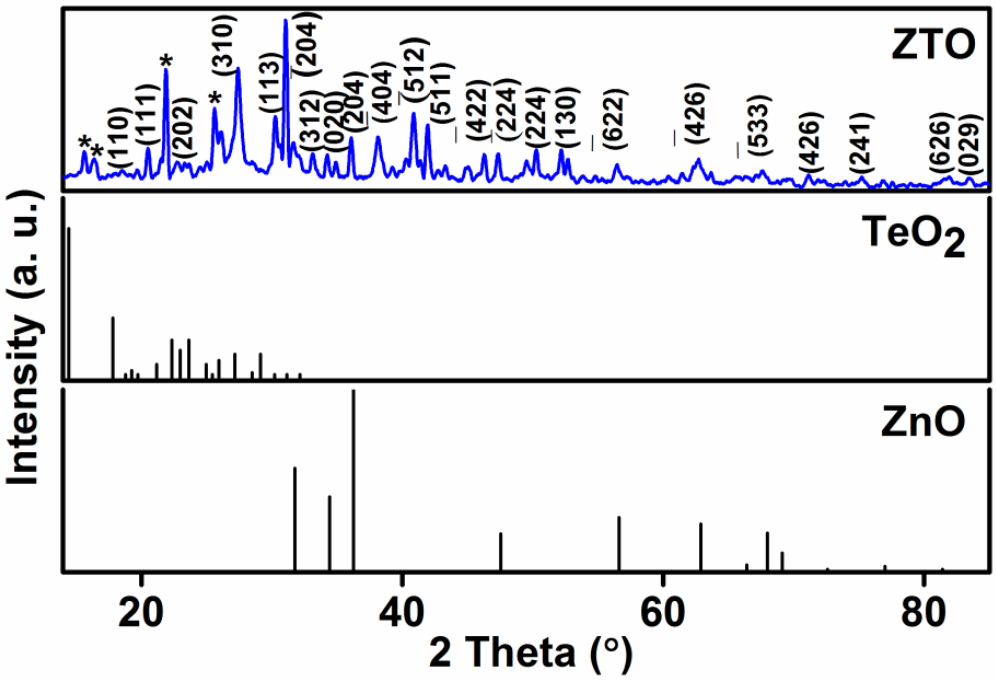

Figure 6.3 XRD of ZTO compared with TeO_2 and ZnO

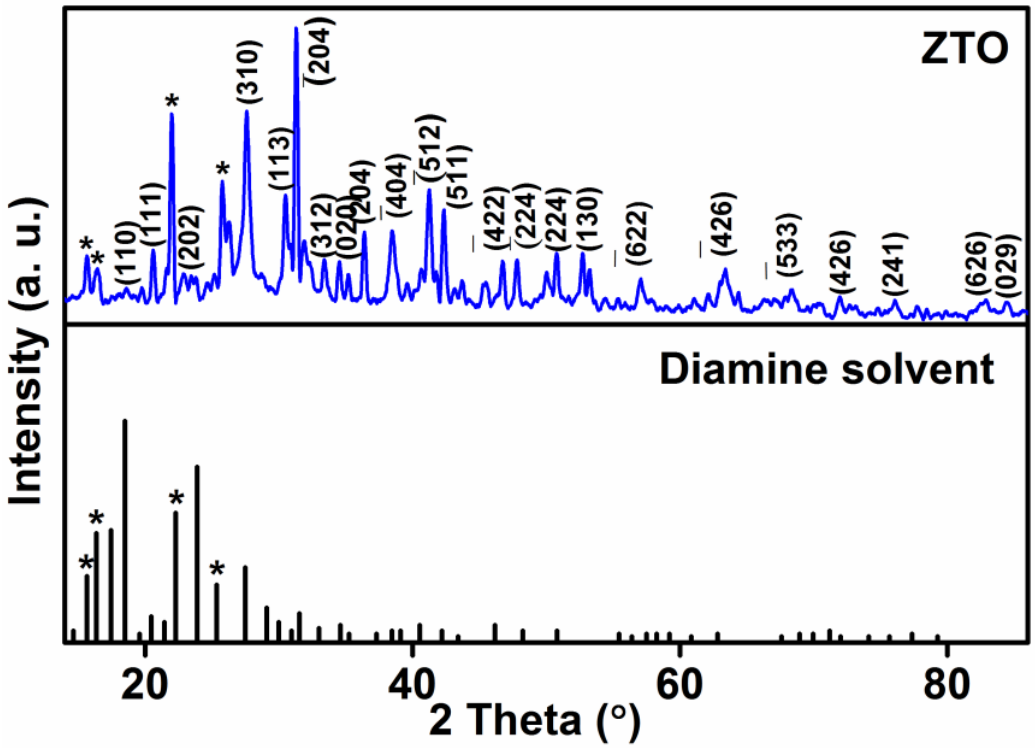

Figure 6.4 XRD of ZTO compared with diamine precursor

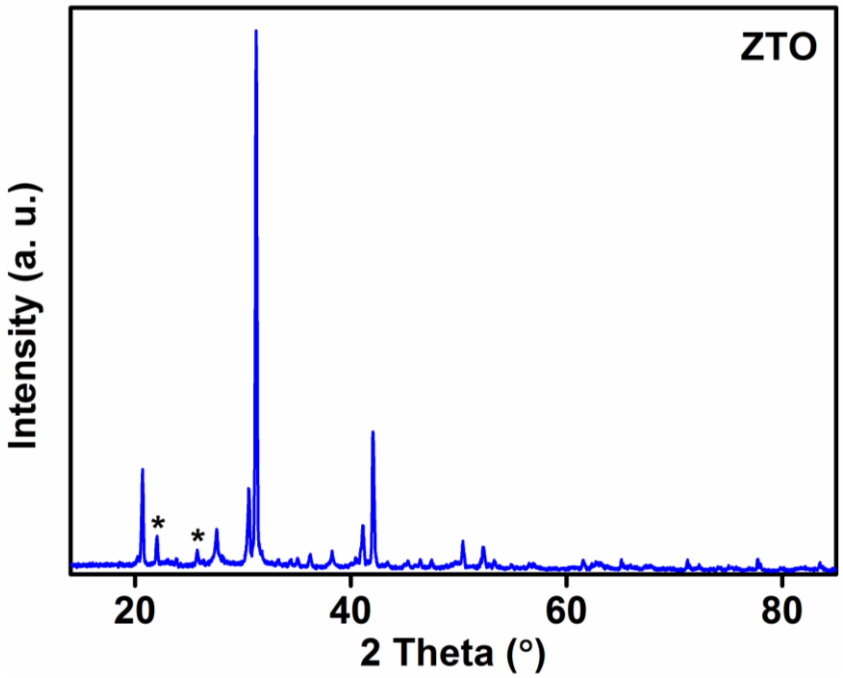

Figure 6.5 XRD of ZTO after repeated washing

A 3D image of crystal structure is constructed using Materials studio 7.0® software from the XRD data using Reflex powder diffraction analysis as shown in Figure 6.6. The details of crystal parameters also are given below. $(Te_3O_8)^{4-}$ anions in ZTO are formed through interconnection of TeO_3 and TeO_4 groups by two Te-O-Te bridges[21]. The comparison of XRD pattern of ZTO with JCPDS file is as shown in Figure 6.7.

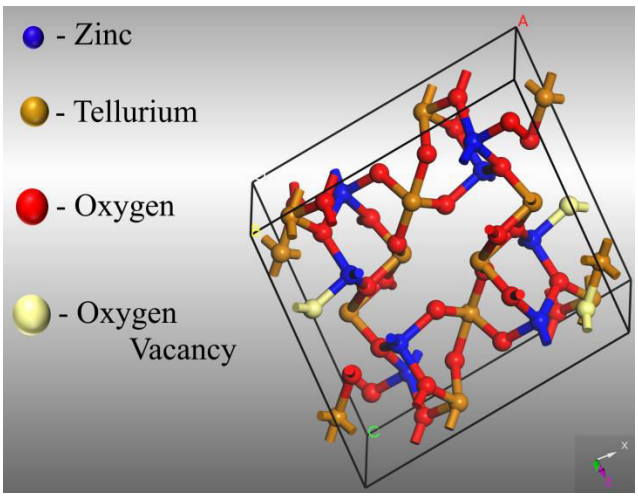

Figure 6.6 3D image of ZTO crystal lattice created by Materials studio software

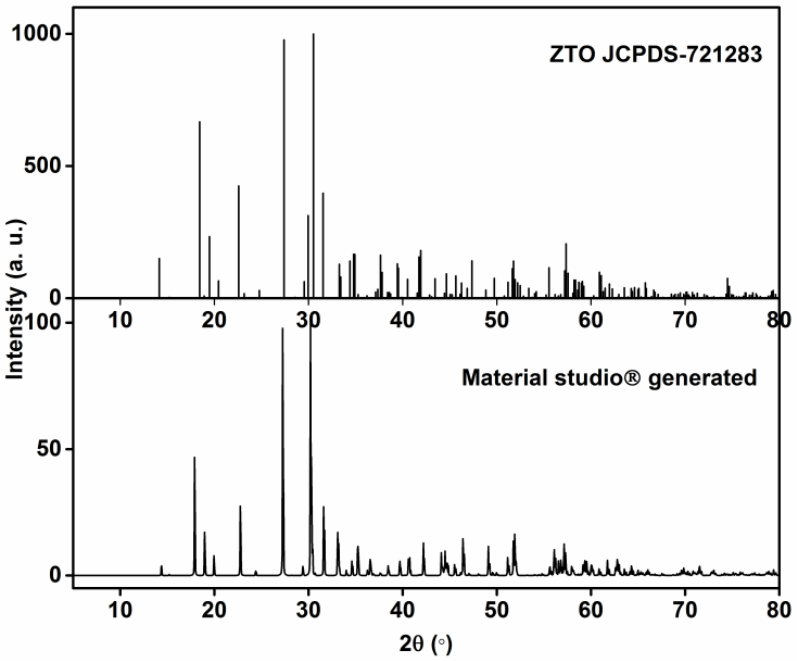

Figure 6.7 Comparison of XRD pattern of ZTO JCPDS with simulated pattern

6.2.1.2 Raman spectroscopy

Figure 6.8 shows the characteristic Raman spectrum of ZTO material. Raman peaks further confirmed the formation of ZTO with sufficient surface oxygen vacancies. Peaks at 78 cm^{-1}, 133 cm^{-1} and 792 cm^{-1} represent characteristics of the Te-O vibrations[23]. Peaks at 447 cm^{-1} and 648 cm^{-1} depict stretching and bending vibrations of Te-O-Te linkage and asymmetric vibrations of Te-O-Te respectively. The peak at 196 cm^{-1} assigns the presence of acoustic phonon overtones[24]. Peaks at 256 cm^{-1} and 380 cm^{-1} stand for laser plasma lines and A1 symmetry polar phonons of Zn-O bonds respectively[25]. Peak at 490 cm^{-1} indicates surface phonons[26] and the one at 726 cm^{-1} indicates stretching vibrations between Te and non-bridging oxygen atoms. Peak at 578 cm^{-1} represents surface oxygen vacancies of the lattice[27]. The broadness of the Raman peaks is also an indication of crystal defects[28].

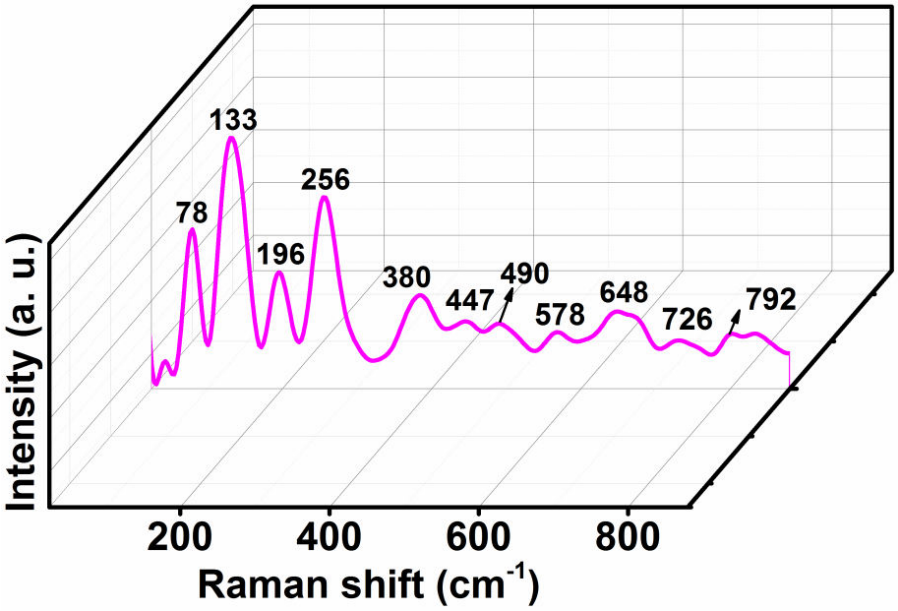

Figure 6.8 Raman spectra of ZTO

6.2.1.3 X-ray photoelectron spectroscopy (XPS)

X-ray Photoelectron Spectroscopy (XPS) has been used to study the chemical composition to confirm the crystal structure and the surface defects in ZTO (Figure 6.9(a-c)). The oxidation states and relative percentage of the element in ZTO are determined from XPS and the spectrum depicts the presence of only Zn, Te and oxygen.

Oxidation states of elements	Atomic concentration (%)	Mass concentration (%)
O^{2-}	69.67	26.05
Te^{4+}	18.97	56.59
Zn^{2+}	11.36	17.36

Table 6.T1 XPS quantification data by area

The deconvoluted spectrum of O 1s shows three peaks at 530.1 eV, 531.3 eV and 532.3 eV confirming the presence of O^{2-} in the lattice, oxygen vacancies and adsorbed oxygen respectively[27]. Zinc 2p spectrum shows dominant peaks of Zn $2p_{3/2}$ at 1021.3 eV and Zn $2p_{1/2}$ at 1044.3 eV indicating the presence of Zn^{2+} in tetrahedral site[29, 30]. In the case of tellurium, two main peaks and two satellite peaks are observed. The main peaks at 575.9 eV

and 586.2 eV originate from Te-O bonds[31, 32]. Two satellite peaks at 572.5 eV and 583 eV depict $3d_{5/2}$ and $3d_{3/2}$ states of Te respectively[31].

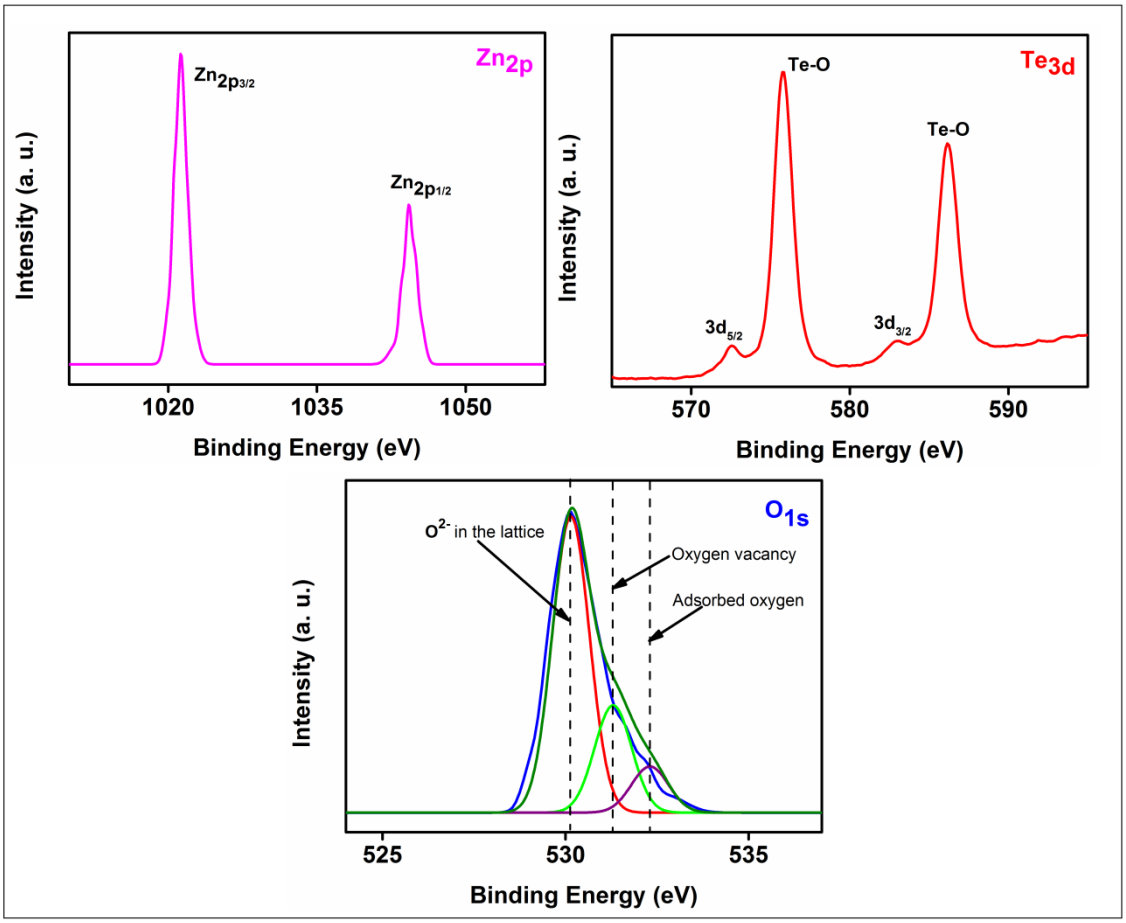

Figure 6.9 XPS spectra of Zn 2p, Te 3d and O 1s

The deconvoluted spectrum of O 1s shows three peaks at 530.1 eV, 531.3 eV and 532.3 eV confirming the presence of O^{2-} in the lattice, oxygen vacancies and adsorbed oxygen respectively[27]. Zinc 2p spectrum shows dominant peaks of Zn $2p_{3/2}$ at 1021.3 eV and Zn $2p_{1/2}$ at 1044.3 eV indicating the presence of Zn^{2+} in tetrahedral site[29, 30]. In the case of tellurium, two main peaks and two satellite peaks are observed. The main peaks at 575.9 eV and 586.2 eV originate from Te-O bonds[31, 32]. Two satellite peaks at 572.5 eV and 583 eV depict $3d_{5/2}$ and $3d_{3/2}$ states of Te respectively[31].

6.2.1.4 Energy dispersive spectrum (EDS)

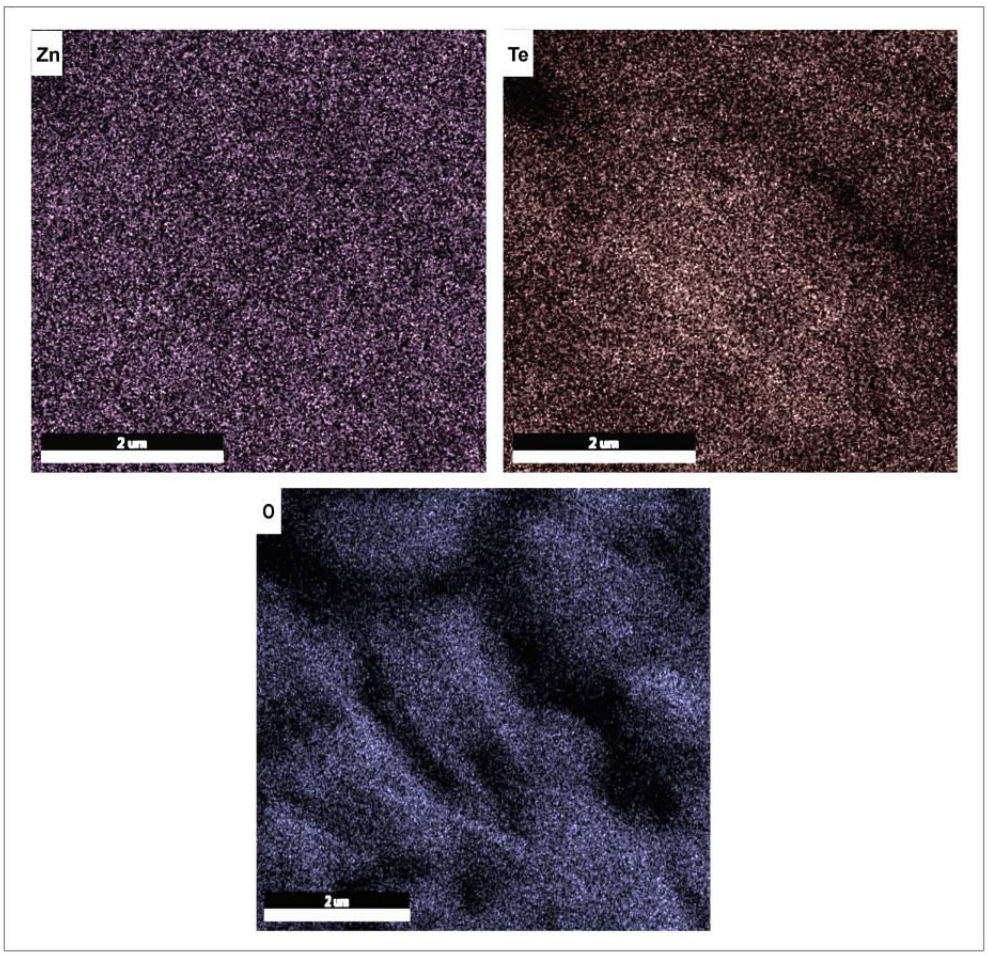

Figure 6.10 Elemental mapping of Zn, Te and Oxygen in ZTO

The elemental mapping (Figure 6.10) was obtained from energy dispersive spectrometer (EDS). The elemental distribution shows that the material contains Zn, Te and Oxygen in stoichiometric proportions and no other trace impurities were observed. In oxygen mapping image, the presence of black area (absence of blue colour) may be due to the presence of oxygen vacancies in the crystal lattice.

6.2.1.5 Scanning electron microscopy (SEM)

Figure 6.11 shows Field-emission scanning electron microscopy (FESEM) image of ZTO

which exhibits a regular and uniform structure. The average size of nanoparticles from the SEM image is about to 30 nm in size.

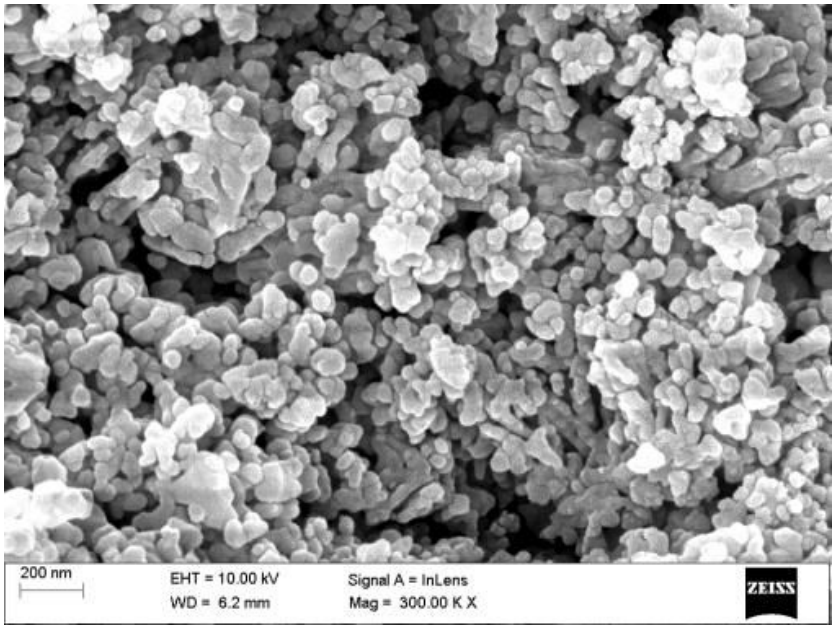

Figure 6.11 FESEM image of ZTO

6.2.2 Optical measurements

6.2.2.1 Diffuse reflectance spectroscopy (DRS)

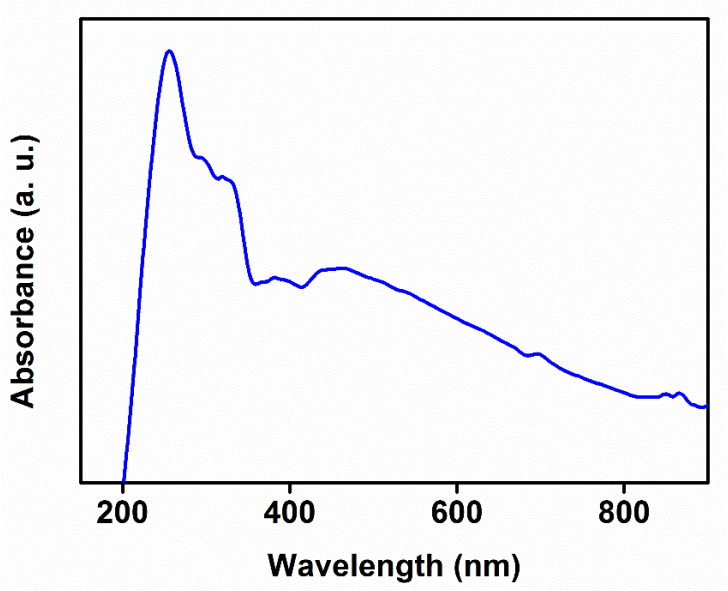

Figure 6.12 DRS spectrum of ZTO

The UV-Vis diffuse reflectance spectrum (Figure 6.12) exhibits almost near infrared absorption which is crucial for the efficiency of a photocatalyst.

6.2.2.2 Tauc plot

From Tauc plot (Figure 6.13) the band gap obtained is 1.86 eV. The wider absorption and the suitable band gap may translate into improved photocatalytic activity[33].

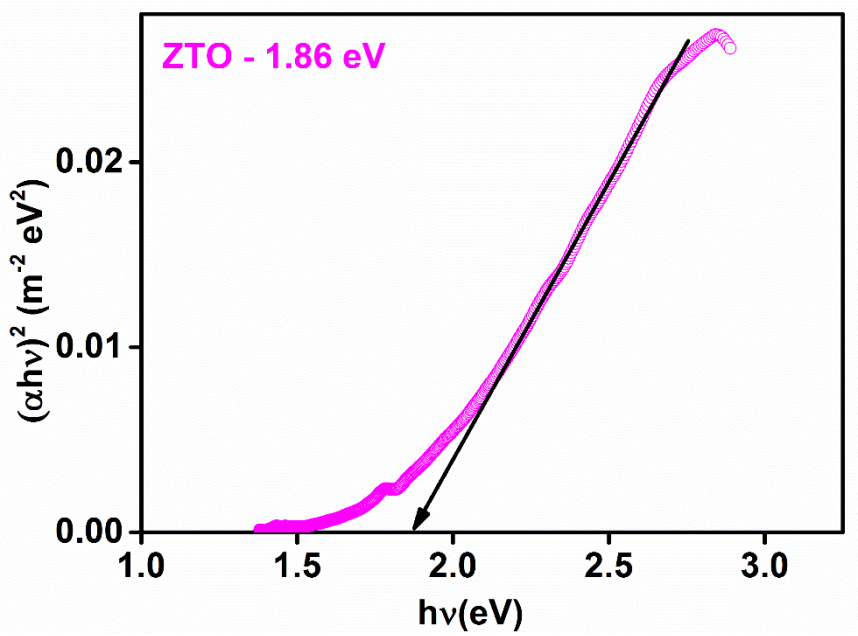

Figure 6.13 Tauc plot of ZTO

6.2.3 Valence band spectrum (VB) and Density of states (DOS)

The valence band XPS spectrum of the compound ZTO shown in Figure 6.14a gives more insight into its density of states. A schematic shown in Figure 6.14b describes the band edge energy positions elucidated with the help of valence band XPS spectrum and optical bandgap.

From the valence band spectrum, the valence band maximum edge obtained is 3.85 eV. The spectrum shows a band tail with a shift of -0.17 eV with respect to the band edge maximum. Combined with the optical bandgap, the conduction band minimum of ZTO is

calculated and is found to be at 2.03 eV. Existence of a conduction band tail, like the valence band tail, due to crystal defects is anticipated[34]. It is attributed here that the defect states near conduction and valence band may form continuum resulting in band tails.

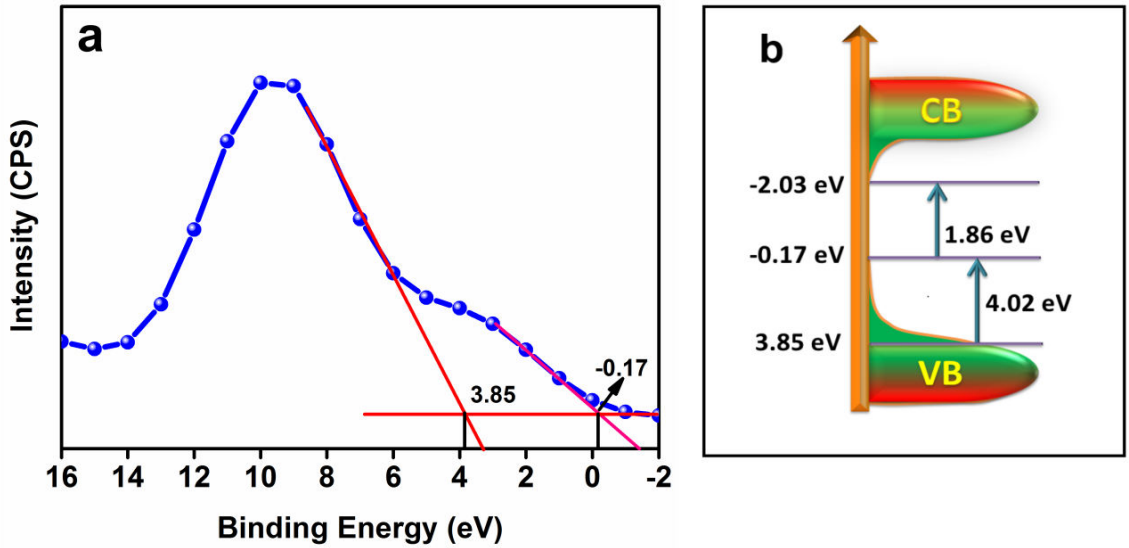

Figure 6.14 Valence band XPS of ZTO (a) and schematic of density of states of ZTO (b)

6.3 APPLICATIONS: PHOTOCATALYSIS

6.3.1 Water treatment - Dye degradation

To compare the activity of photocatalysts, 0.002 wt% aqueous methylene blue dye solution was taken as the model system and the degradation of the dye was monitored within a time frame of 90 minutes as shown in Figure 6.15 (a). 0.05 g photocatalyst was added in to 50 ml of dye solution. This suspension was kept under dark for 30 minutes with stirring to avoid any error due to initial adsorption effect. The stirring in darkness also helps dye adsorption on the surface of the photocatalyst to establish adsorption-desorption equilibrium. After dark analysis, the dye solution was placed inside a photocatalytic reactor under 300 W Xenon lamp. At 15 minutes of periodic exposure, 5 mL aliquots were taken to monitor the dye degradation. The Uv-visible absorption spectra were recorded after centrifuging at 10000 rpm

for 10 minutes to avoid any scattering effect.

Dark adsorption analysis gives 20% primary adsorption of dye on the surface of ZTO. ZTO effectively degrades 95% of MB dye within 90 minutes with a rate constant of 0.00648 min^{-1}. In the absence of photocatalyst only 50% pure MB was found degraded within 90 minutes (Figure 6.15 (b)). The degradation of pure MB is caused by the dissolved oxygen present in the water[35]. The performance stability of the photocatalyst was checked for five consecutive cycles and is shown in Figure 6.15 (c).

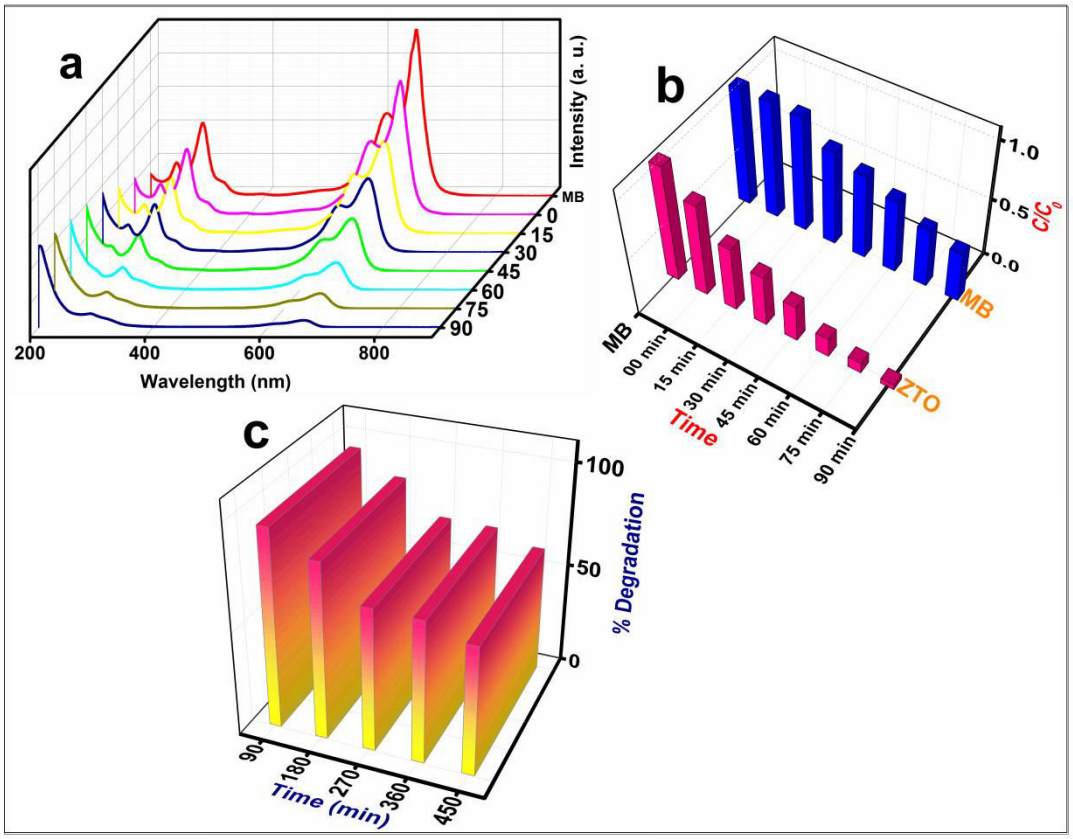

Figure 6.15 (a) Uv-vis spectra of MB photo-degradation in presence of ZTO, (b) Photocatalytic degradation plot of MB with respect to time and (c) Photocatalytic stability of ZTO for five consecutive cycles.

6.3.2 Estimation of reactive oxygen species

Reactive Oxygen Species (ROS) generated from the photocatalysts are mainly responsible for the photocatalytic activity. Florescent method has been applied to detect and quantify the OH^{o} free radicals formed from ZTO during photocatalysis. Terephthalic acid (TTA), a non-fluorescent probe molecule had captured ROS generated from ZTO and converted into fluorescent 2-hydroxyterephthalic acid (HTTA) by hydroxylation. $5x10^{-4}$ M TTA alkaline solution was prepared with NaOH and 50 mL of this solution with 0.01 g photocatalyst was stirred and irradiated for 10 minutes. After irradiation, the solution was centrifuged and takes the photoluminescence spectra of the decanted solution at an excitation wavelength of 315 nm. The intensity of the fluorescence is directly related with the quantity of OH^{o} free radicals captured by TTA. The standard curve obtained before and after light exposure on TTA is depicted in Figure 6.16.

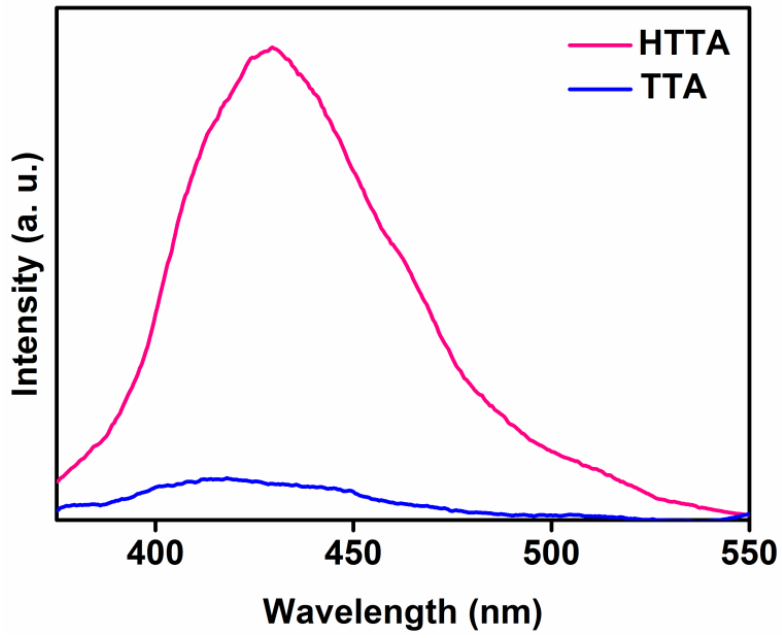

Figure 6.16 Fluorescence spectra of TTA before and after exposure to light

6.3.3 Surface treatment – Contact angle measurements

Ultra wetting surfaces attract special attention because of its broad applications in self-cleaning process[36]. Hydrophilic surfaces behave as anti-fog by forming a homogeneous water

film instead of multiple circular drops. Contact angle measurements were done using the water contact angle measurement (digidrop). The photographs of the contact angle measurements of water with ZTO coated glass surfaces are depicted in Figure 6.17. ZTO powder was mixed with methanol in an agate mortar to make a homogeneous paste. This paste was evenly doctor bladed on to the surface of a glass slide and the film was dried in air. The dynamic contact angle was measured systematically with water on the surface of ZTO film coated over glass substrate. Initially the film exhibited a contact angle of 33.6°. Within hundred seconds the value brought down to 18.5° and finally reaches to 6.4°. Surface with low contact angles make a continuous homogeneous film on the glass substrate and help to avoid optical transmissions[37].

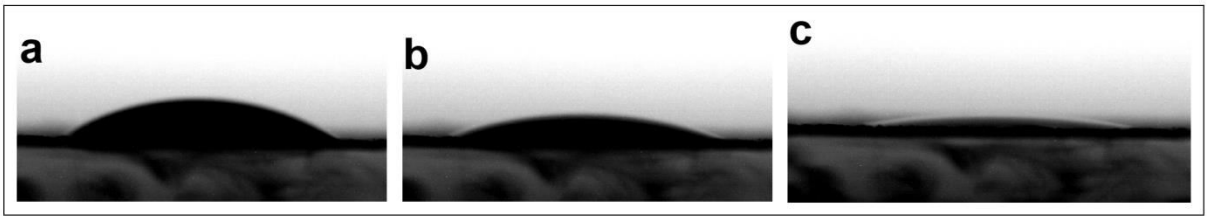

Fig 6.17 Contact angle of ZTO (a) initial (b) within hundred seconds (c) after 2 minutes

6.3.4 Antibacterial activity

The antimicrobial activity of ZTO was evaluated against standard and clinical strain of gram-negative bacterium of *Escherichia. Coli* by the agar well diffusion method[38]. 12 h seed culture was swabbed on the agar dishes using sterile cotton. Required number of wells having diameter 8 mm diameter were punched into the nutrient agar dishes. These wells were filled with water dispersed samples. Clinical disc of Tetracycline (30 mcg/disc- positive control) and distilled water (as negative control) were also used for evaluation. The plates were incubated for 24 h at 37°C inside a temperature controlled incubator in the presence of light (Flourescent lamp; 18W). The zone of inhibition was measured using a zone reader against the test microorganism.

The results show significant growth inhibitory activity of ZTO against *E. coli* compared with that of standard tetracycline (Figure 6.18). Result shows that ZTO exhibit inhibition zone of 25 mm in diameter whereas standard tetracycline exhibit only 24 mm. When flooring tiles are made incorporating these ZTO nanoparticles, the frequent cleaning can be avoided as material undergoes self-cleaning process with the aid of photocatalytic activity. The inhibition of bacterial growth by ZTO takes place with simultaneous processes described below:

1) Bacterial cell wall gets disrupted by the charge neutralization of its surface electric charge, which destroys the nutrients intake of the cell leading to death of the cell[39]
2) Reactive oxygen species released from ZTO leads mechanical damage to the bacterial cell membrane and enter in to intracellular part of the cell ultimately destroying the cell completely[40].

Fig 6.18 Zone of antibacterial inhibition of ZTO against *E. Coli*

The antibacterial activity of pure ZnO was also analyzed to compare the performance (Fig 6.19). It was observed that pure ZnO cannot inhibit the growth of *E. Coli*. The unprecedently growth inhibition of gram negative *E. Coli* by ZTO may be attributed with the positive surface charge of ZTO compared to ZnO.

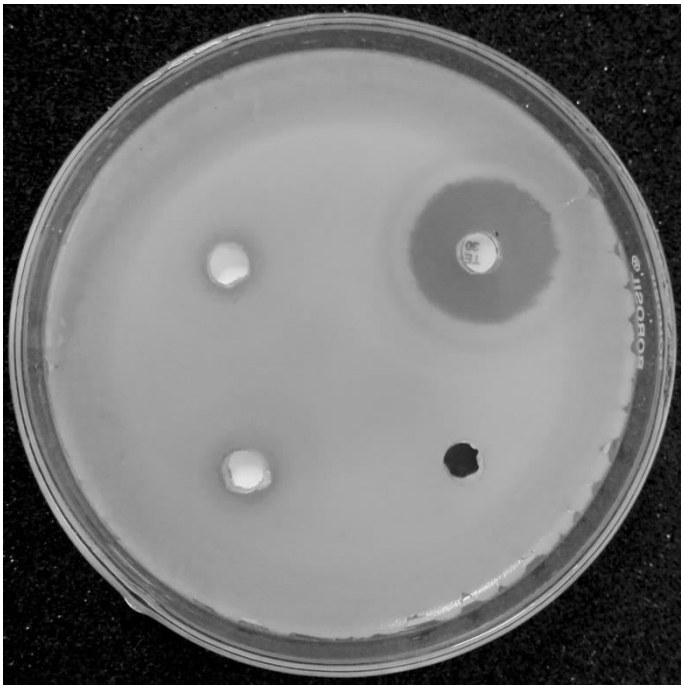

Fig 6.19 Antibacterial activity of ZnO against *E. Coli*

6.4 CONCLUSIONS

In conclusion, we have developed a unique strategy for the synthesis of highly impressive ZTO nanomaterial by adopting robust and vastly reproducible solvothermal method. The material thus synthesized exhibits better dye degradation, superior antibacterial activity and super hydrophilicity. The enhancement in photocatalytic activity can be ascribed to the presence of enormous surface oxygen vacancies and ability to release ROS. The synergistic effect of oxygen vacancies, adsorptivity and broad spectral response contributes to improved photocatalysis. Because of these properties, this material represents a promising photocatalyst for environmental remediation. Moreover, it can be successfully used for various other

futuristic biomedical and sensor applications. We firmly believe that our perspective unravels novel uses of this material.

6.5 References

[1] K. H. Reddy, K. Parida, P. K. Satapathy, *J. Mater. Chem. A,* **2017**, 5, 20359.

[2] Q. Liu, Y. Yan, X. Chu, Y. Zhang, L. Xue, W. Zhang, *J. Mater. Chem. A,* **2017**, 5, 21328.

[3] Priyadharsan, V. Vasanthakumar, S. Karthikeyan, V. Raj, S. Shanavas, P.M. Anbarasan, *J. Photochem. Photobiol. A: Chemistry,* **2017**, 346, 32-45.

[4] J. Garcıa-Fernandez, J. Bartolome, A. Torres-Pardo, A. Peche-Herrero, J. Moreno, J. Ramırez-Castellanos, A. Cremades, J. M. Gonzalez-Calbet, J. Piqueras, *J. Mater. Chem. C,* **2017**, 39, 10176.

[5] R. Ghasemzadeh, M. H. Armanmehr, M. Abedi, D. S. Fateh, Z. Bahreini, J Mol Struct, **2018**, 1151, 106-111.

[6] Y-F. Wang, W-X. Zhao, X-F. Li, D-J. Li, *Electrochim. Acta,* **2015**, 151, 399-406.

[7] Abliz, C-W. Huang, J. Wang, L. Xu, L. Liao, X. Xiao, W-W. Wu, Z. fan, C. Jiang, J. Li, S. Guo, C. Liu, T. Guo, *ACS Appl. Mater. Interfaces,* **2016**, 8, 7862−7868.

[8] J. Wang, X. Li, Y. Xia, S. Komarneni, H. Chen, J. Xu, L. Xiang, D. Xie, *ACS Appl. Mater. Interfaces,* **2016**, 8, 8600−8607.

[9] P. She, S. Yin, Q. He, X. Zhang, K. Xu, Y. Shang, X. Men, S. Zeng, H. Sun, Z. Liu, *Electrochim. Acta,* **2017**, 246, 35-42.

[10] Z. He, Y. Yang, J-W. Liu, S-H. Yu, *Chem. Soc. Rev.,* **2017**, 46, 2732.

[11] S. Lin, W. Li, Z. Chen, J. Shen, B. Ge, Y. Pei, *Nat. Commun.,* **2015**, 7, 10287.

[12] I. Jlassi, H. Elhouichet, S. Hraiech, M. Ferid, *J. Lumin.* **2012**, 132, 832-840.

[13] B. Elgh, N. Yuan, H. S. Cho, D. Magerl, M. Philipp, S. V. Roth, K. B. Yoon, P. Müller-Buschbaum, O. Terasaki, A. E. C. Palmqvist, *APL Materials,* **2014**, 2, 113313.

[14] Z. Yang, Y. Shi, B. Wang, *Appl. Surf. Sci.,* **2017***,* 399*,* 192-199.

[15] D. Chen, Z. Wang, T. Ren, H. Ding, W. Yao, R. Zong, Y. Zhu, *J. Phys. Chem. C,* **2014**, 118, 15300−15307.

[16] Y. Zhao, R. Li, L. Mu, C. Li, *Cryst. Growth Des.,* **2017**, 17, 2923−2928.

[17] D. h. Webber, J. J. Buckley, P. D. Antunez, R. L. Brutchey, *Chem. Sci.,* **2014**, 5, 2498.

[18] L. Schlur, A. Carton, G. Pourroy, *Chem. Comm.,* **2015**, 51, 3367.

[19] V. Briois, Ch. Giorgetti, F. Baudelet, S. Blanchandin, M. S. Tokumoto, S. H. Pulcinelli, C. V. Santilli, *J. Phys. Chem. C*, **2007**, 111, 3253-3258.

[20] B. N. Meethal, N. Pullanjiyot, S. Swaminathan, Mater. Des, **2017**, 130, 426-432.

[21] H-L. Jiang, J-G. Mao, *J. Solid State Chem.* **2008**, 181, 345-354.

[22] J. M. Nawash, K. G. Lynn, *J. Cryst. Growth*, **2008**, 310, 4217-4220.

[23] A. K. Yadav, P. Singh, *RSC Adv.,* **2015**, 5, 67583.

[24] T.Torchynska, B. P. Millan, G. Polupan, M. Kakazey, *Mater. Sci. Semicond. Process.* **2016**, 47, 37–43.

[25] S. Samuel M, J. Koshy, A. Chandran, K. C. George, *Indian J. Pure Appl. Phys.* **2010**, 48 (10), 703–708.

[26] P.-M. Chassaing, F. Demangeot, V. Paillard, A. Zwick, N. Combe, *Appl. Phys. Lett.* **2007**, 91 (5), 53108.

[27] S. Hashimoto, T. Sugie, Z. Zhang, K. Yamashita, M. Noda, *Jpn. J. Appl. Phys.,* **2015**, 54, 10NA12 (1-5).

[28] H. Huang, F. Li, H. Wang, X. Zheng, *RSC Adv.,* 2017, 7, 50056. (b) C.H. Shek, G.M. Lin, J.K.L. Lai, *Nanostruct. Mater.,* **1999**, 11 (7), 831-835.

[29] H. Song, D. Laudenschleger, J. J. Carey, H. Ruland, M. Nolan, M. Muhler, *ACS Catal.* **2017**, 7, 7610−7622.

[30] S. Bera, A. A. M. Prince, S. Velmurugan, P. S. Raghavan, R. Gopalan, G. Panneerselvam, S. V. Narasimhan, *J. Mater. Sci.,* **2001**, 36, 5379-5384.

[31] C. R. Thomas, M. K. Vallon, M. G. Frith, H. Sezen, S. K. Kushwaha, R. J. Cava, J. Schwartz, S. L. Bernasek, *Chem. Mater.* **2016**, 28, 35−39.

[32] J. Fu, S. Song, X. Zhang, F. Cao, L. Zhou, X. Lia, H. Zhang, *CrystEngComm,* **2012**, 14, 2159.

[33] Y. Zhang, N. Zhang, Z-R. Tang, Y-J. Xu, *ACS nano*, **2012**, 6, 9777-9789.

[34] X. Chen, L. Liu, P. Y. Yu, S. S. Mao, *Science*, **2011**, 331, 746-750.

[35] S. G. Ullatil, P. Periyat, *Nanoscale,* **2015**, 7, 19184-19192.

[36] J. Liu, J. Song, G. Wang, F. Chen, S. Liu, X. Yang, J. Sun, H. Zheng, L. Huang, Z. Jin, X. Liu, *ACS Appl. Mater. Interfaces*, **2018**, 10, 7497-7503.

[37] M. W. England, C. Urata, G. J. Dunderdale, A. Hozumi, *ACS Appl. Mater. Interfaces*, **2016**, 8, 4318−4322.

[38] W. Yang, E. Fortunati, D. Gao, G. M. Balestra, G. Giovanale, X. He, Luigi Torre, J. M. Kenny, D. Puglia, *ACS Sustainable Chem. Eng.,* **2018**, 6, 3502-3514.

[39] Y. Xie, Y. He, P. L. Irwin, T. Jin, X. Shi, *Appl. Environ. Microbiol.* **2011**, 77(7), 2325–2331.

[40] V. L. Prasanna, R. Vijayaraghavan, *Langmuir,* **2015**, 31, 9155−9162.

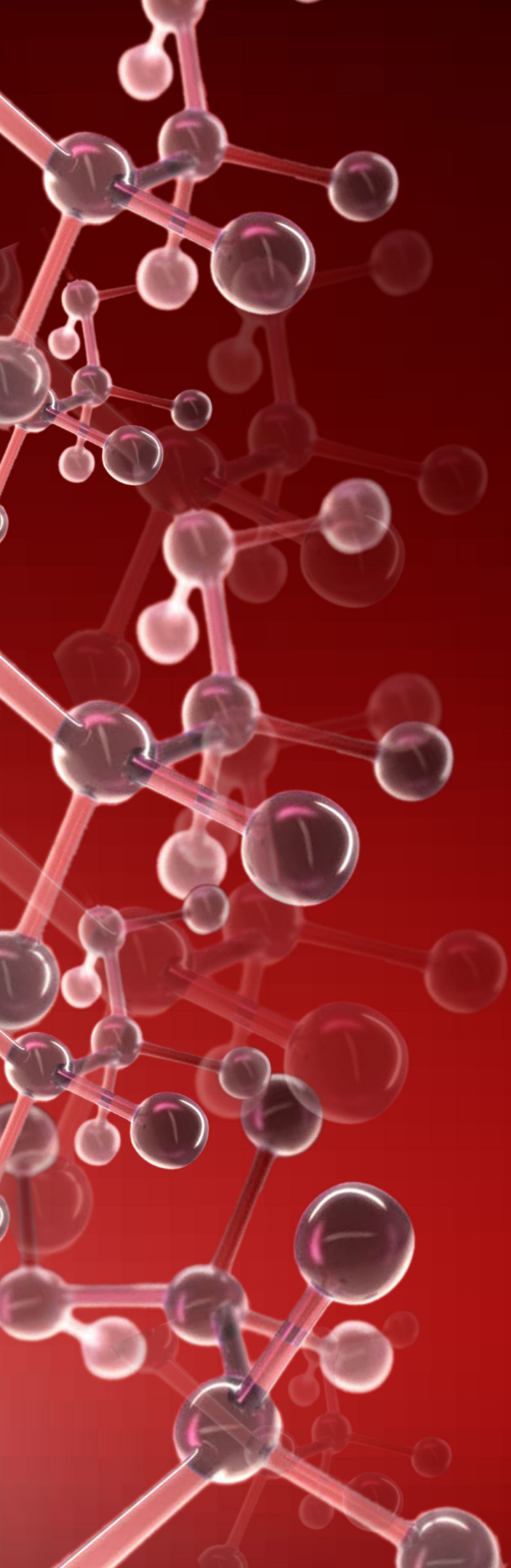

Chapter 7

Conclusion & Future Outlook

7 Conclusion & Future outlook

This work attempts to explore novel approaches to make different ZnO hybrids, using minimum precursors, for efficient photocatalysis. Structural, photophysical and physicochemical properties of the prepared materials were analyzed in detail using various characterization techniques.

One dimensional ZnO with varying surface properties has been prepared by changing zinc to beta-Aminoethylamine ratio of 2:1, 1:2 and 1:1 (21ZE, 12ZE and 11ZE). Various analytical tools were used to study the structural, morphological, photophysical and chemical properties of these samples. Study on the photocatalytic activity of these ZnO nanostructures shows that 11ZE gives stable photocurrent behaviour with better photocatalytic performance by showing hundred percentage degradation of methylene blue. Performances of these three ZnO nanostructures on methylene blue degradation were correlated with the surface chemisorbed oxygen, oxygen related defect density and slow excitonic recombinations. Compared to 11ZE, 21ZE shows smooth surfaced nanotubes whereas; 12ZE shows completely distorted nanotube structure because of high etching rate by the edamine. Among the three samples, 11ZE surface accommodates more chemisorbed oxygen and high dye adsorption capability. All these factors indirectly affect the photocatalytic degradation of methylene blue by producing more superoxides with enhanced carrier lifetime in the oxide structure under illumination. The reactive oxygen species generated from 11ZE was also estimated using terephthalic acid as a probe molecule. Super hydrophilicity of 11ZE films on glass substrate was checked from static mode contact angle measurements and confirms its

self-cleaning and surface wettability nature. The hydrophilic nature of 11ZE also put promising material for anti-fogg applications. Among the three ZnO samples, 11ZE exhibit good overall performance. Further, nanocomposites were prepared by modifying 11ZE into its hybrids by the incorporation of non-metals.

Carbon embedded ZnO nanocomposites were prepared by adopting the self-same method employed in ZnO synthesis. Uniform mixing of the precursors during the formation of the hybrids got ensured through the consistent stirring of the reaction mixture. A conducting polymer (polyaniline), a non-conducting polymer (polyvinylpyrrolidone) and a blend of these two polymers were chosen for the surface modification of ZnO. The synthesized nanocomposites were named as PVZ, PNZ and PPZ. Phase pure carbon embedded short nanotubes of ZnO were prepared by post thermal treatment of these polymer wrapped ZnO nanomaterials and confirmed from various characterization techniques. The calcined products are named as CPVZ, CPNZ and CPPZ. The presence of carbon and absence of nitrogen were verified from X-ray photoelectron spectroscopy (XPS). Enormous surface oxygen vacancies were confirmed from various characterization techniques such as photoluminescence spectra, Raman spectra and XPS. The photocatalytic activity of these nanotubes was evaluated through the degradation of a textile dye. These carbon doped ZnO nanotubes become more Lewis acidic and found to be more photoactive than pure ZnO. Among these three photocatalysts, CPVZ exhibit excellent photocatalytic activity than CPPZ and CPNZ. Smaller particle size, higher adsorption capability and presence of crystal defects support CPVZ to become an efficient photocatalyst. Moreover all three samples exhibit super hydrophilic behavior so that they can be used as anti-fog coatings. Synergetic effect of carbon induced mid-gap energy levels and presence of oxygen vacancies suppress the exciton recombination rate and shows better photocatalytic activity. Estimation of reactive oxygen species, using terethalic acid probe, ratified the results obtained from photocatalytic

performances.

Bromine doped ZnO short nanotubes were also developed systematically through above mentioned aqueous mediated template-free sol precipitation route. Samples with different bromine percentage (2, 4, 6, and 8 %) were tried to get 2DZ, 4DZ, 6DZ and 8DZ samples. Bromine induced defects efficiently support the photocatalytic activity of the doped samples than undoped ZnO. Mutual performances of both these defects exhibit superior photocatalysis in 6DZ towards dye degradation analysis. Moreover, the prepared photocatalysts exhibit good recyclability and stability under ambient conditions. The sample, 6DZ exhibits super-hydrophilicity for the anti-fog application. In addition, the ability of 6DZ to inhibit *E. Coli* pathogenic microbes brings an innovative hygienic solution and can be to introduced into floor or wall tiles for self-cleaning characteristics.

Bromine doped ZnO synthesis and its application study provides good insights about the role of defect chemistry of this material. The doping of nonmetals at the interstitial sites of ZnO surface creates additional trap states along with already existed oxygen vacancies within the ZnO bandgap. These crystal defects pave the way for the migration and separation of photogenerated electrons and holes thereby promote the photocatalysis. Additionally these midgap energy levels impart carrier generations to speed up the photocatalysis process.

Finally a ternary compound of ZnO, highly impressive $Zn_2Te_3O_8$ nanomaterial, was developed by adopting a unique synthetic strategy by adopting robust and vastly reproducible solvothermal method. The material thus synthesized exhibits better dye degradation, superior antibacterial activity and super hydrophilicity. The photocatalytic activity in ZTO can be ascribed to the presence of enormous surface oxygen vacancies and ability to release ROS. The synergistic effect of oxygen vacancies, adsorptivity and broad spectral response contributes to improved photocatalysis. Because of these properties, this material represents a

promising photocatalyst for environmental remediation. We firmly believe that our perspective unravels novel uses of this material.

Moreover these synthesized nanomaterials can be successfully used for various other futuristic biomedical and sensor applications. Surface engineering of these materials remains to be explored comprehensively by varying reaction temperature and changing the alkaline precursor. Metal nanoparticles decorated ZnO nanosystems are another avenue for advanced photocatalytic technology. Reduced graphene oxide or carbon dots can be incorporated with these doped systems for enhanced photocatalytic performances.